

The Electron Transfer Chemistry of Nitrosyl Complexes

Von der Fakultät Chemie der Universität Stuttgart
zur Erlangung der Würde eines
Doktors der Naturwissenschaften
(Dr. rer. nat.)
genehmigte Abhandlung

vorgelegt von

Priti Singh
aus Varanasi (Indien)

Hauptberichter:

Prof. Dr. W. Kaim

Mitberichter:

Prof. Dr. Th. Schleid

Tag der mündlichen Prüfung:

01 Feb. 2008

INSTITUT FÜR ANORGANISCHE CHEMIE DER UNIVERSITÄT STUTTGART

2008

TO MY PARENTS

ACKNOWLEDGEMENTS

This work was completed from September 2004 to January 2008 in the department of Inorganic Chemistry, University of Stuttgart.

First I would like to thank Prof. Dr. W. Kaim, who provided me with the opportunity and the resources to be as creative as I like, inspiring me to do my best, and making sure I am progressing along a forward path. It is these things that have given me the most confidence in my scientific abilities.

Next I would like to take the opportunity to thank all the people who had helped me in one way or another to finish this PhD work.

Prof. N. Singh and Prof S. SenGupta from BHU and Prof. S. N. Datta, Prof P. Mathur and Prof. G. K. Lahiri from IIT Bombay for all the early help with learning chemistry and for always believing in me.

My special thanks to Dr. B. Schwederski for helping me with most in Stuttgart, from teaching me how to run EPR spectrometer to help me with the German translation of the summary of this thesis and also for helping me in all the administrative works,

Prof. Dr. E. Roduner for encouraging me all through my graduate carrier,

Dr. E. Bulak for introducing me to Schlenk line at Stuttgart,

Dr. M. Sieger for helping me in the beginning with the synthetic work,

Mr. J. Fiedler from the Heyrovsky Institute of Physical Chemistry for the help for IR and UV/VIS/NIR spectroelectrochemical measurements,

Dr. S. Zalis from the Heyrovsky Institute of Physical Chemistry for theoretical calculations,

Dr. C. Duboc from the Grenoble High Field Laboratory for her help with high field EPR measurements,

Prof. G. K. Lahiri for the helpful discussion during his visit to Stuttgart and also for the initial correction of this thesis,

Dr. F. Lissner and PD Dr. M. Niemeyer for crystallographic data collection and for solving of crystal structures,

Prof. Dr. C. -Y. Su for solving the structure,

Ms. K. Török for NMR measurements,

Ms. B. Förtsch for elemental analyses,

Dr. J. Opitz, Mr. J. Trinkner and Ms. K. Wohlbold for the mass spectroscopic measurements,

Mr. S. Pana and Mr Münch to solve the electronic problems,

Mr. M. Leboschka and Mr. O. Sarper for solving computer problems,

My research student Ms. C. Schlawne for doing part of the synthetic work,

Mr. J. Schnödt for the German translation of the part of the summary of this thesis,

Mr. Naegelein, Mr. Wesch, Mr. Lenz, Mr. Zahl, Mr. Heim, Mr. Achstetter and Mr. Jergler for their anytime help related with chemicals, glasswares and mechanical work,

Mr. C. Lipp, Dr. A. N. Maity, , Dr. S. Chikkali and Mr. A. K. Das for helping me in various ways with their suggestions,

Dr. A. Gabriellsson and Dr. S. Ye for fruitful discussion on my chemistry.

I would also like to thank

The Graduate College "Modern Methods of Magnetic Resonance in Materials Science" for constantly supporting my travels for various scientific projects,

All the past and present members of the group of Prof. Kaim for creating a nice environment to work. Working in this group helped me to develop into an independent and diversified scientist.

My special thanks to my parents. Through their works and deeds, they always tell me how important it is to see good sides in the trying times and stay true to my aspirations. I cannot imagine how I could come this far without their unconditional love and support,

My sister Nitu and my brother Abhinav for their love,

Ina, Marco, Johannes and Philipp for being the nicest housemates and for making my life much easier at Stuttgart,

My good friends at Stuttgart, Sunitha and Gurneet, who made my stay at Stuttgart more enjoyable.

Finally I would like to thank my beloved Ajeet, without his love, support and encouragement, this work would not have been completed.

CONTENTS

1. Introduction	1
2. The Metal-NO Interaction in the Redox Series $[\text{Cl}_5\text{M}(\text{NO})]^{n-}$, $n = 1-3$ and <i>cis</i>- $[(\text{bpy})_2(\text{Cl})\text{Os}(\text{NO})](\text{PF}_6)_2$	6
2.1. Introduction	6
2.2. Syntheses and Characterisation	7
2.3. Crystal Structure	9
2.4. Cyclic Voltammetry	10
2.5. IR Spectroelectrochemistry	13
2.6. EPR Spectroelectrochemistry	17
2.7. UV/VIS Spectroelectrochemistry	20
2.8. DFT Calculations	21
2.9. Conclusions and Outlook	24
3. Ruthenium Nitrosyl Porphyrin Complexes: Effect of Axial Ligation on Electron Transfer Processes	26
3.1. Introduction	26
3.2. Syntheses and Characterisation	27
3.3. Crystal Structure	29
3.4. Electrochemistry	31
3.5. IR Spectroelectrochemistry	34
3.6. EPR Spectroelectrochemistry	36
3.7. UV/VIS/NIR Spectroelectrochemistry	40
3.8. DFT Calculations	43
3.9. Conclusions and Outlook	45

4. Mononuclear Ruthenium Nitro, Nitrosyl and Acetonitrile Complexes with 2,2'-Bipyrimidine and 2,2':6',2''-Terpyridine	46
4.1. Introduction	46
4.2. Syntheses and Characterisation	47
4.3. Crystal Structures	52
4.4. Electrochemistry	56
4.5. IR Spectroelectrochemistry	59
4.6. Multifrequency EPR Spectroscopy	61
4.6.1. Theory	61
4.6.2. Results	64
4.7. UV/VIS/NIR Spectroelectrochemistry	69
4.8. DFT Calculations	71
4.9. Conclusions and Outlook	73
5. Series of Dinuclear Ruthenium Complexes with 2,2'-Bipyrimidine as Bridging Ligand	75
5.1. Introduction	75
5.2. Syntheses and Characterisation	80
5.3. Crystal Structure	87
5.4. Cyclic Voltammetry	92
5.5. UV/VIS/NIR Spectroelectrochemistry	95
5.6. EPR Spectroelectrochemistry	101
5.7. Conclusions and Outlook	106
6. Experimental Section	107
6.1. Instrumentation	107

6.2. DFT Calculations	109
6.3. Solvents and Working Conditions	111
6.4. Syntheses	112
6.5 Crystallography	119
7. Summary	128
8. Zusammenfassung	137
Appendix	147
Bibliography	
Abbreviations	
List of Publications	
Curriculum Vitae	

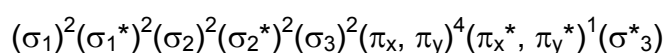
CHAPTER 1

Introduction

The chemistry of nitrogen monoxide (NO), most commonly referred to as nitric oxide, has historically been a topic of great interest to inorganic chemists.^[1,2] After the recent discovery of various essential physiological functions^[3,4,5,6,7,8] of "NO" it has taken on added significance not only in pertinent medical and biosciences research but also in the coordination chemistry^[9,10,11,12,13,14] of the nitrosyl ligand because the controlled generation ("delivery") and uptake ("scavenging") of free NO• in many physiological processes involves the interaction of NO with metal complexes such as the heme group^[15] or artificial systems designed for pharmaceutical purposes.^[16,17,18]

In addition to the general biological significance^[19,20] and the pharmaceutical potential,^[16,21] the catalytic functions of metal nitrosyl complexes as intermediates in technical processes^[22,23] and the photochemistry with respect to metastable non-conventional M(NO) binding^[24] are also of current interest.

In order to understand the vital role of the NO molecule in physiological processes, one needs to look into the electronic property of nitric oxide. NO is a fifteen electron molecule with one unpaired electron residing in the π^* molecular orbital:



This electronic configuration explains the high reactivity of the NO molecule, particularly the formation of nitrosonium cation (NO⁺) on oxidation and the reduction to nitroxide anion (NO⁻), making it a "non-innocent" ligand^[25,26] (Scheme 1.1).



Scheme 1.1. Redox alternatives of the nitrosyl ligand, making it a potentially "non-innocent" ligand.

Transition metal nitrosyl complexes span variable geometries, coordination numbers and electronic properties due to the differences in electronic configurations of the metal centres and possible covalent MNO interactions. In recognition of the covalent nature of the M–N–O interaction and the difficulty of assigning formal oxidation states to the metal and the NO in nitrosyl complexes, Enemark and Feltham proposed a formalism to describe metal nitrosyl complexes which treated the metal nitrosyl as a single entity.^[2] This was represented as $\{M(NO)_x\}^n$, (regardless of the coligands), in which n is the total number of valence electrons associated with the metal d and π^* (NO) orbitals. Notwithstanding this pragmatic scheme, it is still essential to reflect the charge distribution between metal and NO, and therefore, although the $\{MNO\}^x$ moieties are usually rather delocalised, limiting structures are frequently employed for describing the electronic structure in terms of different oxidation states of the NO ligand to interpret the electronic and magnetic properties of metal nitrosyl complexes.

Most of the known stable "nitrosyl" complexes are assumed to contain the diamagnetic π acceptor ligand nitrosonium, NO^+ ,^[9,27,28,29] but there are cases when NO^\bullet or NO^- (nitroxide) can be reasonably postulated as ligands in transition metal complexes.^[30,31] Establishing the actual form of coordinated NO often requires a variety of physical methods^[32] such as IR, EPR, NMR, UV/VIS, resonance Raman, magnetic circular dichroism (MCD), etc., and theoretical calculations.

The reactivity of coordinated nitric oxide in possible redox states of the nitrosyl molecule, NO^+ , NO^\bullet , and NO^- , in the complex framework of (AL)M–NO depends on a variety of factors, including the nature of the metal ions, the oxidation state of the metal and the ancillary ligands (AL). By varying the metal and also the ancillary ligands one can change and tune the reactivity of coordinated NO in metal nitrosyl complexes.

In order to explore the reactivity of coordinated nitric oxide in different oxidation states, the attention of this PhD work is focussed on the synthetic aspects and the structural, spectroscopic and electronic properties of various transition metal nitrosyl complexes. All complexes are characterised and studied using various spectroscopic and electrochemical techniques.

Chapter 2 describes the synthesis and characterisation of the new complex $(n\text{-Bu}_4\text{N})_2[\text{Cl}_5\text{Os}(\text{NO})]$. In addition, it also describes the structural characterisation of the precursor $(\text{Ph}_4\text{P})_2[\text{Cl}_5\text{Os}(\text{NO})]$. The aim of this study was to understand the electronic structures of the two-step redox system $[\text{Cl}_5\text{Os}(\text{NO})]^{n-}$ ($n = 1-3$) and to compare it with the previously studied^[33] related one-step redox systems $[\text{Cl}_5\text{Ru}(\text{NO})]^{n-}$ and $[\text{Cl}_5\text{Ir}(\text{NO})]^{n-}$ ($n = 1, 2$). Chapter 2 also describes the electrochemical and spectrochemical studies on the compound $\text{cis}[(\text{bpy})_2\text{ClOs}(\text{NO})]^{2+/+}$, where the absence of a chloride ligand in *trans* position to NO could enhance the stability of the reduced form and could be used as a reference for EPR and IR data.

Chapter 3 describes studies of ruthenium nitrosyl porphyrins. These synthetic metalloporphyrins were studied as models to understand the interaction of NO with heme, which is the key factor of many physiological processes involving nitric oxide. Extensive electrochemical and spectroelectrochemical studies on structurally characterised $[\text{Ru}(\text{TPP})(\text{NO})(\text{H}_2\text{O})]\text{BF}_4$ and on $[\text{Ru}(\text{TPP})(\text{NO})(\text{X})]\text{BF}_4$ where TPP = tetraphenylporphyrin and X = different pyridines, provide an opportunity to investigate the influence of the axial ligands on the electron transfer processes.

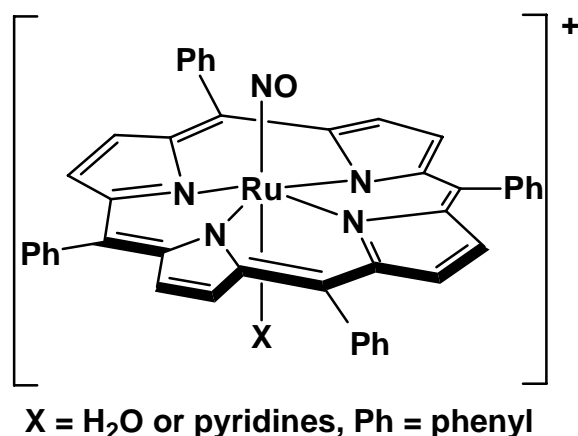


Figure 1.1. Ruthenium nitrosyl porphyrin complexes.

Chapter 4 deals with the mononuclear ruthenium nitro and nitrosyl complexes with the π acceptor ligands 2,2'-bipyrimidine (bpym) and 2,2':6',2''-terpyridine (terpy) (Figure 1.2). These complexes were studied by means of various electrochemical

and spectroelectrochemical methods such as cyclic voltammetry, polarography, UV/VIS, IR spectroelectrochemistry and multifrequency EPR spectroscopy. The studies of these complexes were aimed at the investigation of conformational isomerism in the $\{\text{RuNO}\}^7$ system with the help of high-field EPR, here W-band (95 GHz) and G-band (190 GHz) EPR. The requirement for such a study, a $\{\text{RuNO}\}^7$ complex with sufficient chemical stability in high concentration could be found in the one-electron reduced form of the new complex $[\text{Ru}(\text{NO})(\text{bpym})(\text{terpy})](\text{PF}_6)_3$. Resolution of the g-anisotropy (Δg) by carrying out measurements at higher frequencies provides most sensitive EPR parameters to investigate the possible conformers in $\{\text{RuNO}\}^7$ moities.

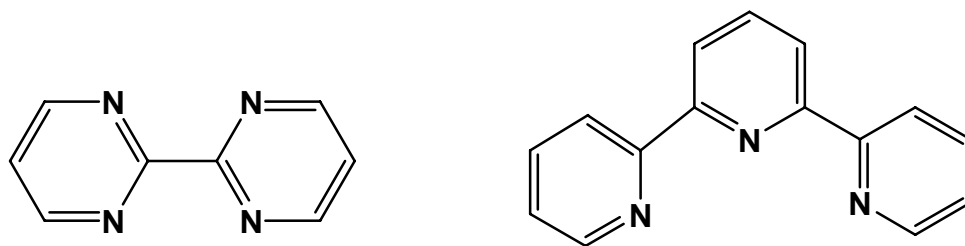


Figure 1.2. The ligands 2,2'-bipyrimidine (left) and 2,2':6',2''-terpyridine (right).

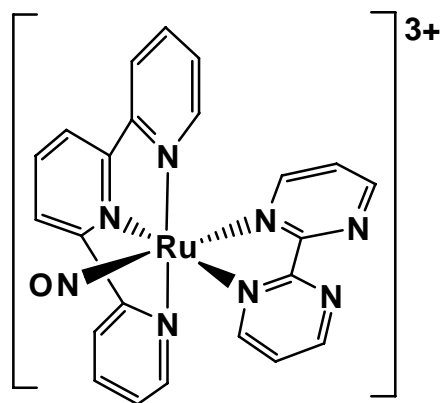


Figure 1.3. The mononuclear ruthenium nitrosyl complex with bpym and terpy.

In Chapter 5, the research is extended to molecule-bridged dinuclear complexes with the aim to study bridging ligand mediated strong intermetallic electronic coupling in their mixed valent state(s) because of the potential application in:

- (i) fabricating molecular electronics devices such as molecular size wires, rods and sensors,^[34,35,36]
- (ii) understanding biological processes,^[37]
- (ii) theoretical studies on electron transfer and charge transfer kinetics.^[38]

Attempts were made to prepare the dinuclear bpym-bridged dinitrosyl compound with terpy as ancillary ligand from the $\{(\mu\text{-bpym})[\text{Ru}(\text{NO}_2)(\text{terpy})]_2\}^{(2+)}$ because this would provide the possibility to study the ligand-mediated interaction of the complex entities $\{\text{RuNO}\}^n$ rather than mere metal centres. The electronic coupling between the metal centres in $\{(\mu\text{-bpym})[\text{RuCl}(\text{terpy})]_2\}^{(2+)}$ and $\{(\mu\text{-bpym})[\text{Ru}(\text{NO}_2)(\text{terpy})]_2\}^{(2+)}$ was probed by cyclic voltammetry, UV/VIS/NIR spectroelectrochemistry, and via EPR investigations.

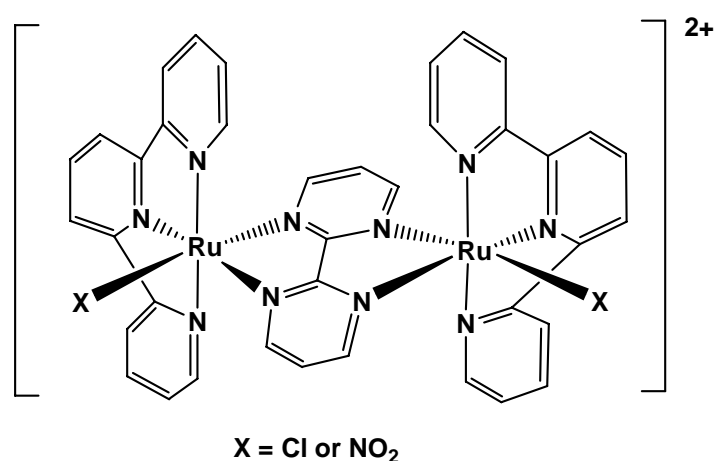


Figure 1.4. Bpym-bridged dinuclear ruthenium complexes, shown in *syn* configuration.

The aim of this research was to explore the field of coordination chemistry of the "non-innocent" nitrosyl ligand by means of chemical variations and advanced methods such as spectroelectrochemistry, high-field EPR spectroscopy, and theoretical calculations.

CHAPTER 2

The Metal-NO Interaction in the Redox Series $[\text{Cl}_5\text{M}(\text{NO})]^{n-}$, $n = 1-3$ and *cis*- $[(\text{bpy})_2\text{ClOs}(\text{NO})](\text{PF}_6)_2$

2.1. Introduction

The chemistry of transition metal nitrosyl complexes, particularly with rare platinum metals, have attracted increasing attention because of their interesting electron transfer properties, pollution controlling abilities and catalytic functions.^[22,23,39,40,41] As an example of catalytic function of transition metal complexes, the systems $[\text{Cl}_5\text{M}(\text{NO})]^{2-}$, $\text{M} = \text{Ru}, \text{Os}$, have been proposed^[42,43] as image contrast enhancing photoelectron trapping dopants in AgCl matrix. Also, $[\text{Cl}_5\text{Ir}(\text{NO})]^{2-}$ has been recently reported as a powerful reagent for the nitrosation of a variety of organic compounds.^[40]

In contrast to numerous studies on iron nitrosyl complexes^[44,45,46,47,48,49] and still many reports on ruthenium compounds^[50,51,52,53,54,55] containing the $\text{NO}^+/\text{NO}^\bullet$ ligand there have been far fewer investigations for nitrosylosmium species.^[56,57,58,59,60,61] Porphyrin^[57] and bipyridine complexes^[58] and their redox behaviour are known, and for simple systems such as $[\text{X}_5\text{Os}(\text{NO})]^{2-}$ ($\text{X} = \text{Cl}, \text{Br}, \text{I}$)^[59] and $[(\text{CN})_5\text{Os}(\text{NO})]^{2-}$ neighbouring redox states could be characterised by EPR spectroscopy.^[60,61]

As mentioned in Chapter 1, the reactivity of coordinated nitric oxide in metal nitrosyl complexes depends on the nature of the metal ions and their oxidation state. Thus, a quantitative understanding of the relative roles of metal in determining the reactivity of coordinated NO with its possible NO^+ , NO^\bullet , NO^- ^[62] and potentially even more negative^[63] oxidation states is essential to understand the catalytic function and reactivity of various metal nitrosyl complexes.

In this Chapter, following a previous study from our group (Kaim *et al.*)^[33] on the $[\text{Cl}_5\text{Ru}(\text{NO})]^{n-}$ and $[\text{Cl}_5\text{Ir}(\text{NO})]^{n-}$ redox pairs ($n = 1, 2$), experimental and

computational results for the potential two-step redox system $[\text{Cl}_5\text{Os}(\text{NO})]^{n-}$ ($n = 1-3$) and for the reference compound $\text{cis}-[(\text{bpy})_2\text{ClOs}(\text{NO})]^{2+/+}$, will be described.

As will become apparent by the results described, the absence of a chloride ligand in *trans* position to NO enhances the stability of the reduced form and allowed us to use this system as a reference for EPR and IR data. The following points will be addressed for $[\text{Cl}_5\text{Os}(\text{NO})]^{n-}$ in comparison to the ruthenium and iridium systems:

- (i) The wide variation of redox potentials,
- (ii) structural aspects in correlation with electrochemical reactivity,
- (iii) the site of electron transfer as evident from low-temperature EPR and IR spectroelectrochemistry,
- (iv) the spin distribution in paramagnetic states as calculated and reflected by g tensor anisotropy,
- (v) the nature of excited states as calculated and as deduced from spectroscopy,
- (vi) configurational aspects of NO^+ binding to osmium(III) (N vs O or η^2 -NO coordination), and
- (vii) conformational aspects of NO^\bullet binding to osmium(II) (eclipsed vs staggered arrangement)^[45,50] in relation to solution and solid state matrix EPR studies.^[42]

Complementing the rapidly increasing work on the potentially useful nitrosylruthenium compounds^[50] by research on osmium analogues draws attention on the established differences between the two metals, viz., on the preference for higher oxidation states and on stronger π back donation from lower oxidation states as well as on the much higher spin-orbit coupling constant of the heavier homologue. In view of the remarkably invariant EPR characteristics of the $\{\text{RuNO}\}^7$ configuration^[50] it is also of interest to study more osmium systems and to interpret the results using DFT approaches. Assigning oxidation states – if only approximate – may be important in estimating and understanding the properties and reactivities of nitrosyl complexes.

2.2. Syntheses and Characterisation

The $[\text{Cl}_5\text{Os}(\text{NO})]^{2-}$ ion was initially obtained as the bis(tetraphenylphosphonium) salt according to the literature,^[59] where the reductive nitrosylation reaction of OsO_4 has

been used in presence of $\text{NH}_2\text{OH}\cdot\text{HCl}$ and $\text{C}_2\text{O}_4^{2-}$ in a slightly acidic medium under aqueous aerobic conditions (Figure 2.2.1). However, the PPh_4^+ ion is irreversibly reduced around -2.1 V against ferrocenium/ferrocene, in a similar potential range as $[\text{Cl}_5\text{Os}(\text{NO})]^{2-}$. Therefore, $(n\text{-Bu}_4\text{N})_2[\text{Cl}_5\text{Os}(\text{NO})]$ was prepared through cation exchange and characterised by IR, UV/VIS spectroscopy and elemental analyses (Chapter 6). The complex $(n\text{-Bu}_4\text{N})_2[\text{Cl}_5\text{Os}(\text{NO})]$ shows a NO stretching band at $\nu(\text{NO}) = 1802$ cm^{-1} in the IR and absorption at 335, 371, 437, 495 and 573 nm in the ultraviolet-visible spectrum. The weak absorptions of $(n\text{-Bu}_4\text{N})_2[\text{Cl}_5\text{Os}(\text{NO})]$ in the visible at 573, 495 and 437 nm are assigned as metal-to-ligand charge transfer and ligand-to-ligand charge transfer (MLCT/LLCT) transitions to the doubly degenerate $\pi^*(\text{NO})$ LUMO.

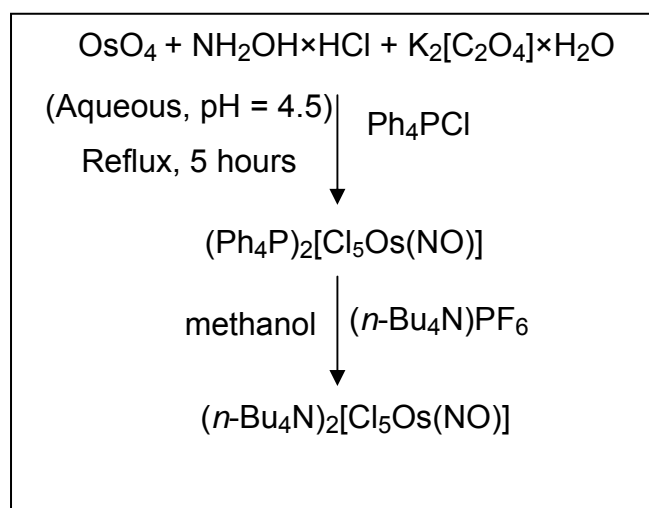


Figure 2.2.1. Synthesis of $(n\text{-Bu}_4\text{N})_2[\text{Cl}_5\text{Os}(\text{NO})]$.

The compound $\text{cis}-[(\text{bpy})_2\text{ClOs}(\text{NO})](\text{PF}_6)_2$ was prepared according to the literature,^[58] following the reaction scheme shown in Figure 2.2.2 and studied by electrochemical and spectroelectrochemical methods.

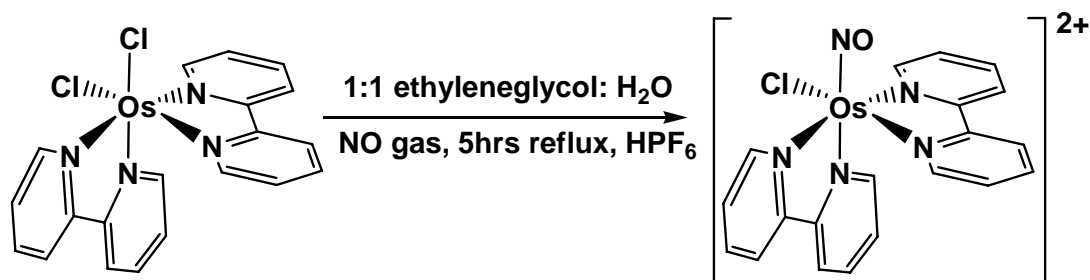


Figure 2.2.2. Synthesis of $\text{cis}-[(\text{bpy})_2\text{ClOs}(\text{NO})](\text{PF}_6)_2$.

2.3. Crystal Structure

The precursor $(\text{Ph}_4\text{P})_2[\text{Cl}_5\text{Os}(\text{NO})]$ was characterised by single-crystal X-ray crystallography. Brown crystals suitable for single-crystal X-ray crystallography were grown by recrystallisation from acetonitrile solution. Figure 2.3.1 shows the molecular structure of the dianion in the crystal of $(\text{Ph}_4\text{P})_2[\text{Cl}_5\text{Os}(\text{NO})]\times 4\text{CH}_3\text{CN}$ at 100 K. Important crystallographic data and final R values are listed in Chapter 6. Unfortunately, the quality of the crystals was relatively poor (structural disorder), nevertheless, the essential data are compared in Table 2.3.1 with DFT calculated values. Table 2.3.1 also includes calculated results for the oxidised ($n = 1$) and reduced forms ($n = 3$) of the redox system $[\text{Cl}_5\text{Os}(\text{NO})]^{n-}$. The structure of the $(\text{PPh}_4)_2[\text{Cl}_5\text{Os}(\text{NO})]$ is established as an $\{\text{MNO}\}^6$ species^[2] with almost linear OsNO arrangement at $178.5(8)^\circ$. Even considering rather high e.s.d. values the comparison between experiment and calculation reveals significant deviations for the $\text{Os}-\text{N}$ and $\text{Os}-\text{Cl}$ bonds, calculated too short and too long, respectively. Like the $\text{N}-\text{O}$ distance (calculated too long) these results indicate an exaggerated degree of metal-nitrosyl π back donation by the DFT approach.

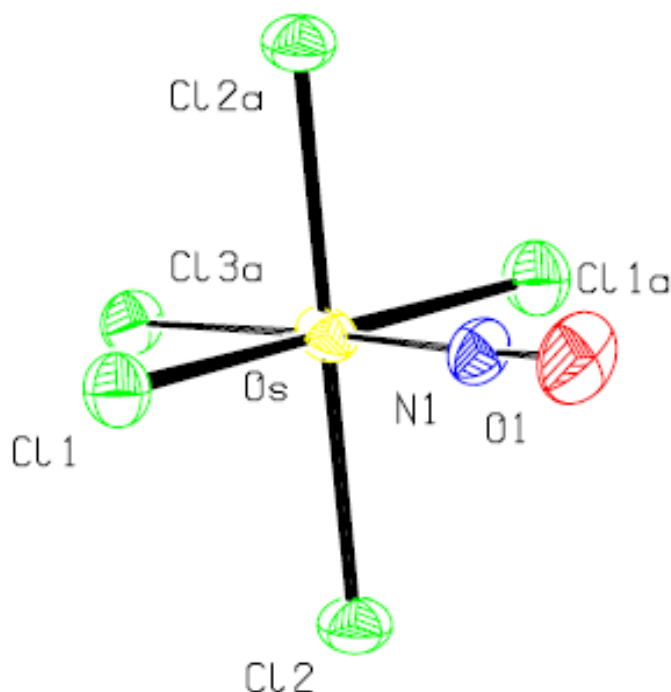


Figure 2.3.1. Molecular structure of the dianion in the crystal of $(\text{Ph}_4\text{P})_2[\text{Cl}_5\text{Os}(\text{NO})]\times 4\text{CH}_3\text{CN}$ at 100 K.

Table 2.3.1. Selected DFT (ADF/BP) calculated bond lengths (Å) and M–N–O angles (deg) within $[\text{Cl}_5\text{Os}(\text{NO})]^{n-}$ complexes

	$[\text{Cl}_5\text{Os}(\text{NO})]^-$	$[\text{Cl}_5\text{Os}(\text{NO})]^{2-}$		$[\text{Cl}_5\text{Os}(\text{NO})]^{3-a}$
	DFT	DFT	exp.	DFT
M–N	1.759	1.733	1.830(5)	1.808
M–Cl _{ax}	2.339	2.392	2.270(1)	2.613
M–Cl _{eq} ^b	2.374	2.444	2.387(4) ^b	2.479 ^c 2.552
N–O	1.170	1.185	1.147(4)	1.246
M–N–O	179.2	180.0	178.5(8)	143.1

^a Energy minimum (staggered conformation).

^b Average value.

^c Cl_{eq} atoms closer to NO ligand.

2.4. Cyclic Voltammetry

Since the PPh_4^+ ion is irreversibly reduced around -2.1 V vs. $\text{FeCp}_2^{+/0}$, in a similar potential range as $[\text{Cl}_5\text{Os}(\text{NO})]^{2-}$, the $(n\text{-Bu}_4\text{N})_2[\text{Cl}_5\text{Os}(\text{NO})]$ salt was prepared through ion exchange. At -70 °C in $n\text{-PrCN}/0.1$ M $n\text{-Bu}_4\text{NPF}_6$ ($n\text{-PrCN}$ = n -butyronitrile) solution the well soluble $(n\text{-Bu}_4\text{N})_2[\text{Cl}_5\text{Os}(\text{NO})]$ showed only a quasi-reversible reduction wave with a small anodic counter-peak in addition to the reversible oxidation^[59] (Figure 2.4.1). At higher temperatures the reduction becomes completely irreversible due to a faster reaction following the primary one-electron transfer (presumably chloride dissociation). Table 2.4.1 lists the potentials in comparison to those of $[\text{Cl}_5\text{Ru}(\text{NO})]^{n-}$ ($n = 1, 2$), $[\text{Cl}_5\text{Ir}(\text{NO})]^{n-}$ ($n = 1, 2$) and $[(\text{CN})_5\text{Os}(\text{NO})]^{n-}$ ($n = 2, 3$).

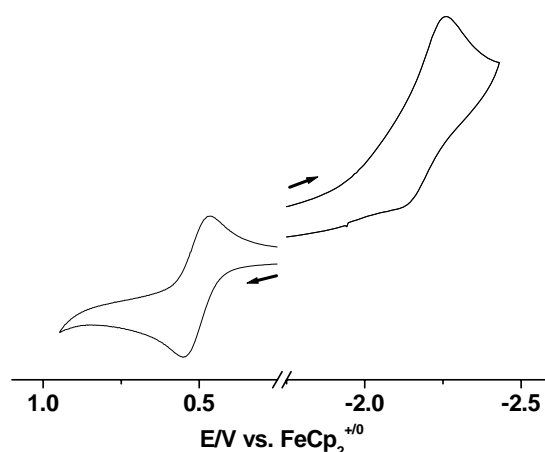


Figure 2.4.1. Cyclic voltammograms of $(n\text{-Bu}_4\text{N})_2[\text{Cl}_5\text{Os}(\text{NO})]$ in $n\text{-PrCN}/0.1\text{ M } n\text{-Bu}_4\text{NPF}_6$ at $-70\text{ }^\circ\text{C}$ (reduction) and $25\text{ }^\circ\text{C}$ (oxidation).

Table 2.4.1. Redox potentials^a of complexes

complex	$E_{1/2}(\text{ox})$	$E_{1/2}(\text{red})$	solvent
$[\text{Cl}_5\text{Os}(\text{NO})]^{2-}$	$0.56\text{ (}25\text{ }^\circ\text{C)}^{\text{b}}$	$-2.18^{\text{c}}\text{ (-}70\text{ }^\circ\text{C)}$	$n\text{-PrCN}$
$[\text{Cl}_5\text{Ru}(\text{NO})]^{2-}$	$1.02\text{ (-}40\text{ }^\circ\text{C)}$	$-1.92^{\text{d}}\text{ (-}60\text{ }^\circ\text{C)}$	$n\text{-PrCN}$
$[\text{Cl}_5\text{Ir}(\text{NO})]^-$	>1.5	$-0.33\text{ (-}60\text{ }^\circ\text{C)}$	$n\text{-PrCN}$
$[(\text{CN})_5\text{Os}(\text{NO})]^{2-}$	n.r.	$-1.50\text{ (}25\text{ }^\circ\text{C)}$	$\text{CH}_3\text{CN}^{\text{e}}$

^aPotentials in V vs. $\text{FeCp}_2^{+/0}$ from cyclic voltammetry in $0.1\text{ M } n\text{-Bu}_4\text{NPF}_6$ solutions.

^bCorresponding results were obtained for the $^+\text{PPh}_4$ salt in acetonitrile (ref. 59).

^cQuasi-reversible wave.

^dPeak potential for irreversible process.

^eFrom ref. 60, 61.

n.r. = not reported.

Obviously, the osmium system exhibits the lowest oxidation and reduction potentials. While it is not unexpected that the $\text{Os}^{\text{II/III}}$ transition is more facile than $\text{Ru}^{\text{II/III}}$ or $\text{Ir}^{\text{III/IV}}$, the very negative potential of the largely NO based reduction of $[\text{Cl}_5\text{Os}(\text{NO})]^{2-}$ is quite remarkable. It illustrates the well known efficient π back donation from osmium(II),^[64]

here to the excellent π acceptor NO^+ , leading to a particular high degree of covalency in that $\{\text{OsNO}\}^6$ configuration and thus to a reluctance in accepting an electron to yield NO^\bullet or Os^{I} in the $\{\text{OsNO}\}^7$ form $[\text{Cl}_5\text{Os}(\text{NO})]^{3-}$. As Table 2.4.1 shows, this effect is less pronounced for the analogous $[(\text{CN})_5\text{Os}(\text{NO})]^{2-}$ because five cyanide acceptor ligands compete with one NO^+ for the π donor capacity of osmium(II). The lability of both compounds $[\text{Cl}_5\text{M}(\text{NO})]^{2-}$, $\text{M} = \text{Ru}$ and Os , on reduction is not only reflected by the negative potentials but also by the calculated lengthening of the bond between M and the axial chloride ligand (*trans* influence) as shown in Table 2.4.2 and as reported previously for ruthenium and iridium analogues.^[33]

Table 2.4.2. Calculated bond lengthening on reduction of complexes $[\text{Cl}_5(\text{NO})\text{M}]^{n-}$

bond lengthening ^a			
	M = Ru, n = 2, 3	M = Os, n = 2, 3	M = Ir, n = 1, 2
$\Delta(\text{M}-\text{N})$	0.069	0.075	0.099
$\Delta(\text{M}-\text{Cl}_{\text{ax}})$	0.308	0.221	0.145
$\Delta(\text{N}-\text{O})$	0.047	0.061	0.045

^a Bond length differences Δ in Å.

The difference $\Delta(\text{M}-\text{Cl}_{\text{ax}})$ decreases from 0.308 Å for $\text{M} = \text{Ru}$ via 0.221 Å for $\text{M} = \text{Os}$ to 0.145 Å for $\text{M} = \text{Ir}$. Accordingly, the ruthenium complex could not be reversibly reduced in solution,^[33] even at the lowest temperatures, whereas the osmium analogue showed quasi-reversibility at -70 °C and the iridium compound reversible reduction at -40 °C.^[33] This labilisation of a normally rather inert $\text{Os}-\text{Cl}$ bond is quite remarkable, it is attributed to strong $d(\text{Os}) \rightarrow \pi^*(\text{NO})$ back donation and to the *trans* position.

In contrast, the reduction of *cis*- $[(\text{bpy})_2\text{ClOs}(\text{NO})]^{2+}$ does not involve chloride labilisation because of the absence of a chloride ligand in *trans* position to NO therefore *cis*- $[(\text{bpy})_2\text{ClOs}(\text{NO})]^{2+}$ undergoes one reversible reduction at $E_{1/2} = -0.70$ V vs. $\text{FeCp}_2^{+/0}$ in $\text{CH}_3\text{CN}/0.1$ M *n*- Bu_4NPF_6 solutions followed by an irreversible reduction at $E_{\text{pc}} = -1.24$ V vs. $\text{FeCp}_2^{+/0}$ (Figure 2.4.2).

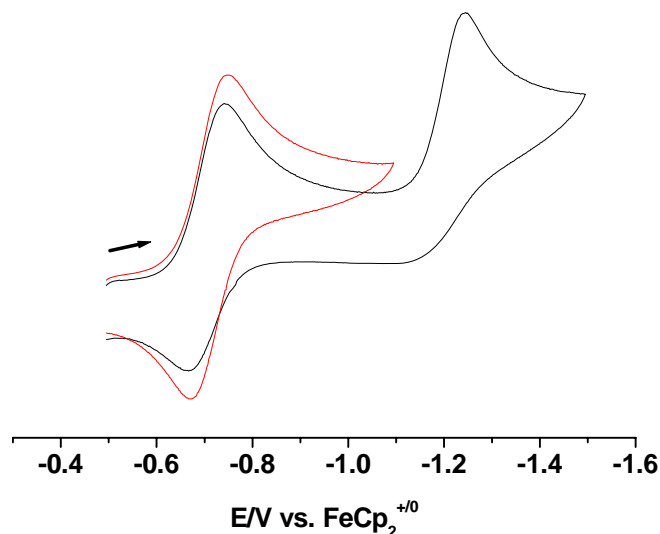


Figure 2.4.2. Cyclic voltammograms of *cis*-[(bpy)₂ClOs(NO)](PF₆)₂ in CH₃CN/0.1 M *n*-Bu₄NPF₆ at 298 K.

2.5. IR Spectroelectrochemistry

The apparent accessibility of the oxidised and reduced forms of the [Cl₅Os(NO)]²⁻ ion and of [(bpy)₂ClOs(NO)]²⁺ allowed us to determine the site of redox processes by low-temperature spectroelectrochemical (EPR and IR) techniques. The $\nu(\text{NO})$ stretching band has been long recognised as an excellent indicator for the oxidation state of that non-innocent ligand in metal complexes.^[2,9,11,65] According to the previously reported^[33] results for the one-step redox systems [Cl₅Ru(NO)]ⁿ⁻ (*n* = 1, 2) and [Cl₅Ir(NO)]ⁿ⁻ (*n* = 1, 2),^[33] the metal-based oxidation produces a small high-energy shift ($\sim 80 \text{ cm}^{-1}$) of $\nu(\text{NO})$ whereas a much larger low-energy shift ($\Delta\nu(\text{NO}) \approx -300 \text{ cm}^{-1}$) is expected for reversible nitrosyl-based reduction.^[33] Obviously, the complex [Cl₅Os(NO)]²⁻ shows a mainly metal-based oxidation as $\Delta\nu(\text{NO}) = 86 \text{ cm}^{-1}$ (Figure 2.5.1, Table 2.5.1) whereas the irreversible reduction produced a comparatively small shift of only $\Delta\nu(\text{NO}) = 1802 - 1650 = 152 \text{ cm}^{-1}$ (Figure 2.5.2).

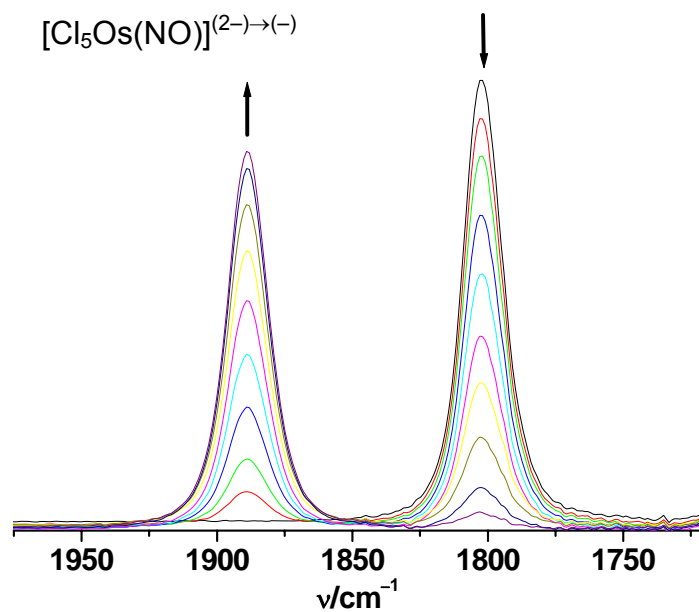


Figure 2.5.1. IR spectroelectrochemical response for the oxidation of $(n\text{-Bu}_4\text{N})_2[\text{Cl}_5\text{Os}(\text{NO})]$ in $\text{CH}_3\text{CN}/0.1 \text{ M } n\text{-Bu}_4\text{NPF}_6$ at 298 K.

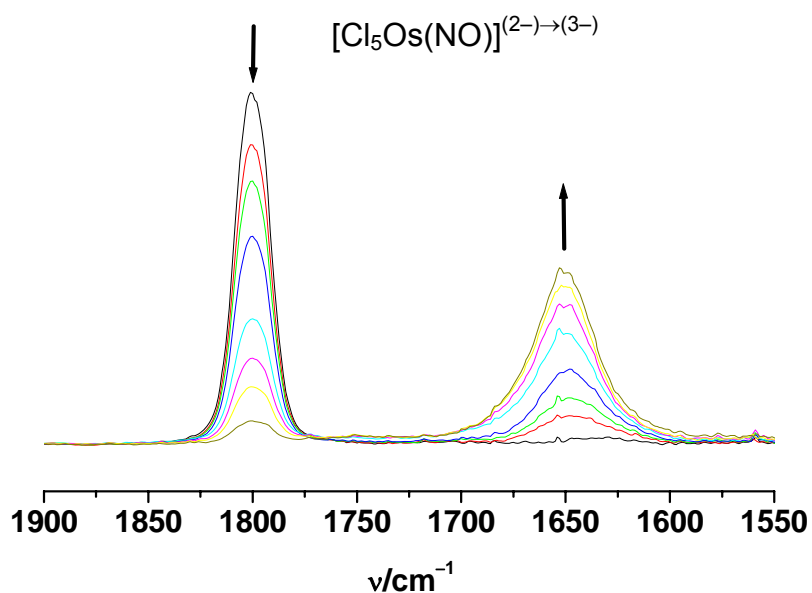


Figure 2.5.2. IR spectroelectrochemical response for the reduction of $(n\text{-Bu}_4\text{N})_2[\text{Cl}_5\text{Os}(\text{NO})]$ in $n\text{-PrCN}/0.1 \text{ M } n\text{-Bu}_4\text{NPF}_6$ at 203 K.

The reduction product, showing $\nu(\text{NO})$ at 1650 cm^{-1} cannot be described as complex containing NO^\bullet , that is, $[\text{Cl}_5\text{Os}(\text{NO}^\bullet)]^{3-}$. Support for this assumption comes from the $1844/1560\text{ cm}^{-1}$ reported^[61] for $[(\text{NC})_5\text{Os}(\text{NO})]^{2-}/[(\text{NC})_5\text{Os}(\text{NO})]^{3-}$ ($\Delta\nu(\text{NO}) = 284\text{ cm}^{-1}$) or the $1890/1577\text{ cm}^{-1}$ measured for *cis*- $[(\text{bpy})_2\text{ClOs}(\text{NO})]^{2+/+}$ ($\Delta\nu(\text{NO}) = 313\text{ cm}^{-1}$; Figure 2.5.3). In addition, the calculated NO stretching value for $[\text{Cl}_5\text{Os}(\text{NO})]^{3-}$ is unusually low at 1513 cm^{-1} , i.e., more than 150 cm^{-1} lower in comparison to the 1665 cm^{-1} calculated (1677 cm^{-1} experimental) for $[\text{Cl}_5\text{Ir}(\text{NO})]^{2-}$ and shifted by more than 300 cm^{-1} with respect to the oxidised form $[(\text{Cl}_5\text{Os}(\text{NO}))]^{2-}$. The calculation thus supports the notion of particularly strong $d(\text{Os}) \rightarrow \pi^*(\text{NO})$ back donation as evident also from the considerable N–O bond lengthening (Table 2.4.2). In consequence, the $\{\text{OsNO}\}^7$ configuration appears to involve a significant amount of the $\text{Os}^{\text{III}}(\text{NO}^-)$ formulation in addition to $\text{Os}^{\text{II}}(\text{NO}^\bullet)$.

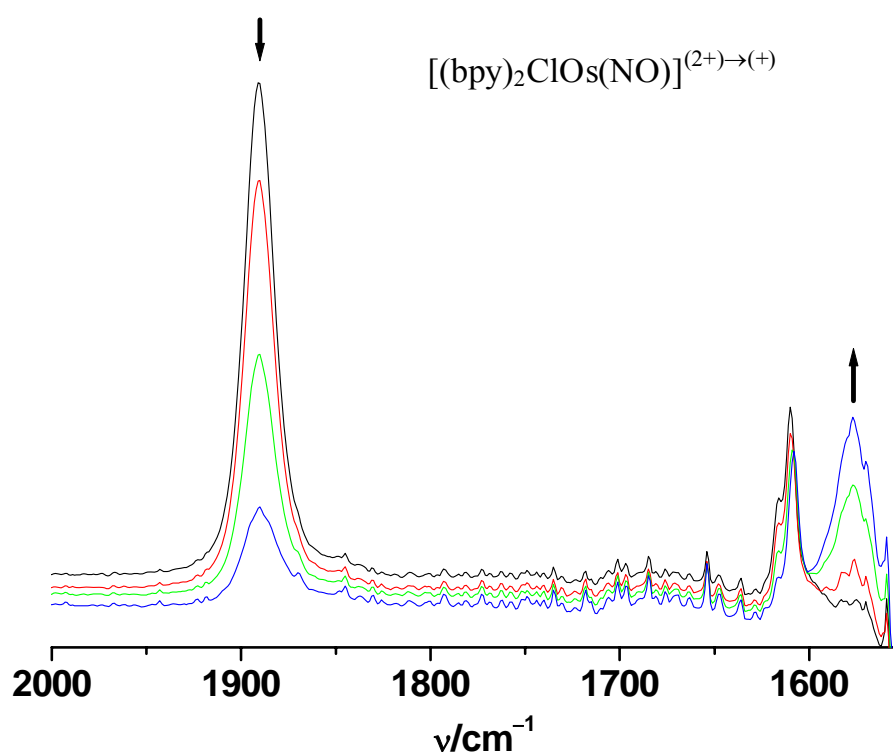


Figure 2.5.3. IR spectroelectrochemical response for the reduction of *cis*- $[(\text{bpy})_2\text{ClOs}(\text{NO})](\text{PF}_6)_2$ in $\text{CH}_3\text{CN}/0.1\text{ M } n\text{-Bu}_4\text{NPF}_6$ at 298 K.

Table 2.5.1. Experimental and G03/BPW91 calculated NO stretching frequencies (ν/cm^{-1}) for $[\text{L}_5\text{Os}(\text{NO})]^{n-}$ complexes

	n=1		n=2		n=3	
	calc.	exp.	calc.	exp.	calc.	exp.
$[\text{Cl}_5\text{Os}(\text{NO})]^{n-}$	1882	1888	1821	1802	1513	^a
$[(\text{CN})_5\text{Os}(\text{NO})]^{n-}$	1902	n.r.	1833	1844 ^b	1574	1560 ^b

^a Observed value of 1650 cm^{-1} not believed to be that of $[\text{Cl}_5\text{Os}(\text{NO})]^{3-}$, see text.

^b From ref. 61.

n.r. = not reported.

In order to understand the influence of the possible loss of chloride on reduction, calculations on different five-coordinate $[\text{Cl}_4\text{Os}(\text{NO})]^{2-}$ species and its solvated forms (*n*-butyronitrile modeled by acetonitrile) were done. The optimised structures together with calculated NO stretching frequencies are depicted in Figure 2.5.4. The calculations indicate that chloride dissociation shifts the NO frequency to higher wavenumbers, however, the possibility of different energy minimum configurations is responsible for the remaining ambiguity as to the exact structure of the follow-up product from the reduction of $[\text{Cl}_5\text{Os}(\text{NO})]^{2-}$.

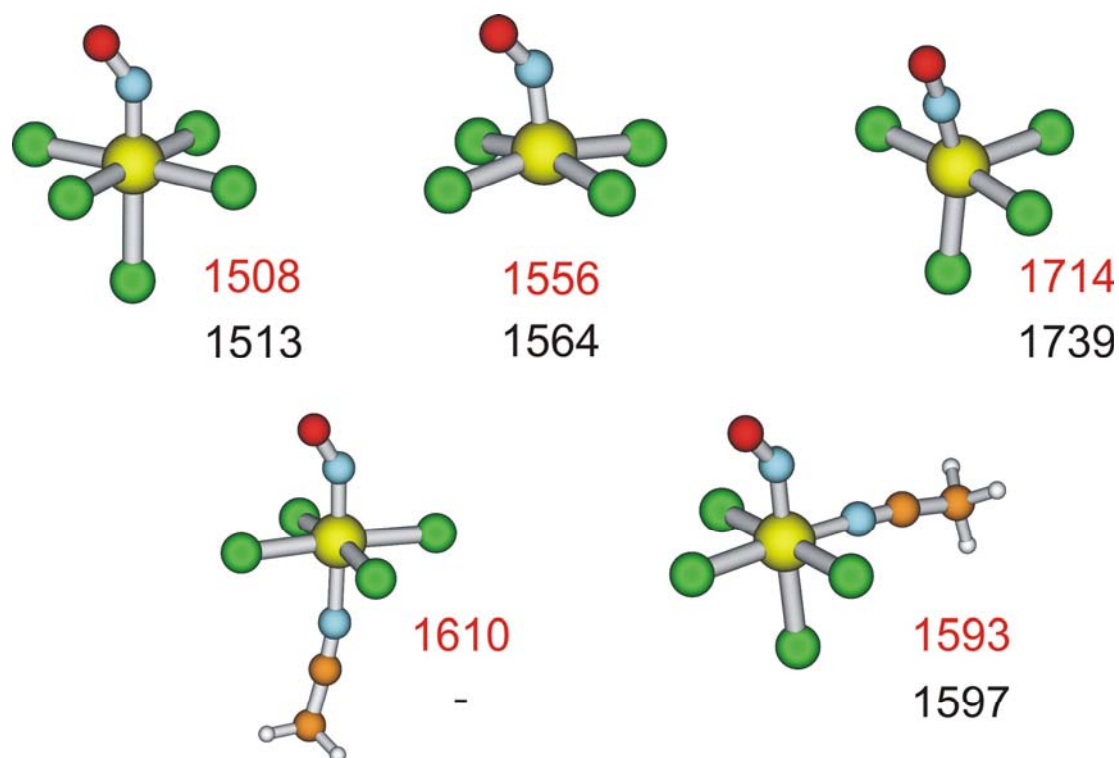


Figure 2.5.4. G03/B3LYP optimised structures of $[\text{Cl}_5\text{Os}(\text{NO})]^{3-}$ and its possible dissociation products. Numbers represent calculated frequencies: G03/B3LYP (in red) and G03/BPW91 (in black).

2.6. EPR Spectroelectrochemistry

EPR spectroscopy (see section 4.6.1 for theory of EPR spectroscopy) from low-temperature electrolysis of $[\text{Cl}_5\text{Os}(\text{NO})]^{2-}$ support these interpretations. The reversibly oxidised form $[\text{Cl}_5\text{Os}(\text{NO})]^-$, also studied previously,^[59] can be described as an $\text{Os}^{\text{III}} = 5d^5$ system with axial splitting of the g components ($g_x > g_y = 2.00$). Individual values, the relatively small g anisotropy Δg , and the average g_{av} are well reproduced by calculations which include spin-orbit coupling (Figure 2.6.1, Table 2.6.1).

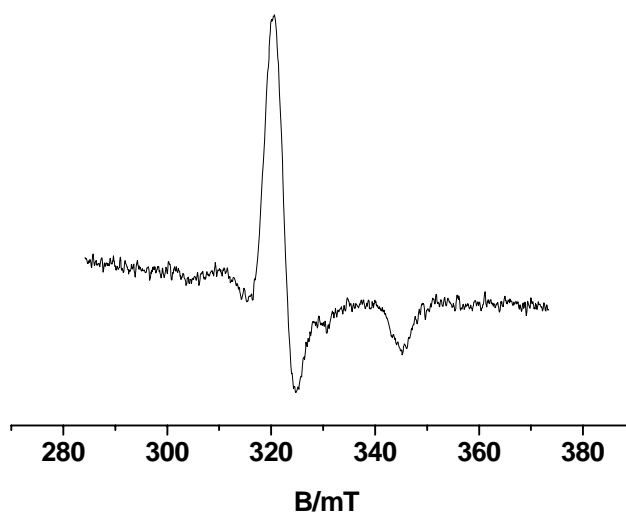


Figure 2.6.1. EPR spectrum of $[\text{Cl}_5\text{Os}^{\text{III}}(\text{NO}^+)]^-$ in $\text{CH}_3\text{CN}/0.1 \text{ M } n\text{-Bu}_4\text{NPF}_6$ at 4 K.

Table 2.6.1. Comparison of experimental and calculated g Values^a for $[\text{Cl}_5\text{Os}(\text{NO})]^-$ and $[\text{Cl}_5\text{Os}(\text{NO})]^{3-}$ at optimised geometry

	$[\text{Cl}_5\text{Os}(\text{NO})]^-$		$[\text{Cl}_5\text{Os}(\text{NO})]^{3-}$				
	exp.	calc.	exp.			calc.	
			$3V^b$	$2V^b$	nV^b	staggered	eclipsed
g_{11}	2.136	2.151	1.998	2.103	2.128	2.122	1.984
g_{22}	2.136	2.149	1.949	1.890	1.864	1.827	1.856
g_{33}	1.998	2.007	1.703	1.638	1.602	1.529	1.604
$g_{11} - g_{33}$	0.138	0.144	0.295	0.465	0.526	0.593	0.380
g_{iso}^c	2.090	2.102	1.888	1.887	1.877	1.830	1.815

^a Spin-restricted calculations including spin-orbit coupling (basis I).

^b Species reported from electron trapping in AgCl (from ref 42,43). $3V$, $2V$ and nV ($n = 1$ or 0) refers to the number of proximal Ag^+ vacancies.

^c Calculated from $\langle g \rangle = \sqrt{(g_1^2 + g_2^2 + g_3^2)}/3$.

Reduced forms generated from $[\text{Cl}_5\text{Os}(\text{NO})]^{2-}$ had been analysed by detailed EPR spectroscopy in AgCl host matrices where these complex may serve as

(photo)electron traps. Several sets of signals for such species were obtained and assigned to different sites with varying proximal Ag^+ vacancies.^[42,43] After electrolysis at $-70\text{ }^\circ\text{C}$ in *n*-butyronitrile/0.1 M *n*- Bu_4NPF_6 a signal with $g_{\parallel} = 2.15$ and $g_{\perp} = 2.002$ was observed in frozen solution at 110 K. Such a signal with rather high g components would not be compatible with a $[\text{Cl}_5\text{Os}(\text{NO}^\bullet)]^{3-}$ structure as suggested by the data from AgCl matrix studies (Table 2.6.1) or by the values obtained for $[(\text{NC})_5\text{Os}(\text{NO})]^{3-}$ ($g_1 = 1.959$, $g_2 = 1.931$, $g_3 = 1.634$)^[60] or for *cis*- $[(\text{bpy})_2\text{ClOs}(\text{NO})]^+$ ($g_1 = 1.98$, $g_2 = 1.89$, $g_3 = 1.62$; Figure 2.6.2).

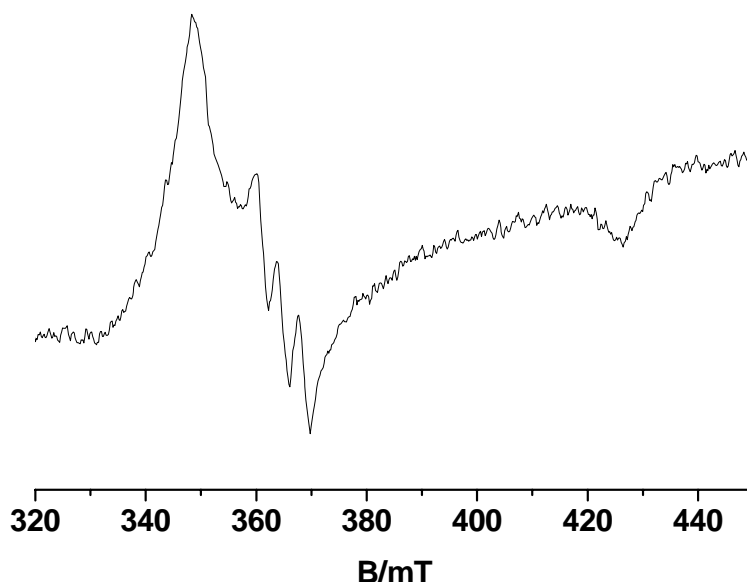


Figure 2.6.2. EPR spectrum of reduced *cis*- $[(\text{bpy})_2\text{ClOs}(\text{NO})](\text{PF}_6)_2$ in $\text{CH}_3\text{CN}/0.1\text{ M}$ *n*- Bu_4NPF_6 at 4 K: $g_1 = 1.98$, $g_2 = 1.89$, $g_3 = 1.62$, $A_2(^{14}\text{N}) = 3.9\text{ mT}$.

Both the IR and EPR spectroelectrochemical studies thus point to an EC process in fluid solution, possibly a dissociation of the chloride in *trans* position. Calculations reveal that the conceivable products, a pentacoordinate species or a hexacoordinate solvent or hydride complex would exhibit less shifted NO stretching bands and less lowered g components, as similarly shown by Lehnert and coworkers for nitrosyliron compounds.^[47] However, at this point the follow-up product of the process cannot be positively identified; the product obtained at low temperature by *in situ* (IR, EPR)

electrochemical reduction undergoes further reactions (decomposition) when the temperature is increased.

Kaim *et al.* pointed out, earlier,^[33] that the very sensitive g tensor components are highly dependent on the conformation of the bent NO group in an $\{MNO\}^7$ configuration, i.e., in a staggered, eclipsed or intermediate situation (Figure 2.6.3). The staggered conformation of $[Cl_5Os(NO)]^{3-}$ is favored over the eclipsed one by only 105 cm^{-1} , nevertheless, the calculations show significant differences of g components between the conformers (Table 2.6.1). Interestingly, the different sets of EPR signals reported^[42,43] for $[Cl_5Os(NO)]^{3-}$ at different sites in AgCl are well reproduced by the ideally staggered (nV, 2V) and eclipsed (3V) conformations, suggesting that these sites induce different conformations and high barriers for rotational interconversion.

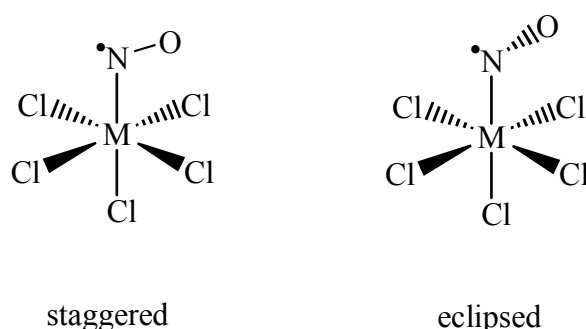


Figure 2.6.3. Staggered and eclipsed configurations of $[Cl_5Os(NO^*)]^{3-}$.

2.7. UV/VIS Spectroelectrochemistry

The UV/VIS spectroelectrochemical reduction experiment for $cis-[(bpy)_2ClOs(NO)]^{2+}$ (Figure 2.7.1) shows shifted and split metal-to-ligand charge transfer (MLCT) and intra-ligand (IL) transitions $d(Os) \rightarrow \pi^*(bpy)$ and $\pi(bpy) \rightarrow \pi^*(bpy)$ as intense bands at 294, 269 and 237 nm. In addition, the electrogenerated $cis-[(bpy)_2ClOs(NO)]^+$ exhibits several weaker shoulders in the visible region (400, 470, 550br, 680br) which were attributed to MLCT transitions $d(Os) \rightarrow \pi^*(NO^*)$ and to LLCT processes $\pi^*(NO^*) \rightarrow \pi^*(bpy)$. Transitions involving osmium are generally influenced by the spin-orbit coupling and by considerable ligand contributions due to partially covalent

bonding. In contrast, intense $d(\text{Os}) \rightarrow \pi^*(\text{bpy})$ and $\pi(\text{bpy}) \rightarrow \pi^*(\text{bpy})$ transitions were observed in the UV region (322 and 235 nm) for $[(\text{bpy})_2\text{ClOs}(\text{NO})]^{2+}$,^[58] as illustrated in Figure 2.7.1.

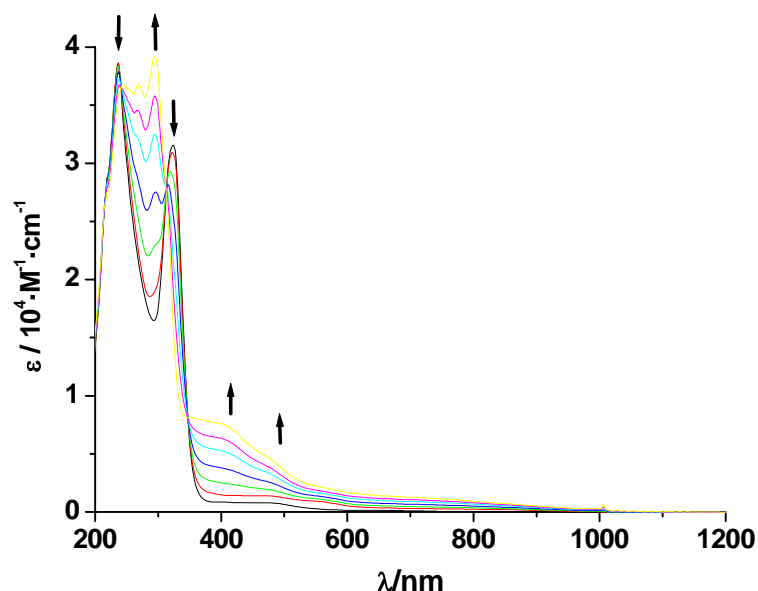


Figure 2.7.1. UV/VIS spectroelectrochemical response for the conversion $\text{cis}-[(\text{bpy})_2\text{ClOs}(\text{NO})]^{(2+) \rightarrow (+)}$ in $\text{CH}_3\text{CN}/0.1 \text{ M } n\text{-Bu}_4\text{NPF}_6$ at 298 K.

2.8. DFT Calculations

The DFT calculations on $[\text{Cl}_5\text{Os}(\text{NO})]^{2-}$ indicate the highest occupied molecular orbital (HOMO), $6b_2$, is composed from 58% 5d Os and 41% equatorial 3p Cl orbitals and the doubly degenerate lowest unoccupied molecular orbital (LUMO), $22e$, is mainly formed from π^* orbitals of the NO ligand (61%) with 34% contribution from 5d Os (Figure 2.8.1, Table 2.8.1). Therefore oxidation of $[\text{Cl}_5\text{Os}(\text{NO})]^{2-}$ occurs largely on the metal and hence, the oxidised form $[\text{Cl}_5\text{Os}(\text{NO})]^-$ contains Os^{III} in a linear $\{\text{OsNO}\}^5$ configuration. Table 2.8.2 shows that the underlying spin density distribution (Os: 0.711) confirms the predominant metal centring of the unpaired electron. On the other side, the reduction is largely NO-centred and causes Os–N–O bending (symmetry lowering) which, together with spin-orbit interactions, results the originally degenerate e-molecular levels to split into non-degenerate ones (Figure 2.8.1).

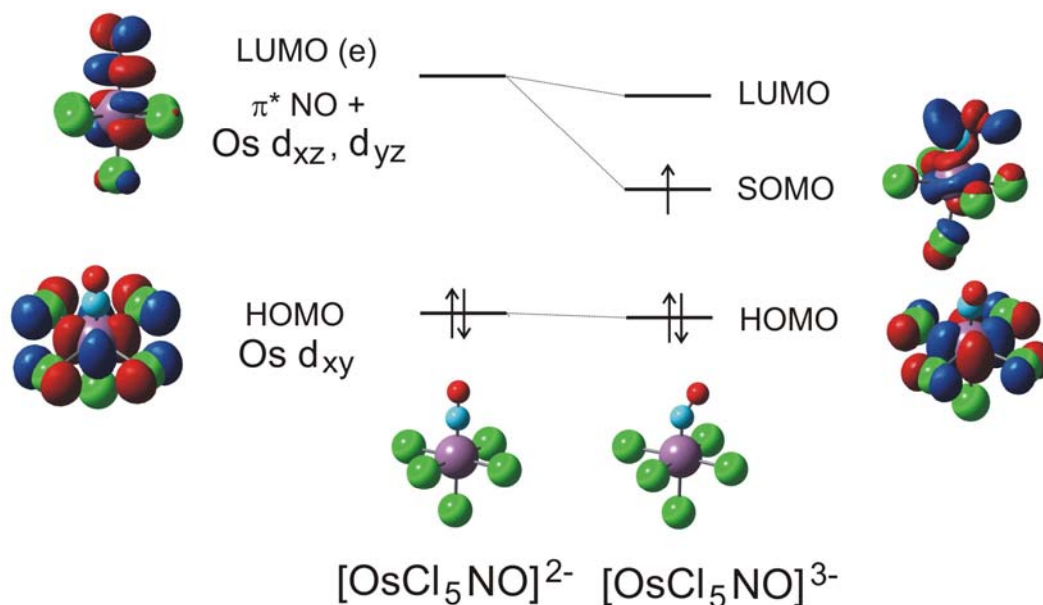


Figure 2.8.1. Representation of HOMO and LUMO in $[\text{Cl}_5\text{Os}(\text{NO})]^{2-}$ and $[\text{Cl}_5\text{Os}(\text{NO})]^{3-}$.

As mentioned before, nitrosyl radical complexes with bent metal-NO arrangement can adopt eclipsed or staggered conformations with respect to the coordinated atoms in the equatorial plane (Figure 2.6.3).^[45,50] For $[\text{Cl}_5\text{Os}(\text{NO})]^{3-}$ the staggered structure is favored over the eclipsed one by $0.013 \text{ eV} = 105 \text{ cm}^{-1}$, the bending angle is calculated slightly larger at 144.1° for the eclipsed conformer. For comparison, it should be noted that staggered and eclipsed conformers of nitrosylhemeiron(I) species were calculated to be isoenergetic with the consequence of free rotation around the Fe-(NO) bond.^[45] Detailed analyses of the conformational dependence of the g anisotropy suggest that the different reduced species reported previously for $[\text{Cl}_5\text{Os}(\text{NO})]^{3-}$ in AgCl host lattices may be distinct in terms of eclipsed or staggered conformations of the bent NO^\bullet axial ligand relative to the $\text{Os}^{\text{II}}\text{Cl}_4$ equatorial plane.

A rather large degree of metal-NO back donation is estimated to occur in the $\{\text{OsNO}\}^7$ configuration of $[\text{Cl}_5\text{Os}(\text{NO})]^{3-}$ which leads to an unusual low value of 1513 cm^{-1} calculated for $\nu(\text{NO})$, signifying contributions from an $\text{Os}^{\text{III}}(\text{NO}^-)$ formulation. All three states of $[\text{Cl}_5\text{Os}(\text{NO})]^{n-}$ prefer N-terminal bonded nitrosyl over the NO-side-on bonded alternatives by 1.86 eV ($n = 1$), 1.84 eV ($n = 2$) and 1.69 eV ($n = 3$), respectively.

Table 2.8.1. ADF/SAOP calculated compositions (in %) of frontier molecular orbitals of $[\text{Cl}_5\text{Os}(\text{NO})]^{2-}$, expressed in terms of individual fragments

	E(eV)	prevailing character	Os	Cl _{eq}	Cl _{ax}	NO
11b ₁	1.01	Os + Cl	59	41		
22e (LUMO)	0.54	NO + Os	34 (d _{xz} , d _{yz})	3	2	61
6b ₂ (HOMO)	-1.62	Os + Cl _{eq}	58 (d _{xy})	41		
2a ₂	-2.59	Cl _{eq}		99		
21e	-2.60	Cl _{eq} + NO + Os	9	77	4	10
20e	-2.93	Cl _{ax}	6	11	71	12
19e	-3.07	Cl _{eq}		99		
10b ₁	-3.15	Cl _{eq}		99		

Table 2.8.2. DFT (ADF/BP) calculated spin densities

	$[\text{Cl}_5\text{Os}(\text{NO})]^-$	$[\text{Cl}_5\text{Os}(\text{NO})]^{3-}$
M	0.711	0.486
Cl _{eq} ^a	0.098	0.002
Cl _{ax}	0.001	0.038
N	-0.060	0.303
O	-0.045	0.151

^a Averaged values.

Singlet and triplet transitions were calculated using TD-DFT (Tables 2.8.3, 2.8.4). The calculated long-wavelength singlet transitions in the visible agree reasonably with the observed absorption bands (Table 2.8.3). A remarkable result is the low intensity of these metal-to-ligand charge transfer (MLCT) transitions, confirmed here by TD-DFT; this is an aspect which has been noted before for MLCT bands involving $\pi^*(\text{NO})$ as target orbitals.^[58,66]

Table 2.8.3. Selected ADF/SAOP calculated lowest allowed TD-DFT singlet transitions for $[\text{Cl}_5\text{Os}(\text{NO})]^{2-}$

state	main character (in %)	ADF/SAOP		experiment
		transition energy ^a	oscillator strength	$\lambda_{\text{max}}/\epsilon^{\text{b}}$
¹ E	99 (6b ₂ →22e)	2.29 (542)	0.0003	573/48
¹ E	99 (2a ₂ →22e)	3.12 (397)	0.0005	437/71
¹ A ₁	79 (21e→22e); 17 (20e→22e)	3.46 (358)	0.008	371/147
¹ A ₁	98 (19e→22e)	3.59 (345)	0.0005	335/147
¹ E	90 (10b ₁ →22e)	3.67 (337)	0.002	
¹ A ₁	81 (10b ₁ →11b ₁); 13 (20e→22e)	4.23 (293)	0.025	
¹ A ₁	47 (20e→22e); 19 (10b ₁ →11b ₁)	4.25 (292)	0.047	

^a Transition energies in eV (wavelengths in nm).

^b Absorption maxima (λ_{max}) in nm, molar extinction coefficients (ϵ) in $\text{M}^{-1}\cdot\text{cm}^{-1}$.

Table 2.8.4. Selected ADF/SAOP calculated lowest TD-DFT triplet transitions for $[\text{Cl}_5\text{Os}(\text{NO})]^{2-}$

state	main character (in %)	transition energy ^a
³ E	99 (6b ₂ →22e)	2.03 (611)
³ A ₂	99 (6b ₂ →11b ₁)	2.44 (508)
³ A ₁	78 (21e→22e); 19 (20e→22e)	2.72 (455)
³ B ₁	93 (21e→22e)	2.97 (417)

^a Transition energies in eV (wavelengths in nm).

2.9. Conclusion and Outlook

Concluding, this Chapter has demonstrated the applicability of experimental and theoretical methodology for the study of relatively simple nitrosylmetal complexes.

While basic concepts have been established in this field for quite some time,^[2,11,67,68] reactive open-shell species containing heavy metals clearly pose considerable challenges. Using two chloronitrosyl osmium redox systems, the effects of electron transfer in these compounds and the electronic structures of the thus generated species have been investigated. Remarkably, the pentachloro compound could not be reversibly reduced in fluid solution even at $-70\text{ }^{\circ}\text{C}$ despite its established^[42,43] stability in an AgCl matrix. On the other hand, the complex $[(\text{bpy})_2\text{ClOs}(\text{NO})]^+$ with *cis* positioned NO^{\bullet} and Cl groups is stable and exhibits EPR features similar to $[(\text{NC})_5\text{Os}(\text{NO})]^{3-}$. The good agreement between experimental and DFT computed g factor components supports the confidence in the calculated spin distribution which is estimated at about 2/3 NO-centred and 1/3 metal based. These results quantify the notion of significant metal d and $\pi^*(\text{NO})$ orbital mixing, justifying the concept of “covalent triatomic MNO species” as expressed by the Enemark-Feltham notation.^[2] Two different examples of simple paramagnetic complexes containing the “NO” ligand have been observed. Whereas $[(\text{bpy})_2\text{ClOs}(\text{NO})]^+$, a $\{\text{MNO}\}^7$ species, is predominantly a low-spin d^6 metal complex of the radical form NO^{\bullet} (**A**), the $[\text{Cl}_5\text{Os}(\text{NO})]^-$ ion, an $\{\text{MNO}\}^5$ system, must be formulated according to $\text{Ru}^{\text{III}}/\text{NO}^+$, i.e., involving metal-centred spin (**B**). The third alternative (**C**), the localisation of spin on an ancillary ligand, can be observed in species such as $[(\text{TPP}^{\bullet-})(\text{L})\text{Ru}^{\text{II}}(\text{NO}^+)]^{2+}$ or $(\alpha\text{-diimine}^{\bullet})\text{Co}^{-1}(\text{CO})(\text{NO}^+)^{\bullet}$ which will be discussed in next Chapter.

A: $(\text{L})\text{M}(\text{NO}^{\bullet})$,

B: $(\text{L})\text{M}^{\bullet}(\text{NO}^+)$,

C: $(\text{L}^{\bullet-})\text{M}(\text{NO}^+)$.

CHAPTER 3

Ruthenium Nitrosyl Porphyrin Complexes: Effect of Axial Ligation on Electron Transfer Processes

3.1. Introduction

The interaction of nitric oxide with heme-proteins plays a very important role in many physiological processes.^[3,4,5,6,19,20,69,70,71,72,73] NO is biosynthesised by a class of enzymes called nitric oxide synthases (NOSs)^[70] which contain heme as a prosthetic group. Soluble guanylate cyclase (sGC) is one of the other heme containing enzymes acting as biological receptor for NO.^[71] In addition to its significance in physiology, the interaction of NO with heme is also responsible in the nitrogen cycle.^[15] Because of the general importance of heme-NO interaction, a large amount of research has been carried out towards the synthesis of corresponding model systems. These investigations use synthetic porphyrins such as tetraphenylporphyrin (TPP) or octaethylporphyrin (OEP), and iron nitrosyl complexes with these synthetic porphyrins have been extensively studied.^[44,47,48,49,74,75,76,77] Many investigations on iron nitrosyl porphyrins have included variations of the axial ligand in the *trans* position to NO, ranging from N donors^[74,75] such as pyridine, imidazole or piperidine to S donors such as thiolates^[47,49] in order to understand the role of axial ligands on the properties of coordinated NO.

Going to the heavier analogue of iron, ruthenium nitrosyl porphyrins have also been anticipated as promising models to study interactions of NO with heme because of their enhanced stability relative to iron nitrosyl complexes.^[48,53,78,79] However, in contrast to several reports on the syntheses^[78,79,80,81] and structural studies^[18,82,83] of ruthenium nitrosyl porphyrins there have been far fewer investigations on the electrochemistry^[52,84] and on the spectroelectrochemistry^[85,86,87,88,89] of ruthenium nitrosyl porphyrins although these would be essential to understand electron transfer processes. Also, the unambiguous assignment of the NO oxidation state^[2,9,11] for NO-coordinated ruthenium porphyrin complexes [(Por)Ru(NO)(X)] with different porphyrins (Por) and various axial ligands (X) can be useful to understand the

electron transfer processes. All three components, the porphinato ligands ($\text{Por}^{-/2-/3-}$), the metal ($\text{Ru}^{2+/3+}$) and $\text{NO}^{+/0/-}$ are redox active in the central redox potential region and thus the determination of individual oxidation state combinations is not trivial.

In this Chapter, extensive experimental and theoretical studies of ruthenium nitrosyl tetraphenylporphyrin (TPP) complexes are described varying axial ligand from aqua ligand to acceptor or donor substituted pyridines. The effect of axial ligands on the redox properties of ruthenium nitrosyl tetraphenylporphyrin complexes has been investigated by means of electrochemical and various spectroelectrochemical methods.

3.2. Syntheses and Characterisation

The complex $[(\text{TPP})\text{Ru}(\text{NO})(\text{H}_2\text{O})]\text{BF}_4$, TPP = tetraphenylporphyrin, was prepared according to the literature,^[52] following the reaction scheme shown in Figure 3.2.1 and characterised by ^1H NMR and IR spectroscopy and elemental analyses. The complex $[\text{Ru}(\text{TPP})(\text{NO})(\text{H}_2\text{O})]\text{BF}_4$ shows the $\nu(\text{NO})$ at 1872 cm^{-1} in KBr and at 1875 cm^{-1} in dichloromethane. Intense Soret band at 410 nm and Q band at 558 nm are observed in optical spectrum of $[\text{Ru}(\text{TPP})(\text{NO})(\text{H}_2\text{O})]\text{BF}_4$ in dichloromethane (see section 3.7). The reduction studies on $[(\text{TPP})\text{Ru}(\text{NO})(\text{X})]\text{BF}_4$ where X = pyridine, 4-cyanopyridine or 4-N,N-dimethylaminopyridine were performed after electrocatalysed exchange in the solution of the aqua complex and excess (ca. tenfold) of the respective pyridine complex (Figure 3.2.2).^[52] Replacement of H_2O by pyridine shifted the $\nu(\text{NO})$ to higher-value by 10 cm^{-1} (Figure 3.2.3). The exchange could be effected electrocatalytically by reduction at ca. 200 mV before the cathodic peak maximum was reached (Figure 3.2.3).

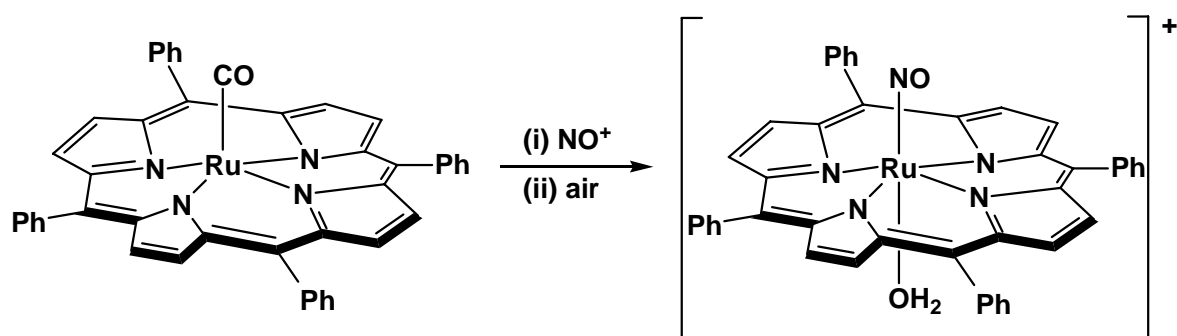


Figure 3.2.1. Synthesis of [(TPP)Ru(NO)(H₂O)]BF₄.

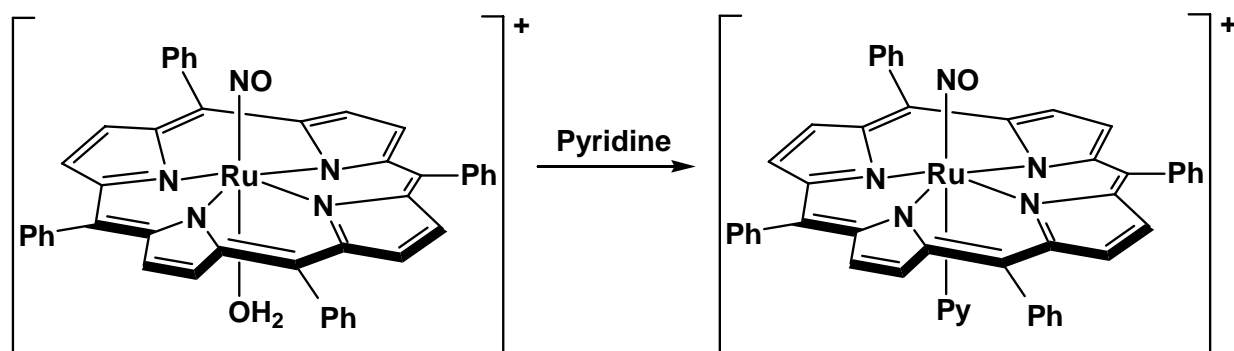


Figure 3.2.2. Electrocatalysed formation of [(TPP)Ru(NO)(Py)]BF₄ on addition of pyridine to [(TPP)Ru(NO)(H₂O)]BF₄.

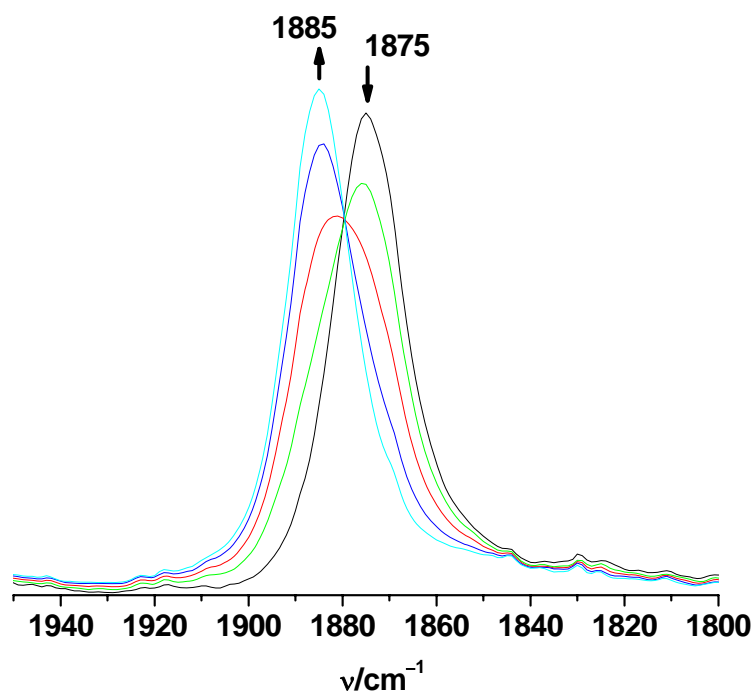


Figure 3.2.3. IR spectroelectrochemical response of $[(\text{TPP})\text{Ru}(\text{NO})(\text{H}_2\text{O})]\text{BF}_4$ with tenfold excess of pyridine in $\text{CH}_2\text{Cl}_2/0.1 \text{ M } n\text{-Bu}_4\text{NClO}_4$ at 298 K; Potential set ca. 200 mV positive relative to voltammetric reduction peak maximum.

3.3. Crystal Structure

Dark red crystals of $[(\text{TPP})\text{Ru}(\text{NO})(\text{H}_2\text{O})]\text{BF}_4$ suitable for single-crystal X-ray measurement were grown by slow diffusion of hexane in the dichloromethane solution at $-4 \text{ }^\circ\text{C}$. The molecular structure in the crystal confirms the $\{\text{RuNO}\}^6$ configuration,^[2] formally $[(\text{TPP}^{2-})\text{Ru}^{\text{II}}(\text{NO})^+(\text{H}_2\text{O})]\text{BF}_4$ valence state via the nearly linear ($178.1(3)^\circ$) RuNO and the typical^[18,82,83,90] Ru–N ($1.726(3) \text{ \AA}$) and N–O ($1.143(4) \text{ \AA}$) bond lengths (Figure 3.3.1, Table 3.3.1). The experimental geometry is well described by DFT calculations (Table 3.3.1). Both G03/PBE0 and ADF/BP methods indicate almost linear Ru–N–O bond, the Ru–N bond lengths are reproduced within 0.02 \AA . The calculations overestimate the Ru–H₂O distance (G03/PBE0 calculated Ru–O bond length 2.154 \AA vs. experimental 2.066 \AA).

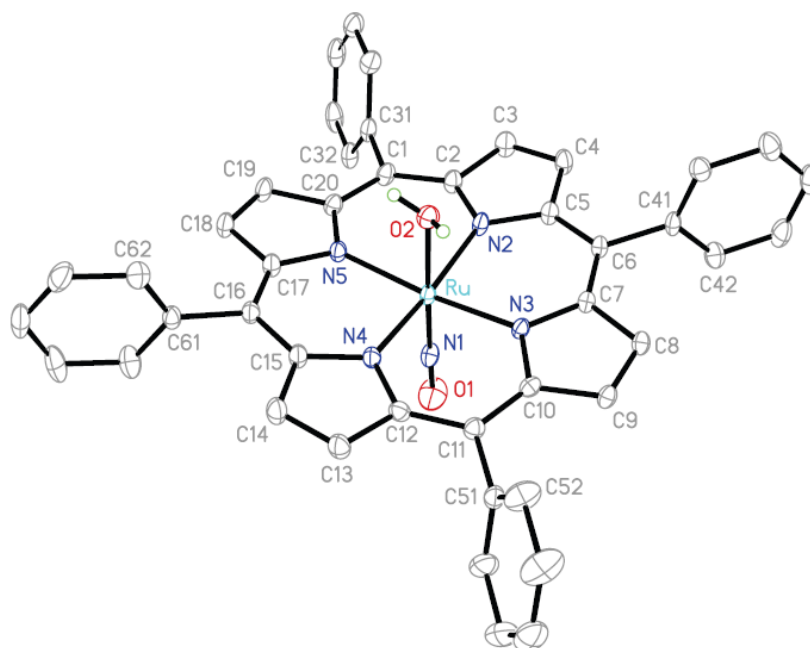


Figure 3.3.1. Molecular structure of the cation in the crystal of $[(\text{TPP})\text{Ru}(\text{NO})(\text{H}_2\text{O})]\text{BF}_4 \cdot 2\text{H}_2\text{O}$ at 173 K.

Table 3.3.1. Comparison of selected bond lengths (Å) and angles (deg) of $[(\text{TPP})\text{Ru}(\text{NO})(\text{H}_2\text{O})]^+$ with DFT calculated results

	ADF/BP calc.	G03/PBE0 calc.	exp.
Ru–N1	1.724	1.704	1.726(3)
Ru–N2	2.054	2.056	2.049(3)
Ru–N3	2.050	2.056	2.054(3)
Ru–N4	2.052	2.056	2.049(3)
Ru–N5	2.061	2.061	2.046(3)
Ru–O2	2.182	2.154	2.066(3)
N1–O1	1.146	1.146	1.143(4)
Ru–N1–O1	179.5	179.5	178.1(3)
N1–Ru–N5	95.7	95.7	94.82(12)
N2–Ru–N3	89.4	89.4	90.21(11)
N2–Ru–N4	89.2	89.2	89.27(11)
N2–Ru–N5	179.1	179.1	171.16(11)

3.4. Electrochemistry

Extensive cyclic voltammetry has been employed to study the precursor compound $[(\text{TPP})\text{Ru}(\text{NO})(\text{H}_2\text{O})]\text{BF}_4$ and the analogue containing pyridines in *trans* position to NO. A cyclic voltammogram of $[(\text{TPP})\text{Ru}(\text{NO})(\text{H}_2\text{O})]\text{BF}_4$ in $\text{CH}_2\text{Cl}_2/0.1 \text{ M } n\text{-Bu}_4\text{NClO}_4$ is shown in Figure 3.4.1. The compound undergoes two one-electron oxidation processes. The first oxidation is reversible process at $E_{1/2}(\text{ox1}) = 0.78 \text{ V vs. FeCp}_2^{+/0}$ while the second oxidation step at $E_{1/2}(\text{ox2}) = 1.14 \text{ V vs. FeCp}_2^{+/0}$ is only partially reversible (Figure 3.4.2). In contrast to the oxidations, even the first reduction of the $[(\text{TPP})\text{Ru}(\text{NO})(\text{H}_2\text{O})]\text{BF}_4$ complex was irreversible^[52] and thus not investigated further (Figure 3.4.1).

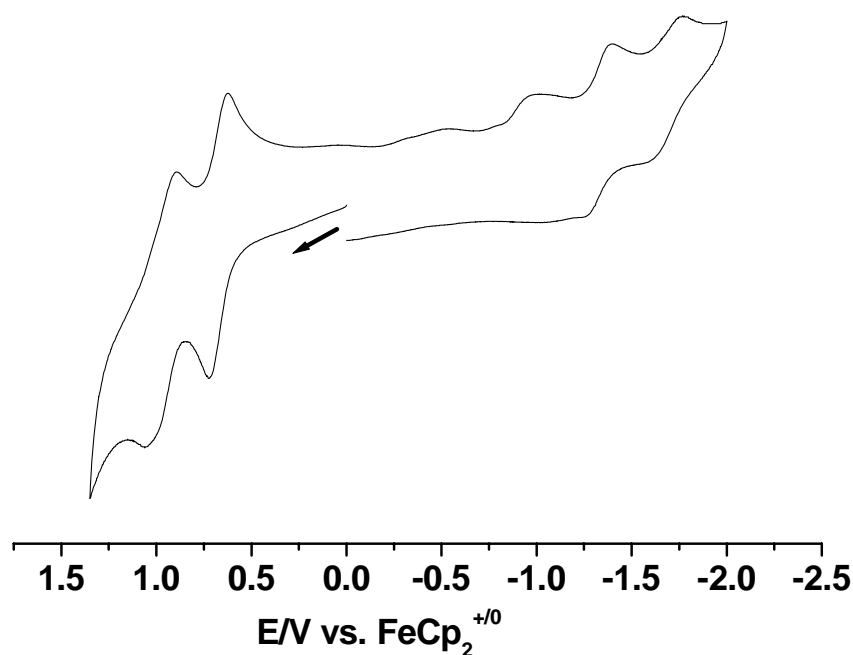


Figure 3.4.1. Cyclic voltammogram of $[(\text{TPP})\text{Ru}(\text{NO})(\text{H}_2\text{O})]\text{BF}_4$ in $\text{CH}_2\text{Cl}_2/0.1 \text{ M } n\text{-Bu}_4\text{NClO}_4$ at $25 \text{ }^\circ\text{C}$; Scan rate = 200 mV/s .

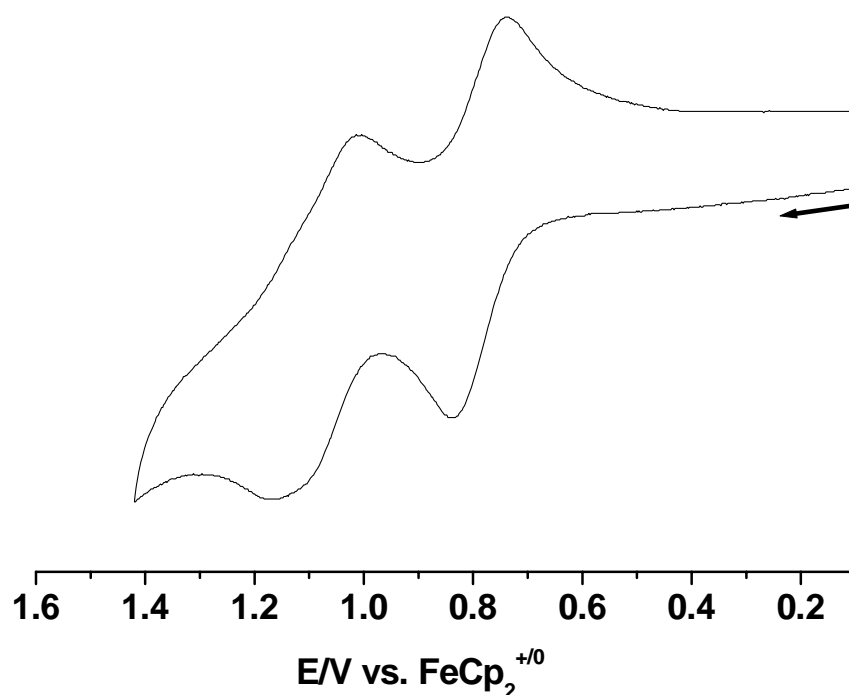


Figure 3.4.2. Cyclic voltammogram of $[(\text{TPP})\text{Ru}(\text{NO})(\text{H}_2\text{O})]\text{BF}_4$ in $\text{CH}_2\text{Cl}_2/0.1 \text{ M } n\text{-Bu}_4\text{NClO}_4$ at 25°C showing only oxidation steps; Scan rate = 200 mV/s .

As reported previously,^[52] the addition of pyridine to solutions of $[(\text{TPP})\text{Ru}(\text{NO})(\text{H}_2\text{O})]\text{BF}_4$ forms $[(\text{TPP})\text{Ru}(\text{NO})(\text{Py})]\text{BF}_4$ (Figure 3.2.2) which is reversibly reduced at $E_{1/2}(\text{red1}) = -0.79 \text{ V vs. FeCp}_2^{+/0}$ (Figure 3.4.3). Varying the electronic effect of the pyridine by means of substitution in *para* position, we observed the shifts of the redox potential for the reduction process (Table 3.4.1). 4-Cyanopyridine, a better electron acceptor than pyridine, shifts the potential for the first reduction of $[(\text{TPP})\text{Ru}(\text{NO})(\text{X})]\text{BF}_4$ to a less negative-value ($-0.68 \text{ V vs. FeCp}_2^{+/0}$), on the other hand 4-N,N-dimethylaminopyridine, a better electron donor but poorer electron acceptor than unsubstituted pyridine, makes the complex harder to reduce by shifting the potential to a more negative-value of $-0.90 \text{ V vs. FeCp}_2^{+/0}$. The sites of reversible processes, the oxidation of $[(\text{TPP})\text{Ru}(\text{NO})(\text{H}_2\text{O})]\text{BF}_4$ and the reduction of $[(\text{TPP})\text{Ru}(\text{NO})(\text{X})]\text{BF}_4$ were determined by spectroelectrochemical measurements.

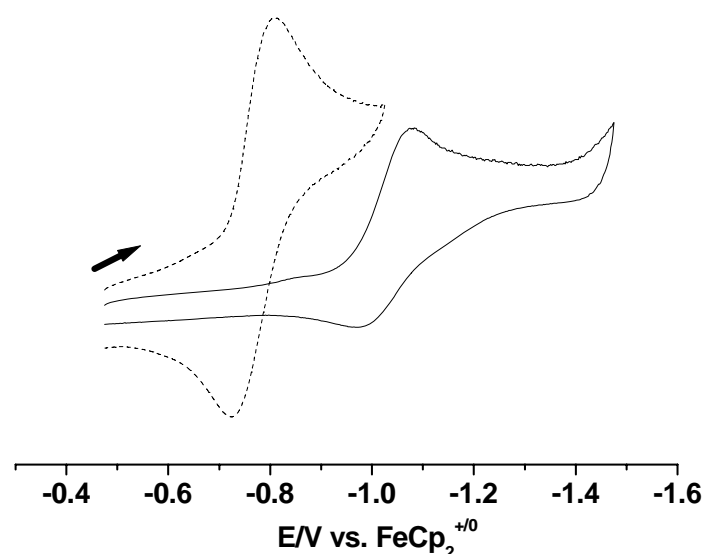


Figure 3.4.3. Cyclic voltammograms of [(TPP)Ru(NO)(H₂O)]BF₄ (solid line; irreversible reduction; $E_{pc} = -1.08$ V vs. FeCp₂⁺⁰) and [(TPP)Ru(NO)(Py)]BF₄ (dotted line, reversible reduction; $E_{1/2} = -0.79$ V vs. FeCp₂⁺⁰) in CH₂Cl₂/0.1 M *n*-Bu₄NClO₄ at 298 K; Scan rate = 200 mV/s.

Table 3.4.1. Electrochemical data^a of complexes

complex	$E_{1/2}(\text{ox1})$	$E_{1/2}(\text{ox2})$	$E_{1/2}(\text{red1})$	solvent
[(TPP)Ru(NO)(H ₂ O)]BF ₄	0.78	1.14 ^b	^c	CH ₂ Cl ₂
[(TPP)Ru(NO)(py)]BF ₄	^c	n.o.	-0.79	CH ₂ Cl ₂
[(TPP)Ru(NO)(4-CN-Py)]BF ₄	^c	n.o.	-0.68	CH ₂ Cl ₂
[(TPP)Ru(NO)(4-N,N-Me ₂ N-Py)]BF ₄	^c	n.o.	-0.90	CH ₂ Cl ₂

^a Potentials in V vs. FeCp₂⁺⁰ from cyclic voltammetry in 0.1 M *n*-Bu₄NClO₄ solutions at 298 K.

^b Only partially reversible.

^c Irreversible process.

n.o. = not observed.

3.5. IR Spectroelectrochemistry

The apparent accessibility of the oxidised form of $[(\text{TPP})\text{Ru}(\text{NO})(\text{H}_2\text{O})]\text{BF}_4$ and reduced form of the $[(\text{TPP})\text{Ru}(\text{NO})(\text{X})]\text{BF}_4$ allowed us to investigate the site of the redox processes by IR spectroelectrochemistry. Table 3.5.1 summarises the data on vibrational frequency of NO in different oxidation states together with calculated results. Oxidation of the aqua complex $[(\text{TPP})\text{Ru}(\text{NO})(\text{H}_2\text{O})]\text{BF}_4$ causes comparatively small positive shift in vibrational frequency ($\Delta(\nu_{\text{NO}}) = 20 \text{ cm}^{-1}$) in $\text{CH}_2\text{Cl}_2/0.1 \text{ M } n\text{-Bu}_4\text{NClO}_4$ suggesting that the oxidation occurs neither on NO or Ru but on the porphyrin ring (Figure 3.5.1). Similar shifts were noted for CO analogues.^[86] DFT calculations give a ca. 20 cm^{-1} positive shift of the NO stretching frequencies in agreement with the experiments. Moreover, the appearance of porphyrin radical anion ("radical cation")^[91] diagnostic ring vibrational bands^[92] at 1290 cm^{-1} for $\text{TPP}^{\bullet-}$ after the oxidation of $[(\text{TPP})\text{Ru}(\text{NO})(\text{H}_2\text{O})]\text{BF}_4$ also indicate that the porphyrin ring being the target of electron transfer process on oxidation.^[85,86,87,88]

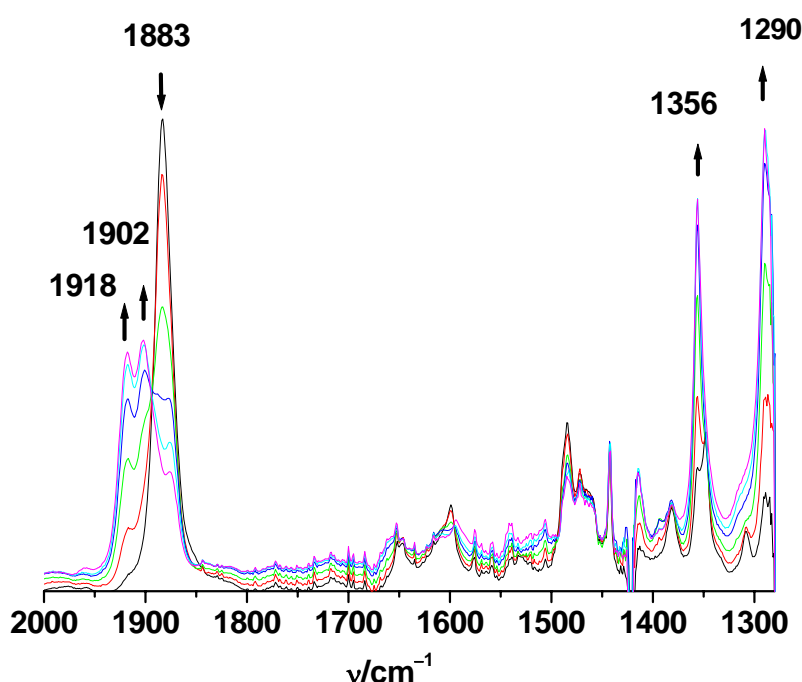


Figure 3.5.1. IR spectroelectrochemical response for the conversion $[(\text{TPP})\text{Ru}(\text{NO})(\text{H}_2\text{O})]^{(+)\rightarrow(2+)}$ in $\text{CH}_2\text{Cl}_2/0.1 \text{ M } n\text{-Bu}_4\text{NClO}_4$ at 298 K.

The presence of another band at 1918 cm^{-1} in addition to the band at 1902 cm^{-1} in nitrosyl region (Figure 3.5.1) suggests that species formed after first oxidation of $[(\text{TPP})\text{Ru}(\text{NO})(\text{H}_2\text{O})]^+$ undergoes chemical reaction on the time scale of spectrochemical measurements which probably cause the formation of two compounds containing coordinated NO. At this point, the follow up product after first oxidation of $[(\text{TPP})\text{Ru}(\text{NO})(\text{H}_2\text{O})]^+$ could not be identified.

The vibrational stretching band of NO shifts to lower-values by a much larger amount (ca. -300 cm^{-1}) on the reduction of $[(\text{TPP})\text{Ru}(\text{NO})(\text{Py})]\text{BF}_4$ (Py = pyridine) complex (Figure 3.5.2). Such large negative shifts in the vibrational frequency of NO are typical^[33,51,60] for the reduction involving mainly electron uptake by nitrosyl based orbitals. The DFT calculations indicate the formation of the typical bent Ru–N–O structure (Ru–N–O angle of 140.5°) on reduction, accompanied by negative shifts of the calculated NO stretching frequencies by about 240 cm^{-1} .

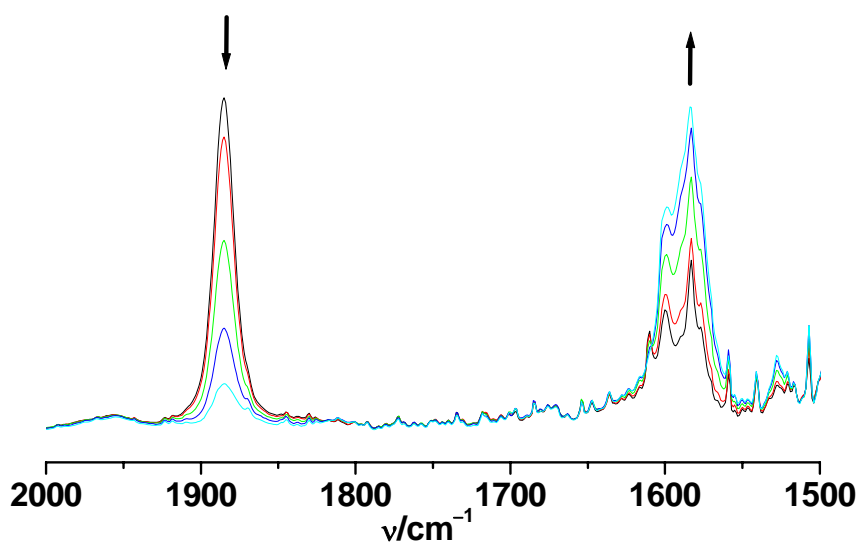


Figure 3.5.2. IR spectroelectrochemical response for conversion $[(\text{TPP})\text{Ru}(\text{NO})(\text{Py})]^{(+)\rightarrow(0)}$ in $\text{CH}_2\text{Cl}_2/0.1\text{ M } n\text{-Bu}_4\text{NClO}_4$ at 298 K.

Table 3.5.1. Experimental and G03/BPW91 calculated NO stretching frequencies (ν/cm^{-1}) for $[(\text{TPP})\text{Ru}(\text{NO})(\text{X})]^{n+}$ complexes

	n = 2		n = 1		n = 0	
	calc.	exp. ^a	calc.	exp. ^a	calc.	exp. ^a
$[(\text{TPP})\text{Ru}(\text{NO})(\text{H}_2\text{O})]^{n+}$	1921.5	1902	1903.6	1875	-	n. o.
$[(\text{TPP})\text{Ru}(\text{NO})(\text{Py})]^{n+}$	-	n. o.	1902.9	1885	1665.4	1584

^a From spectroelectrochemical measurement in $\text{CH}_2\text{Cl}_2/0.1 \text{ M } n\text{-Bu}_4\text{NClO}_4$ at 298 K.

n.o. = not observed.

3.6. EPR Spectroelectrochemistry

EPR spectroscopy supports the above interpretations. The reversibly obtained oxidised forms $[(\text{TPP})\text{Ru}(\text{NO})(\text{H}_2\text{O})]^{2+}$ show EPR signal at $g_{\text{iso}} = 2.0002$ and line widths of about 25 G (Figure 3.6.1). Such EPR signals with $g_{\text{iso}} \approx 2.00$ and without noticeable g anisotropy (Figure 3.6.2) in the frozen state at X-band frequency (9.5 GHz) are typical for organic radicals, here for paramagnetic species containing the spin almost exclusively in the conjugated π system of the porphyrin ring.^[85,86,87,88,93,94,95,96,97,98] Metal based oxidation should result in rather large g anisotropy, well detectable at X-band frequency, and $g_{\text{iso}} > 2$ for a $4d^5$ (Ru^{III}) configuration because of the high spin-orbit coupling constant of Ru^{III} ,^[99] thus the formation of ruthenium(III) on first oxidation can be excluded.

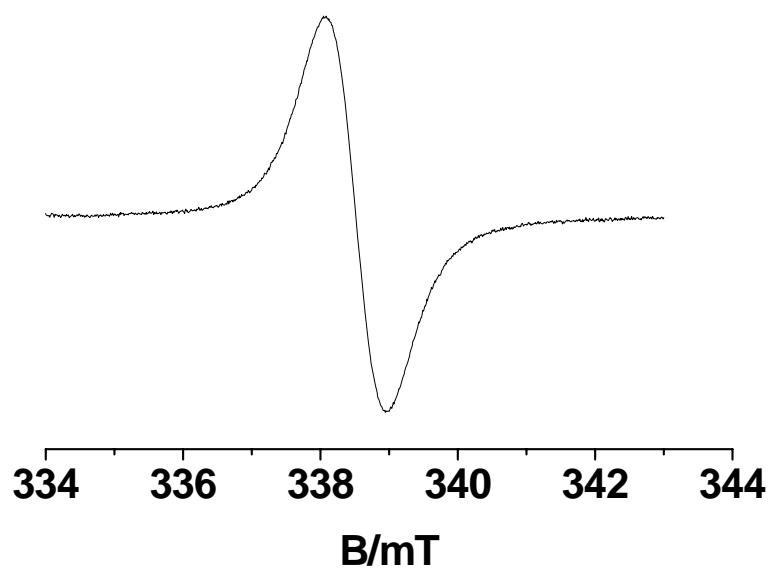


Figure 3.6.1. EPR spectrum of oxidised $[(\text{TPP})\text{Ru}(\text{NO})(\text{H}_2\text{O})]\text{BF}_4$ in $\text{CH}_2\text{Cl}_2/0.1 \text{ M } n\text{-Bu}_4\text{NClO}_4$ at 298 K.

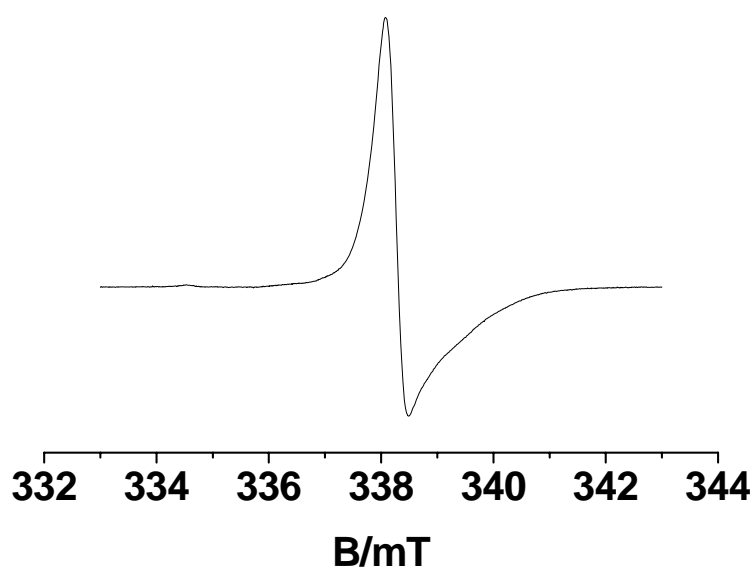


Figure 3.6.2. EPR spectrum of oxidised $[(\text{TPP})\text{Ru}(\text{NO})(\text{H}_2\text{O})]\text{BF}_4$ in $\text{CH}_2\text{Cl}_2/0.1 \text{ M } n\text{-Bu}_4\text{NClO}_4$ at 110 K.

The EPR spectra of the obtained reduced species $[(\text{TPP})\text{Ru}(\text{NO})(\text{X})]^0$ (Figure 3.6.3, Table 3.6.1) show typically^[50] invariant EPR characteristics ($g_1 > 2$, $g_2 \approx 2.0$, $g_3 < 2$; $A_2(^{14}\text{N}) \approx 3.4$ mT) of $\{\text{RuNO}\}^7$ species which have been observed before for a large number of very different complexes containing RuNO where the spin resides mainly (ca. 70%) on the NO ligand.^[50] Figure 3.6.4 shows the difference between spin densities calculated for oxidised $[(\text{TPP})\text{Ru}(\text{NO})(\text{H}_2\text{O})]^{2+}$ (spin density on porphyrin) and reduced $[(\text{TPP})\text{Ru}(\text{NO})(\text{py})]$ (spin density of 0.68 on the NO ligand). The DFT calculated EPR parameters listed in Table 3.6.1 agree satisfactorily with the experimental data, the calculations confirm either porphyrin or NO-centred processes in the course of oxidation or reduction, respectively.

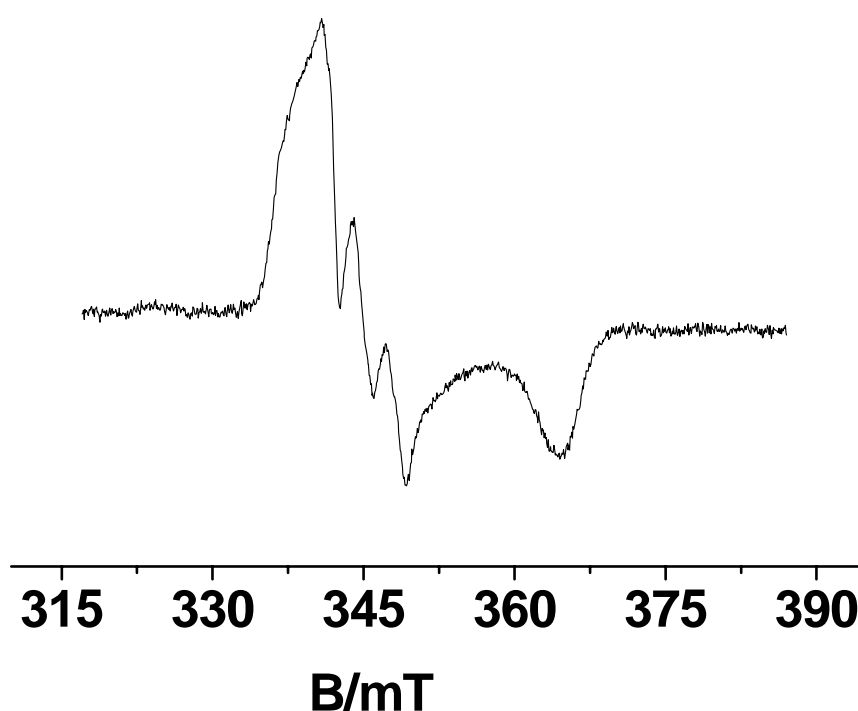


Figure 3.6.3. EPR spectrum of reduced $[(\text{TPP})\text{Ru}(\text{NO})(\text{Py})]\text{BF}_4$ in $\text{CH}_2\text{Cl}_2/0.1$ M $n\text{-Bu}_4\text{NClO}_4$ at 110 K.

Table 3.6.1. The g values and A (^{14}N) for $[(\text{TPP})\text{Ru}(\text{NO})(\text{X})]^{0\text{a}}$ with three different pyridines

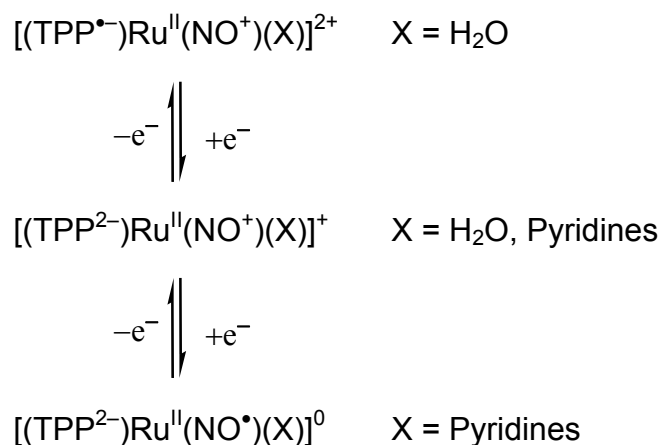
axial ligand (X)	g_1	g_2	g_3	$\langle g \rangle^{\text{b}}$	$A_2(^{14}\text{N})$
4-cyanopyridine	2.036	1.985	1.886	1.970	33 G
pyridine	2.036	1.985	1.880	1.968	33 G
	2.027 ^c	1.983 ^c	1.923 ^c		
4-N,N-dimethylaminopyridine	2.036	1.985	1.878	1.967	33 G

^a Electrochemically generated in $\text{CH}_2\text{Cl}_2/0.1 \text{ M } n\text{-Bu}_4\text{NClO}_4$; measurements at 110 K.

^b $\langle g \rangle = \sqrt{(g_1^2 + g_2^2 + g_3^2)/3}$.

^c Calculated values.

Following theoretical and experimental results, especially the combined EPR and IR spectroelectrochemical measurements, we have thus established the sequence of oxidation state combinations as shown in Scheme 3.6.1:



Scheme 3.6.1. Electronic structure formulation for ruthenium nitrosyl porphyrin complexes in different oxidation states.

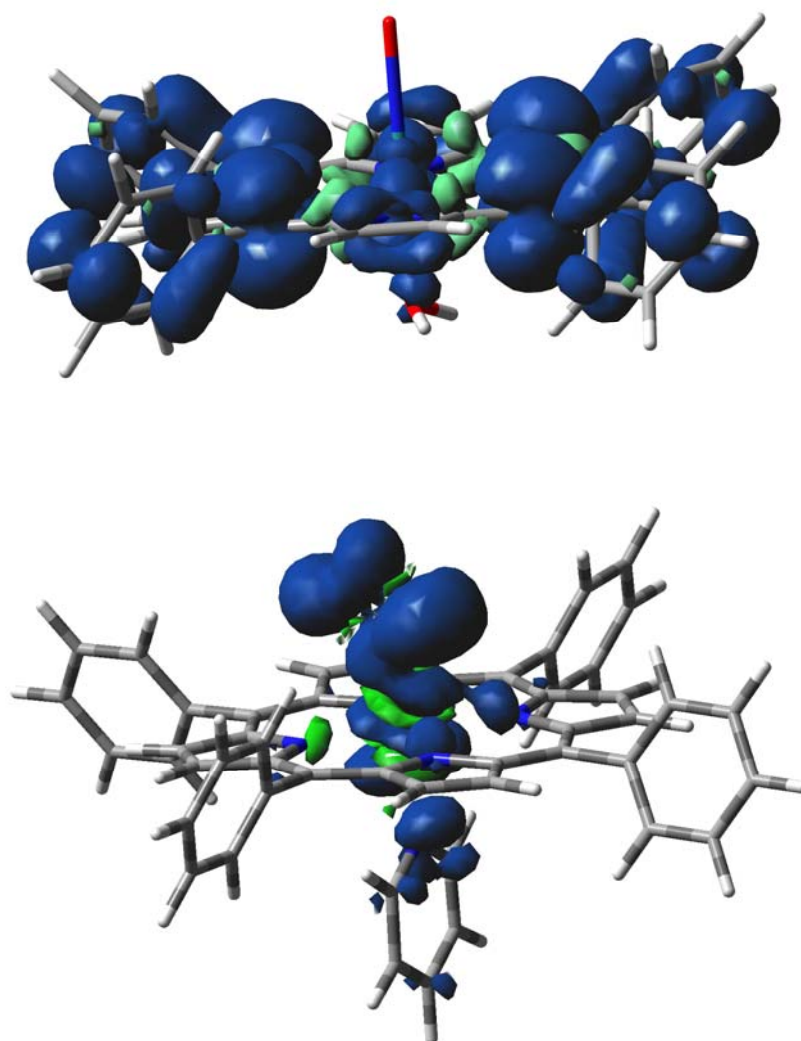


Figure 3.6.4. Representation of spin densities of $[(\text{TPP})\text{Ru}(\text{NO})(\text{H}_2\text{O})]^{2+}$ (top) and $[(\text{TPP})\text{Ru}(\text{NO})(\text{py})]$ (bottom).

3.7. UV/VIS/NIR Spectroelectrochemistry

As known from numerous work on porphyrins and their metal complexes,^[81,85,86,87,88,93] the UV/VIS absorption spectra of ruthenium nitrosyl porphyrins show blue shifted Q bands and a very sharp Soret band (Table 3.7.1). As illustrated in Figure 3.7.1, the spectrum of oxidised $[(\text{TPP})\text{Ru}(\text{NO})(\text{H}_2\text{O})]^{(+)\rightarrow(2+)}$ displays a decrease in intensity of the Soret band and also of the Q band at 558 nm which seems to disappear completely at the cost of new broad bands at 616, 658 and 742 nm. Such change in absorption spectra is typical^[81,85,86,87,88,93] for the formation of

porphyrin π radicals. The UV/VIS spectroelectrochemical reduction experiments for $[(\text{TPP})\text{Ru}(\text{NO})(\text{py})]\text{BF}_4$ (Figure 3.7.2) show nitrosyl based reduction^[33,50,51,60] as evident from the appearance of new bands in the visible region which were attributed in part to MLCT transitions $d(\text{Ru}) \rightarrow \pi^*(\text{NO}^\bullet)$ and to ligand-to-ligand charge transfer processes $\pi^*(\text{NO}^\bullet) \rightarrow \pi^*(\text{Por})$.

Table 3.7.1. Absorption data^a of complexes

compound	λ/nm ($\epsilon/\text{M}^{-1}\cdot\text{cm}^{-1}$)
$[(\text{TPP})\text{Ru}(\text{NO})(\text{H}_2\text{O})]^+$	410 (78000), 558 (12 000)
$[(\text{TPP})\text{Ru}(\text{NO})(\text{H}_2\text{O})]^{+\text{b}}$	391 (1.248) 391 (1.228) 482(0.065) 483 (0.068) 610 (0.026) 621 (0.029)
$[(\text{TPP})\text{Ru}(\text{NO})(\text{H}_2\text{O})]^{2+}$	408(84000), 496sh, 616(17000), 658(15700), 742(5900)
$[(\text{TPP})\text{Ru}(\text{NO})(\text{Py})]^+$	278, 324, 400, 422, 492, 540, 573, 620
$[(\text{TPP})\text{Ru}(\text{NO})(\text{Py})]^{+\text{b}}$	326 (0.187) 396 (1.197) 397 (1.125) 501 (0.056) 503 (0.055) 674 (0.016) 679 (0.016)
$[(\text{TPP})\text{Ru}(\text{NO})(\text{Py})]^0$	279, 310, 394, 430, 538, 574

^a From spectroelectrochemistry in an OTTLE cell in $\text{CH}_2\text{Cl}_2/0.1 \text{ M } n\text{-Bu}_4\text{NClO}_4$ at 298 K.

^b TD DFT calculated; calculated values - λ/nm (oscillator strength).

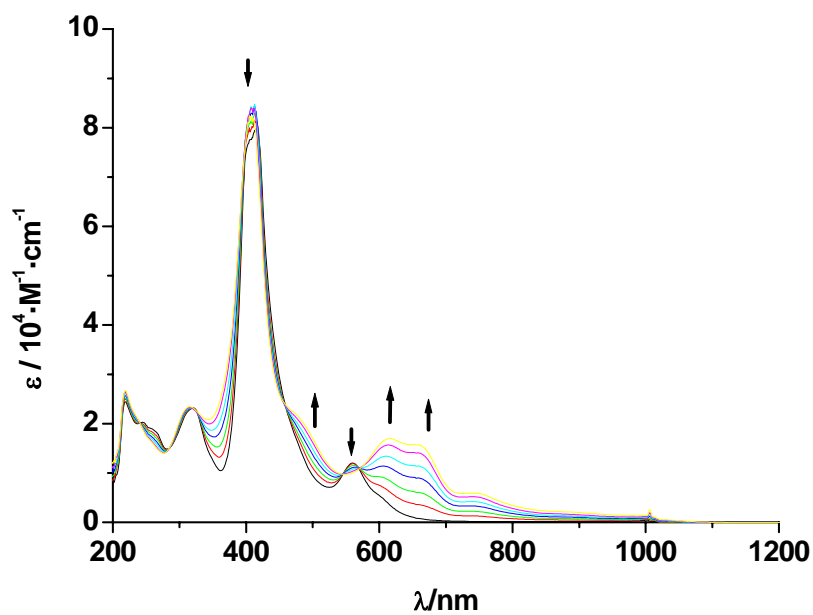


Figure 3.7.1. UV/VIS spectroelectrochemical response for the conversion $[(\text{TPP})\text{Ru}(\text{NO})(\text{H}_2\text{O})]^{(+)} \rightarrow (2^+)$ in $\text{CH}_2\text{Cl}_2/0.1 \text{ M } n\text{-Bu}_4\text{NClO}_4$ at 298 K.

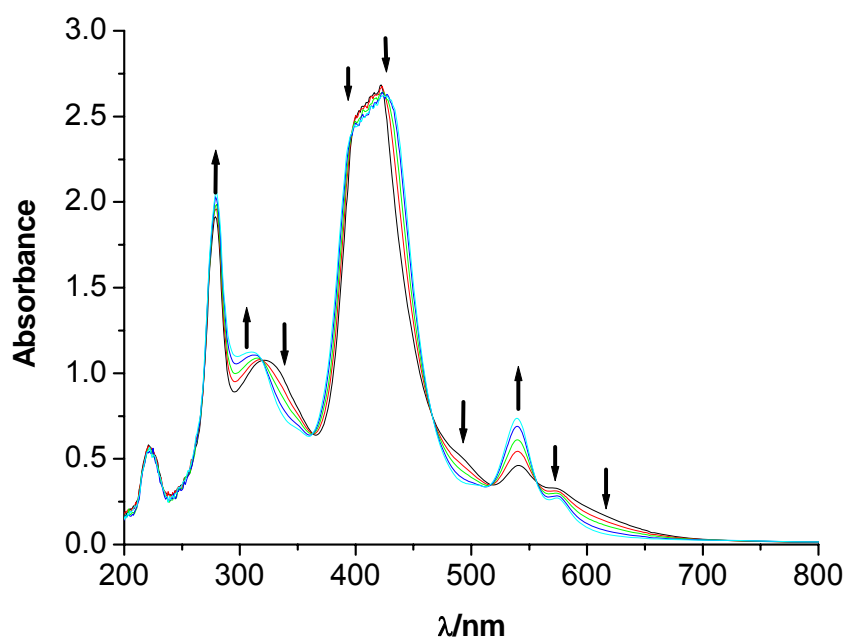


Figure 3.7.2. UV/VIS spectroelectrochemical response for the conversion $[(\text{TPP})\text{Ru}(\text{NO})(\text{Py})]^{(+)} \rightarrow (0)$ in $\text{CH}_2\text{Cl}_2/0.1 \text{ M } n\text{-Bu}_4\text{NClO}_4$ at 298 K.

3.8. DFT Calculations

The compositions of DFT calculated frontier orbitals of $[(\text{TPP})\text{Ru}(\text{NO})(\text{H}_2\text{O})]^+$ and $[(\text{TPP})\text{Ru}(\text{NO})(\text{py})]^+$ complexes are listed in Tables 3.8.1 and 3.8.2. Two closely lying highest occupied orbitals (HOMO and HOMO–1) of $[(\text{TPP})\text{Ru}(\text{NO})(\text{H}_2\text{O})]^+$, are composed mainly from π porphyrin orbitals (98%) (Figure 3.8.1, Table 3.8.1). The set of two almost degenerated lowest unoccupied molecular orbitals (LUMO and LUMO+1) $[(\text{TPP})\text{Ru}(\text{NO})(\text{py})]^+$, are mainly formed by π^* orbitals of NO ligand (53%) with contributing 4d (Ru) orbitals (17%) and π porphyrine orbitals (25%) (Figure 3.8.2). Pyridine and H_2O do not contribute substantially to frontier orbitals, the most significant such effect concerns the LUMO of $[(\text{TPP})\text{Ru}(\text{NO})(\text{py})]^+$ with 4% contribution from pyridine. Accordingly, the stabilisation of the reduced forms has been achieved with pyridine axial ligands.

Table 3.8.1. DFT G03/PBE0 calculated one-electron energies and compositions of selected highest occupied and lowest unoccupied molecular orbitals of $[(\text{TPP})\text{Ru}(\text{NO})(\text{H}_2\text{O})]^+$ complex expressed in terms of composing fragments

MO	E (eV)	prevailing character	Ru	NO	Por	H ₂ O
unoccupied						
LUMO+3	–4.91	π Por + Ru	14	21	65	0
LUMO+2	–4.93	π^* Por + Ru	14	21	64	0
LUMO+1	–5.37	π NO + Ru	15	45	40	0
LUMO	–5.40	π^* NO + Ru	15	47	38	0
occupied						
HOMO	–8.17	π Por	1	0	98	1
HOMO–1	–8.45	π Por	0	0	100	0
HOMO–2	–9.27	π Por	0	0	100	0
HOMO–3	–9.30	π Por	0	0	100	0

Table 3.8.2. DFT G03/PBE0 calculated one-electron energies and compositions of selected highest occupied and lowest unoccupied molecular orbitals of [(TPP)Ru(NO)(py)]⁺ complex expressed in terms of composing fragments

MO	E (eV)	prevailing character	Ru	NO	Por	py
unoccupied						
LUMO+3	-4.80	π^* Por + Ru	11	15	73	0
LUMO+2	-4.82	π^* Por + Ru	10	12	77	2
LUMO+1	-5.30	π^* NO + Ru	17	52	30	1
LUMO	-5.32	π^* NO + Ru	17	53	25	4
occupied						
HOMO	-7.98	π Por	1	0	98	1
HOMO-1	-8.27	π Por	0	0	100	0
HOMO-2	-9.17	π Por	0	0	100	0
HOMO-3	-9.18	π Por	0	0	100	0

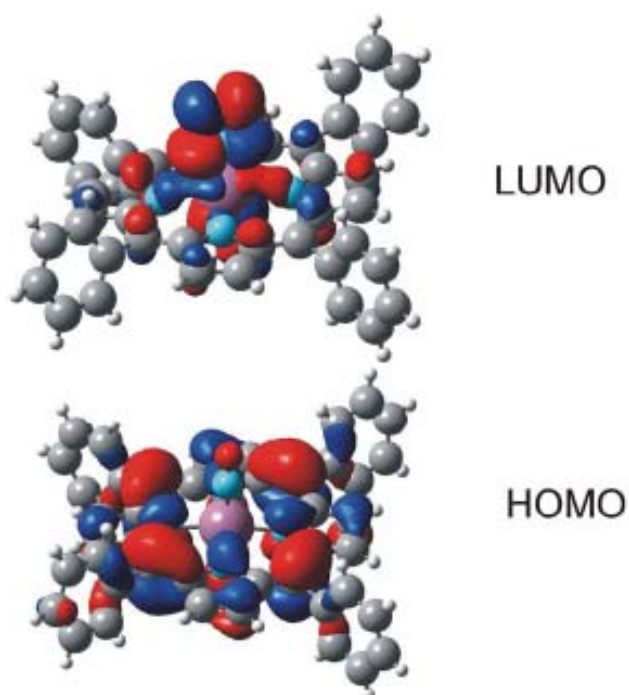


Figure 3.8.1. Representation of HOMO and LUMO in [(TPP)Ru(NO)(H₂O)]⁺.

3.9. Conclusion and Outlook

The reversible electron transfer processes for ruthenium nitrosyl porphyrins have been observed by varying the axial ligand. Except for the redox potentials, the differences between complexes involving different pyridine ligands have been small. The complexes of the type $[(\text{TPP})\text{Ru}(\text{NO})(\text{X})]\text{BF}_4$ containing X as neutral O donor aqua ligand show a two-step oxidation, and with X as neutral N donor pyridine ligands they show reversible reduction. The sites of all processes have been determined by means of spectroelectrochemical measurements and through theoretical support. The first oxidation of $[(\text{TPP})\text{Ru}(\text{NO})(\text{H}_2\text{O})]^+$ occurs on the porphyrin ring. The reduction of $[(\text{TPP})\text{Ru}(\text{NO})(\text{Py})]^+$ is mainly NO-centred, as noted similarly for many other $\{\text{RuNO}\}^7$ systems.^[50] The fascinating metal/NO interaction relevant to biochemistry,^[100] and organic chemistry,^[40,101] can thus be probed via an array of spectroelectrochemical methods.

CHAPTER 4

Mononuclear Ruthenium Nitro, Nitrosyl and Acetonitrile Complexes with 2,2'-Bipyrimidine and 2,2':6',2''-Terpyridine

4.1. Introduction

After the discovery of the variegated physiological roles^[3,4,5,6] of “NO”, there has been considerable interest in the area of developing NO donors as therapeutic agents^[16,102] because these synthetic NO donors under physiological condition release nitric oxide and thus can cure the diseases which arise from the deficiency of NO.^[6] A variety of organic compounds such as nitrites (e.g., trinitroglycerol), or nitrosothiols and metal nitrosyl complexes such as the sodium nitroprusside (SNP) have been widely used in clinical treatments.^[6] The major problems with the existing drugs are their side effects e.g., cyanide poisoning in case of SNP and nitrate tolerance for trinitroglycerol.^[8] Thus, the development of new chemotherapeutic agents is essential for improving the selectivity of drugs and lowering the harmful side effects.

Recent studies concerning polypyridyl ruthenium complexes which are well known for their interesting photophysical and redox properties suggest that these complexes can act as antitumor and antiseptic agents^[103] and therefore can be used for medical-pharmaceutical purposes.^[17,18,54] In order to identify new chemotherapeutic agents based on ruthenium polypyridyl based drugs with better selectivity and lower toxicity, a better understanding of their synthetic aspects, spectroscopic and reactivity properties is essential.

In this Chapter, the redox series $[\text{Ru}(\text{NO})(\text{bpym})(\text{terpy})]^{3+/2+/+0}$ has been investigated by cyclic voltammetry, spectroelectrochemistry in the UV/VIS/NIR and IR ($\nu(\text{NO})$) regions and by multi-frequency EPR spectroscopy. These studies were undertaken because the presence of three different π acceptors (NO^+ , bpym, terpy) as ligands to π electron donating ruthenium(II) raises various possibilities for electron and charge

transfer processes; the sequence of low lying π^* levels was to be established through the combination of spectroscopic methods and through DFT calculations.

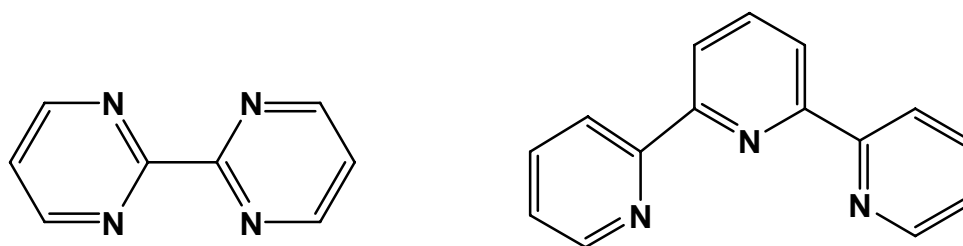


Figure 4.1.1. The ligands 2,2'-bipyrimidine (left) and 2,2':6',2''-terpyridine (right).

Also, the considerably covalent metal-ligand bonding as expressed by the Enemark-Feltham^[2] notation $\{MNO\}^n$ has been well vindicated by the almost invariant X-band (9.5 GHz) EPR characteristics (g factors, $A(^{14}N)$) of a number of $\{RuNO\}^7$ species with very diverse ligand configurations.^[50] Confirmation and additional information for these X-band EPR results was now sought with the help of high-field EPR, here W-band (95 GHz) and G-band (190 GHz) EPR. The requirement for such a study, a $\{RuNO\}^7$ complex with sufficient chemical stability in high concentration was found in the one-electron reduced form of the new $[Ru(NO)(bpym)(terpy)](PF_6)_3$, bpym = 2,2'-bipyrimidine and terpy = 2,2':6',2''-terpyridine.

4.2. Syntheses and Characterisation

The nitro complex $[Ru(NO_2)(bpym)(terpy)](PF_6)$ (**4a**) was prepared, in analogy to previously reported procedures,^[50,51,54,104] by the reaction of $Ru(terpy)Cl_3$ ^[105] with 2,2'-bipyrimidine in EtOH/H₂O (1/1, v/v) mixture under refluxing condition followed by the addition of NaNO₂ (Figure 4.2.1). The nitro precursor $[Ru(NO_2)(bpym)(terpy)](PF_6)$ was converted into $[Ru(NO)(bpym)(terpy)](PF_6)_3$ (**4b**) by treating it with 3 M HCl, followed by the precipitation from NH₄PF₆ (Figure 4.2.1).

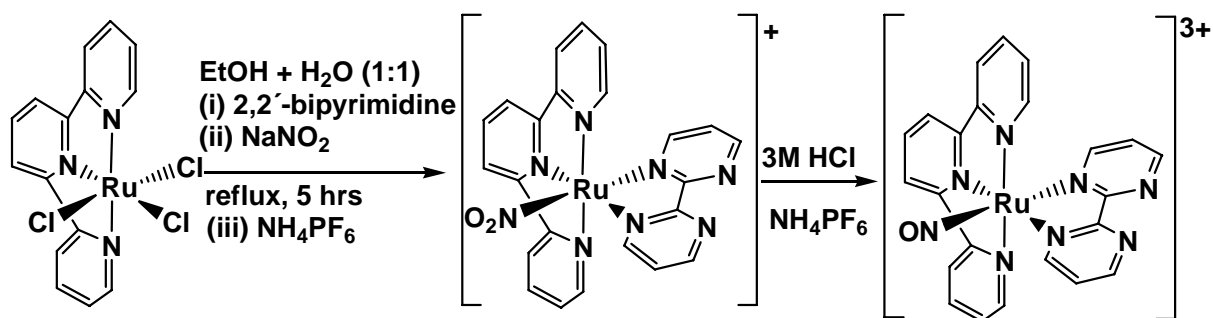


Figure 4.2.1. Reaction scheme showing syntheses of $[\text{Ru}(\text{NO}_2)(\text{bpym})(\text{terpy})](\text{PF}_6)$ and $[\text{Ru}(\text{NO})(\text{bpym})(\text{terpy})](\text{PF}_6)_3$.

The nitro and nitrosyl complexes were characterised by ^1H 1D and 2D NMR at 400 MHz, IR and UV/VIS spectroscopy and elemental analyses (Chapter 6). Attempts to recrystallise $[\text{Ru}(\text{NO})(\text{bpym})(\text{terpy})](\text{PF}_6)_3$ in methanol/acetonitrile (1/1, v/v) mixture gave the crystals of $[\text{Ru}(\text{CH}_3\text{CN})(\text{bpym})(\text{terpy})](\text{PF}_6)_2$ (**4c**) which were analysed by single crystal X-ray crystallography, ^1H NMR and elemental analyses.

The ^1H 1D NMR spectra of $[\text{Ru}(\text{NO}_2)(\text{bpym})(\text{terpy})]^+$ and $[\text{Ru}(\text{NO})(\text{bpym})(\text{terpy})]^{3+}$ in CD_3CN at 400 MHz with the assignment of peaks are shown in Figures 4.2.3 and 4.2.5. The numbering of hydrogens is shown in the Figure 4.2.2. The assignment of peaks are done with the help of ^1H - ^1H COSY NMR spectra (Figures 4.2.4, 4.2.6). The complexes display 12 resonances in the aromatic region between $\delta = 7.0$ to 11.0 ppm. This matches well with the calculated 12 types of proton in the compounds, 6 from terpy and 6 from bpym. The total intensity of all signals corresponds to the total of 17 protons in the compounds. The chemical shifts values in ppm for all hydrogens in the complexes, **4a**, **4b**, **4c**, and in the ligands, bpym and terpy are tabulated in Table 4.2.1.

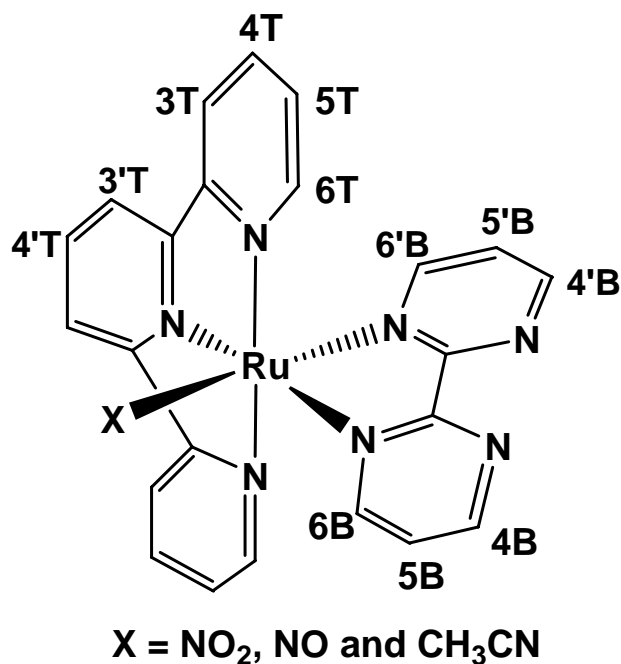


Figure 4.2.2. The numbering of hydrogen atoms in $[\text{Ru}(\text{NO}_2)(\text{bpy})(\text{terpy})]^+$, $[\text{Ru}(\text{NO})(\text{bpy})(\text{terpy})]^{3+}$ and $[\text{Ru}(\text{CH}_3\text{CN})(\text{bpy})(\text{terpy})]^{2+}$.

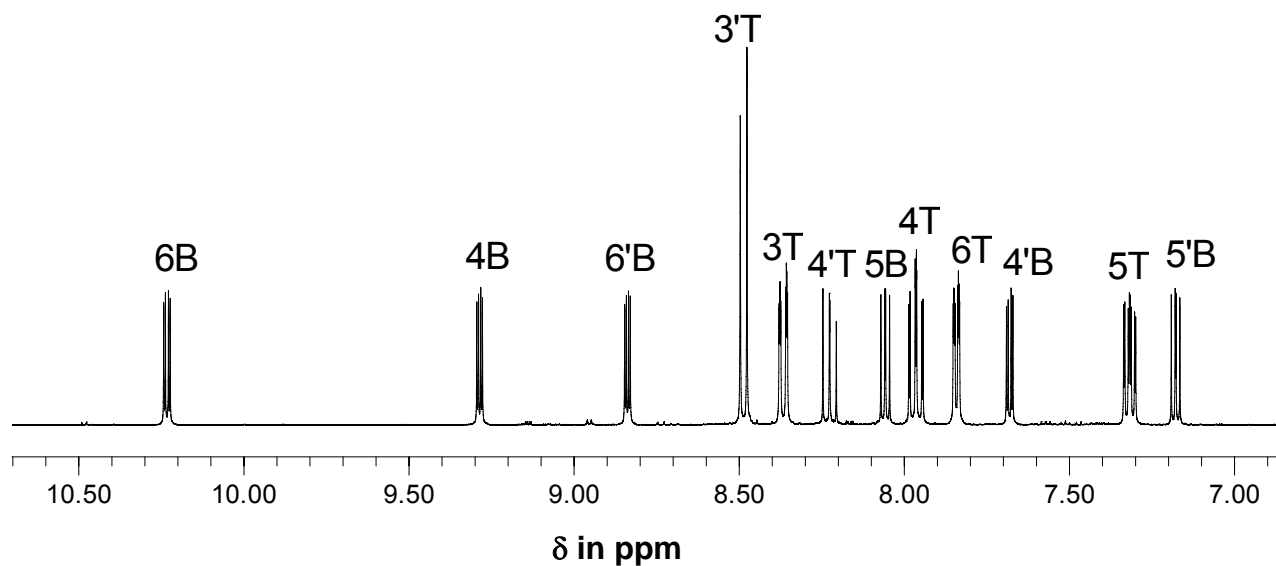


Figure 4.2.3. ¹H NMR of $[\text{Ru}(\text{NO}_2)(\text{bpy})(\text{terpy})](\text{PF}_6)$ in CD_3CN at 400 MHz.

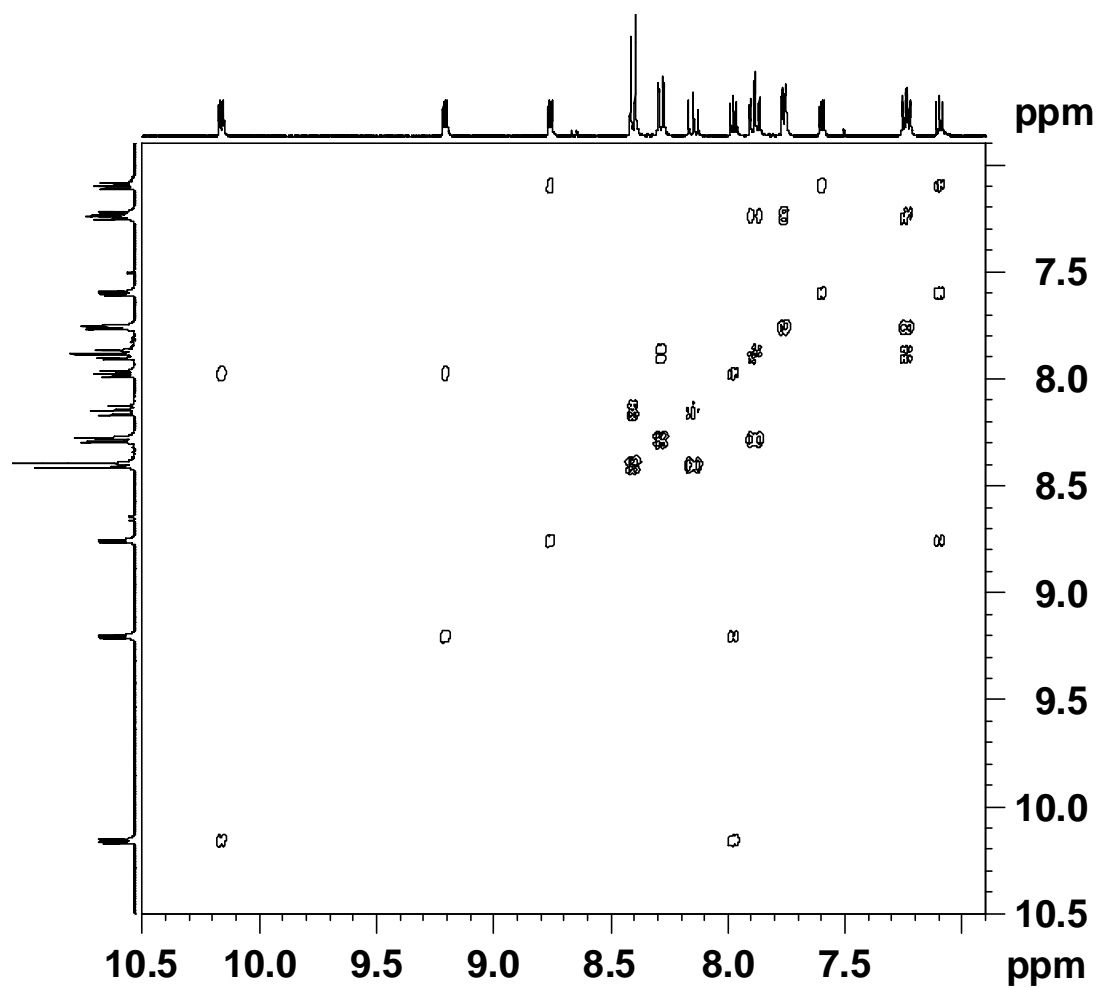


Figure 4.2.4. ^1H - ^1H COSY spectrum of $[\text{Ru}(\text{NO}_2)(\text{bpym})(\text{terpy})](\text{PF}_6)$ in CD_3CN at 400 MHz.

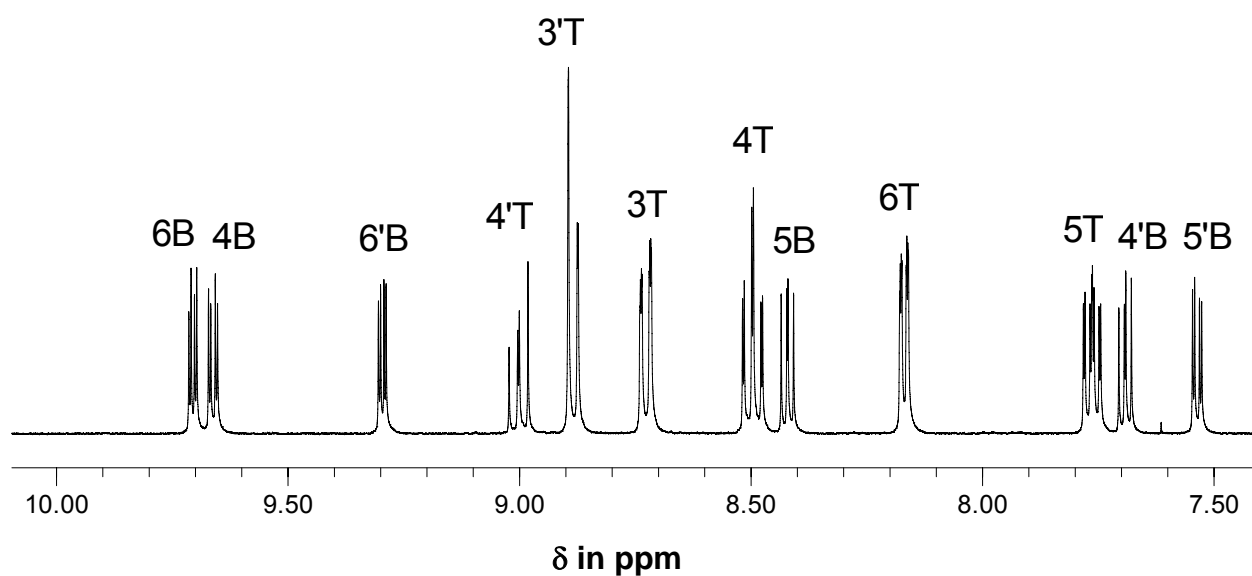


Figure 4.2.5. ^1H NMR of $[\text{Ru}(\text{NO})(\text{bpym})(\text{terpy})](\text{PF}_6)_3$ in CD_3CN at 400 MHz.

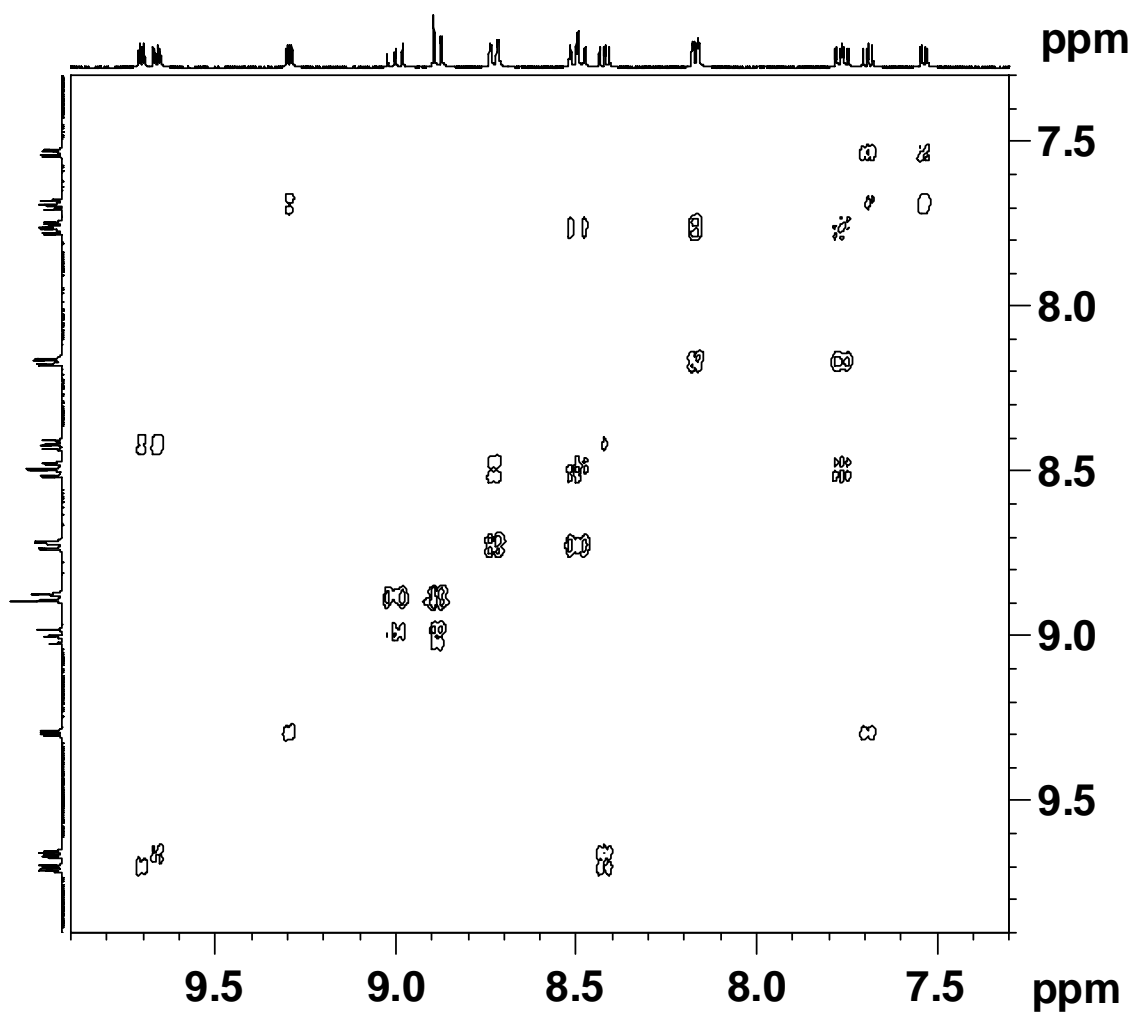


Figure 4.2.6. ^1H - ^1H COSY spectrum of $[\text{Ru}(\text{NO})(\text{bpym})(\text{terpy})](\text{PF}_6)_3$ in CD_3CN at 400 MHz.

Table 4.2.1. Proton chemical shift values (ppm) for the terpy, bpym, **4a** (nitro), **4b** (nitrosyl) and **4c** (acetonitrile) in CD_3CN

proton	δ in ppm				
	compound				
	terpy	bpym	(4a)	(4b)	(4c)
5T	7.44		7.24	7.76	7.40
4T	7.97		7.88	8.50	8.06

Table 4.2.1 *continued*

4'T	8.05	8.15	9.00	8.37
3'T	8.49	8.40	8.88	8.59
3T	8.67	8.28	8.73	8.45
6T	8.72	7.76	8.16	7.83
4B	8.96	9.20	9.66	9.40
5B	7.50	7.97	8.42	8.10
6B	8.96	10.16	9.71	9.85
4'B	8.96	7.60	7.69	7.64
5'B	7.50	7.09	7.54	7.23
6'B	8.96	8.76	9.30	8.87

The nitro compound $[\text{Ru}(\text{NO}_2)(\text{bpym})(\text{terpy})](\text{PF}_6)$ shows $\nu(\text{NO}_2\text{asym})$ and $\nu(\text{NO}_2\text{sym})$ at 1342 cm^{-1} and 1286 cm^{-1} respectively. The nitrosyl compound $[\text{Ru}(\text{NO})(\text{bpym})(\text{terpy})]^{3+}$ exhibits a rather high value of 1957 cm^{-1} for $\nu(\text{NO})$ which illustrates the π acceptor influence^[104] from both bpym and terpy. The UV/VIS spectra of the complexes are discussed in section 4.6.

4.3. Crystal Structures

The precursor compound $[\text{Ru}(\text{NO}_2)(\text{bpym})(\text{terpy})](\text{PF}_6)$ could be crystallised to exhibit a typical^[51,106,107] nitro complex structure (Figure 4.3.1, Table 4.3.1). The meridional binding of terpy^[107] causes one metal bound N of coordinated bpym to lie in *cis* and another one to lie in *trans* position to NO_2^- . The "polar" axis of terpy lies approximately in the O_2NRu plane. The molecular structure of the trication in the crystal of $[\text{Ru}(\text{NO})(\text{bpym})(\text{terpy})](\text{PF}_6)_3$ confirms the $\{\text{RuNO}\}^6$ state^[2] via the nearly linear ($175.2(4)^\circ$) RuNO configuration and the typical^[51] Ru–N ($1.770(5)\text{ \AA}$) and N–O ($1.129(6)\text{ \AA}$) bond lengths (Figure 4.3.2, Table 4.3.1). Table 4.3.1 confirms that the DFT optimised geometries of $[\text{Ru}(\text{NO})(\text{bpym})(\text{terpy})]^{3+}$ and $[\text{Ru}(\text{NO}_2)(\text{bpym})(\text{terpy})]^+$ agree with the experimental structural data. The Ru–N1 and Ru–N2 bond lengths are reproduced within 0.02 \AA , the remaining Ru–N bond lengths are slightly

Table 4.3.1 *continued*

Ru–N4	2.068(5)	2.075	2.088(5)	2.121
Ru–N5	2.070(5)	2.099	2.088(5)	2.126
Ru–N6	2.090(5)	2.119	2.093(5)	2.136
N1–O1	1.264(6)	1.253	1.129(6)	1.143
			(N1–O)	
N1–O2	1.246(6)	1.240		
N1–Ru–N5	174.8(2)	172.1	172.1(2)	172.0
N2–Ru–N6	172.50(19)	176.3	168.59(18)	169.6
N3–Ru–N4	159.01(19)	158.1	159.40(19)	157.2
N1–Ru–N2	90.18(19)	88.4	96.7(2)	95.7
N1–Ru–N3	91.8(2)	88.6	92.3(2)	93.9
N1–Ru–N4	87.0(2)	88.4	95.4(2)	94.0
N1–Ru–N6	96.8(2)	95.3	94.6(2)	94.7
N2–Ru–N3	80.4(2)	79.4	80.20(19)	79.0
N2–Ru–N4	78.7(2)	78.8	79.95(19)	79.0
N2–Ru–N5	94.93(19)	99.5	91.03(19)	92.3
N3–Ru–N5	88.41(19)	92.2	87.02(18)	87.6
N4–Ru–N5	94.7(2)	93.7	87.88(18)	87.5
N4–Ru–N6	104.2(2)	100.6	100.91(18)	100.3
N5–Ru–N6	78.0(2)	76.8	77.66(18)	77.3
O–N1–Ru			175.2(4)	177.4
O1–N1–O2	118.6(5)	121.7		

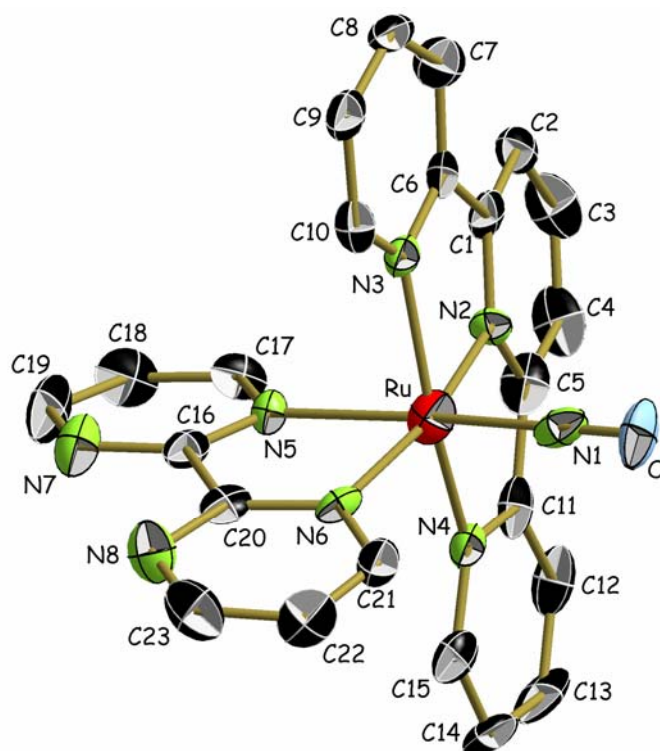


Figure 4.3.2. Molecular structure of the trication of [Ru(NO)(bpym)(terpy)](PF₆)₃ in the crystal at 100 K.

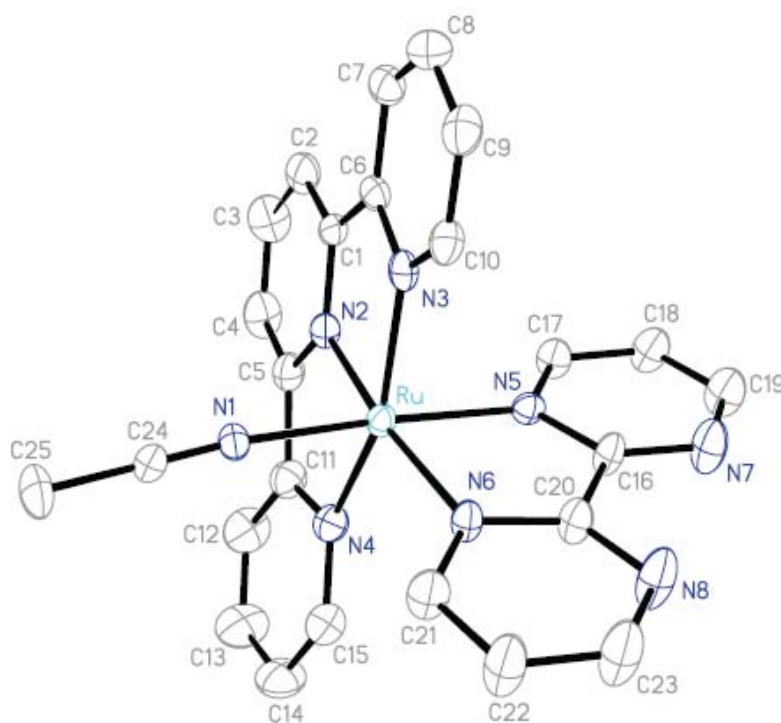


Figure 4.3.3. Molecular structure of the dication of [Ru(CH₃CN)(bpym)(terpy)](PF₆)₂ in the crystal at 173 K.

Table 4.3.2. Selected bond lengths (Å) and angles (deg) for complex [Ru(CH₃CN)(bpym)(terpy)](PF₆)₂

Ru–N1	2.046(7)
Ru–N2	1.979(7)
Ru–N3	2.094(7)
Ru–N4	2.086(7)
Ru–N5	2.053(7)
Ru–N6	2.078(7)
N1–C24	1.112(11)
C24–C25	1.470(13)
N1–Ru–N5	172.8(3)
N2–Ru–N6	171.7(3)
N3–Ru–N4	158.2(3)
N1–Ru–N2	93.6(3)
N1–Ru–N3	91.8(3)
N1–Ru–N4	86.5(3)
N1–Ru–N6	94.7(3)
N2–Ru–N3	79.7(3)
N2–Ru–N4	78.7(3)
N2–Ru–N5	93.4(3)
N3–Ru–N5	87.9(3)
N4–Ru–N5	96.4(3)
N4–Ru–N6	101.6(3)
N5–Ru–N6	78.3(3)

4.4. Electrochemistry

Cyclic voltammetry and polarography were employed to study the nitro precursor and electron deficient [Ru(NO)(bpym)(terpy)](PF₆)₃. The nitro complex [Ru(NO₂)(bpym)(terpy)](PF₆) exhibits a conventional electrochemical pattern (Figure 4.4.1, Table 4.4.1) with a metal-centred oxidation at $E_{1/2} = 0.79$ V vs. FeCp₂⁺⁰

(reversible only at higher scan rate (2 V/s) at 298 K or at $-40\text{ }^{\circ}\text{C}$) and two ligand centred reductions at $E_{1/2}(\text{red1}) = -1.55\text{ V}$ and $E_{1/2}(\text{red2}) = -1.93\text{ V}$ vs. $\text{FeCp}_2^{+/0}$. The interpretation for the site of redox processes is not only in agreement with the redox potentials^[108] but also with EPR results for electrogenerated species (see section 4.6.2).

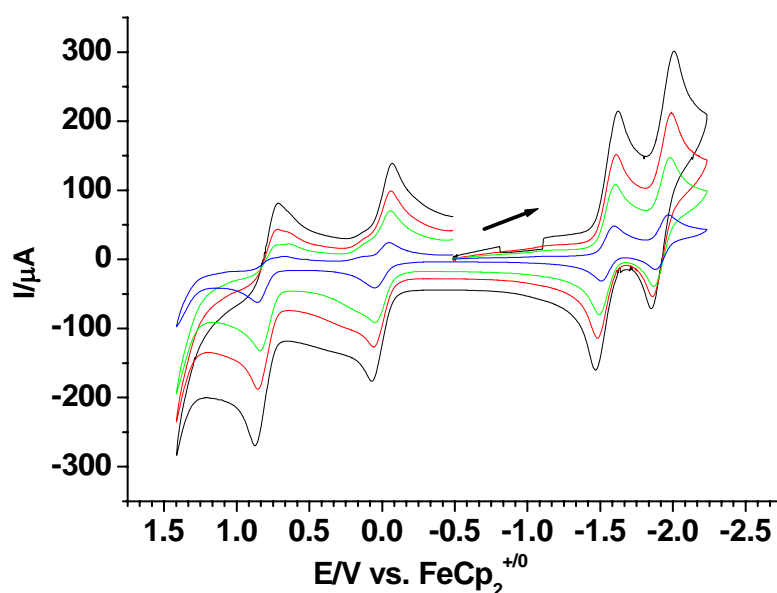


Figure 4.4.1. Cyclic voltammograms of $[\text{Ru}(\text{NO}_2)(\text{bpym})(\text{terpy})](\text{PF}_6)$ (1 mM) in $\text{CH}_3\text{CN}/0.1\text{ M } n\text{-Bu}_4\text{NPF}_6$ at 298 K at variable scan rates (100 (blue), 500 (green), 1000 (red), 2000 (black) mV/s); second peak from left: ferrocene standard.

The compound $[\text{Ru}(\text{NO})(\text{bpym})(\text{terpy})](\text{PF}_6)_3$ undergoes three reversible one-electron reduction processes. The very positive first reduction potential at $E_{1/2}(\text{red1}) = +0.17\text{ V}$ vs. $\text{FeCp}_2^{+/0}$ of $[\text{Ru}(\text{NO})(\text{bpym})(\text{terpy})](\text{PF}_6)_3$ in $\text{CH}_3\text{CN}/0.1\text{ M } n\text{-Bu}_4\text{NPF}_6$ explains the the π acceptor influence from both bpym and terpy.^[51,109] After a second clean one-electron reversible reduction at $E_{1/2}(\text{red2}) = -0.47\text{ V}$, the third electron addition at $E_{pc}(\text{red3}) = -1.61\text{ V}$ evokes the appearance of a sharp desorption spike in the reverse scan of the cyclic voltammogram (Figure 4.4.2, Table 4.4.1). Electrode adsorption of the reduction product results from the neutrality of the generated species $[\text{Ru}(\text{NO})(\text{bpym})(\text{terpy})]^0$ which contains an extended π system in terpy; polarography confirmed the otherwise reversible one-electron transition at this step. Although not accessible by spectroelectrochemistry, the potential of -1.61 V

suggests reduction of Ru^{II} coordinated 2,2'-bipyrimidine.^[108] The difference of 0.65 V between the potentials for first and second reduction is similar to that observed of other complexes involving the NO^{+•/•-} redox system,^[50,51,54,104] however, spectroelectrochemistry was required to establish this assertion for NO being the target of the first two electron additions.

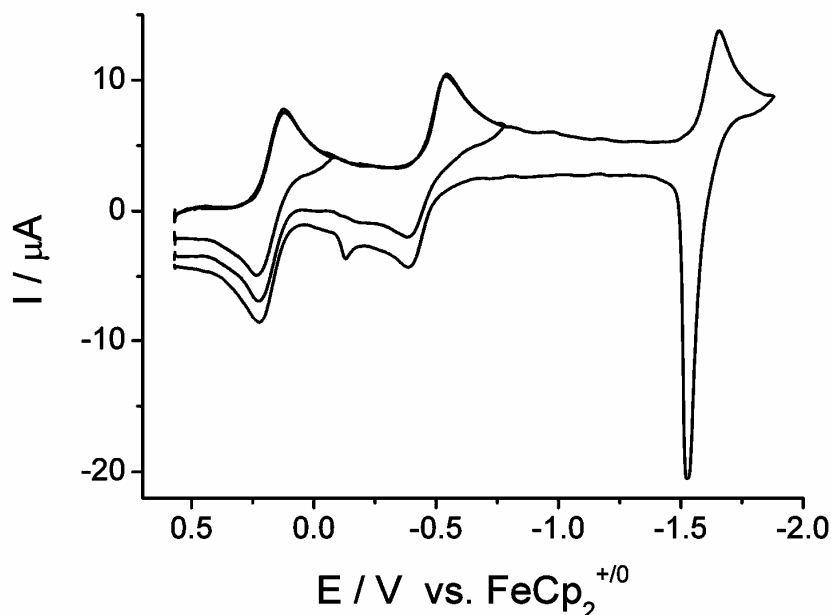


Figure 4.4.2. Cyclic voltammograms of [Ru(NO)(bpym)(terpy)](PF₆)₃ (1 mM) in CH₃CN/0.1 M *n*-Bu₄NPF₆ at 298 K at 200 mV/s.

Table 4.4.1. Electrochemical data^a of complexes

	E _{ox1}	E _{red1}	E _{red2}	E _{red3}
[Ru(NO ₂)(bpym)(terpy)](PF ₆)	0.79 ^b	-1.55	-1.93	n.o.
[Ru(NO)(bpym)(terpy)](PF ₆) ₃	n.o.	+0.17	-0.47	-1.61 ^c

^a From cyclic voltammetry in CH₃CN/0.1 M *n*-Bu₄NPF₆ at 200 mV/s: Half-wave potentials E in V vs. FeCp₂^{+•/0}.

^b Reversible at 2 V/s at 298 K or at 200 mV/s at -40 °C.

^c Adsorption.

n.o. = not observed.

4.5. IR Spectroelectrochemistry

Due to strong electrode adsorption during the third reduction step the optically transparent thin-layer electrode (OTTLE) spectroelectrochemical measurements in $\text{CD}_3\text{CN}/0.1 \text{ M } n\text{-Bu}_4\text{NPF}_6$ could be carried out only for the first two reduction processes. As said in Chapter 2, the $\nu(\text{NO})$ stretching band has been long recognised as an excellent indicator for the oxidation state of that "non-innocent" ligand in metal complexes.^[2,,9,11,54,65,110] The starting form $[\text{Ru}(\text{NO})(\text{bpym})(\text{terpy})]^{3+}$ exhibits a rather high value of 1957 cm^{-1} for $\nu(\text{NO})$ which illustrates the π acceptor influence from both bpym and terpy just like the positive reduction potential.^[51,104] The shift of $\nu(\text{NO})$ on one-electron reduction to 1665 cm^{-1} (Figure 4.5.1), i.e., by 292 cm^{-1} signifies a largely NO-centred electron addition to form a complex of NO^\bullet .^[2,11,51,110] The second reversible one-electron reduction causes a similar shift by 277 cm^{-1} to produce a band at 1388 cm^{-1} with diminished intensity (Figure 4.5.2) which would be a typical value for metal coordinated NO^- .^[2,11,51,110,111]

From this experiment we conclude that the first two reductions involve mainly the NO ligand, a result which is partially supported for the paramagnetic intermediate $[\text{Ru}(\text{NO})(\text{bpym})(\text{terpy})]^{2+}$ by EPR spectroscopy.

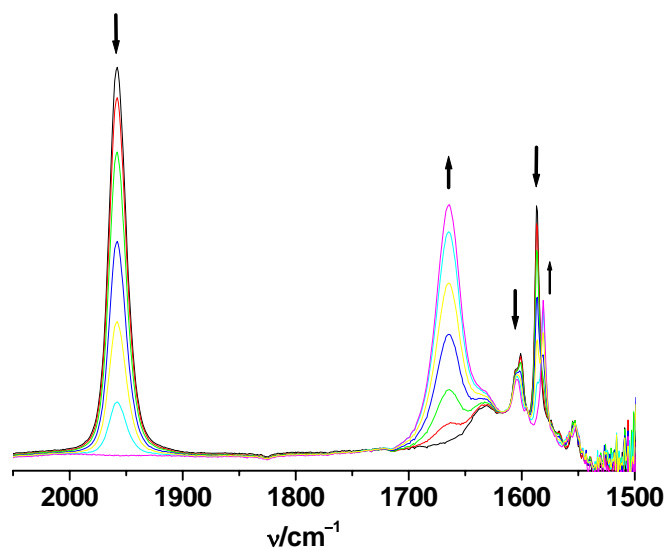


Figure 4.5.1. IR spectroelectrochemical response of $[\text{Ru}(\text{NO})(\text{bpym})(\text{terpy})](\text{PF}_6)_3$ in $\text{CD}_3\text{CN}/0.1 \text{ M } n\text{-Bu}_4\text{NPF}_6$ on first reduction step at 298 K.

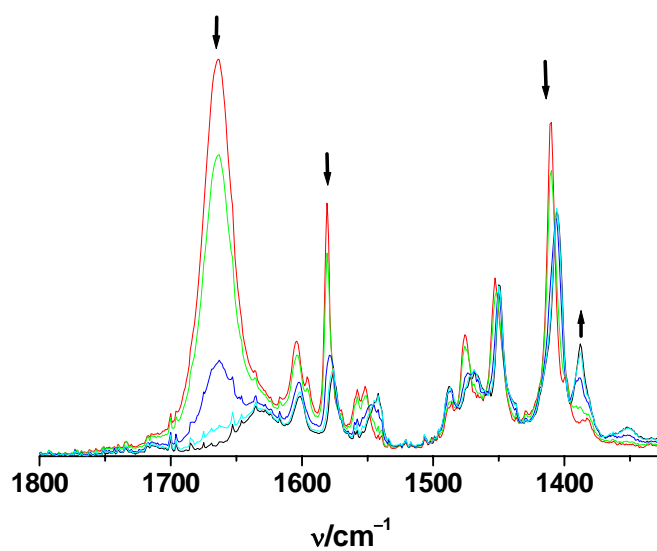


Figure 4.5.2. IR spectroelectrochemical response of $[\text{Ru}(\text{NO})(\text{bpym})(\text{terpy})](\text{PF}_6)_3$ in $\text{CD}_3\text{CN}/0.1 \text{ M } n\text{-Bu}_4\text{NPF}_6$ on second reduction step at 298 K.

4.6. Multifrequency EPR Spectroscopy

4.6.1. Theory

Electron Paramagnetic Resonance (EPR) is the ideal spectroscopic method for identification and characterisation of radicals and metal-centred spin.^[112] EPR gives three sources of information:

The isotropic g-value: Deviations of g from the free electron g factor (g_e) can be attributed to the contribution of other excited states with non-zero angular momentum to the radical ground state. They arise from spin-orbit interactions which are proportional to the spin-orbit coupling constants of the involved atoms which increases with the atomic number as Z^5 . The sign of the deviation is indicative of the frontier orbital situation according to Stone's approximation (Eq. 4.6.1.1.).^[113,114,115]

$$g = g_e - \frac{2}{3} \sum_i \sum_n \sum_{kj} \frac{\langle \Psi_0 | \xi_k L_{ik} \delta_k | \Psi_n \rangle \langle \Psi_n | L_{ij} \delta_j | \Psi_0 \rangle}{E_n - E_0} = g_e + \Delta g_s \quad \text{Eq. 4.6.1.1.}$$

$$g_e = 2.0023$$

ψ_0 : MO of the unpaired electron in the ground state

ψ_n : all other MOs

ξ_k : spin-orbit coupling constant

$L_{ik/ij}$: angular momentum operator for AO at nucleus k,j

$L_{ik}\delta_k$: = 0 except at atom k

E_0 : energy of a singly occupied molecular orbital (SOMO)

E_n : energies of empty or doubly occupied molecular orbitals (LUMO or HOMO)

Considering the denominator of the equation, only the neighbouring levels have a significant contribution to Δg . This means that heavy atoms which are bound near the radical centre have a large effect on the g value. However, two cases are possible (Figure 4.6.1.1):

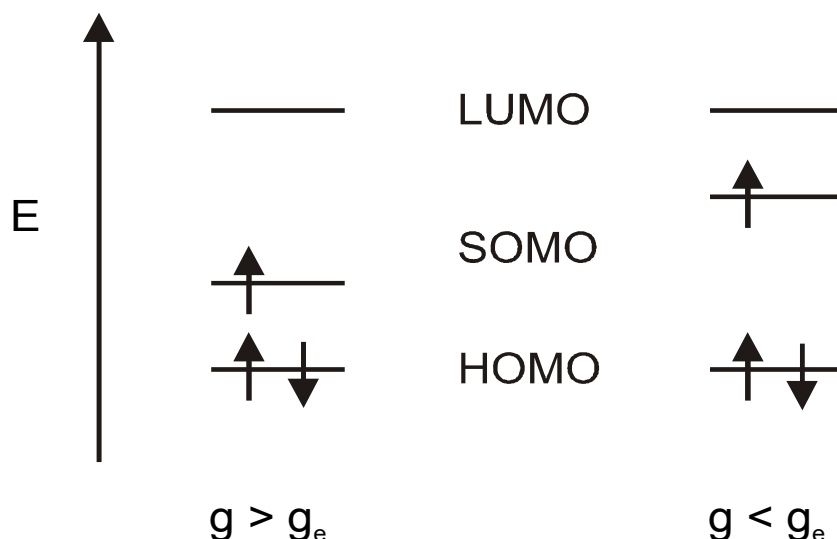


Figure 4.6.1.1. Energy level diagram.

If $E_0 > E_n$, that means when SOMO lies closer to the HOMO than to the LUMO, a deviation to higher-values than g_e is to be expected which is generally observed for metal complexes of $O_2^{\bullet-}$ where the occupation of the former $e(\pi^*)$ level with *three* electron causes a particular closeness of HOMO and SOMO and, consequently g components typically larger than 2.^[116]

If $E_0 < E_n$, the SOMO lies closer to LUMO than to the HOMO, a deviation to lower values than g_e is to be expected This is generally the case for metal complexes containing NO^{\bullet} where closeness of π^* orbital (LUMO) to the SOMO shift to lower g values.^[60]

The g anisotropy ($\Delta g = g_1 - g_3$) from measurements of powders or glassy frozen solutions is largely a result of contributions from elements with high spin-orbit coupling constants. In the EPR spectra of transition metal complexes where the spin is predominantly on the metal centre, the g anisotropy is usually quite large. However, in the case of transition metal complexes with anion radical ligands the g anisotropy is generally small, even in species which contain 5d metal centres like osmium or rhenium. Moreover, the broadness of the lines, sometimes in adjunction with insufficiently resolved metal hyperfine splitting, can preclude the determination of

the expected g anisotropy for complexes with heavy transition metal elements at conventional EPR frequencies (X-band). Thus, it is often necessary to go to high fields/high frequencies (≥ 95 GHz) to resolve it.

The hyperfine coupling between the unpaired electron and the various nuclei of the radical species is another most informative source of insight from EPR.^[115] Ideally, all nuclei with non-zero nuclear spins should couple to a certain extent with the unpaired electron and thus reveal the nature of the SOMO. Unfortunately, it is not always possible to obtain such information from conventional EPR experiments: the intrinsic line-width may be too large for the resolution of the hyperfine structure, the dominant metal hyperfine splitting can obscure the hyperfine splitting from the spin-bearing ligand atoms, and the low natural abundance and/or low nuclear magnetic moment of isotopes can lead to undetectable hyperfine coupling.

The technique of high-field EPR spectroscopy^[117]

In high-field/high-frequency EPR spectroscopy, different kinds of spectrometers are used than in X-band spectroscopy. The W-band (94 GHz) spectrometers are commercially available whereas home-made spectrometers exist with different, sometimes variable, frequencies up to 700 GHz. Both kinds of spectrometers have their advantages, even though commercially available spectrometers are restricted to frequencies up to 94 GHz, corresponding to a wavelength of 3 mm. These spectrometers are built with a conventional resonator which allows for the determination of precise g -values. With the increase of the frequency the resonator has to become smaller. Thus, the sample size becomes very small for such spectrometers. On most home-made spectrometers, the size of the sample is designed in agreement with the purpose of the spectrometer. Larger samples can be used but there is no resonator and absolute g -values cannot be obtained directly through measurements.

Since the measurements had to be done for immobilised species, it was preferred to carry them out in frozen solutions at 5 K in order to minimise intermolecular dipolar interactions between the radicals. The samples were either obtained as radical

complexes during the synthesis or they were generated chemically by reduction with Zn. The samples consisted of saturated solutions of the radical complexes. Thus, the concentration was not the same for all studied samples, and when the complex had to be reduced *in situ* the amount of radical species was particularly unpredictable. Because of the nature of the sample holder, only those species could be studied by this technique which are either stable radicals under ambient conditions or can be converted to stable radicals by chemical reduction.

The measurements at 95 and 190 GHz were carried out at the Grenoble High Magnetic Field Laboratory. The amount of sample used for these measurements was about 0.3 mL.

Experimental field values were converted to g-values according to the following formula:^[99]

$$g = \frac{h\nu_e}{\beta_e B} = 0.07144775 \frac{\nu_e}{B}$$

with h: Planck constant
 ν_e : frequency/GHz
 β_e : Bohr magneton
 B: Magnetic field/T

4.6.2. Results

EPR Spectroscopy of electrogenerated $[\text{Ru}(\text{NO}_2)(\text{bpym})(\text{terpy})]^{2+}$ and $[\text{Ru}(\text{NO}_2)(\text{bpym})(\text{terpy})]^0$ indicated a "conventional" electronic situation: The metal-centred oxidation leads to a ruthenium(III) species with $g_{1,2} = 2.365$ and $g_3 = 2.025$ at 110 K (Figure 4.6.2.1). Such values are typical for the low-spin $4d^5$ configuration of largely unperturbed Ru^{III} .^[118,119] On the other hand, one-electron reduction produces a radical complex with a slight rhombic g anisotropy at $g_1 = 2.006$, $g_2 = 1.999$, $g_3 = 1.994$ at 110 K (Figure 4.6.2.2) with $g_{\text{iso}} = 1.995$ at 298 K (Figure 4.6.2.3), a characteristic result for ruthenium(II) complexes of "polypyridine" radicals.^[120]

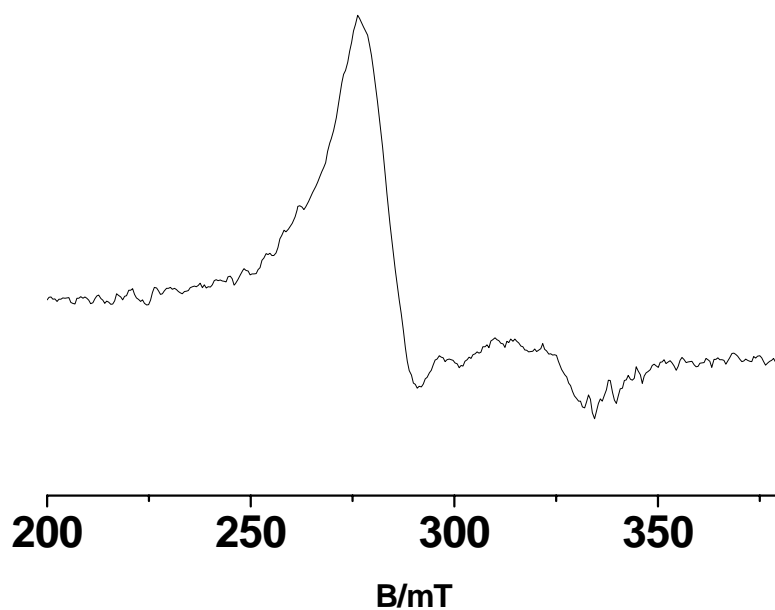


Figure 4.6.2.1. X-band EPR spectrum of electrogenerated $[\text{Ru}(\text{NO}_2)(\text{bpym})(\text{terpy})]^{2+}$ in $\text{CH}_3\text{CN}/0.1 \text{ M } n\text{-Bu}_4\text{NPF}_6$ at 110 K; $g_{1,2} = 2.365$, $g_3 = 2.025$.

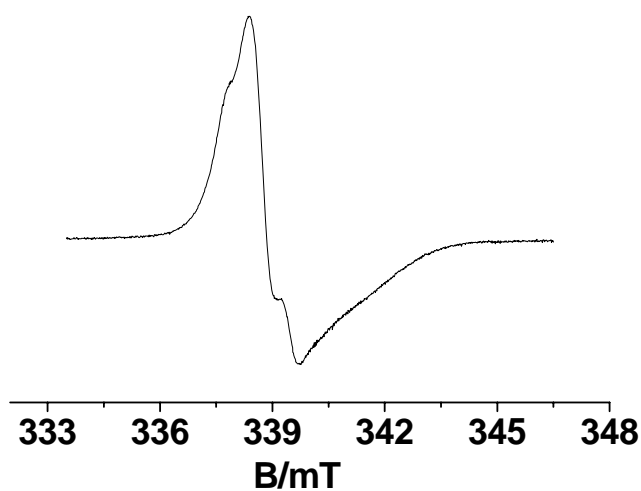


Figure 4.6.2.2. X-band EPR spectrum of electrogenerated $[\text{Ru}(\text{NO}_2)(\text{bpym})(\text{terpy})]^0$ in $\text{CH}_3\text{CN}/0.1 \text{ M } n\text{-Bu}_4\text{NPF}_6$ at 110 K; $g_1 = 2.006$, $g_2 = 1.999$, $g_3 = 1.994$.

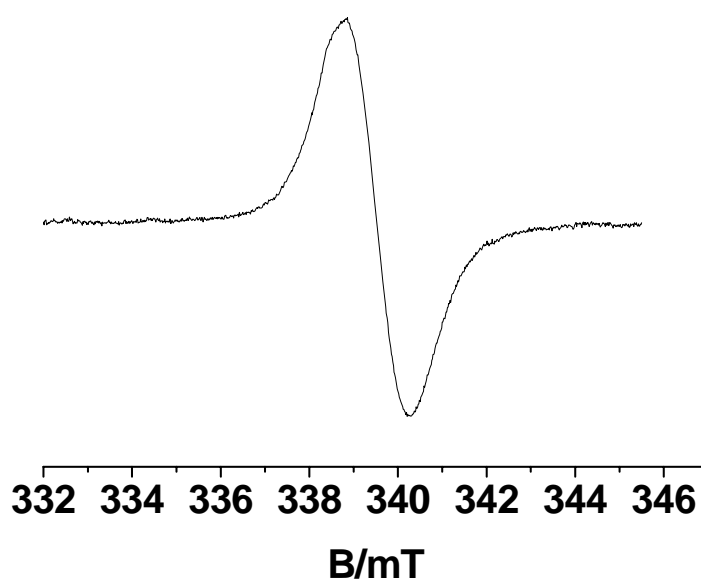


Figure 4.6.2.3. X-band EPR spectrum of electrogenerated $[\text{Ru}(\text{NO}_2)(\text{bpym})(\text{terpy})]^0$ in $\text{CH}_3\text{CN}/0.1 \text{ M } n\text{-Bu}_4\text{NPF}_6$ at 298 K; $g_{\text{iso}} = 1.995$.

The X-band measurements of $[\text{Ru}(\text{NO})(\text{bpym})(\text{terpy})]^{2+}$ showed the typical invariant EPR characteristics^[50] (g factors $g_1 > 2$, $g_2 \approx 2.0$, $g_3 < 2$; $A_2(^{14}\text{N}) \approx 3.4 \text{ mT}$, Figure 4.6.2.4) of $\{\text{RuNO}\}^7$ species which have been observed before for quite a number of different complexes containing that moiety RuNO .^[50] In the present case $g_1 = 2.021$, $g_2 = 1.995$, $g_3 = 1.885$, $A_2 = 3.4 \text{ mT}$. This result justifies once more the concept of rather covalent metal-ligand bonding as expressed in the Enemark-Feltham notation^[2] $\{\text{MNO}\}^n$.

The very positive first reduction potential at $E_{1/2}(\text{red1}) = +0.17 \text{ V vs. FeCp}_2^{+/0}$ of $[\text{Ru}(\text{NO})(\text{bpym})(\text{terpy})](\text{PF}_6)_3$ in $\text{CH}_3\text{CN}/0.1 \text{ M } n\text{-Bu}_4\text{NPF}_6$ facilitated the generation of the intermediate $[\text{Ru}(\text{NO})(\text{bpym})(\text{terpy})]^{2+}$ with sufficient stability and concentration to carry out the high-field EPR investigations. The intermediate $[\text{Ru}(\text{NO})(\text{bpym})(\text{terpy})]^{2+}$ was obtained from reduction with Zn for the EPR measurement at high frequencies using W-band (95 GHz) and G-band (190 GHz). High-field EPR studies of metal nitrosyl entities have been reported before for copper^[121] and iron^[122] systems.

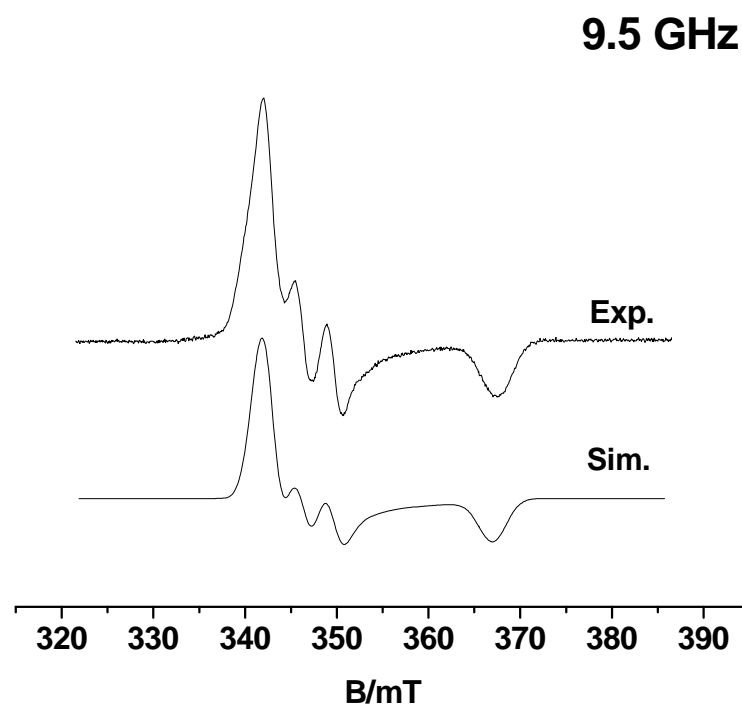


Figure 4.6.2.4. X-band (9.5 GHz) EPR spectrum of electrogenerated $[\text{Ru}(\text{NO})(\text{bpym})(\text{terpy})]^{2+}$ in $\text{CH}_3\text{CN}/0.1 \text{ M } n\text{-Bu}_4\text{NPF}_6$ at 110 K; $g_1 = 2.021$, $g_2 = 1.995$, $g_3 = 1.885$ and $A_2(^{14}\text{N}) = 3.4 \text{ mT}$.

The high-frequency EPR studies show the g factor components with better separation and unobstructed by hyperfine splitting. However, the 95 GHz (Figure 4.6.2.5) and especially the 190 GHz (Figure 4.6.2.6) spectra also reveal two g_1 and two g_2 components, suggesting the presence of two slightly different species. An explanation of this observation is based on the well-known bending of the $\{\text{MNO}\}^7$ configuration^[33,60,110] which can lead to different conformers (staggered, eclipsed) as discussed previously for $[\text{M}(\text{NO}^*)\text{Cl}_5]$ systems.^[33,110] In the present situation with only one possible structure configuration (Figures 4.3.1-4.3.3), the bending of RuNO can produce two different staggered conformations, having the RuNO plane between two neighbouring pyridyl groups of terpy or between one terminal pyridine of terpy and the bpym plane and two possible eclipsed conformations. For $[\text{Os}(\text{NO})\text{Cl}_5]^{n-}$, a computational study has shown that the g signature of different conformers can vary considerably (Chap 2).^[110] Different such species characterised experimentally in matrices^[42] have been associated with conformational isomerism.^[110]

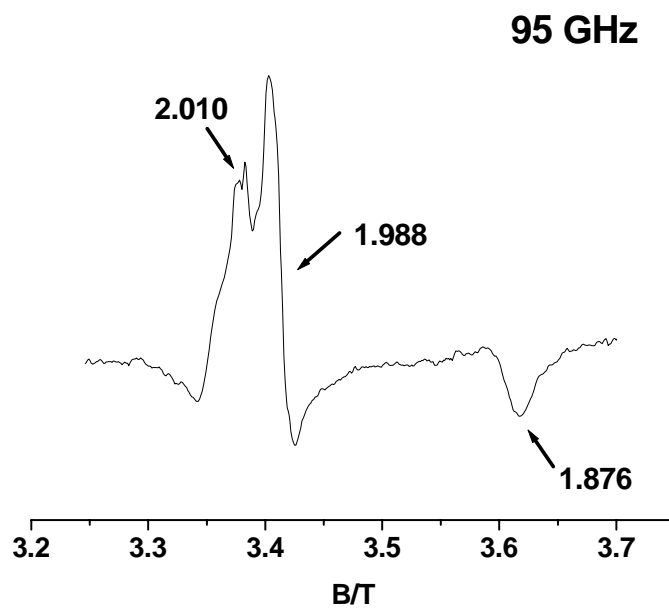


Figure 4.6.2.5. W-band (95 GHz) EPR spectrum of $[\text{Ru}(\text{NO})(\text{bpym})(\text{terpy})]^{2+}$ in CH_3CN at 10 K.

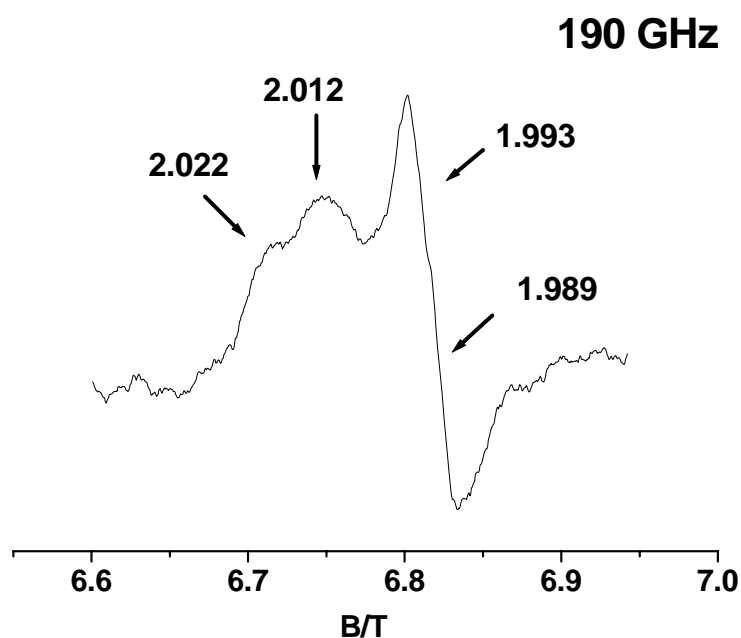


Figure 4.6.2.6. Central section (g_1 , g_2) of the G-band (190 GHz) EPR spectrum of $[\text{Ru}(\text{NO})(\text{bpym})(\text{terpy})]^{2+}$ in CH_3CN at 4.2 K.

4.7. UV/VIS/NIR Spectroelectrochemistry

In comparison to intense metal-to-ligand charge transfer (MLCT) bands involving large π systems such as bpym or terpy the MLCT absorptions involving NO^+ are usually weak.^[51,66] The unreduced $[\text{Ru}(\text{NO})(\text{bpym})(\text{terpy})]^{3+}$, thus, shows long wavelength absorption maxima at 362 and 312 nm, i.e., in the UV region, which most likely comprise $d(\text{Ru}) \rightarrow \pi^*(\text{bpym})$ ^[108] and $d(\text{Ru}) \rightarrow \pi^*(\text{terpy})$ transitions (Figure 4.7.1, Table 4.7.1).

On one-electron reduction in $\text{CH}_3\text{CN}/0.1 \text{ M } n\text{-Bu}_4\text{NPF}_6$ there is additional absorption intensity in the visible and below 350 nm, however, the first observable band maximum lies at 309 nm. Apparently, transitions involving the half-occupied $\pi^*(\text{NO})$ orbital are too weak to make themselves observable as intense absorption bands. After second reduction, on the other hand, there are two bands in the visible region with maxima at 743 and 454 nm (Figure 4.7.2, Table 4.7.1). These low-energy features are attributed to ligand-to-ligand charge transfer (LLCT) transitions from the doubly reduced nitrosyl ligand, i.e., electron rich NO^- ,^[51] to the bpym and terpy acceptors. The interpretation of a π^* MO energy sequence $(\text{NO}) < \text{bpym} < \text{terpy}$ is supported by the above results and by the less negative reduction potential of free bpym (-1.73 V vs. SCE)^[123] vs. free terpy (-2.00 V vs. SCE)^[107,124] as well as by DFT calculations.

Table 4.7.1. UV/VIS spectroelectrochemical data^a for mononuclear ruthenium nitrosyl complexes

compound	λ/nm ($\epsilon/\text{M}^{-1}\cdot\text{cm}^{-1}$)
$[\text{Ru}(\text{NO})(\text{bpym})(\text{terpy})]^{3+}$	265 (10800), 291 (8930), 312sh, 331sh, 362 (5120), 455sh
$[\text{Ru}(\text{NO})(\text{bpym})(\text{terpy})]^{2+}$	268 (11400), 309 (11200), 450sh
$[\text{Ru}(\text{NO})(\text{bpym})(\text{terpy})]^+$	268 (12440), 306 (12550), 454 (4500), 743 (680)

^a From spectroelectrochemistry in an OTTLE cell in $\text{CH}_3\text{CN}/0.1 \text{ M } n\text{-Bu}_4\text{NPF}_6$ at 298 K.

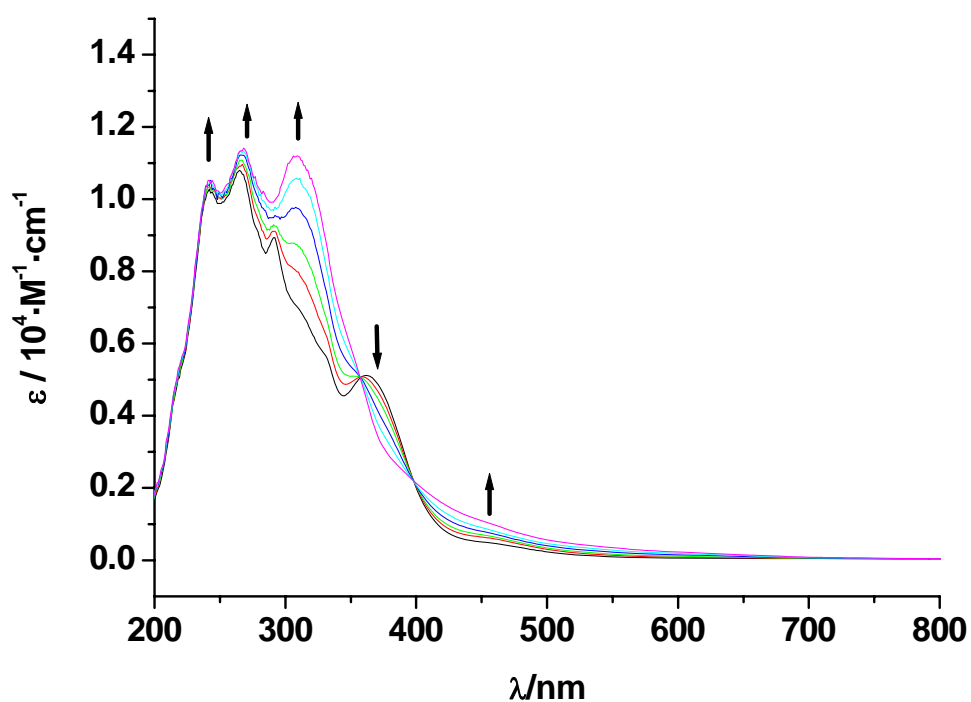


Figure 4.7.1. UV/VIS spectroelectrochemical response of the conversion $[\text{Ru}(\text{NO})(\text{bpym})(\text{terpy})]^{(3+) \rightarrow (2+)}$ in $\text{CH}_3\text{CN}/0.1 \text{ M } n\text{-Bu}_4\text{NPF}_6$ at 298 K.

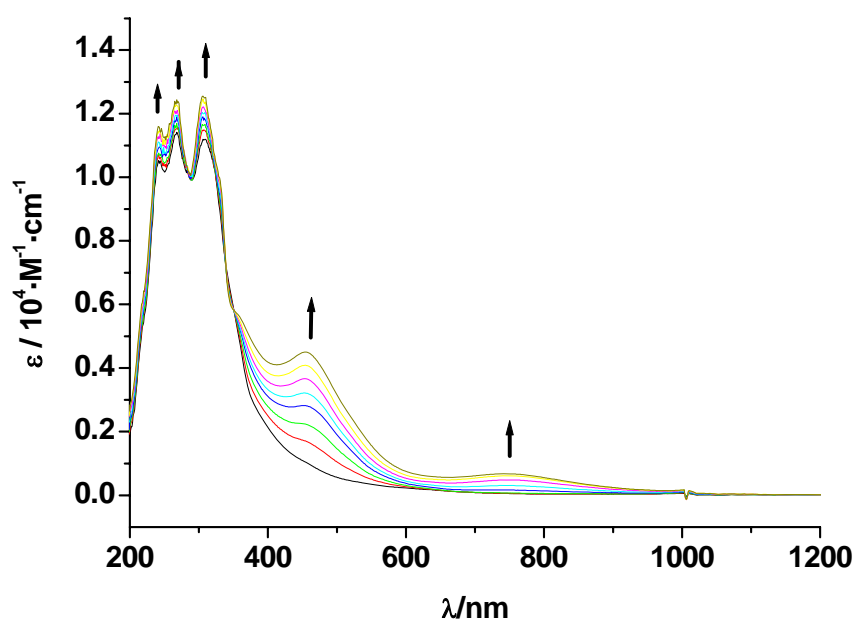


Figure 4.7.2. UV/VIS spectroelectrochemical response of the conversion $[\text{Ru}(\text{NO})(\text{bpym})(\text{terpy})]^{(2+) \rightarrow (+)}$ in $\text{CH}_3\text{CN}/0.1 \text{ M } n\text{-Bu}_4\text{NPF}_6$ at 298 K.

4.8. DFT Calculations

As documented in Table 4.8.1, the DFT optimised geometries well describe the experimental structure of unreduced $[\text{Ru}(\text{NO})(\text{bpym})(\text{terpy})]^{3+}$. The added electron causes the largest changes in the Ru–N–O part of the molecule, characterised by a Ru–N–O angle bending to about 140° - 147° and elongation of the Ru–N and N–O bonds, depending on the conformation. Table 4.8.1 shows the variation of ADF/BP calculated bond parameters, the analogous geometry variations due to the reduction were obtained by G03/B3LYP calculations.

The geometry variation in the course of the reduction reflects the electronic structure of $[\text{Ru}(\text{NO})(\text{bpym})(\text{terpy})]^{3+}$. In this complex the lowest unoccupied molecular orbital (LUMO) is of e -symmetry, based on the π^* orbitals of the nitrosyl ligand (around 66%) with 23% contributions from 4d orbitals of Ru and 10% from π^* orbitals of the bpym and terpy ligands. Closely lying occupied and unoccupied molecular orbitals are mainly formed by the π orbitals of the bpym and terpy ligands, with small contributions from metal d orbitals (less than 10%). During the reduction the added electron is accepted by the LUMO and the originally degenerate e -orbital splits into non-degenerate ones. Figure 4.8.1 shows the distribution of spin density in $[\text{Ru}(\text{NO})(\text{bpym})(\text{terpy})]^{2+}$ resulting from the single occupancy of an NO based redox orbital.

Irrespective of the functional used for geometry optimisation of $[\text{Ru}(\text{NO})(\text{bpym})(\text{terpy})]^{2+}$, the DFT calculations indicate two energy minima, one eclipsed (RuNO plane almost coinciding with the RuN1N2 plane) and one staggered configuration (the RuNO plane between one terminal pyridine of terpy and the bpym plane), as depicted in Figure 4.8.2. The barrier between two different conformations allows for the detection of two different isomers of $[\text{Ru}(\text{NO})(\text{bpym})(\text{terpy})]^{2+}$ with different g factor components at 4 K. ADF/BP calculations give two slightly different sets of g-values, viz., $g_1 = 2.0319$, $g_2 = 1.9884$, $g_3 = 1.8907$ and $g_1 = 2.0163$, $g_2 = 2.0000$, $g_3 = 1.9065$ for the staggered and eclipsed configuration, respectively. These values well reproduce the results from the EPR experiments.

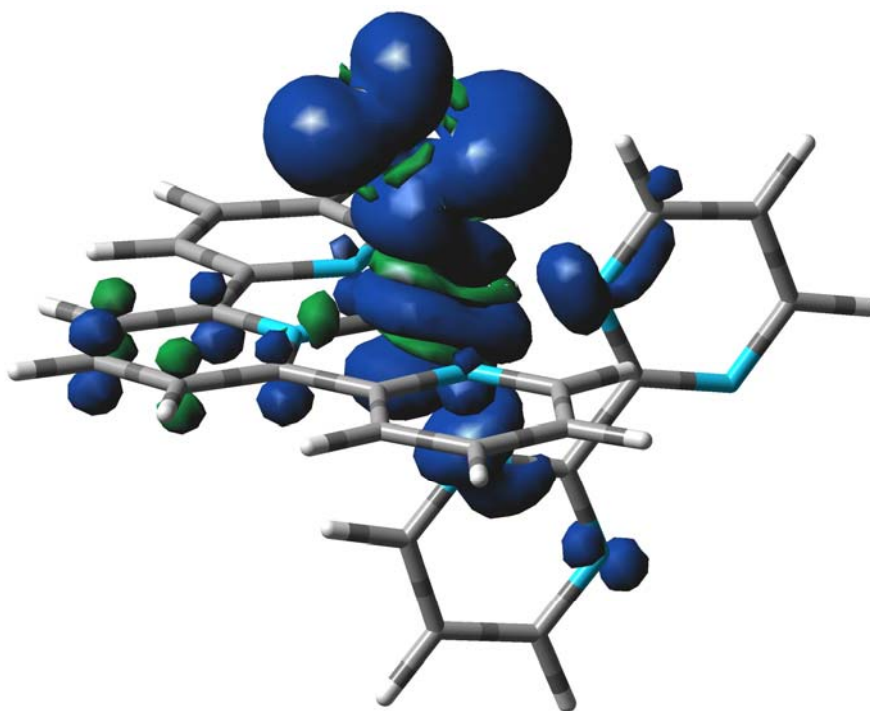


Figure 4.8.1. Representation of spin density in the eclipsed conformation of $[\text{Ru}(\text{NO})(\text{bpym})(\text{terpy})]^{2+}$.

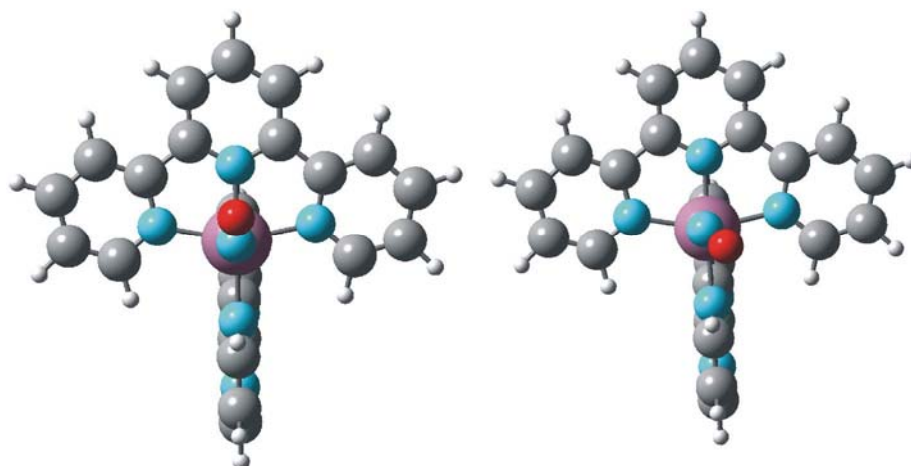


Figure 4.8.2 Different DFT optimised conformations of $[\text{Ru}(\text{NO})(\text{bpym})(\text{terpy})]^{2+}$ resulting from Ru-N-O bending. Eclipsed on the left, staggered on the right.

Table 4.8.1. Selected ADF/BP calculated bond lengths (Å) and angles (deg) for complexes $[\text{Ru}(\text{NO})(\text{bpym})(\text{terpy})]^{n+}$

	n=3	n=2 staggered	n=2 eclipsed
Ru–N1	1.775	1.836	1.891
Ru–N2	2.012	1.988	1.999
Ru–N3	2.121	2.120	2.109
Ru–N4	2.121	2.116	2.114
Ru–N5	2.126	2.119	2.111
Ru–N6	2.136	2.120	2.139
N1–O1	1.143	1.185	1.188
O–N1–Ru	177.4	147.3	139.6

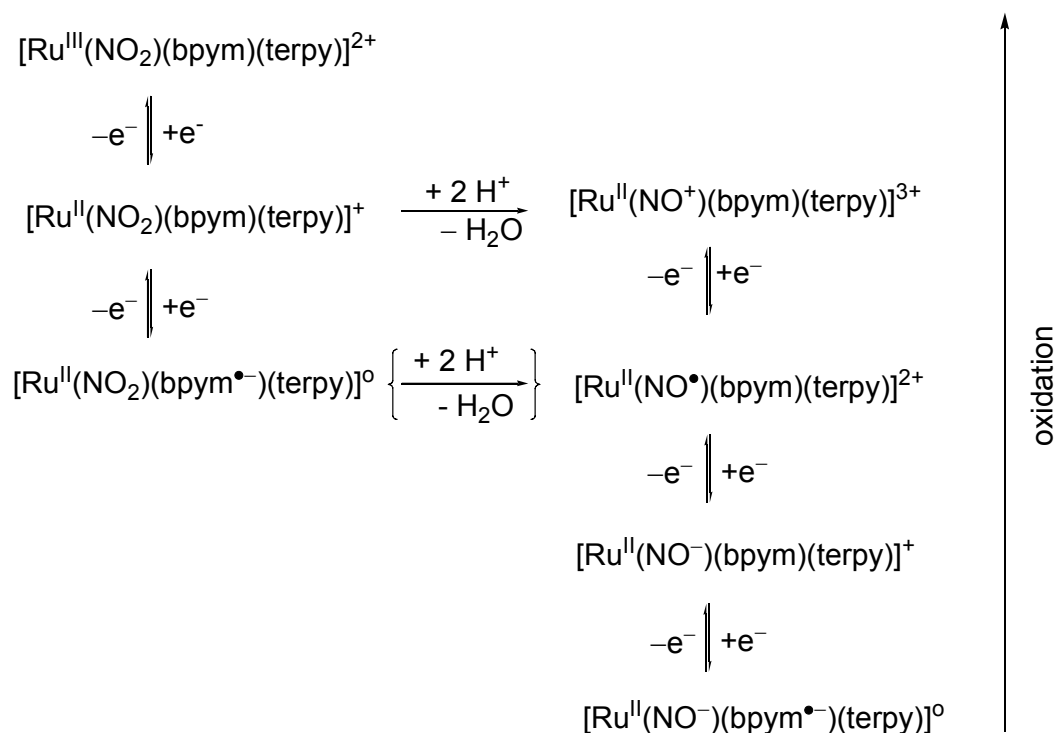
The G03/BPW91 calculations slightly underestimate the $\nu(\text{NO})$ stretching frequency (calculated at 1939 cm^{-1}), however, the uptake of an electron into the NO based LUMO is indeed reflected by the lowering of this band by 216 cm^{-1} . The second reduction causes a further low-energy shift of 181 cm^{-1} . Scaled B3LYP values indicate shifts of similar size. The underestimation of frequency shifts is probably caused by the overestimation of the Ru 4d contribution to the redox orbital.

4.9. Conclusion and Outlook

Concluding this Chapter, the combination of three different π acceptor ligands bonded to ruthenium(II) in $[\text{Ru}(\text{NO})(\text{bpym})(\text{terpy})](\text{PF}_6)_3$ has resulted in the opportunity to study two one-electron reduction processes, both of which involve the NO ligand. The stability of the paramagnetic intermediate $[\text{Ru}(\text{NO})(\text{bpym})(\text{terpy})]^{2+}$ could be used to study the EPR behaviour by high-frequency methods which revealed the existence of two species, probably conformers. While the UV/VIS spectra of this intermediate are inconspicuous, the doubly reduced form $[\text{Ru}(\text{NO})(\text{bpym})(\text{terpy})]^+$ exhibits absorption bands in the visible which are attributed to

LLCT transitions. Taken together with the more conventional response from the nitro precursor complex Scheme 4.9.1 illustrates how the conversion from the NO_2^- to the NO^n ligand does not only shift the reduction potentials but also results in a completely different electron transfer series by insertion of a $\pi^*(\text{NO})$ orbital as the lowest unoccupied MO.

Accordingly, one of the perspectives arising from this work involves the $\text{NO}_2^-/\text{NO}^+$ conversion^[10,125] of the one-electron reduced forms in comparison to the non-reduced species.



Scheme 4.9.1. Reaction scheme showing electron transfer in nitro and nitrosyl complexes.

CHAPTER 5

Series of Dinuclear Ruthenium Complexes with 2,2'-Bipyrimidine as Bridging Ligand

5.1. Introduction

Mixed-valence materials – materials that contain an element in more than one oxidation state – have been the subject of interest in both theoretical and experimental^[126,127,128,129] research and have generally received a great deal of attention. This is especially true for the intersections of multidisciplinary areas, such as the search for a better understanding of some important life processes^[37] where mixed-valence units are commonly found. Examples are Fe^{II}/Fe^{III} in ferredoxins, Mn^{II}/Mn^{III}/Mn^{IV} clusters in photosystem II, and Cu^I/Cu^{II} in cytochrome c oxidase. Interest in mixed-valence has also been sparked by their potential for molecular electronics,^[34,36,38] their use as model compounds for intramolecular electron transfer,^[38] their unusual spectroscopic properties,^[130,131,132] and their function as test systems for theoretical approaches.^[133,134] In fact, for the understanding and interpretation of electron transfer processes, H. Taube^[38] and R. A. Marcus^[135] were awarded Nobel Prizes in Chemistry in 1984 and 1992, respectively. While the oldest and most familiar mixed-valent coordination compound is still Prussian Blue, formulated as Fe^{III}₄[Fe^{II}(CN)₆],^[136] another prominent mixed-valent complex is the dinuclear Creutz-Taube ion^[38,126,127,128,129,137,138] (Figure 3.1.1) which has been extensively studied both experimentally and theoretically since 1969.^[38,126,127,128,129]

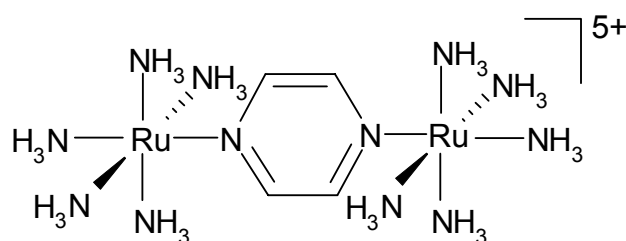


Figure 5.1.1. The Creutz-Taube ion.

One of the main themes which, has been a subject of continuous debate with respect to the Creutz-Taube ion is the question of electron (de)localisation (the so called metal-metal "coupling"). The alternative formulations Ru^{II}-Ru^{III} vs. Ru^{2.5}-Ru^{2.5} have prompted researchers to carry out a host of different experiments on this system.^[126,127,128,129]

The term metal-metal coupling, used to describe the interaction between metal centres in mixed-valent compounds, can have various meanings, on the basis of either (i) electrochemical, (ii) spectroscopic, or (iii) magnetic measurements.^[139]

(i) The very existence of any mixed-valent intermediate state is quantified by the comproportionation constant K_c according as following:

$$K_c = 10^{\Delta E/59\text{mV}} = \frac{[M^{(n-1)}]^2}{[M^n][M^{(n-2)}]} \quad (\text{at } 298 \text{ K})$$

$$M^n + M^{(n-2)} \rightleftharpoons 2 M^{(n-1)}$$

The values for ΔE are obtained from cyclic voltammetry. K_c can range from 4, the statistical value^[126,127,128,129] to more than 10^{15} .^[139]

(ii) A different measure of metal-metal interaction uses information from absorption spectroscopy, specifically the energies and intensities of characteristic long-wavelength bands (metal-to-metal charge transfer, MMCT, or inter-valence charge transfer, IVCT).

Robin and Day had classified mixed-valent systems on the basis of six different criteria.^[140] In the article of Robin and Day, apart from spectroscopic, electrical and magnetic characteristics, one criteria for distinguishing mixed-valent compounds was the symmetry and strength of the ligand field around the two metal centres. Thus, strictly according to the Robin and Day classification, a Class I system should have two metal centres with different ligand field symmetry/strength (for example: octahedral vs. tetrahedral). However, over the years this definition has been broadened to include symmetrical mixed-valent systems as well.^[126,141] Thus, a

symmetrical mixed valent system is characterised as Class I, II or III depending on the strength of the interaction between the two sites, ranging from essentially zero (Class I) via moderate (Class II) to very strong (Class III). The properties of Class I systems are essentially those of the separate sites, Class II systems possess new properties in addition to those of the separate sites. However, the interaction between the sites is sufficiently weak so that Class II systems are valence trapped or charge localised and can be described by a double well potential. In Class III systems the interaction between the two sites is so great that two separate minima are no longer discernible and the energy surface features a single minimum. The electron is delocalised and the system has its own unique properties.

The free energy of activation for electron transfer, ΔG^* is related to the electronic (metal-metal) coupling parameter, H_{AB} and the reorganisation parameter, λ according to the following equation:^[141]

$$\Delta G^* = (\lambda - 2H_{AB})^2/4\lambda \quad (1)$$

Thus, when H_{AB} has a negligible value (Class I), $\Delta G^* = \lambda/4$ and electron transfer either does not take place or is very slow.

When $0 < H_{AB} < \lambda/2$ (Class II), the system is still valence trapped or charge localised but electron transfer can now take place. Equation (1) can be used for this case to get ΔG^* . The ground state in this case is still described by a double well potential and there is a barrier to electron transfer.

In Class III systems the interaction between the two sites is so large that the ground state has only a single minimum. This is the delocalised case which occurs when $H_{AB} \geq \lambda/2$. This condition follows readily from the zero barrier limit ($\Delta G^* = 0$).

The potential energy diagrams for the three Robin and Day Classes are shown in Figure 5.1.2.

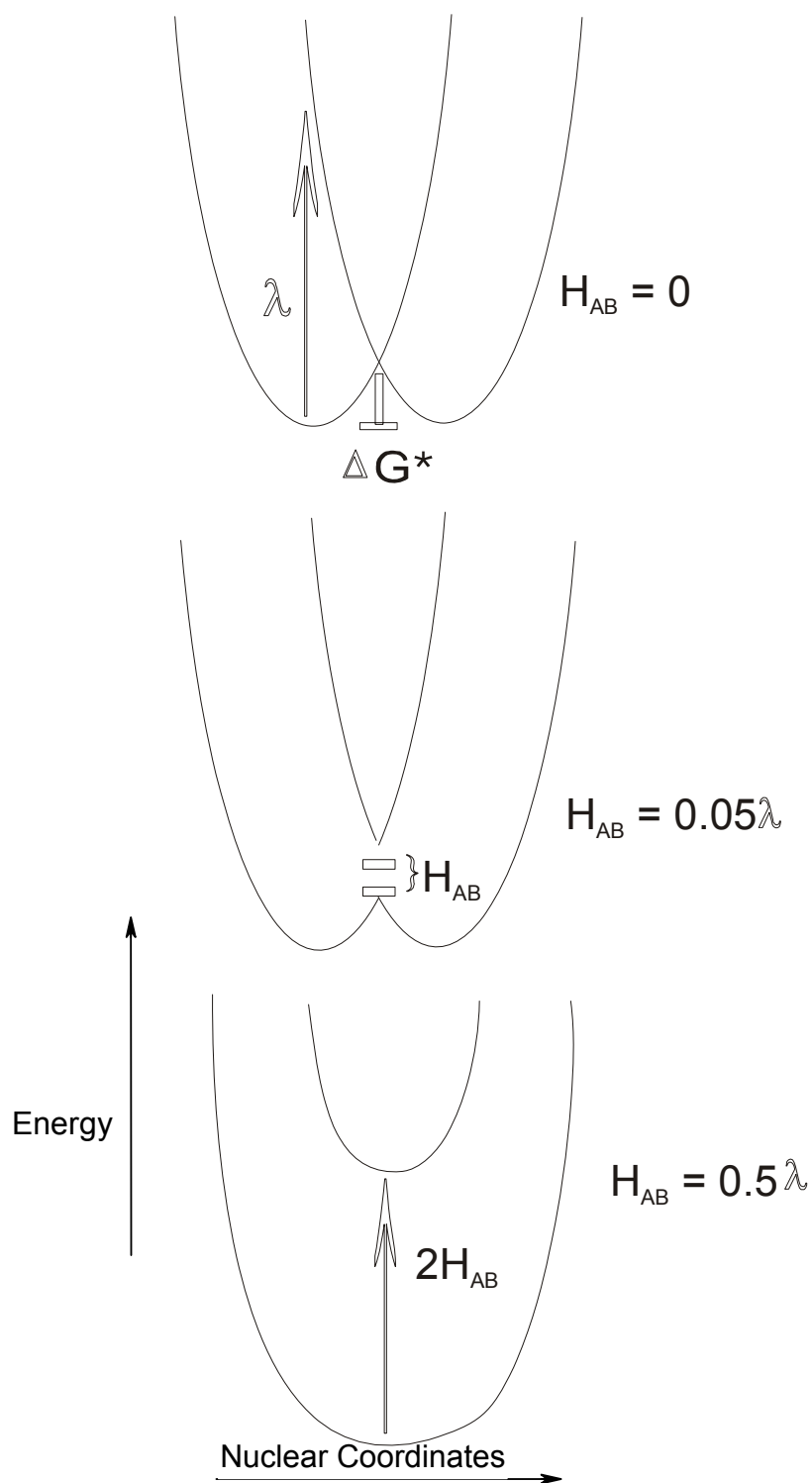


Figure 5.1.2. Potential energy vs. nuclear coordinate plot for Class I (top), Class II (middle) and Class III (bottom) systems.

(iii) Finally, the terms "interaction" and "coupling" are also used to describe magnetic exchange in coordination compounds. Mixed-valent species can involve more than one paramagnetic centre, such as the high spin Fe^{II}-Fe^{III} sites in proteins.^[130]

In metal complexes, delocalisation can be varied by making changes of the metal, the bridging ligand, the ancillary ligands, or the solvent. The metal complex fragments most commonly employed for generating mixed-valent intermediates are the ones which provide for a d⁵/d⁶ mixed-valent situation. Thus, mixed-valent complexes of Fe, Ru and Os in their +II and +III oxidation states are most commonly encountered. This is because these metals (esp. Ru and Os) provide for a substitutionally inert coordination environment while allowing for facile electron transfer.^[126]

In order to determine the factors which control the extent of electron (de)localisation in such systems, many research groups have tried to synthesise new mixed valent systems which have similar properties as the prototypical Creutz-Taube ion.^[34,35,36,126,127,128,129,139,142] Also, Extension of this concept to organic^[143,144] and elementorganic^[145] systems or to organometallic reaction centres^[146, 147] has begun to provide further clues to the mechanism of complex redox processes.

In this Chapter, attempts have been made to synthesise molecules which contain potentially coupled electroactive metal-ligand moieties. Of these, the robust and electronically rather invariant^[7] nitrosylruthenium entity has become our focus. This is not only because of the vital importance of the coordinated NO⁺/NO[•]/NO⁻ redox system ("non-innocent ligand"), but also because of the added Ru^{II}/Ru^{III} ambivalence. Therefore, we adopt the Enemark-Feltham formulation² {RuNO}ⁿ for the two states involved and attempted to synthesise the complex ion {(μ-bpym)[Ru(NO)(terpy)]₂}⁶⁺, employing the well-employed, small bis-chelating 2,2'-bipyrimidine bridge^[108,123] (Figure 5.1.3) and the meridionally tridentate co-ligand terpy (Figure 5.1.3).^[107] Also, the precursor redox series {(μ-bpym)[RuCl(terpy)]₂}ⁿ and {(μ-bpym)[Ru(NO₂)(terpy)]₂}ⁿ, n = (0)-(4+) are studied with respect to their mixed-valent properties.

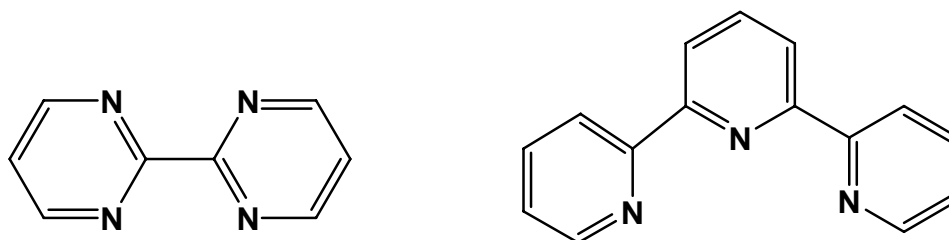


Figure 5.1.3. The ligands 2,2'-bipyrimidine (left) and 2,2':6',2''-terpyridine (right).

5.2. Syntheses and Characterisation

The diruthenium dichloro complex $\{(\mu\text{-bpym})[\text{RuCl}(\text{terpy})]_2\}(\text{PF}_6)_2$ (**5a**) was prepared from $\text{Ru}(\text{terpy})\text{Cl}_3$ ^[105] and bpym ligand as shown in Figure 5.2.1. The complex was characterised by ^1H NMR, mass spectroscopy and elemental analyses (Chapter 6) The ^1H NMR spectrum (Figure 5.2.3) of **5a** showed the formation of *syn* and *anti* isomers with respect to the central bpym ring system in 5:4 ratio (Figure 5.2.2). The assignment of peaks is done with the help of ^1H - ^1H COSY NMR spectrum (Figure 5.2.4, Table 5.2.1).

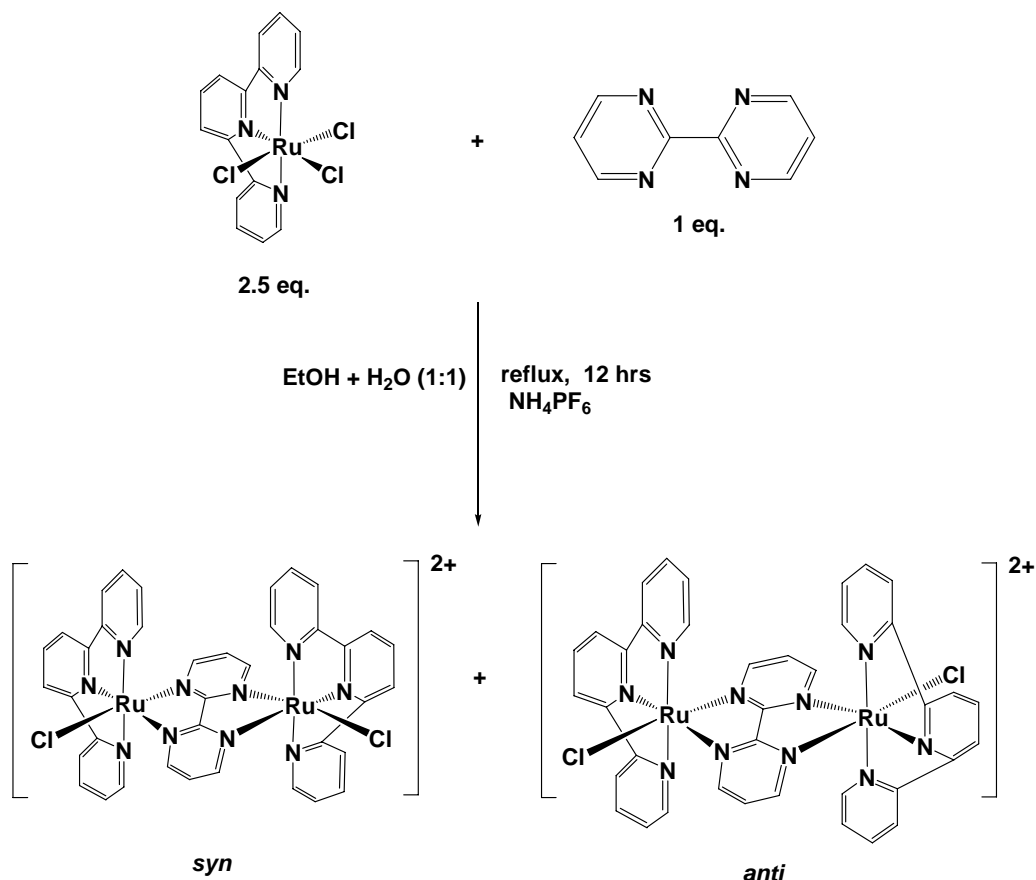


Figure 5.2.1. Synthesis of $\{(\mu\text{-bpym})[\text{RuCl}(\text{terpy})]_2\}(\text{PF}_6)_2$.

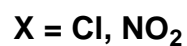
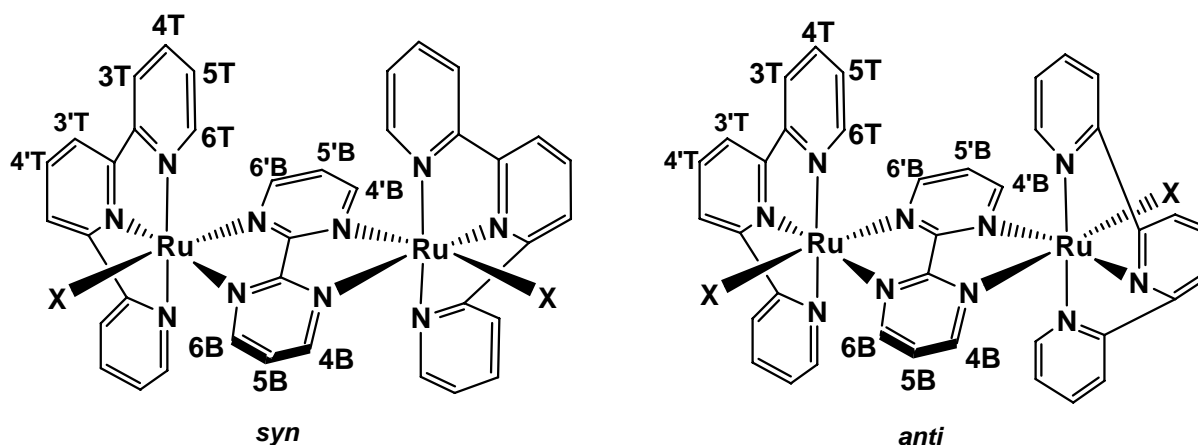


Figure 5.2.2 Numbering of protons in the *syn* and *anti* configurations of bpym-bridged Ru(terpy)X complexes.

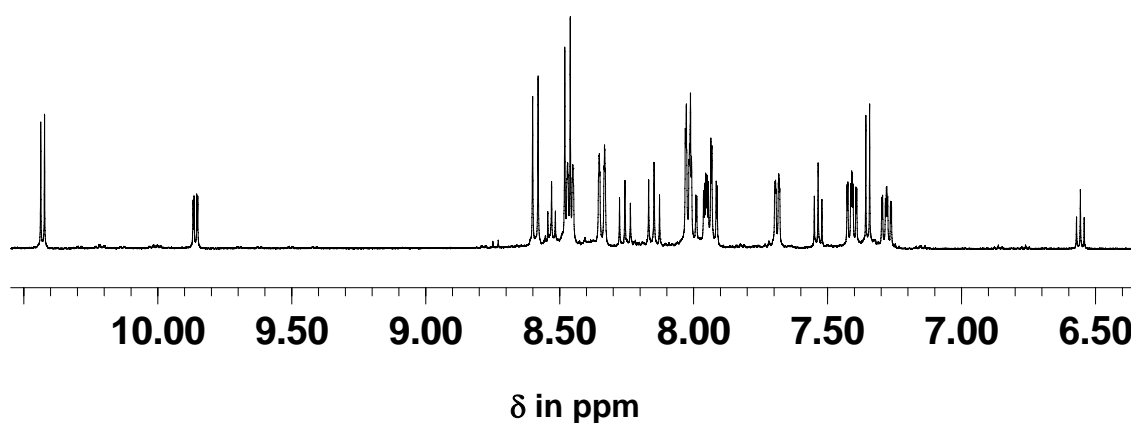


Figure 5.2.3. ^1H NMR of $\{(\mu\text{-bpym})[\text{RuCl}(\text{terpy})]_2\}(\text{PF}_6)_2$ in CD_3CN at 400 MHz showing the formation of two possible isomers.

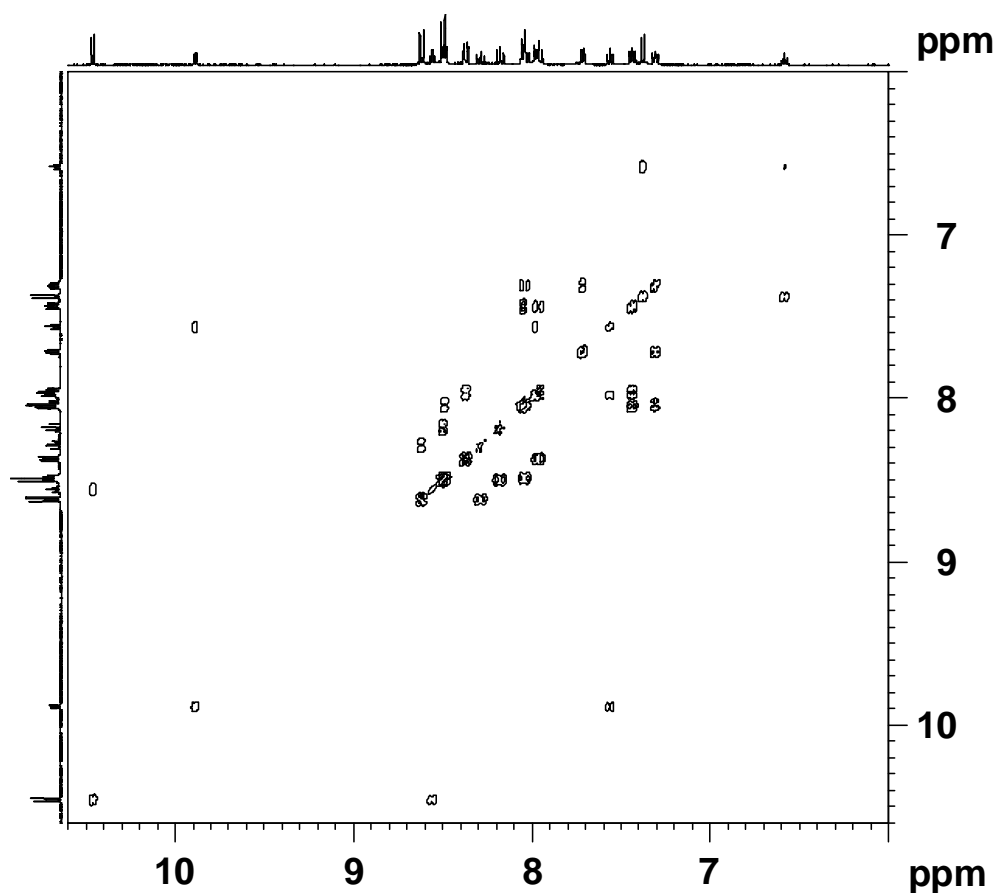


Figure 5.2.4. ^1H - ^1H COSY NMR of $\{(\mu\text{-bpym})[\text{RuCl}(\text{terpy})]_2\}(\text{PF}_6)_2$ in CD_3CN at 400 MHz.

The dinitro complex $\{(\mu\text{-bpym})[\text{Ru}(\text{NO}_2)(\text{terpy})]_2\}(\text{PF}_6)_2$ (**5b**) was synthesised from dichloro precursor, **5a** by treating it with excess of NaNO_2 in $\text{CH}_3\text{CN}/\text{H}_2\text{O}$ (1/5, v/v) in refluxing condition as shown in Figure 5.2.5. The complex **5b** was characterised by ^1H NMR spectroscopy and elemental analyses (Chapter 6). The ^1H NMR spectra of **5b** (Figures 5.2.6, 5.2.7, Table 5.2.1) also showed presence of *syn* and *anti* isomers (Figure 5.2.2). The dinitro compound **5b** shows $\nu\text{NO}_2\text{asym}$ and $\nu\text{NO}_2\text{sym}$ at 1342 cm^{-1} and 1286 cm^{-1} respectively. The UV/VIS spectra of **5a** and **5b** are discussed in section 5.5.

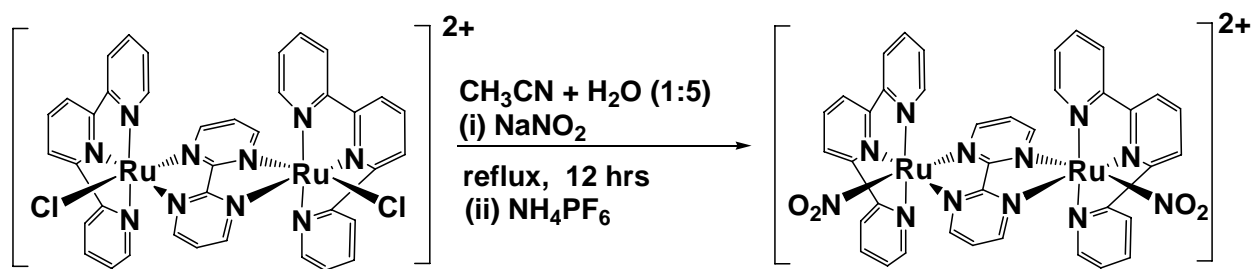


Figure 5.2.5. Synthesis of $\{(\mu\text{-bpy})[\text{Ru}(\text{NO}_2)(\text{terpy})]_2\}(\text{PF}_6)_2$.

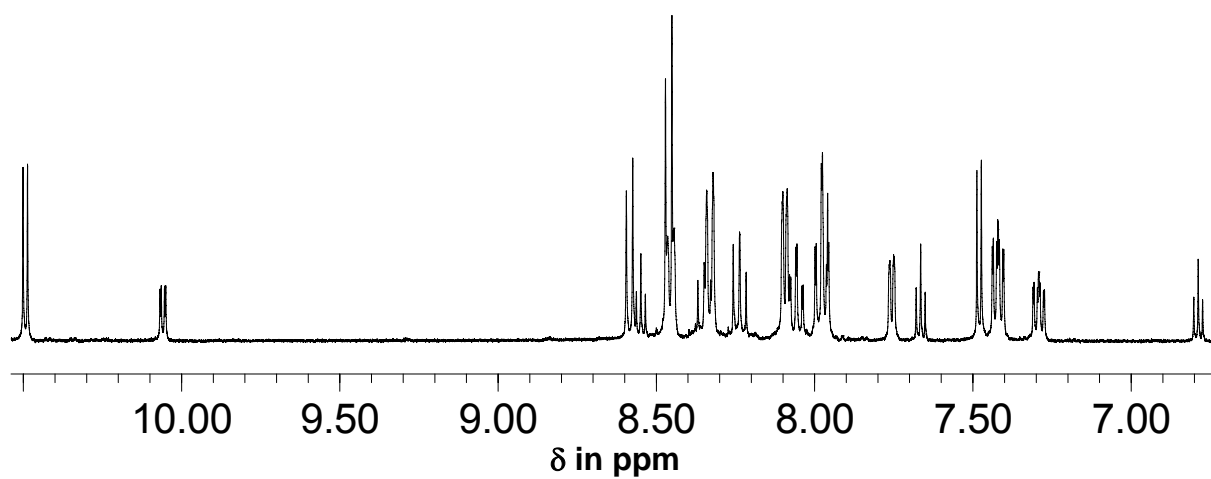


Figure 5.2.6. ^1H NMR of $\{(\mu\text{-bpy})[\text{Ru}(\text{NO}_2)(\text{terpy})]_2\}(\text{PF}_6)_2$ in CD_3CN at 400 MHz.

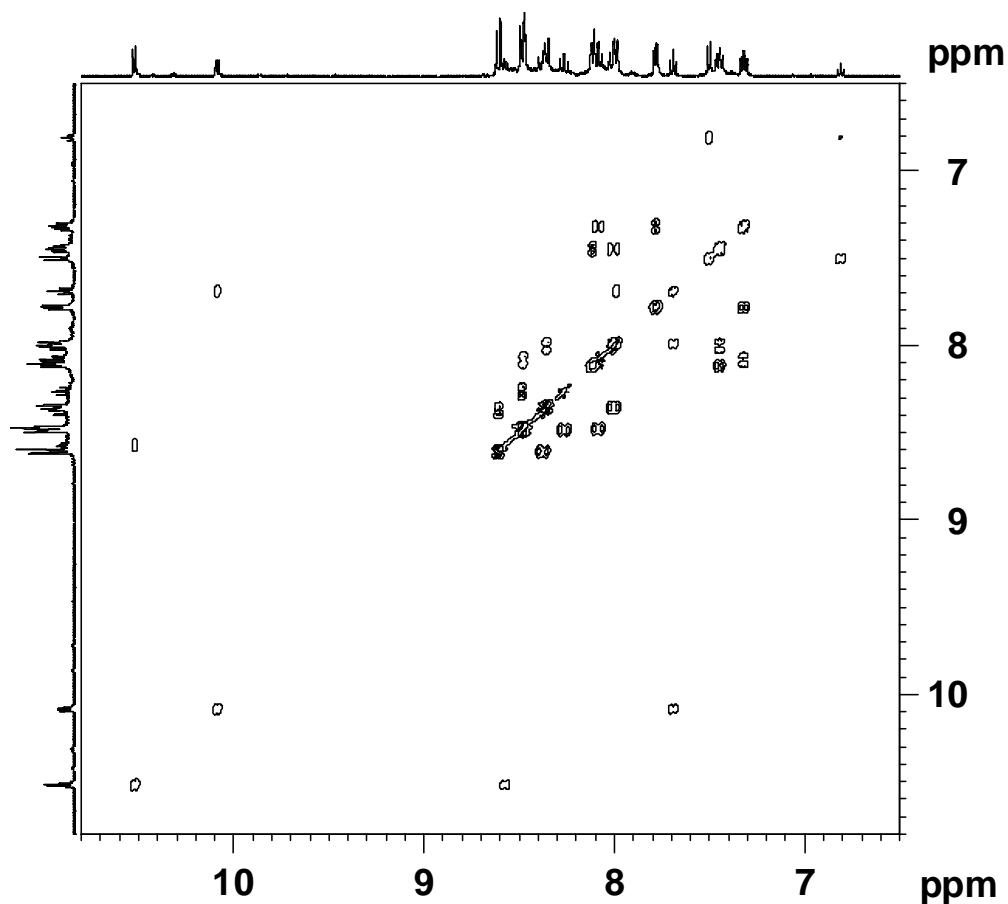


Figure 5.2.7. ^1H - ^1H COSY NMR of $\{(\mu\text{-bpym})[\text{Ru}(\text{NO}_2)(\text{terpy})]_2\}(\text{PF}_6)_2$ in CD_3CN at 400 MHz.

Table 5.2.1. Proton chemical shift value (ppm) for terpy, bpym, **5a** and **5b** in CD_3CN .

proton	δ in ppm					
	compound					
	terpy	bpym	5a (<i>syn</i>)	5a (<i>anti</i>)	5b (<i>syn</i>)	5b (<i>anti</i>)
5T	7.44		7.43	7.20	7.44	7.32
4T	7.97		7.93	8.01	8.01	8.08
4'T	8.05		8.17	8.25	8.26	8.37
3'T	8.49		8.49	8.60	8.48	8.61
3T	8.67		8.37	8.46	8.35	8.46
6T	8.72		8.05	7.69	8.11	7.78
4B		8.96	10.44	9.86	10.52	10.08

Table 5.2.1 *continued*

5B	7.50	8.55	7.53	8.58	7.69
6B	8.96	10.44	7.95	10.52	7.98
4'B	8.96	10.44	7.95	7.50	7.98
5'B	7.50	6.58	7.53	6.81	7.69
6'B	8.96	7.37	9.86	7.50	10.08

The dinitrosyl complex was synthesised applying the common procedure of acidifying the solution of a nitro complex.^[50,51,54,104] Here acidification of $\{(\mu\text{-bpym})[\text{Ru}(\text{NO}_2)(\text{terpy})]_2\}(\text{PF}_6)_2$ does not lead to the expected $\{(\mu\text{-bpym})[\text{Ru}(\text{NO})(\text{terpy})]_2\}^{6+}$ but, probably because of the high charge, to the insoluble but structurally (see section 5.3) and IR-spectroscopically (Figure 5.2.9) characterised dinitrosyl pseudo-base product $\text{syn}\{(\mu\text{-bpym-(4-OH)})[\text{Ru}(\text{NO})(\text{terpy})]_2\}(\text{PF}_6)_5$ (**5c**) as shown in Figure 5.2.8.

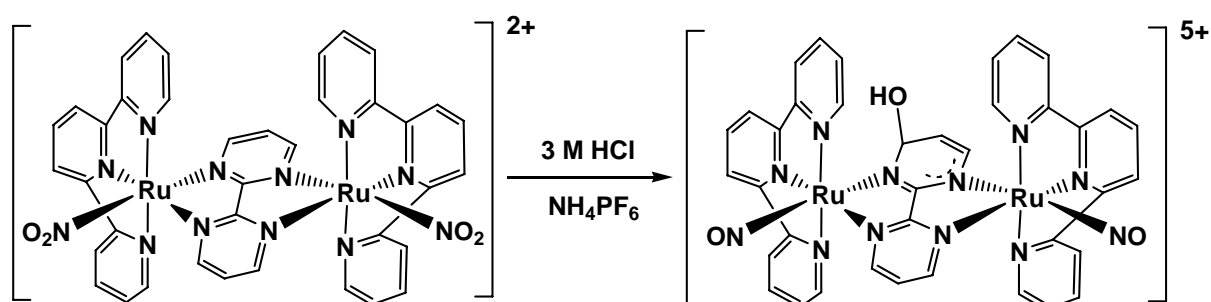


Figure 5.2.8. Synthesis of $\{(\mu\text{-bpym-(4-OH)})[\text{Ru}(\text{NO})(\text{terpy})]_2\}(\text{PF}_6)_5$.

In addition to the expected strong IR bands from NO^+ stretching and PF_6^- vibration, an IR-spectroscopically detectable OH group was observed at $\nu_{\text{OH}} = 3440 \text{ cm}^{-1}$ (broad; Figure 5.2.9).

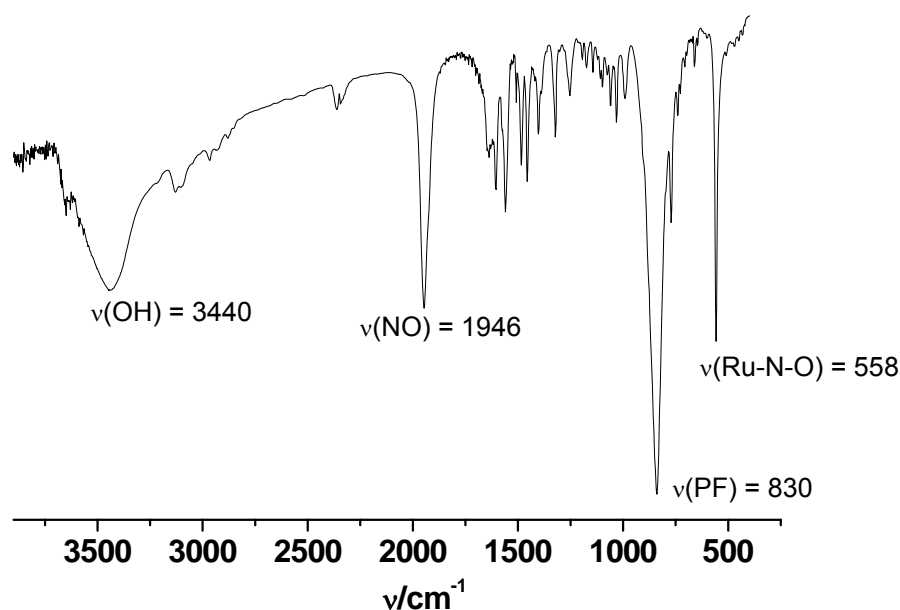


Figure 5.2.9. Solid state IR spectrum of $\{(\mu\text{-bpym-(4-OH)})[\text{Ru}(\text{NO})(\text{terpy})]_2\}(\text{PF}_6)_5$.

Addition of hydroxide to the α -carbon atom of an electron deficient N-heterocycle is a behaviour known from organic chemistry^[148,149] and from certain coordination compounds,^[150,151] often referred to as pseudo-base formation. The driving force is obviously the too high charge concentration in the targeted hexacation $\{(\mu\text{-bpym})[\text{Ru}(\text{NO})(\text{terpy})]_2\}^{6+}$. Unfortunately, the presence of a potentially hydrogen-bonding OH function lowers the solubility significantly, so that measurements in solution could not be performed or were accompanied by disintegration to form the identified mononuclear $[\text{Ru}(\text{NO})(\text{bpym})(\text{terpy})]^{3+}$.

The asymmetry in $\{(\mu\text{-bpym-(4-OH)})[\text{Ru}(\text{NO})(\text{terpy})]_2\}(\text{PF}_6)_5$ seems to become manifest through the broadening of the (combined) NO stretching band at 1946 cm^{-1} ($\Delta\nu_{1/2} = 30 \text{ cm}^{-1}$; Figure 5.2.10) in comparison to that of the mononuclear analogue $[\text{Ru}(\text{NO})(\text{bpym})(\text{terpy})]^{3+}$ ($\Delta\nu_{1/2} = 15 \text{ cm}^{-1}$; Figure 5.2.10).

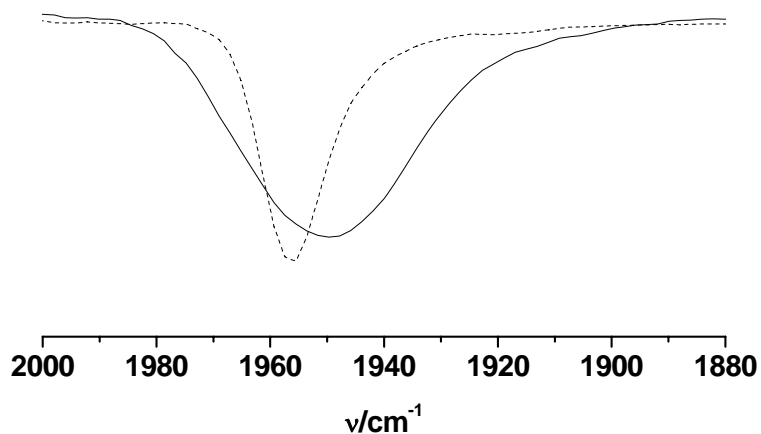


Figure 5.2.10. Comparison of NO stretching bands for $[\text{Ru}(\text{NO})(\text{bpym})(\text{terpy})](\text{PF}_6)_3$ (dotted line) and $\{(\mu\text{-bpym-(4-OH)})[\text{Ru}(\text{NO})(\text{terpy})]_2\}(\text{PF}_6)_5$ (solid line) from solid state IR spectroscopy.

5.3. Crystal Structure

Although the crystal structure determination (Figure 5.3.1) of $\{(\mu\text{-bpym-(4-OH)})[\text{Ru}(\text{NO})(\text{terpy})]_2\}(\text{PF}_6)_5$ was affected by solvent molecules (H_2O), the resulting bonding parameters are quite revealing: The bond lengths within the hydroxide-attacked pyrimidine ring show a conspicuous variation which suggest much lowered bond orders, in effect single bonds, for the connections involving the now sp^3 configured OH-bearing carbon C^4 , corresponding to the formulation of Figure 5.3.2. In other words, the π conjugation in one of the aromatic pyrimidine ring is interrupted, the loss of aromaticity being compensated by the lowered overall charge. Combining meridionally tridentate $\text{terpy}^{[107]}$ and bidentate bpym must cause the $\{\text{RuNO}\}$ group to lie in the π nodal plane of the stronger acceptor bpym , here in a bridging mode. Hydroxide addition in the pseudo-base situation (Figures 5.3.1, 5.3.2) will attenuate the acceptor effect but the position of the π type orbitals of NO in the nodal π plane of the π acceptor bridge is also expected to allow for only very little interaction between the $\{\text{RuNO}\}$ moieties. The inter-ring bond $\text{C}(4)\text{-C}(5)$ between the two pyrimidine rings

is indicative for the amount of π back donation from electron rich metal centres such as Ru^{II} into the π^* MO,^[108,152] with 1.452(9) Å. This value is typical for dinuclear complexes with moderate π back bonding interaction.^[108,152,153,154]

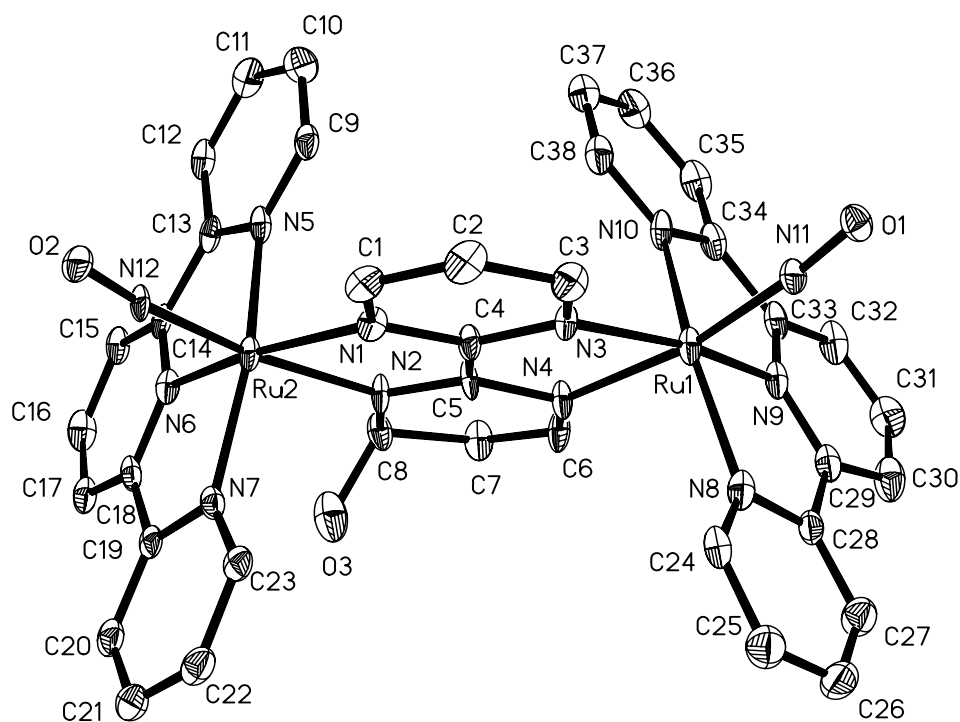


Figure 5.3.1. Molecular structure of the pentacation in the crystal of $\{(\mu\text{-bpym-(4-OH)})[\text{Ru}(\text{NO})(\text{terpy})]_2\}(\text{PF}_6)_5 \cdot 2.5\text{H}_2\text{O}$.

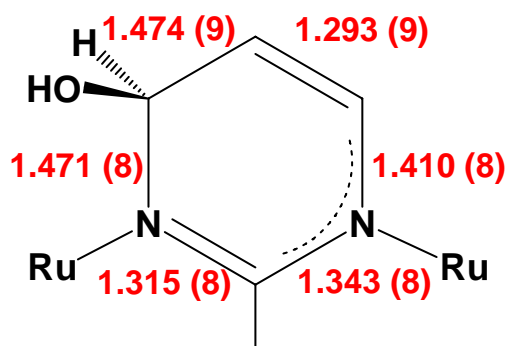


Figure 5.3.2. Intra-ring bond lengths (Å) and bond orders in the 4-hydroxide attacked pyrimidine ring of $\{(\mu\text{-bpym-(4-OH)})[\text{Ru}(\text{NO})(\text{terpy})]_2\}^{5+}$.

Table 5.3.1. Structure parameters (bond lengths in Å and bond angles in (deg) of complex $\{(\mu\text{-bpym-(4-OH)})[\text{Ru}(\text{NO})(\text{terpy})]_2\}(\text{PF}_6)_5 \times 2.5\text{H}_2\text{O}$

Ru(1)–N(11)	1.784(5)
Ru(1)–N(9)	1.993(5)
Ru(1)–N(4)	2.066(5)
Ru(1)–N(10)	2.085(6)
Ru(1)–N(8)	2.088(6)
Ru(1)–N(3)	2.121(5)
Ru(2)–N(12)	1.796(5)
Ru(2)–N(12)	1.796(5)
Ru(2)–N(6)	1.990(5)
Ru(2)–N(2)	2.068(5)
Ru(2)–N(7)	2.069(6)
Ru(2)–N(5)	2.092(6)
Ru(2)–N(1)	2.133(5)
N(1)–C(4)	1.331(8)
N(1)–C(1)	1.337(8)
N(2)–C(5)	1.315(8)
N(2)–C(8)	1.471(8)
N(3)–C(3)	1.334(8)
N(3)–C(4)	1.338(8)
N(4)–C(5)	1.343(8)
N(4)–C(6)	1.410(8)
N(5)–C(9)	1.319(9)
N(11)–O(1)	1.121(7)
N(12)–O(2)	1.101(6)
C(1)–C(2)	1.373(10)
C(2)–C(3)	1.388(10)
C(4)–C(5)	1.452(9)
C(6)–C(7)	1.293(9)
C(7)–C(8)	1.474(9)
C(8)–O(3)	1.407(9)

Table 5.3.1 continued

O(1)–N(11)–Ru(1)	174.1(5)
O(2)–N(12)–Ru(2)	172.3(5)
O(3)–C(8)–N(2)	109.1(6)
N(11)–Ru(1)–N(9)	95.5(2)
N(11)–Ru(1)–N(4)	169.8(2)
N(9)–Ru(1)–N(4)	91.2(2)
N(11)–Ru(1)–N(10)	91.6(2)
N(9)–Ru(1)–N(10)	79.7(2)
N(4)–Ru(1)–N(10)	81.9(2)
N(11)–Ru(1)–N(8)	96.0(2)
N(9)–Ru(1)–N(8)	80.0(2)
N(4)–Ru(1)–N(8)	92.7(2)
N(10)–Ru(1)–N(8)	158.9(2)
N(11)–Ru(1)–N(3)	94.9(2)
N(9)–Ru(1)–N(3)	169.6(2)
N(4)–Ru(1)–N(3)	78.5(2)
N(10)–Ru(1)–N(3)	100.2(2)
N(8)–Ru(1)–N(3)	98.7(2)
N(12)–Ru(2)–N(6)	98.0(2)
N(12)–Ru(2)–N(2)	171.1(2)
N(6)–Ru(2)–N(2)	89.9(2)
N(12)–Ru(2)–N(7)	93.9(2)
N(6)–Ru(2)–N(7)	79.6(2)
N(2)–Ru(2)–N(7)	91.3(2)
N(12)–Ru(2)–N(5)	91.8(2)
N(6)–Ru(2)–N(5)	79.9(2)
N(2)–Ru(2)–N(5)	85.7(2)
N(7)–Ru(2)–N(5)	159.3(2)
N(12)–Ru(2)–N(1)	93.3(2)
N(6)–Ru(2)–N(1)	168.7(2)
N(7)–Ru(2)–N(1)	100.6(2)
N(5)–Ru(2)–N(1)	98.9(2)
N(2)–Ru(2)–N(1)	78.8 (2)

Positional structural alternatives (A-D; Figure 5.3.3) exist with respect to the orientation of the {RuNO} groups relative to the bridge and to each other. In the observed crystal structure the arrangement is A, i.e., a *syn* configuration with both RuNO vectors pointing away from the hydroxide-attacked pyrimidine ring. The preference for this configuration is not immediately obvious; it may reflect maximum OH/NO/NO repulsion.

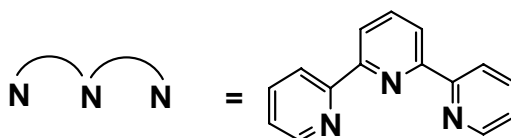
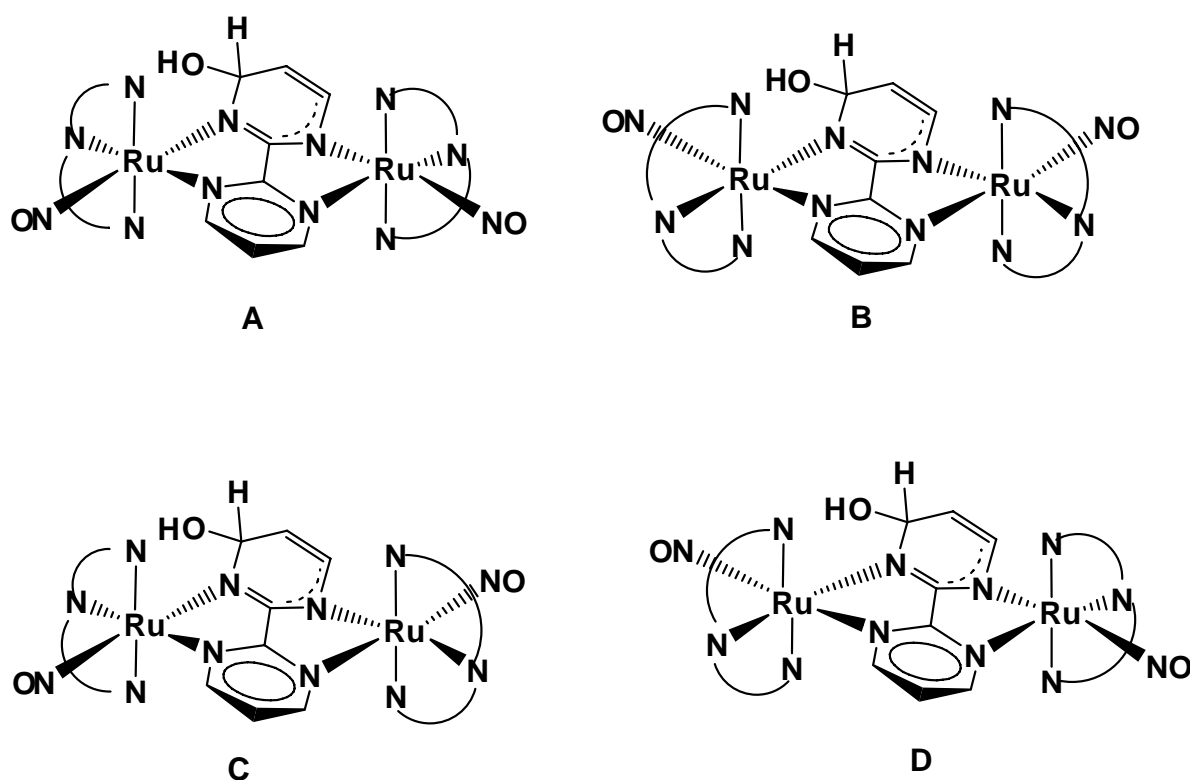


Figure 5.3.3. Two *syn* and two *anti* configurations of $\{(\mu\text{-bpym-(4-OH)})[\text{Ru}(\text{NO})(\text{terpy})]_2\}^{5+}$.

The asymmetry caused by only one hydroxide adding to a pyrimidine C⁴ carbon atom is only little reflected by the {RuNO} moieties: The group lying on the same side as

the attacked carbon atom (Ru2–N12–O2) shows a slightly shorter N–O distance (1.101(6) vs 1.121(7) Å) and a marginally smaller Ru–N–O angle (172.3(5) vs 174.1(5)°). The Ru–NO bonds are hardly affected (1.796(5) vs 1.784(5) Å). As mentioned already, the asymmetry seems to become manifest, however, through the broadening of the (combined) NO stretching band at 1946 cm^{-1} ($\Delta\nu_{1/2} = 30\text{ cm}^{-1}$) in comparison to that of the mononuclear analogue $[\text{Ru}(\text{NO})(\text{bpym})(\text{terpy})]^{3+}$ ($\Delta\nu_{1/2} = 15\text{ cm}^{-1}$; Figure 5.2.10).

5.4. Cyclic Voltammetry

As was discussed in the introduction to this Chapter, one of the important parameters to determine metal-metal interaction in mixed-valent systems is the electrochemical comproportionation constant, K_c which determines the potential range of the mixed-valent system. The method of choice to determine ΔE factor for calculating K_c is cyclic voltammetry. Figure 5.4.1 and Figure 5.4.2 show the cyclic voltammograms of **5a** and **5b** respectively. The electrochemical data for **5a** and **5b** complexes are listed in Table 5.4.1.

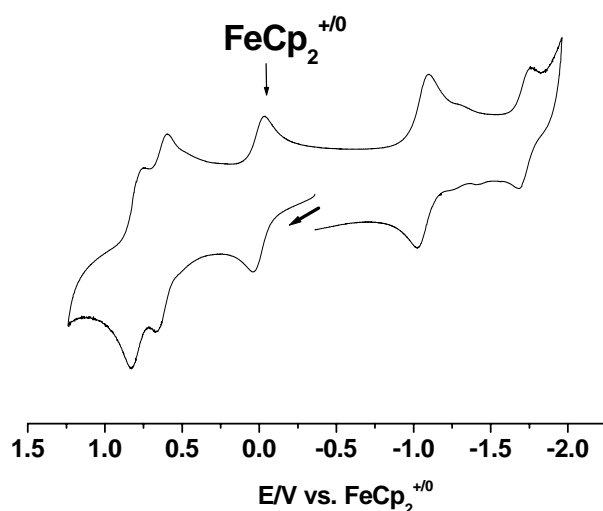


Figure 5.4.1. Cyclic voltammogram of $\{(\mu\text{-bpym})[\text{RuCl}(\text{terpy})]_2\}(\text{PF}_6)_2$ in $\text{CH}_3\text{CN}/0.1\text{ M } n\text{-Bu}_4\text{NPF}_6$ at 298 K; scan rate = 200 mV/s.

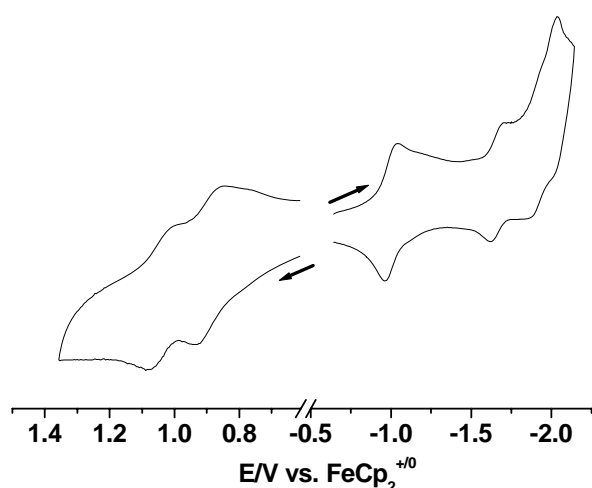


Figure 5.4.2. Cyclic voltammograms of $\{(\mu\text{-bpym})[\text{Ru}(\text{NO}_2)(\text{terpy})]_2\}(\text{PF}_6)_2$ in $\text{CH}_3\text{CN}/0.1 \text{ M } n\text{-Bu}_4\text{NPF}_6$ (reduction at 298 K) and (Oxidation at -40°C); Scan rate = 200 mV/s.

Table 5.4.1. Electrochemical data^a for the first two oxidations of dinuclear complexes

complex	$E_{1/2}(\text{ox})$	$E_{1/2}(\text{ox}2)$	K_c^b	solvent
$\{(\mu\text{-bpym})[\text{RuCl}(\text{terpy})]_2\}(\text{PF}_6)_2$	0.67 (63)	0.80 (65)	$10^{2.8}$	CH_3CN
$\{(\mu\text{-bpym})[\text{Ru}(\text{NO}_2)(\text{terpy})]_2\}(\text{PF}_6)_2$	0.91 (71) ^c	1.06 (74) ^c	$10^{2.5}$	CH_3CN

^a Potentials in V vs. $\text{FeCp}_2^{+/0}$; the potential of $\text{FeCp}_2^{+/0}$ being 0.48 V more positive than SCE and the potential of SCE is 0.02 V more positive than Ag/AgCl . ΔE_{pp} (in mV) in parentheses.

^b K_c is the comproportionation constant for the mixed-valent state.

^c Reversible at 200 mV/s at -40°C .

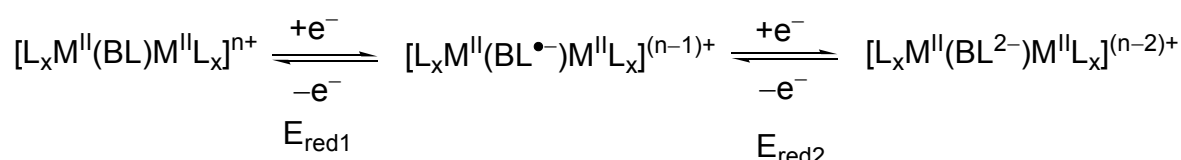
Scheme 5.4.1 shows the two oxidation processes whose potentials are listed in Table 5.4.1. One-electron oxidation of a bridged diruthenium(II) species is normally expected to produce a $\text{Ru}^{\text{III}}\text{Ru}^{\text{II}}$ mixed-valent intermediate of a two-step redox system.^[127,128,129] Characteristically variable comproportionation constants K_c

Table 5.4.2. Electrochemical data^a for the first two reductions of dinuclear complexes

complex	$E_{1/2}(\text{red1})$	$E_{1/2}(\text{red2})$	K_c^b	solvent
$\{(\mu\text{-bpym})[\text{RuCl}(\text{terpy})]_2\}(\text{PF}_6)_2$	-1.06 (69)	-1.70 (74)	$10^{10.8}$	CH ₃ CN
$\{(\mu\text{-bpym})[\text{Ru}(\text{NO}_2)(\text{terpy})]_2\}(\text{PF}_6)_2$	-1.03 (73)	-1.68 (81)	$10^{11.0}$	CH ₃ CN

^a Potentials in V vs. $\text{FeCp}_2^{+/0}$; the potential of $\text{FeCp}_2^{+/0}$ being 0.48 V more positive than SCE and the potential of SCE is 0.02 V more positive than Ag/AgCl. ΔE_{pp} (in mV) in parentheses.

^b K_c is the comproportionation constant for the one-electron reduced state.



M = Ru

BL = bridging ligand

L_x = ancillary ligand

Scheme 5.4.2. Redox processes involved with the two one-electron reduction processes.

5.5. UV/VIS/NIR Spectroelectrochemistry

In order to determine the electronic metal-metal coupling, one has to resort to measurements in the VIS/NIR region. The so called inter-valence charge transfer (IVCT) band usually occurs at long wavelengths because of the very small energy gap between the completely filled and half filled d orbitals in such systems. Using an optically transparent thin-layer electrode (OTTLE) cell it is possible to monitor the spectroscopic changes in the UV/VIS/NIR region on oxidising or reducing a species. The spectral changes on oxidising **5a** and **5b** are shown in Figures 5.5.1-5.5.4. The changes associated with reduction of **5a** and **5b** are shown in Figures 5.5.5, 5.5.6. The UV/VIS/NIR data for the complexes **5a** and **5b** are listed in Table 5.5.1.

The native states ($\text{Ru}_2^{\text{II,II}}$) of all complexes are distinguished by the typical low-energy metal($d\pi$)-to-bpym(π^*) charge transfer (MLCT) transitions (Table 5.5.1). All compounds exhibit typical metal($d\pi$)-to-tpy(π^*) MLCT transitions at higher energies at ca. 350–450 nm and further intra-ligand transitions in the UV region.

After the first oxidation, the resulting mixed-valent diruthenium(III,II) complexes $\{(\mu\text{-bpym})[\text{RuX}(\text{terpy})]_2\}^+$, X = Cl or NO_2 , show a decrease of the intense MLCT bands in the visible while a very weak absorption emerges in the near-infrared (NIR) region around 1500 nm for X = Cl and around 1400 for X = NO_2 (Figures 5.5.1, 5.5.3, Table 5.5.1). These bands are the most interesting feature known as inter-valence charge transfer (IVCT) bands, position and intensity of which are variable and depends on the metal, the bridging ligand and on the ancillary ligands. Here, the low molar extinction coefficient of only $100\text{--}300 \text{ M}^{-1}\cdot\text{cm}^{-1}$ seems to confirm a weak interaction (Class II behaviour^[127,128,129,140,160]) although bis-bidentate acceptor bridged diruthenium(III,II) systems are often distinguished by very low intensity IVCT features in spite of otherwise apparent strong metal-metal coupling.^[158,159] On second oxidation, the NIR feature disappears and further decrease of the intense MLCT bands in the visible occur (Figures 5.5.2, 5.5.4, Table 5.5.1).

On one-electron reduction from $[\text{M}^{\text{II}}(\text{BL})\text{M}^{\text{II}}]^{n+}$ to $[\text{M}^{\text{II}}(\text{BL}^{\bullet-})\text{M}^{\text{II}}]^{(n-1)+}$ (M = Ru, BL = bridging ligand) the MLCT band corresponding to the M($d\pi$)-to bpym(π^*) transition is generally shifted to higher energies (Figures 5.5.5, 5.5.6, Table 5.5.1). The addition of electron occurs into the π^* orbital (LUMO) of the bpym and thus, the absorption spectrum of $\{(\mu\text{-bpym})[\text{RuCl}(\text{terpy})]_2\}^+$ shows weak intra-ligand absorption emerging at about 1100 nm and that of $\{(\mu\text{-bpym})[\text{Ru}(\text{NO}_2)(\text{terpy})]_2\}^+$ at about 1040 nm for bpym $^{\bullet-}$ (Figures 5.5.5, 5.5.6, Table 5.5.1).^[161] The second reduction step for both complexes proved to be irreversible in spectroelectrochemistry experiments.

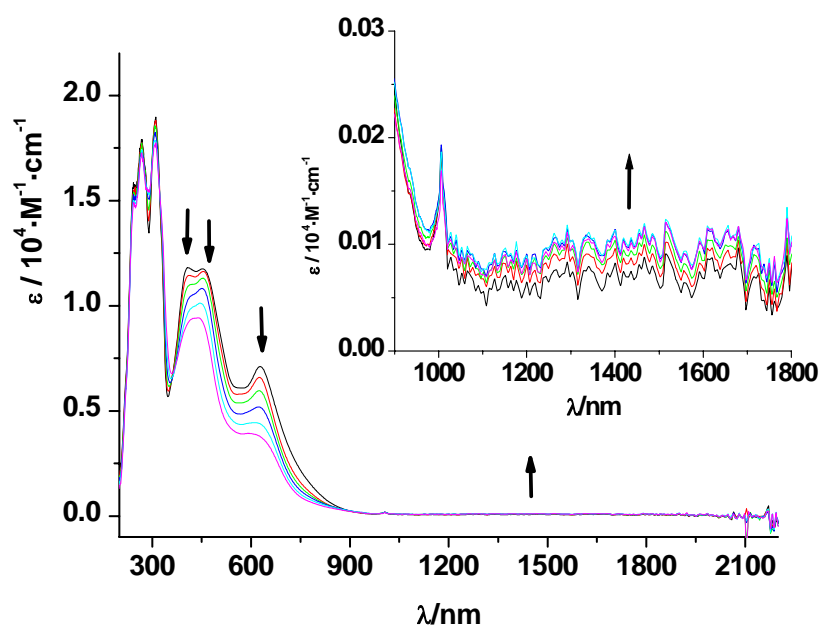


Figure 5.5.1. UV/VIS/NIR spectroelectrochemical response of the reversible transition $\{(\mu\text{-bpym})[\text{RuCl}(\text{terpy})]_2\}^{(2+) \rightarrow (3+)}$ in $\text{CH}_3\text{CN}/0.1 \text{ M } n\text{-Bu}_4\text{NPF}_6$ at 298 K.

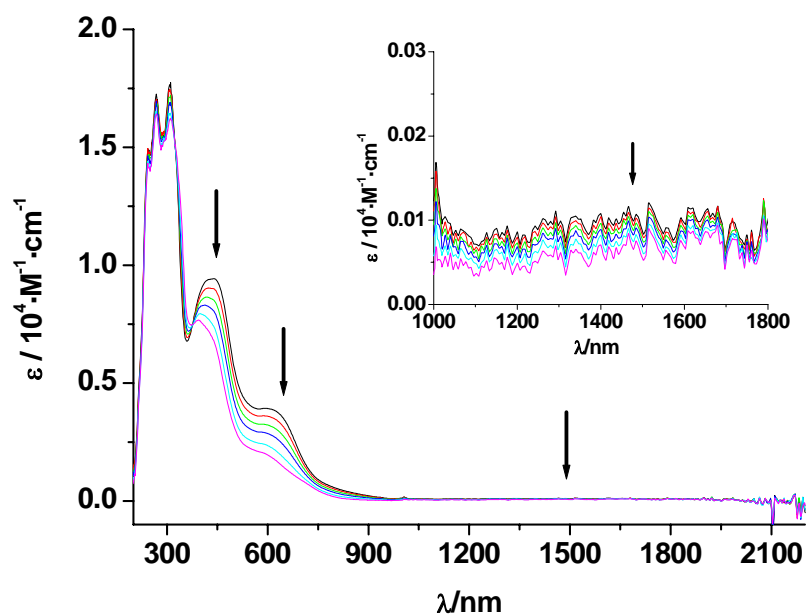


Figure 5.5.2. UV/VIS/NIR spectroelectrochemical response of the reversible transition $\{(\mu\text{-bpym})[\text{RuCl}(\text{terpy})]_2\}^{(3+) \rightarrow (4+)}$ in $\text{CH}_3\text{CN}/0.1 \text{ M } n\text{-Bu}_4\text{NPF}_6$ at 298 K.

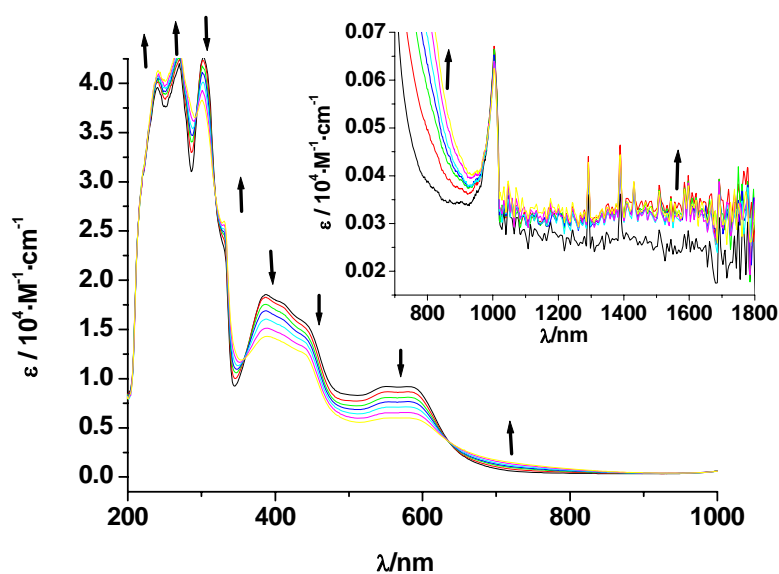


Figure 5.5.3. UV/VIS/NIR spectroelectrochemical response of the reversible transition $\{(\mu\text{-bpym})[\text{Ru}(\text{NO}_2)(\text{terpy})]_2\}^{(2+)\rightarrow(3+)}$ in $\text{CH}_3\text{CN}/0.1 \text{ M } n\text{-Bu}_4\text{NPF}_6$ at -40°C .

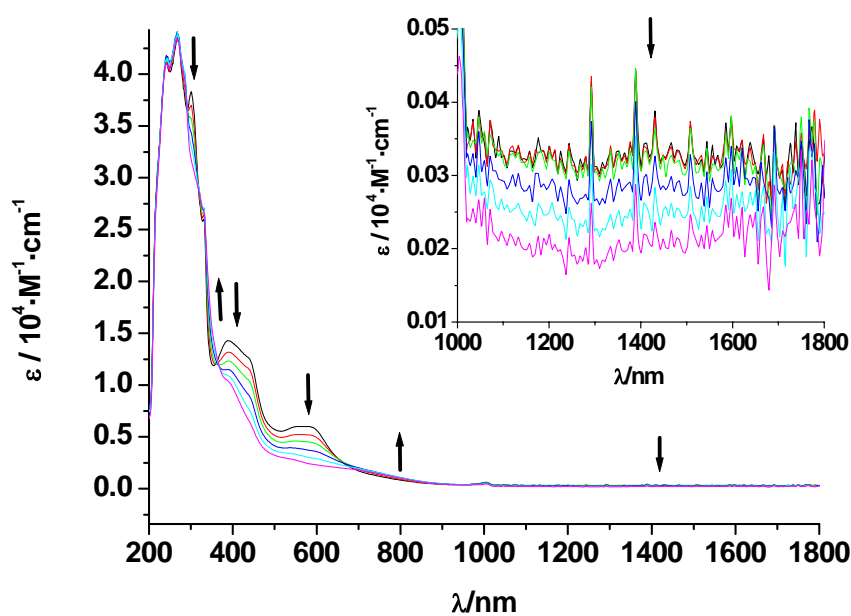


Figure 5.5.4. UV/VIS/NIR spectroelectrochemical response of the reversible transition $\{(\mu\text{-bpym})[\text{Ru}(\text{NO}_2)(\text{terpy})]_2\}^{(3+)\rightarrow(4+)}$ in $\text{CH}_3\text{CN}/0.1 \text{ M } n\text{-Bu}_4\text{NPF}_6$ at -40°C .

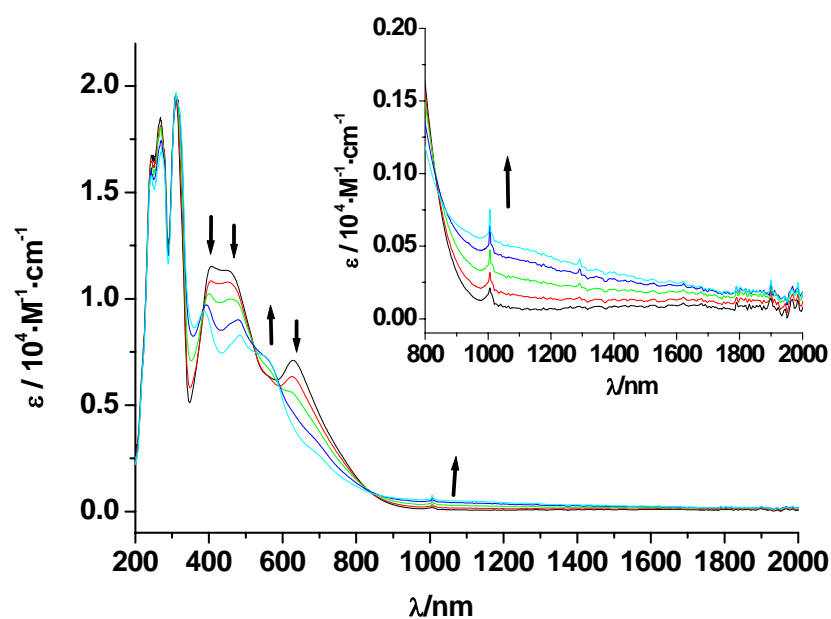


Figure 5.5.5. UV/VIS/NIR spectroelectrochemical response of the reversible transition $\{(\mu\text{-bpym})[\text{RuCl}(\text{terpy})]_2\}^{(2+)\rightarrow(+)}$ in $\text{CH}_3\text{CN}/0.1 \text{ M } n\text{-Bu}_4\text{NPF}_6$ at 298 K.

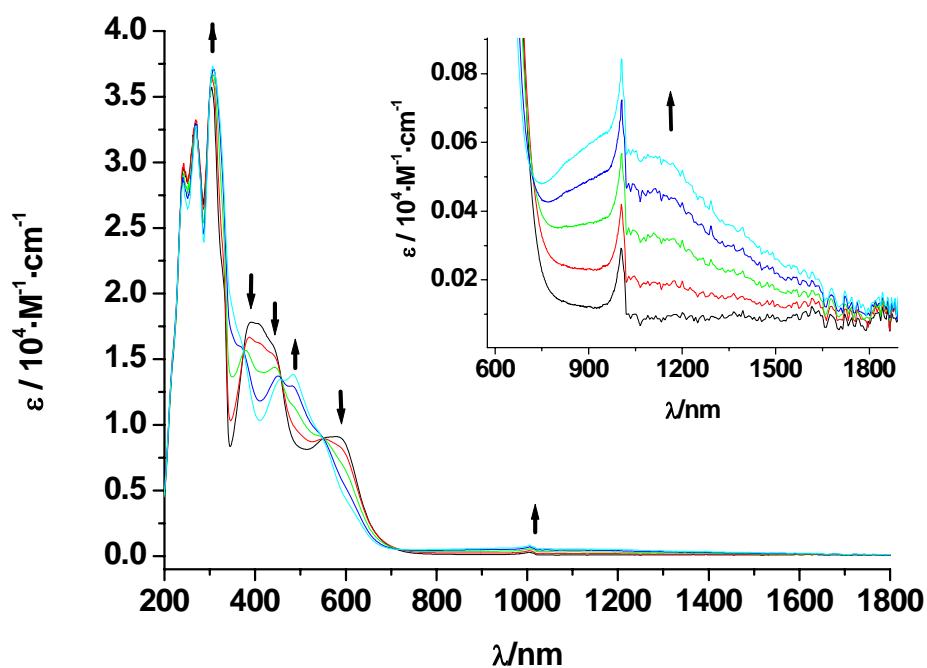


Figure 5.5.6. UV/VIS/NIR spectroelectrochemical response of the reversible transition $\{(\mu\text{-bpym})[\text{Ru}(\text{NO}_2)(\text{terpy})]_2\}^{(2+)\rightarrow(+)}$ in $\text{CH}_3\text{CN}/0.1 \text{ M } n\text{-Bu}_4\text{NPF}_6$ at 298 K.

Table 5.5.1. UV/VIS/NIR spectroelectrochemical data^a for dinuclear ruthenium complexes

compound	λ/nm ($\epsilon/\text{M}^{-1}\cdot\text{cm}^{-1}$)
$\{(\mu\text{-bpym})[\text{RuCl}(\text{terpy})]_2\}^{4+}$	243(14940), 268(17270), 311(17750), 440(9430), 630sh
$\{(\mu\text{-bpym})[\text{RuCl}(\text{terpy})]_2\}^{3+}$	243(14330), 269(16420), 309(16160), 437sh, 600sh, 1500(100)
$\{(\mu\text{-bpym})[\text{RuCl}(\text{terpy})]_2\}^{2+}$	243(16470), 268(18530), 310(19370), 404(11500), 460(11240), 628(7100)
$\{(\mu\text{-bpym})[\text{RuCl}(\text{terpy})]_2\}^+$	243(15810), 271(16950), 311(19600), 387(9420), 484(8290), 560sh, 1160sh
$\{(\mu\text{-bpym})[\text{Ru}(\text{NO}_2)(\text{terpy})]_2\}^{4+b}$	240(41820), 270(41120), ^c
$\{(\mu\text{-bpym})[\text{Ru}(\text{NO}_2)(\text{terpy})]_2\}^{3+b}$	240(41240), 270(43585), 300(38250), 322(25780), 346sh, 388(14300), 443sh, 556(6005), 590(5920), 730sh, 1400(300)
$\{(\mu\text{-bpym})[\text{Ru}(\text{NO}_2)(\text{terpy})]_2\}^{2+}$	240(29470), 270(32790), 304(35720), 325sh, 390(17820), 450sh, 552(8900), 594(8850)
$\{(\mu\text{-bpym})[\text{Ru}(\text{NO}_2)(\text{terpy})]_2\}^+$	242(28270), 270(32760), 307(37340), 370sh, 455(13465), 480(13840), 550sh, 1040(1570)

^a From spectroelectrochemistry in an OTTLE cell in $\text{CH}_3\text{CN}/0.1 \text{ M } n\text{-Bu}_4\text{NPF}_6$.

^b At $-40 \text{ }^\circ\text{C}$.

^c Slope without clear absorptions in the visible.

5.6. EPR Spectroelectrochemistry

The oxidation to the mixed-valent intermediates $\{(\mu\text{-bpym})[\text{Ru}(\text{X})(\text{terpy})]_2\}^{3+}$, X = Cl and NO_2 , in $\text{CH}_3\text{CN}/0.1 \text{ M } n\text{-Bu}_4\text{NPF}_6$ is accompanied by EPR signals indicating metal centred spin via the large g shift and anisotropy (Figures 5.6.1, 5.6.2). For X = Cl a rhombic splitting is observed ($g_1 = 2.79$, $g_2 = 2.22$, $g_3 = 2.04$ and $\Delta g = 0.754$) and for X = NO_2 an axial pattern ($g_{1,2} = 2.36$, $g_3 = 2.03$ and $\Delta g = 0.328$). The EPR signals are broad at 110 K which may partially reflect the presence of isomers, in agreement with similar observations for diruthenium(III,II) species^[155,156] no signals were detected in fluid solution. However, the EPR parameters with $g_{1,2} > 2$, $g_3 \approx 2$ and the deviation of the calculated isotropic g-values (2.35; X = Cl and 2.25; X = NO_2) from the free electron g factor ($g_e = 2.0023$) clearly points to a predominantly metal-centred spin corresponding to low-spin $4d^5$ situation as expected for ruthenium(III).^[119,162] Although the question of delocalised (Class III) or localised valencies (Class II)^[140,160] on the EPR (10^{-8} s) or vibrational time scale (10^{-12} s) cannot be answered with certainty, the available data point to weakly coupled systems. In the EPR data listed in Table 5.6.1, the isotropic g value is always greater than the free electron g factor. This points to an orbital situation where the singly occupied molecular orbital (SOMO) is closer to the $d\pi$ HOMO than to the π^* LUMO (Figure 4.6.6.1).

Table 5.6.1. X-band EPR data^a of the one-electron oxidised form of dinuclear complexes

compound	g_1	g_2	g_3	$\langle g \rangle^b$	Δg^c
$\{(\mu\text{-bpym})[\text{RuCl}(\text{terpy})]_2\}^{3+}$	2.794	2.224	2.040	2.35	0.754
$\{(\mu\text{-bpym})[\text{Ru}(\text{NO}_2)(\text{terpy})]_2\}^{3+}$	2.355	2.355	2.027	2.25	0.328

^a From electrochemically generated species in $\text{CH}_3\text{CN}/0.1 \text{ M } n\text{-Bu}_4\text{NPF}_6$.

^b $\langle g \rangle = \sqrt{(g_1^2 + g_2^2 + g_3^2)}/3$.

^c $\Delta g = g_1 - g_3$.

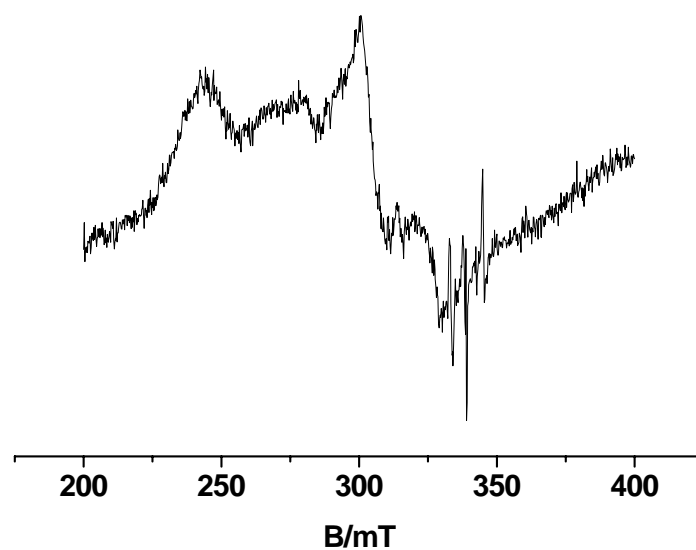


Figure 5.6.1. X-band EPR spectrum of electrogenerated $\{(\mu\text{-bpym})[\text{RuCl}(\text{terpy})]_2\}^{3+}$ in $\text{CH}_3\text{CN}/0.1 \text{ M } n\text{-Bu}_4\text{NPF}_6$ at 110 K; $g_1 = 2.794$, $g_2 = 2.224$, $g_3 = 2.040$.

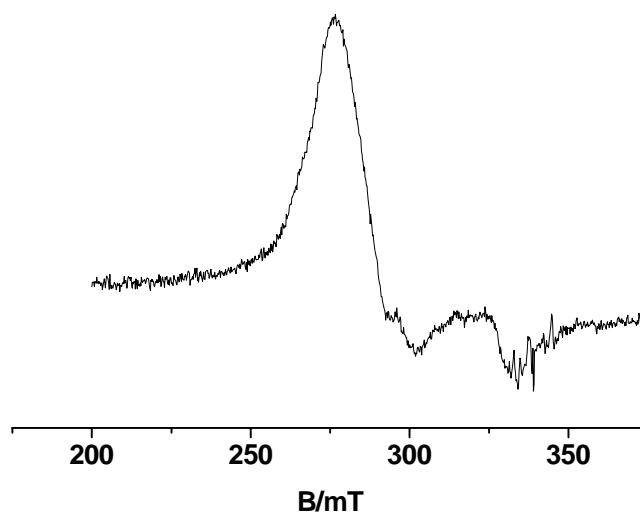


Figure 5.6.2. X-band EPR spectrum of electrogenerated $\{(\mu\text{-bpym})[\text{Ru}(\text{NO}_2)(\text{terpy})]_2\}^{3+}$ in $\text{CH}_3\text{CN}/0.1 \text{ M } n\text{-Bu}_4\text{NPF}_6$ at 110 K; $g_{1,2} = 2.355$ and $g_3 = 2.027$.

The reduction $\{(\mu\text{-bpym})[\text{Ru}(\text{X})(\text{terpy})]_2\}^{(2+)\rightarrow(+)}$, X = Cl, NO₂, yield typical narrow diruthenium(II) radical EPR signals in both cases (X = Cl: $g_{\text{iso}} = 1.985$ or X= NO₂: $g_{\text{iso}} = 1.989$, Figures 5.6.3-5.6.6, Table 5.6.2) with g_{iso} slightly smaller than 2.^[120] Clearly, the reduction is centred at the bridging ligand which has a lower lying π^* MO than terpy (corresponding to a less negative reduction potential^[163]), especially after double metal coordination.^[108,152] The one-electron reduced forms are radical anion complexes with the spin predominantly localised on the bridging bipyrimidine unit. The closeness of the g -values to the free electron g factor ($g_e = 2.0023$), the unresolved g -values at X-band frequencies for the Ru complexes and the relatively small g -anisotropy all point to the spin being predominantly localised on the bridging ligand.

Table 5.6.2. X-band EPR data^a of the one-electron reduced forms of dinuclear ruthenium complexes

compound	g_1	g_2	g_3	$\langle g \rangle^b$	g_{iso}^c	Δg
$\{(\mu\text{-bpym})[\text{RuCl}(\text{terpy})]_2\}^+$	2.004	1.997	1.958	1.986	1.985	0.046
$\{(\mu\text{-bpym})[\text{Ru}(\text{NO}_2)(\text{terpy})]_2\}^+$	d	d	d	n.o.	1.989	n.o.

^a From electrochemically generated species in CH₃CN/0.1 M *n*-Bu₄NPF₆.

^b $\langle g \rangle = \sqrt{(g_1^2 + g_2^2 + g_3^2)}/3$.

^c Isotropic g value from measurements at 298 K.

^d Not resolved in the X-band.

n.o. = not observed.

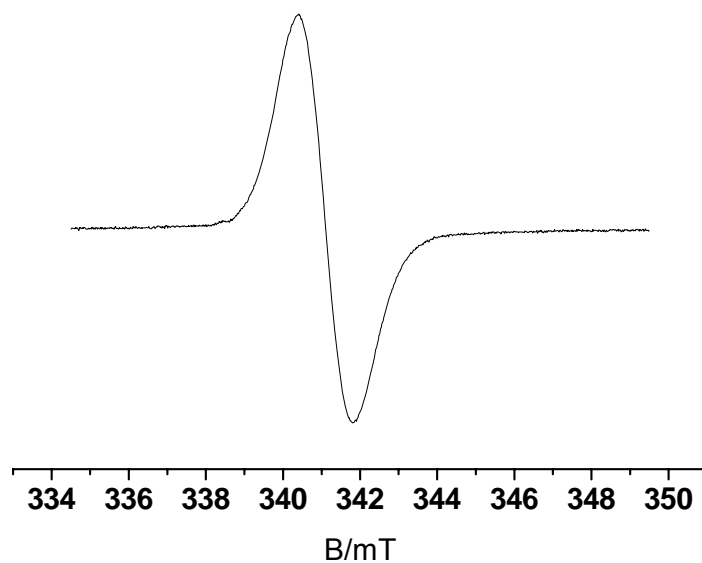


Figure 5.6.3. X-band EPR spectrum of electrogenerated $\{(\mu\text{-bpym})[\text{RuCl}(\text{terpy})]_2\}^+$ in $\text{CH}_3\text{CN}/0.1 \text{ M } n\text{-Bu}_4\text{NPF}_6$ at 298 K; $g_{\text{iso}} = 1.985$.

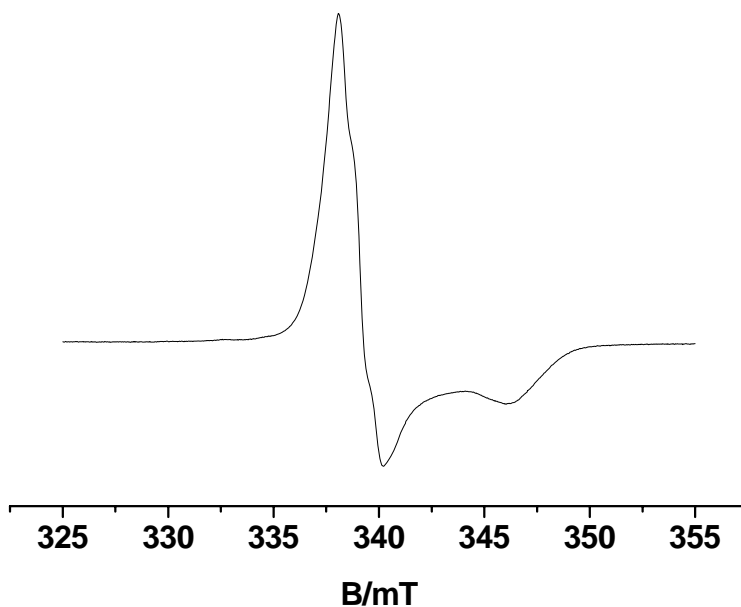


Figure 5.6.4. X-band EPR spectrum of electrogenerated $\{(\mu\text{-bpym})[\text{RuCl}(\text{terpy})]_2\}^+$ in $\text{CH}_3\text{CN}/0.1 \text{ M } n\text{-Bu}_4\text{NPF}_6$ at 110 K; $g_1 = 2.004$, $g_2 = 1.997$, $g_3 = 1.958$.

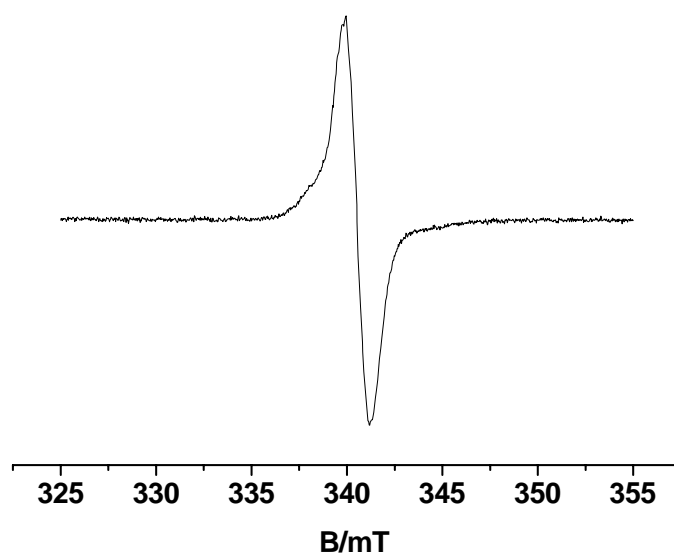


Figure 5.6.5. X-band EPR spectrum of electrogenerated $\{(\mu\text{-bpym})[\text{Ru}(\text{NO}_2)(\text{terpy})]_2\}^+$ in $\text{CH}_3\text{CN}/0.1 \text{ M } n\text{-Bu}_4\text{NPF}_6$ at 298 K; $g_{\text{iso}} = 1.989$.

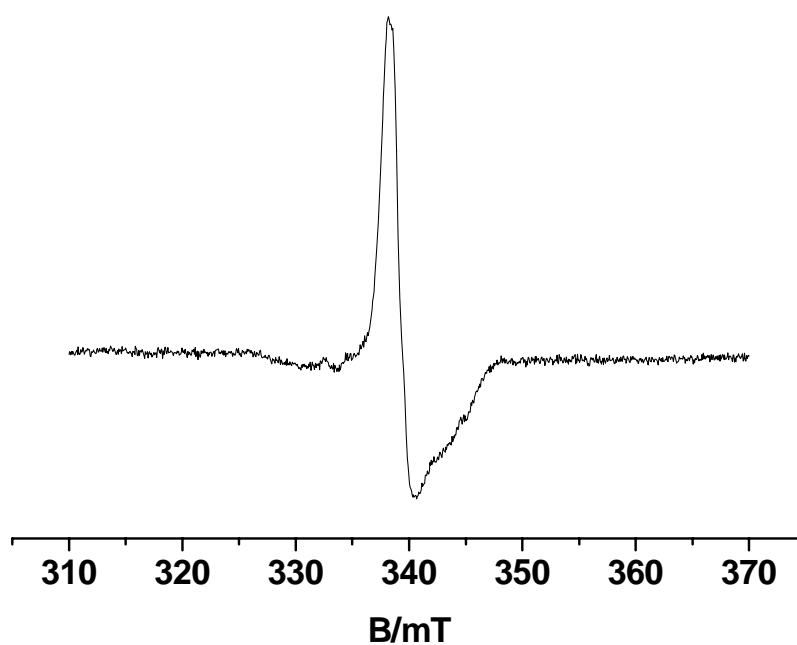


Figure 5.6.6. X-band EPR spectrum of electrogenerated $\{(\mu\text{-bpym})[\text{Ru}(\text{NO}_2)(\text{terpy})]_2\}^+$ in $\text{CH}_3\text{CN}/0.1 \text{ M } n\text{-Bu}_4\text{NPF}_6$ at 110 K.

5.7. Conclusion and Outlook

Concluding, the redox series $\{(\mu\text{-bpym})[\text{RuCl}(\text{terpy})]_2\}^n$ and $\{(\mu\text{-bpym})[\text{Ru}(\text{NO}_2)(\text{terpy})]_2\}^n$, $n = (0)-(4+)$ have been studied with respect to their mixed-valent properties and attempts have been made to prepare the complex $\{(\mu\text{-bpym})[\text{Ru}(\text{NO})(\text{terpy})]_2\}^{6+}$. The ^1H NMR spectra for $\{(\mu\text{-bpym})[\text{RuX}(\text{terpy})]_2\}^{2+}$, $\text{X} = \text{Cl}$ and NO_2 , indicate the formation of both *syn* and *anti* isomers. Both dinuclear complexes $\{(\mu\text{-bpym})[\text{RuX}(\text{terpy})]_2\}^{2+}$, $\text{X} = \text{Cl}$ and NO_2 , can undergo two reversible bpym-centred one-electron reduction processes and two metal-centred one-electron oxidation steps, the latter involving mixed-valent intermediates with weak intermetallic coupling as evident from the low comproportionation constant K_c and weak IVCT bands in NIR. Acidification of $\{(\mu\text{-bpym})[\text{Ru}(\text{NO}_2)(\text{terpy})]_2\}(\text{PF}_6)_2$ does not lead to the expected $\{(\mu\text{-bpym})[\text{Ru}(\text{NO})(\text{terpy})]_2\}^{6+}$ but, probably because of the high charge, to the insoluble but structurally and IR-spectroscopically characterised pseudo-base product *syn*- $\{(\mu\text{-bpym-(4-OH)})[\text{Ru}(\text{NO})(\text{terpy})]_2\}(\text{PF}_6)_5$.

The formation of the pseudo-base product *syn*- $\{(\mu\text{-bpym-(4-OH)})[\text{Ru}(\text{NO})(\text{terpy})]_2\}(\text{PF}_6)_5$ suggest that the structural coupling of $\{\text{RuNO}\}$ moieties by a π acceptor ligand bridge is possible. In the present case the electronic interaction is affected by the in-plane arrangement of these moieties which results from the meridionally tridentate coordination of the terpy co-ligand; the use of facially tridentate co-ligands such as neutral ligand tris(1-pyrazolyl)methane or anionic ligand tris(1-pyrazolyl)borate should lead to RuNO vectors orthogonal to the π plane and the possible coupling of terminal NO ligands bound to redox-active, ligand-bridged diruthenium complexes can be unravelled and exploratory chemistry in this area can provide clues to the mechanism of complex redox processes.

CHAPTER 6

Experimental Section

6.1. Instrumentation

EPR spectroscopy

X-band EPR spectra at about 9.5 GHz were obtained on a Bruker system ESP 300 equipped with a HEWLETT-PACKARD frequency counter 5350B, a Bruker ER035M gaussmeter for g-value determination and a continuous flow cryostat ESR 900 of Oxford Instruments for measurements at liquid helium temperatures (4 K). For measurements between 110-300 K, the same instrumental configurations were used with a liquid nitrogen cryostat. After the upgrade of instrument, EPR spectra in the X-band were recorded with a Bruker EMX System. EPR spectra at W-band (95 GHz) and G-band (190 GHz) were recorded using a multifrequency spectrometer.^[164,165] A Gunn diode operating at 95 GHz and equipped with a third harmonic generator has been used as a radiation source. An InSb bolometer (QMC Instruments) was used for detection. The main magnetic field was provided by a superconducting magnet (Cryogenics Consultant) which generates fields up to 12 T. Owing to different field sweep conditions, the absolute values of the g components were obtained by calibrating the precisely measured g anisotropy data with the isotropic g-value from X-band measurements. While this procedure does not account for the temperature dependence of g, the values extracted are identical with those obtained using an added standard. The accuracy of g-values is estimated at ± 0.0003 . Electrochemical generation of radicals was carried out by using a two-electrode configuration (platinum wires) for measurements at X-band frequencies.^[120] For high field measurements the radicals were generated by chemical reduction using zinc and then rapidly transferred into the sample holder and frozen. Simulations of the spectra were done using the Bruker WINEPR/Simfonia programs.

NMR spectroscopy

^1H NMR spectroscopy at a frequency of 400 MHz was carried out by Ms. K. Török on a Bruker AC 400 spectrometer. Tetramethylsilane (TMS) was used as an external chemical shift standard.

IR spectroscopy

IR spectra were obtained using Perkin-Elmer FTIR 684 and 283 instruments or a Philips FTIR PU 9800 spectrometer or Nicolet 6700 FTIR instrument. The solid state IR measurements were performed with an ATR unit (smart orbit with diamond crystal) on Nicolet 6700 FTIR instrument. The spectra were taken from solutions using CaF_2 windows.

UV/VIS/NIR and IR spectroscopy

Absorption spectra were recorded on J&M TIDAS and Shimadzu UV 3101 PC spectrophotometers. The measurements were done in solution using quartz cuvettes of 1 cm or 1 mm path length.

UV/VIS/NIR and IR spectroelectrochemistry

UV/VIS/NIR and IR spectroelectrochemistry measurements were performed under argon atmosphere using an optically transparent thin-layer electrode (OTTLE) cell developed by M. Krejčík.^[166] The windows of the cell consist of CaF_2 plates. Between the plates there is a spacer into which the working (platinum mesh), auxiliary (platinum mesh) and reference electrodes (silver wire as pseudo reference) are melt-sealed.

Cyclic voltammetry

Cyclic and square-wave voltammetry measurements were performed on an EG&G PAR 273 potentiostat. The measurements were carried out under an argon atmosphere in 0.1 M tetrabutylammonium hexafluorophosphate or in 0.1 M tetrabutylammonium perchlorate solutions using a three-electrode configuration (glassy carbon as working electrode, platinum as counter electrode and silver as pseudoreference electrode). The ferrocene/ferrocenium couple served as internal reference. Polarography was performed using a PAR 263A instrument.

Elemental analyses

C, H, N analyses were performed on a Perkin Elmer Analyser 240 by Ms. B. Förtsch.

ESI-Mass-spectroscopy

ESI mass spectra were recorded on Bruker Daltonics-micrOTOF-Q by Dr. J. Opitz, Mr. J. Trinkner and Ms. K. Wohlbold.

6.2. DFT Calculations

DFT calculations were performed by Dr. S. Zalis from J. Heyrovsky Institute of Physical Chemistry, Prague.

6.2.1. $[\text{Cl}_5\text{Os}(\text{NO})]^{n-}$ ($n = 1-3$)

Ground state electronic structure calculations on $[\text{Cl}_5\text{Os}(\text{NO})]^{n-}$ ($n = 1-3$) complexes have been done on the base of density-functional theory (DFT) methods using the ADF2004.1^[167,168] and Gaussian 03^[169] program packages.

Within the ADF program, Slater type orbital (STO) basis sets of triple- ζ quality with two polarisation functions were employed. Basis I was represented by frozen core approximation (1s for N, O, 1s-2p for Cl and 1s-4d for Os were kept frozen), basis II includes also core electrons. The following density functional was used within ADF: The local density approximation (LDA) with VWN parametrisation of electron gas data, or the functional including Becke's gradient correction^[170], to the local exchange expression in conjunction with Perdew's gradient correction^[171] to the LDA expression (ADF/BP). The scalar relativistic (SR) zero order regular approximation (ZORA) was used within ADF calculations. The g tensor was obtained from a spin-nonpolarised wave function after incorporating the spin-orbit (SO) coupling. A tensors and the g tensor are obtained by first-order perturbation theory from ZORA Hamiltonian in the presence of time-independent magnetic field.^[172,173] Electronic transition energies and compositions were calculated by the asymptotically correct SAOP functional (ADF/SAOP),^[174] which is more accurate for higher-lying MO's and electronic transitions. Core electrons were included in ADF/SAOP calculations.

Within Gaussian-03 Dunning's polarised valence double- ζ basis sets^[175] were used for N, O and Cl atoms and the quasirelativistic effective core pseudopotentials and corresponding optimised set of basis functions^[176] Os. The vibrational analysis was also done with the "pure" density functional BPW91^[170,177] and hybrid functional B3LYP.^[178]

The geometries of all complexes were optimised without any symmetry constraints, open shell systems within the spin-unrestricted open shell Kohn–Sham (UKS) approach. As geometry optimisations of $[\text{Cl}_5\text{Os}(\text{NO})]^{2-}$ lead to approximate C_{4v} symmetry, calculations on this systems were performed in C_{4v} constrained symmetry, the z axis coinciding with C_4 symmetry axis. All results discussed correspond to optimised geometries using the corresponding functional.

6.2.2. $[\text{Ru}(\text{TPP})(\text{NO})(\text{H}_2\text{O})]^{n+}$ ($n = 1, 2$) and $[\text{Ru}(\text{TPP})(\text{NO})(\text{Py})]^{n+}$ ($n = 0, 1$)

The electronic structures of $[\text{Ru}(\text{TPP})(\text{NO})(\text{H}_2\text{O})]^{n+}$ ($n = 1, 2$) and $[\text{Ru}(\text{TPP})(\text{NO})(\text{Py})]^{n+}$ ($n = 0, 1$) were calculated by density functional theory (DFT) methods using the Gaussian 03^[169] and ADF2006.01^[179,180] program packages. The calculations of the vibrational frequencies were performed at optimised geometries.

The hybrid functional of Perdew, Burke and Ernzerhof^[181] (PBE0) was used within Gaussian (G03/PBE0) together with 6-31G* polarised double- ζ basis sets^[182] for C, N, H and O atoms and effective core pseudopotentials and corresponding optimised sets of basis functions for Ru atoms.^[176] The triple- ζ basis augmented by diffuse functions (aug-cc-pvtz)^[183] was used for O within the H_2O ligand. The vibrational analysis was done with the "pure" density functional BPW91.^[170,177]

Slater type orbital (STO) basis sets of triple- ζ quality with two polarisation functions for the Ru atom and of triple- ζ quality with one polarisation function for the remaining atoms were employed within ADF2006.01. The inner shells were represented by the frozen core approximation (1s for C, N, O, 1s-3d for Ru were kept frozen). The calculations were done with the functional including Becke's gradient correction¹⁸³ to the local exchange expression in conjunction with Perdew's gradient correction¹⁷¹ to the local correlation (ADF/BP). The scalar relativistic (SR) zero order regular approximation (ZORA) was used within ADF calculations. The g tensor was obtained from a spin-nonpolarised wave function after incorporating the spin-orbit (SO)

coupling. A and g tensors were obtained by first-order perturbation theory from a ZORA Hamiltonian in the presence of a time-independent magnetic field.^[172,173] Core electrons were included in calculations of A tensors.

6.2.3. $[\text{Ru}(\text{NO}_2)(\text{bpym})(\text{terpy})]^+$ and $[\text{Ru}(\text{NO})(\text{bpym})(\text{terpy})]^{n+}$ (n=1-3)

The electronic structures of $[\text{Ru}(\text{NO})(\text{bpym})(\text{terpy})]^{n+}$ (n=1-3) and $[\text{Ru}(\text{NO}_2)(\text{bpym})(\text{terpy})]^+$ were calculated by density functional theory (DFT) methods using the Gaussian 03^[169] and ADF2006.01^[179,180] program packages. The calculations of the vibrational frequencies were performed at optimised geometries.

For the H, C, N, and O atoms 6-31G* polarised double- ζ basis sets^[182] (G03) were used together with quasirelativistic effective core pseudopotentials and a corresponding optimised set of basis functions for Ru.^[176] The vibrational analysis was done with the “pure” density functional BPW91.^[170,177]

Slater type orbital (STO) basis sets of triple- ζ quality with two polarisation functions for the Ru atom and of triple- ζ quality with one polarisation function for the remaining atoms were employed within ADF2006.0. The inner shells were represented by the frozen core approximation (1s for C, N, O, 1s-3d for Ru were kept frozen). The calculations were done with the functional including Becke's gradient correction^[170] to the local exchange expression in conjunction with Perdew's gradient correction^[171] to the local correlation (ADF/BP). The scalar relativistic (SR) zero order regular approximation (ZORA) was used within ADF calculations. The g tensor was obtained from a spin-nonpolarised wave function after incorporating the spin-orbit (SO) coupling. A and g tensors were obtained by first-order perturbation theory from a ZORA Hamiltonian in the presence of a time-independent magnetic field.^[172,173]

6.3. Solvents and Working Conditions

All metal complexes were synthesised under an argon atmosphere using conventional Schlenk techniques. Solvents were dried by refluxing under argon over calcium hydride (dichloromethane, acetonitrile, hexane and methanol), calcium chloride (acetone), magnesium oxide (ethanol). They were degassed by the freeze-pump-thaw method.

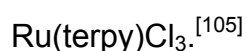
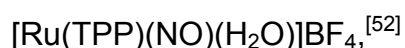
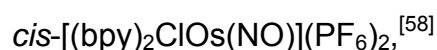
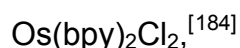
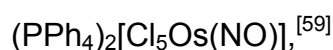
6.4. Syntheses

6.4.1 Commercially available compounds:

OsO₄, (NH₄)₂[OsCl₆], [Ru(TPP)(CO)] and NaNO₂ from Aldrich,
NH₂OH×HCl, *n*-Bu₄NPF₆, Ph₄PCl from Fluka,
RuCl₃×*x*H₂O from Merck,
NOBF₄, 2,2'-bipyridine, 2,2'-bipyrimidine and 2,2':6',2''-terpyridine from Alfa Aesar.

6.4.2 Syntheses of reported compounds:

The following compounds are prepared according to literature procedures.



6.4.3. Syntheses of new compounds:

(NBu₄)₂[Cl₅Os(NO)]

A solution of 72 mg (0.186 mmol) (*n*-Bu₄N)PF₆ in 10 mL methanol was added to a solution of 100 mg (0.093 mmol) (Ph₄P)₂[Cl₅Os(NO)] in 20 mL methanol with constant stirring at room temperature. The mixture was stirred for 1 hour at room temperature and the resulting solid, (Ph₄P)PF₆, was separated by filtering the mixture. The light brown filtrate contained the desired compound. A small amount of (*n*-Bu₄N)PF₆ was added to the filtrate to ensure the complete precipitation of the phosphonium salt and remove any further precipitate. The filtrate was evaporated to dryness and the grey solid residue was ground with 20 mL water to remove most of (*n*-Bu₄N)PF₆ which is poorly soluble in water. Evaporating the filtrate to dryness and drying the grey residue in vacuum yielded the analytical pure compound.

Yield: 74 mg (0.084 mmol, 90%).

Elemental analysis: $C_{32}H_{72}Cl_5N_3OOs$ (882.40 g/mol).

Calculated: C: 43.56% H: 8.22% N: 4.76%

Found: C: 43.83% H: 8.32% N: 4.50%

UV/VIS (CH_3CN): λ_{max}/nm ($\epsilon/M^{-1}\cdot cm^{-1}$) = 573(48), 437(71), 371(147), 335(147).

IR (KBr): 1802 cm^{-1} (ν_{NO}).

[Ru(NO₂)(bpym)(terpy)](PF₆)

An amount of 100 mg (0.227 mmol) Ru(terpy)Cl₃ and 107 mg (0.681 mmol) bpym were heated to reflux for 4 hours in a 50 mL ethanol/water (1/1, v/v) mixture under an argon atmosphere. An amount of 300 mg (4.347 mmol) NaNO₂ was added to the reddish brown solution and refluxing was continued for 3 hours. After cooling, the dark red solution was filtered and a concentrated solution of NH₄PF₆ (5 mL) was added to the filtrate. The reddish brown precipitate was filtered off and the filtrate (mother liquor) was kept for slow crystallisation. After one day red shiny crystals had grown in the solution, which were analytical pure. The solid obtained by the first filtration was recrystallised from a mixture of acetonitrile and diethylether (1/3) to get more analytical pure compound. Single crystals were grown by slow diffusion of diethylether into an acetonitrile solution at room temperature.

Yield: 120 mg (0.176 mmol, 77%).

Elemental analysis: $C_{23}H_{17}F_6N_8O_2PRu$ (683.48 g/mol).

Calculated: C: 40.42% H: 2.51% N: 16.39%

Found: C: 40.27% H: 2.32% N: 16.19%

¹H NMR (acetone-d₆): δ/ppm = 7.37 (dd, 1H), 7.43 (m, 2H), 8.08 (m, 5H), 8.24 (dd, 1H, J = 4.73 and 5.79 Hz), 8.36 (t, 1H, 8.08Hz), 8.62 (dd, 2H), 8.76 (d, 2H, 8.08Hz), 8.94 (dd, 1H, J = 4.73 and 2.05 Hz), 9.38 (dd, 1H, J = 4.73 and 2.03 Hz), 10.39 (dd, 1H, J = 5.95 and 2.13 Hz).

^1H NMR (CD_3CN): $\delta/\text{ppm} = 7.09$ (dd, 1H, 5'B, bpym, $J = 5.64$ and 4.70 Hz), 7.24 (m, 2H, 5T, terpy), 7.60 (dd, 1H, 4'B, bpym, 5.50 and 2.05 Hz), 7.76 (m, 2H, 6T, terpy), 7.88 (dt, 2H, 4T, terpy, $J(3) = 7.63$ and $J(2) = 1.45$ Hz), 7.97 (dd, 1H, 5B, bpym, $J = 4.73$ and 5.56 Hz), 8.15 (t, 1H, 4'T, terpy, $J = 8.16$ Hz), 8.28 (m, 2H, 3T, terpy), 8.40 (d, 2H, 3'T, terpy, $J = 8.16$ Hz), 8.76 (dd, 1H, 6'B, bpym, $J = 4.42$ and 2.05 Hz), 9.20 (dd, 1H, 4B, bpym, $J = 4.50$ and 2.13 Hz), 10.16 (dd, 1H, 6B, bpym, $J = 5.64$ and 2.13 Hz).

IR (KBr): 1342 cm^{-1} ($\nu_{\text{NO}_2\text{asym}}$) and 1286 cm^{-1} ($\nu_{\text{NO}_2\text{sym}}$).

UV/VIS (CH_3CN): $\lambda_{\text{max}}/\text{nm}$ ($\epsilon/\text{M}^{-1}\cdot\text{cm}^{-1}$) = $238(26900)$, $264(23280)$, $308(25600)$, 330sh $362(6100)$, $470(6500)$.

[Ru(NO)(bpym)(terpy)](PF₆)₃

10 mL of 3 M HCl were added slowly to 100 mg of [Ru(NO₂)(bpym)(terpy)](PF₆) with constant stirring which continued for 15 minutes. The deep red colour of the solution changed to yellow-brown. A saturated solution of NH₄PF₆ (10 mL) was added to the mixture and 10 mL of more water were added to complete the precipitation. A light yellow solid was filtered from the orange solution and washed with ice-cold water. The analytically pure compound was obtained by dissolving the solid in a minimum volume of CH₃CN, followed by precipitation with diethylether. Single crystals were grown by slow diffusion of dichloromethane into an acetonitrile solution at room temperature.

Yield: 134 mg (0.140 mmol, 96%).

Elemental analysis: C₂₃H₁₇F₁₈N₈OP₃Ru (957.42 g/mol).

Calculated:	C: 28.85%	H: 1.79%	N: 11.70%
Found:	C: 28.82%	H: 1.83%	N: 11.79%

^1H NMR (acetone- d_6): δ/ppm = 7.80 (dd, 1H, J = 4.80 and 6.02 Hz), 7.85 (m, 2H), 8.22 (dd, 1H, J = 4.73 and 5.79 Hz), 8.60 (m, 5H), 9.02 (d, 2H, 8.08Hz), 9.19 (m, 3H), 9.39 (dd, 1H, J = 4.50 and 1.83 Hz), 9.79 (dd, 1H, J = 4.73 and 2.03 Hz), 10.32 (dd, 1H, J = 5.72 and 1.90 Hz).

^1H NMR (CD_3CN): δ/ppm = 7.54 (dd, 1H, 5'B, bpym, J = 5.87 and 1.90 Hz), 7.69 (dd, 1H, 4'B, bpym, J = 5.64 and 4.80 Hz), 7.76 (m, 2H, 5T, terpy), 8.16 (m, 2H, 6T, terpy), 8.42 (dd, 1H, 5B, bpym, J = 4.80 and 5.57 Hz), 8.50 (dt, 2H, 4T, terpy, $J(3)$ = 7.93 and $J(2)$ = 1.44 Hz), 8.73 (m, 2H, 3T, terpy), 8.88 (d, 2H, 3'T, terpy J = 7.78 Hz), 9.00 (t, 1H, 4'T, terpy, J = 7.78 Hz), 9.30 (dd, 1H, 6'B, bpym, J = 4.65 and 1.90 Hz), 9.66 (dd, 1H, 4B, bpym, J = 5.72 and 1.90 Hz), 9.71 (dd, 1H, 6B, bpym, J = 4.80 and 1.90 Hz).

IR (KBr): 1957 cm^{-1} (ν_{NO}), 835 cm^{-1} (ν_{PF_6}) and 558 cm^{-1} ($\nu_{\text{Ru-N-O}}$).

UV/VIS (CH_3CN): $\lambda_{\text{max}}/\text{nm}$ ($\epsilon/\text{M}^{-1}\cdot\text{cm}^{-1}$) = 265(10800), 291(8930), 312sh, 331sh, 362(5120).

[Ru(CH_3CN)(bpym)(terpy)](PF_6)₂

Attempts to recrystallise [Ru(NO)(bpym)(terpy)](PF_6)₃ in methanol/acetonitrile (1/1, v/v) mixture yielded the crystals of [Ru(CH_3CN)(bpym)(terpy)](PF_6)₂ which were analysed by single crystal X-ray crystallography, ^1H NMR and elemental analysis.

Elemental analysis: $\text{C}_{25}\text{H}_{20}\text{F}_{12}\text{N}_8\text{P}_2\text{Ru}$ (823.50 g/mol).

Calculated: C: 26.46% H: 2.45% N: 13.61%

Found: C: 36.42% H: 2.49% N: 13.55%

^1H NMR (CD_3CN): δ/ppm = 7.23 (dd, 1H, 5'B, bpym, J = 5.79 and 6.02 Hz), 7.40 (m, 2H, 5T, terpy), 7.64 (dd, 1H, 4'B, bpym, 5.72 and 2.05 Hz), 7.83 (m, 2H, 6T, terpy), 8.06 (dt, 2H, 4T, terpy, $J(3)$ = 7.86 and $J(2)$ = 1.53 Hz), 8.10 (dd, 1H, 5B, bpym, J = 6.02 and 4.82 Hz), 8.37 (t, 1H, 4'T, terpy, 8.10 Hz), 8.45 (m, 2H, 3T, terpy), 8.59 (d,

2H, 3'T, terpy, 8.15 Hz.), 8.87 (dd, 1H, 6'B, bpym, $J = 4.73$ and 2.04 Hz), 9.40 (dd, 1H, 4B, bpym, $J = 4.73$ and 2.04 Hz), 9.85 (dd, 1H, 6B, bpym, $J = 5.72$ and 2.05 Hz).

{{ μ -bpym}[RuCl(terpy)]₂}(PF₆)₂

Amounts of 100 mg (0.227 mmol) Ru(terpy)Cl₃ and of 15 mg (0.0908 mmol) bpym were heated to reflux for 12 hours in 40 mL 1:1 ethanol and water mixture under an argon atmosphere. After one hour, the colour of reaction mixture was reddish brown which turned into dark green after 12 hours. The resulting green mixture was cooled to room temperature and filtered. A concentrated solution of NH₄PF₆ (10 mL) was added to the filtrate. A dark green solid was filtered and purified by adding 50 mL of dichloromethane, in which mononuclear impurities are soluble. This treatment was repeated three times to obtain analytical pure material. ¹H NMR spectroscopy of the pure compound shows the presence of both isomers (*syn/anti*: 5/4) in acetonitrile solution.

Yield: 65 mg (0.055 mmol, 58%).

Elemental analysis: C₃₈H₂₈Cl₂F₁₂ N₁₀P₂Ru₂ (1187.69 g/mol).

Calculated: C: 38.43% H: 2.38% N: 11.69%

Found: C: 36.26% H: 2.66% N: 11.19%

¹H NMR (CD₃CN): δ (in ppm, assignment of the peaks was done with the help of 2D ¹H-¹H COSY NMR, see Chap. 5).

syn isomer = 6.58 (t, 1H, 5'B, bpym, $J = 5.68$ Hz), 7.37 (d, 2H, 4'B and 6'B, bpym, $J = 5.64$ Hz), 7.43 (m, 4H, 5T, terpy), 7.93 (dt, 4H, 4T, terpy, $J(3) = 7.70$ and $J(2) = 1.44$ Hz), 8.05 (m, 4H, 6T, terpy), 8.17 (t, 2H, 4'T, terpy, $J = 8.12$ Hz), 8.37 (m, 4H, 3T, terpy), 8.49 (d, 4H, 3'T, $J = 8.16$ Hz, terpy), 8.55 (t, 1H, 5B, bpym, $J = 5.60$ Hz), 10.44 (d, 2H, 4B and 6B, bpym, $J = 5.64$ Hz).

anti isomer = 7.20 (m, 4H, 5T, terpy), 7.53(t, 2H, 5B and 5'B, bpym, $J = 5.66$ Hz), 7.69 (m, 4H, 6T, terpy), 7.95 (dd, 2H, 4'B and 6B, bpym, $J = 5.72$ and 1.51 Hz), 8.01

(m, 4H, 4T, terpy), 8.25 (t, 2H, 4'T, terpy, $J = 8.04$ Hz), 8.46 (m, 4H, 3T, terpy), 8.60 (d, 4H, 3'T, terpy, $J = 8.16$ Hz), 9.86 (dd, 2H, 6'B and 4B, bpym, $J = 5.57$ and 1.51 Hz).

The positive ion electrospray mass spectrum in acetonitrile showed the molecular ion peak centred at $m/z = 1043.0$, corresponding to $\{[(\mu\text{-bpym})[\text{RuCl}(\text{terpy})]_2](\text{PF}_6)_2 - \text{PF}_6\}^+$; calculated molecular mass: 1042.96 g/mol.

UV/VIS (CH_3CN): $\lambda_{\text{max}}/\text{nm}$ ($\epsilon/\text{M}^{-1}\cdot\text{cm}^{-1}$) = 243(16470), 268(18530), 310(19370), 404(11500), 460(11240), 628(7100).

$\{[(\mu\text{-bpym})[\text{Ru}(\text{NO}_2)(\text{terpy})]_2](\text{PF}_6)_2$

An amount of 100 mg (0.0841 mmol) $\{[(\mu\text{-bpym})[\text{RuCl}(\text{terpy})]_2](\text{PF}_6)_2$ was dissolved in 10 mL of acetonitrile and 800 mg (11.594 mmol) of NaNO_2 and 20 mL of H_2O were added to solution. The mixture was heated to reflux for 18 hours under an argon atmosphere. The resulting dark red mixture was filtered hot and the filtrate was cooled to room temperature. A concentrated solution of NH_4PF_6 (5 mL) was added to it. The brownish red solid was filtered and purified by adding dichloromethane where mononuclear impurities are soluble. This treatment was repeated three times to isolate analytically pure material. ^1H NMR spectroscopy of the pure compound showed the presence of both isomer (*syn/anti*: 5/4) in acetonitrile solution.

Yield: 85 mg (0.0703 mmol, 83%).

Elemental analysis: $\text{C}_{38}\text{H}_{28}\text{F}_{12}\text{N}_{12}\text{O}_4\text{P}_2\text{Ru}_2$ (1208.8 g/mol).

Calculated:	C: 37.76%	H: 2.33%	N: 13.90%
Found:	C: 36.91%	H: 2.33%	N: 14.24%

^1H NMR (CD_3CN): δ (in ppm, assignment of the peaks was done with the help of 2D ^1H - ^1H COSY NMR, see Chap. 5).

syn isomer = 6.81 (t, 1H, 5'B, bpym, J = 5.60 Hz), 7.44 (m, 4H, 5T, terpy), 7.50 (d, 2H, 4' B and 6'B, bpym, J = 5.64 Hz), 8.01 (dt, 4H, 4T, terpy, J(3) = 8.05 and J(2) = 1.52 Hz), 8.11 (m, 4H, 6T, terpy), 8.26 (t, 2H, 4'T, terpy, J = 8.16 Hz), 8.35 (m, 4H, 3T, terpy), 8.48 (d, 4H, 3'T, terpy, J = 8.08 Hz), 8.58 (t, 1H, 5B, bpym, J = 5.68 Hz), 10.52 (d, 2H, 4B and 6B, bpym, J = 5.72 Hz).

anti isomer = 7.32 (m, 4H, 5T, terpy), 7.69 (t, 2H, 5B and 5'B, bpym, J = 5.66 Hz), 7.78 (m, 4H, 6T, terpy), 7.98 (dd, 2H, 4'B and 6B, bpym, J = 5.64 and 1.60 Hz), 8.08 (m, 4H, 4T, terpy), 8.37 (t, 2H, 4'T, terpy, J = 7.78 Hz), 8.46 (m, 4H, 3T, terpy), 8.61 (d, 4H, 3'T, terpy, J = 8.09 Hz), 10.08 (dd, 2H, 6'B and 4B, bpym, J = 5.72 and 1.62 Hz).

The positive ion electrospray mass spectrum in acetonitrile showed the molecular ion peak centred at $m/z = 1065.0$, corresponding to $[(\mu\text{-bpym})[\text{Ru}(\text{NO}_2)(\text{terpy})]_2](\text{PF}_6)_2 - \text{PF}_6]^+$; calculated molecular mass: 1065.01 g/mol.

IR (solid): 1342 cm^{-1} ($\nu_{\text{NO}_2\text{asym}}$) and 1286 cm^{-1} ($\nu_{\text{NO}_2\text{sym}}$).

UV/VIS (CH_3CN): $\lambda_{\text{max}}/\text{nm}$ ($\epsilon/\text{M}^{-1}\cdot\text{cm}^{-1}$) = 240(29470), 270(32790), 304(35720), 325sh, 390(17820), 450sh, 552(8900), 594(8850).

***syn*- $\{(\mu\text{-bpym-(4-OH)})[\text{Ru}(\text{NO})(\text{terpy})]_2\}(\text{PF}_6)_5$**

100 mg of $\{(\mu\text{-bpym})[\text{Ru}(\text{NO}_2)(\text{terpy})]_2\}(\text{PF}_6)_2$ was dissolved in 20 mL of 6 M HCl and stirred for 2 hours till the colour of the solution changed to deep red. A concentrated solution of NH_4PF_6 (10 mL) was added. The analytically pure reddish brown product was filtered from orange-yellow solution and analysed by elemental analysis. The filtrate (orange-yellow) was kept for slow crystallisation. Brown crystals had grown after 5 hours which were analysed by X-ray crystallography.

Yield: 121 mg (0.0745 mmol, 90%).

Elemental analysis: $\text{C}_{38}\text{H}_{29}\text{F}_{30}\text{N}_{12}\text{O}_3\text{P}_5\text{Ru}_2$ (1628.72 g/mol).

Calculated:	C: 28.02%	H: 1.79%	N: 10.32%
Found:	C: 27.88%	H: 2.01%	N: 10.54%

IR (solid): 3440 cm^{-1} (ν_{OH}), 1946 cm^{-1} (ν_{NO}), 830 cm^{-1} (ν_{PF_6}) and 558 cm^{-1} ($\nu_{\text{Ru-N-O}}$).

The ^1H NMR spectrum observed after dissolution in CD_3CN shows the presence of mononuclear species indicating that the compound is unstable in acetonitrile solution. The complex is insoluble in dichloromethane or chloroform.

6.5. Crystallography

Crystallographic data collection was carried out by Dr. F. Lissner and Priv. Doz. Dr. M. Niemeyer. Structure solving was carried out by Dr. F. Lissner, Priv. Doz. Dr. M. Niemeyer and Prof. Dr. C. -Y. Su.

Suitable crystals were selected under a cover of viscous hydrocarbon oil (Paratone N, Exxon), attached to a glass fiber, and instantly placed in a low-temperature N_2 -stream.^[185] The crystals were sealed in capillaries for the measurements. Data collection for compounds $[\text{Ru}(\text{TPP})(\text{NO})(\text{H}_2\text{O})]\text{BF}_4 \times 2\text{H}_2\text{O}$, $[\text{Ru}(\text{NO}_2)(\text{bpym})(\text{terpy})](\text{PF}_6)$, and $[\text{Ru}(\text{CH}_3\text{CN})(\text{bpym})(\text{terpy})](\text{PF}_6)_2$ was performed at 173 K on a Siemens P4 four-circle diffractometer with graphite-monochromatised $\text{Mo-K}\alpha$ radiation ($\lambda = 0.71073 \text{ \AA}$), using the ω - 2θ scan technique. Data for compounds $(\text{PPh}_4)_2[\text{Cl}_5\text{Os}(\text{NO})] \times 4\text{CH}_3\text{CN}$, $[\text{Ru}(\text{NO})(\text{bpym})(\text{terpy})](\text{PF}_6)_3$, and *syn*- $\{(\mu\text{-bpym-(4-OH)})[\text{Ru}(\text{NO})(\text{terpy})]_2\}(\text{PF}_6)_5 \times 2.5\text{H}_2\text{O}$ were collected at 100 K on a BRUKER NONIUS Kappa-CCD with graphite-monochromatised $\text{Mo-K}\alpha$ radiation ($\lambda = 0.71073 \text{ \AA}$).

Calculations were performed with the programme SHELXTL PC 5.03^[186] and SHELXL-97^[187] program systems installed on a local PC. The structures were solved by direct methods (SHELXS)^[188] and refined on F_o^2 by full-matrix least-squares refinement (SHELXTL)^[189]. Absorption corrections were applied using semiempirical ψ -scans or numerically using the programme HABITUS.^[190] All non-hydrogen atoms

were refined anisotropically, hydrogen atoms were introduced at appropriate positions. The graphical representation was done using the program DIAMOND.^[191]

Crystallographic parameters:

GOF = $\{\sum w(|F_o|^2 - |F_c|^2)^2 / (n - m)\}^{1/2}$ where n = number of data and m = number of variables

$$R = (\sum ||F_o| - |F_c||) / \sum |F_o|$$

$$wR = \{\sum [w(|F_o|^2 - |F_c|^2)^2] / \sum [w(F_o^4)]\}^{1/2}$$

The crystallographic data and refinement parameter for all the structures are listed in Tables 6.5.1-6.5.6

6.5.1 (PPh₄)₂[Cl₅Os(NO)]×4CH₃CN

Brown plates for X-ray diffraction were obtained by recrystallisation from solution in acetonitrile.

Table 6.5.1. Crystallographic data and refinement parameters for (PPh₄)₂[Cl₅Os(NO)]×4CH₃CN

formula	C ₅₆ H ₅₂ Cl ₅ N ₅ OOSp ₂
molecular mass (gmol ⁻¹)	1240.42
T (K)	100(2)
wavelength (Å)	0.71073
colour, habit	brown, plate
crystal size (mm)	0.60 × 0.35 × 0.15
crystal system	monoclinic
space group	<i>P</i> 2 ₁ / <i>c</i> (no. 14)
<i>a</i> (Å)	9.5056(1)
<i>b</i> (Å)	19.4011(2)
<i>c</i> (Å)	14.8581(2)
<i>α</i> (deg)	90

β (deg)	98.262(6)
γ (deg)	90
V (Å ³)	2711.68(5)
Z	2
$\rho_{\text{calc.}}$ (g/cm ³)	1.519
μ (mm ⁻¹)	2.701
θ range (deg)	2.96-28.29
collected data	59742
unique data/ R_{int}	6695/0.0602
data with $I > 2\sigma(I)$ (N_o)	6160
number of parameters (N_p)	359
$R1, wR2$ (for $I > 2\sigma$)	0.0183, 0.0536
$R1, wR2$ (for all data)	0.0211, 0.0548
GOF	1.581
largest residual density (e ⁻ /Å ³)	0.440/-1.192

6.5.2. [Ru(TPP)(NO)(H₂O)]BF₄×2H₂O

Dark red plates suitable for single-crystal X-ray diffraction were obtained slow diffusion of hexane in dichloromethane solution at -4 °C.

Table 6.5.2. Crystallographic data and refinement parameters for [Ru(TPP)(NO)(H₂O)]BF₄×2H₂O

formula	C ₄₄ H ₃₀ BF ₄ N ₅ O ₄ Ru
molecular mass (g mol ⁻¹)	880.61
T (K)	173(2)
wavelength (Å)	0.71073
colour, habit	dark red, plate
crystal size (mm)	0.55 × 0.50 × 0.15
crystal system	monoclinic
space group	$P2_1/n$ (no. 14)

a (Å)	15.558(3)
b (Å)	15.255(3)
c (Å)	17.567(3)
α (deg)	90
β (deg)	93.355(14)
γ (deg)	90
V (Å ³)	4162.3(12)
Z	4
$\rho_{\text{calc.}}$ (g/cm ³)	1.405
μ (mm ⁻¹)	0.443
θ range (deg)	2.16-26.51
collected data	8952
unique data/ R_{int}	8632/0.0288
data with $I > 2\sigma(I)$ (N_o)	6155
number of parameters (N_p)	569
$R1, wR2$ (for $I > 2\sigma$)	0.0437, 0.1151
$R1, wR2$ (for all data)	0.0645, 0.1205
GOF	0.972
largest residual density (e ⁻ /Å ³)	0.999/-0.902

6.5.3 [Ru(NO₂)(bpym)(terpy)](PF₆)

Red needles suitable for single-crystal X-ray diffraction were obtained by vapour diffusion of diethylether in acetonitrile solution at room temperature.

Table 6.5.3. Crystallographic data and refinement parameters for [Ru(NO₂)(bpym)(terpy)](PF₆)

formula	C ₂₃ H ₁₇ F ₆ N ₈ O ₂ PRu
molecular mass (gmol ⁻¹)	683.49
T (K)	173(2)
wavelength (Å)	0.71073

colour, habit	red, needle
crystal size (mm)	0.65 × 0.12 × 0.06
crystal system	monoclinic
space group	$P2_1/n$ (no. 14)
a (Å)	8.9165(17)
b (Å)	15.8829(19)
c (Å)	19.321(3)
α (deg)	90
β (deg)	95.216(15)
γ (deg)	90
V (Å ³)	2724.9(7)
Z	4
$\rho_{\text{calc.}}$ (g/cm ³)	1.666
μ (mm ⁻¹)	0.713
θ range (deg)	2.12-26.00
collected data	5651
unique data/ R_{int}	5303/0.0563
data with $I > 2\sigma(I)$ (N_o)	2898
number of parameters (N_p)	371
$R1, wR2$ (for $I > 2\sigma$)	0.0534, 0.1201
$R1, wR2$ (for all data)	0.1053, 0.1316
GOF	0.827
largest residual density (e ⁻ /Å ³)	0.98/-1.17

6.5.4 [Ru(NO)(bpym)(terpy)](PF₆)₃

Yellow rods suitable for single-crystal X-ray diffraction were obtained by vapour diffusion of dichloromethane in acetonitrile solution at room temperature.

Table 6.5.4. Crystallographic data and refinement parameters for [Ru(NO)(bpym)(terpy)](PF₆)₃

formula	C ₂₃ H ₁₇ F ₁₈ N ₈ OP ₃ Ru
molecular mass (g mol ⁻¹)	957.43
<i>T</i> (K)	100(2)
wavelength (Å)	0.71073
colour, habit	yellow, rod
crystal size (mm)	0.3 × 0.05 × 0.05
crystal system	orthorhombic
space group	<i>Pbca</i> (no. 61)
<i>a</i> (Å)	14.7169(2)
<i>b</i> (Å)	17.8342(2)
<i>c</i> (Å)	23.8615(2)
<i>α</i> (deg)	90
<i>β</i> (deg)	90.00
<i>γ</i> (deg)	90
<i>V</i> (Å ³)	6262.79(12)
<i>Z</i>	8
$\rho_{\text{calc.}}$ (g/cm ³)	2.031
μ (mm ⁻¹)	0.800
θ range (deg)	3.69-28.28
collected data	57209
unique data/ <i>R</i> _{int}	7661/0.1767
data with <i>I</i> > 2 σ (<i>I</i>) (<i>N</i> _o)	5474
number of parameters (<i>N</i> _p)	487
<i>R</i> ₁ , <i>wR</i> ₂ (for <i>I</i> > 2 σ)	0.0868, 0.1241
<i>R</i> ₁ , <i>wR</i> ₂ (for all data)	0.1383, 0.1367
GOF	1.189
largest residual density (e ⁻ /Å ³)	0.87/-1.11

6.5.5 [Ru(CH₃CN)(bpym)(terpy)](PF₆)₂

Red needles suitable for single-crystal X-ray diffraction were obtained by recrystallisation of [Ru(NO)(bpym)(terpy)](PF₆)₃ from methanol/acetonitrile (1/1, v/v) mixture.

Table 6.5.5. Crystallographic data and refinement parameters for [Ru(CH₃CN)(bpym)(terpy)](PF₆)₂

formula	C ₂₅ H ₂₀ F ₁₂ N ₈ P ₂ Ru
molecular mass (g mol ⁻¹)	823.50
<i>T</i> (K)	173(2)
wavelength (Å)	0.71073
colour, habit	red, needle
crystal size (mm)	0.50×0.12×0.12
crystal system	monoclinic
space group	<i>P</i> 2 ₁ / <i>n</i> (no. 14)
<i>a</i> (Å)	10.532(2)
<i>b</i> (Å)	12.828(3)
<i>c</i> (Å)	23.516(5)
<i>α</i> (deg)	90
<i>β</i> (deg)	94.148(13)
<i>γ</i> (deg)	90
<i>V</i> (Å ³)	3168.7(12)
<i>Z</i>	4
<i>ρ</i> _{calc.} (g/cm ³)	1.726
<i>μ</i> (mm ⁻¹)	0.699
<i>θ</i> range (deg)	2.07-27.01
collected data	7278
unique data/ <i>R</i> _{int}	6905/0.0525
data with <i>I</i> > 2σ(<i>I</i>) (<i>N</i> _o)	3364
number of parameters (<i>N</i> _p)	434
<i>R</i> ₁ , <i>wR</i> ₂ (for <i>I</i> > 2σ)	0.0763, 0.1759

R1, wR2 (for all data)	0.1737, 0.2232
GOF	1.003
largest residual density ($e^{-}/\text{\AA}^3$)	0.95/-0.72

6.5.6 *syn*- $\{(\mu\text{-bpym-(4-OH)})[\text{Ru}(\text{NO})(\text{terpy})]_2\}(\text{PF}_6)_5 \times 2.5\text{H}_2\text{O}$

Light brown plates for X-ray diffraction were obtained by slow recrystallisation from solution in H_2O and HCl .

Table 6.5.6. Crystallographic data and refinement parameters for $[(\mu\text{-bpym-OH})\{\text{Ru}(\text{tpy})(\text{NO})\}_2](\text{PF}_6)_5 \times 2.5\text{H}_2\text{O}$

formula	$\text{C}_{76}\text{H}_{68}\text{F}_{60}\text{N}_{24}\text{O}_{11}\text{P}_{10}\text{Ru}_4$
molecular mass (g mol^{-1})	3347.52
T (K)	100(2)
wavelength (\AA)	0.71073
colour, habit	light brown, plate
crystal size (mm)	0.32 \times 0.28 \times 0.20
crystal system	monoclinic
space group	$P2_1/n$ (no. 14)
a (\AA)	10.9387(2)
b (\AA)	26.0442(6)
c (\AA)	19.3827(4)
α (deg)	90
β (deg)	98.3190(10)
γ (deg)	90
V (\AA^3)	5463.8(2)
Z	2
$\rho_{\text{calc.}}$ (g/cm^3)	2.035
μ (mm^{-1})	0.860
θ range (deg)	1.89-26.25
collected data	72690

unique data/ R_{int}	10983/0.2026
data with $I > 2\sigma(I)$ (N_o)	7316
number of parameters (N_p)	839
R1, wR2 (for $I > 2\sigma$)	0.0979, 0.1945
R1, wR2 (for all data)	0.1495, 0.2181
GOF	1.044
largest residual density ($e^-/\text{\AA}^3$)	1.604/-0.856

CHAPTER 7

Summary

In this thesis, various transition metal complexes of the "non-innocent" nitrosyl ligand (Scheme 7.1) were studied with respect to their synthetic, structural and electronic structural aspects using a number of spectroscopic techniques. The reactivity of coordinated nitric oxide and electron transfer occurring in metal nitrosyl complexes were investigated varying metal and coligand environment.



Scheme 7.1. Redox alternatives of the nitrosyl ligand, making it a potentially "non-innocent" ligand.

In Chapter 2, experimental and computational results for the two-step redox system $[\text{Cl}_5\text{Os}(\text{NO})]^{n-}$ ($n = 1-3$) are discussed in comparison to the related one-step redox systems $[\text{Cl}_5\text{Ru}(\text{NO})]^{n-}$ and $[\text{Cl}_5\text{Ir}(\text{NO})]^{n-}$ ($n = 1, 2$). The osmium system exhibits remarkably low oxidation and reduction potentials. The structure of the precursor $(\text{PPh}_4)_2[\text{Cl}_5\text{Os}(\text{NO})]$ is established as an $\{\text{MNO}\}^6$ species^[2] with almost linear OsNO arrangement at $178.5(8)^\circ$ (Figure 7.1).

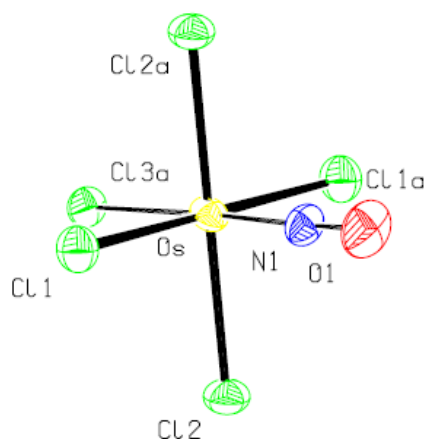


Figure 7.1. Molecular structure of the dianion in the crystal of $(\text{Ph}_4\text{P})_2[\text{Cl}_5\text{Os}(\text{NO})] \cdot 4\text{CH}_3\text{CN}$ at 100 K.

DFT Calculations confirm this result, and a comparison of structures calculated for several oxidation states reveals an increased labilisation of the *trans*-positioned M–Cl bond on reduction in the order $M = \text{Ir} < \text{Os} < \text{Ru}$. Accordingly, the intact reduced form $[\text{Cl}_5\text{Os}(\text{NO})]^{3-}$ could not be observed in fluid solution even on electrolysis at $-70\text{ }^\circ\text{C}$ in *n*-butyronitrile solution, as confirmed both by DFT calculations and by comparison with the EPR and IR spectroelectrochemically characterised redox pairs *cis*- $[(\text{bpy})_2\text{ClOs}(\text{NO})]^{2+/+}$ and $[(\text{CN})_5\text{Os}(\text{NO})]^{2-/3-}$. The DFT calculations indicate that the oxidation of $[\text{Cl}_5\text{Os}(\text{NO})]^{2-}$ occurs largely on the metal, the HOMO of the $[\text{Cl}_5\text{Os}(\text{NO})]^{2-}$ being composed of Os 5d (58%) and Cl_{eq} 3p orbitals (41%). As for the related $[(\text{CN})_5\text{Os}(\text{NO})]^{2-}$, the reduction is largely NO-centred, the LUMO of $[\text{Cl}_5\text{Os}(\text{NO})]^{2-}$ has 61% $\pi^*(\text{NO})$ character with significant 5d Os contributions (34%) (Figure 7.2).

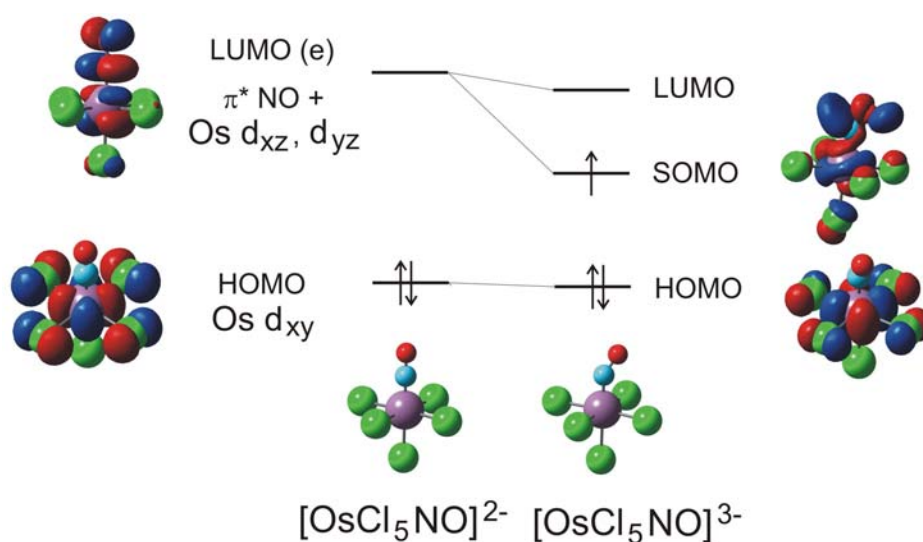
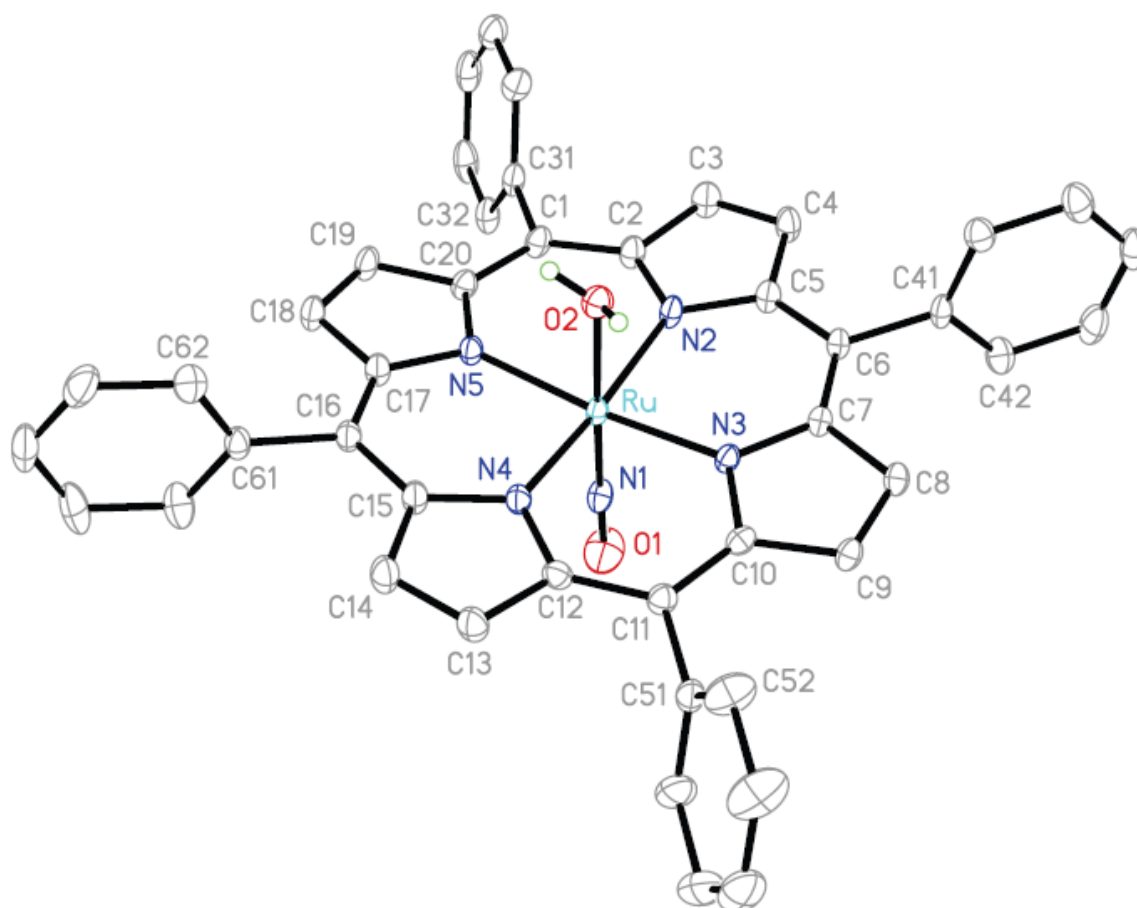


Figure 7.2. Representation of HOMO/LUMO in $[\text{Cl}_5\text{Os}(\text{NO})]^{2-}$ and $[\text{Cl}_5\text{Os}(\text{NO})]^{3-}$.

Detailed analyses of the conformational dependence of the *g* anisotropy suggest that the different reduced species reported previously^[42,43] for $[\text{Cl}_5\text{Os}(\text{NO})]^{3-}$ in AgCl matrix may be distinct in terms of eclipsed or staggered conformations of the bent NO^\bullet axial ligand relative to the $\text{Os}^{\text{II}}\text{Cl}_4$ equatorial plane. The staggered form is calculated to be more stable by 105 cm^{-1} . The weak absorptions of $[\text{Cl}_5\text{Os}(\text{NO})]^{2-}$ at 573, 495 and 437 nm are assigned as metal-to-ligand charge transfer and ligand-to-ligand charge transfer (MLCT/LLCT) transitions to the doubly degenerate $\pi^*(\text{NO})$ LUMO. The oxidised form $[\text{Cl}_5\text{Os}(\text{NO})]^-$ contains Os^{III} in an $\{\text{OsNO}\}^5$ configuration

with a spin density of 0.711 on Os. In all three states of $[\text{Cl}_5\text{Os}(\text{NO})]^{n-}$ the N bonded form is vastly preferred over the NO-side-on bonded alternative.

In Chapter 3, extensive experimental and theoretical studies of ruthenium nitrosyl tetraphenylporphyrin complexes $[(\text{TPP})\text{Ru}(\text{NO})(\text{X})]\text{BF}_4$, TPP = tetraphenylporphyrin, X = H_2O , pyridine, 4-cyanopyridine and 4-N,N-dimethylaminopyridine, are described. The effect of axial ligands on the redox properties of ruthenium nitrosyl porphyrin complexes has been investigated by means of electrochemical and various spectroelectrochemical methods. The structure of $[(\text{TPP})\text{Ru}(\text{NO})(\text{H}_2\text{O})]\text{BF}_4$ is established as an $\{\text{MNO}\}^6$ species^[2] with almost linear RuNO arrangement at $178.1(3)^\circ$ (Figure 7.3).



The compound $[(\text{TPP})\text{Ru}(\text{NO})(\text{H}_2\text{O})]\text{BF}_4$ undergoes two one-electron oxidation processes in cyclic voltammetry. Spectroelectrochemical measurements (IR, UV/VIS/NIR and EPR) indicate that the first oxidation occurs on the porphyrin ring as evident from the appearance of diagnostic porphyrin radical anion vibrational bands at 1290 cm^{-1} , from the small shift of ν_{NO} ($\sim 20\text{ cm}^{-1}$) and from the observation of an EPR signal at $g_{\text{iso}} \approx 2.00$ and a line width of $\sim 25\text{ G}$. The second oxidation is irreversible in the spectroelectrochemical measurements. The compounds $[(\text{TPP})\text{Ru}(\text{NO})(\text{X})]\text{BF}_4$, $\text{X} =$ pyridine, 4-cyanopyridine and 4-N,N-dimethylaminopyridine, undergo a reversible one-electron reduction, the site of which was determined by spectroelectrochemical studies as NO-centred ($\sim 300\text{ cm}^{-1}$ shift of ν_{NO}). The EPR response was essentially unaffected by the variation of the substituted pyridine X. The DFT calculations support the experimental results as the HOMO of $[(\text{TPP})\text{Ru}(\text{NO})(\text{H}_2\text{O})]^+$ was calculated to be composed of mainly porphyrin orbitals (98%) whereas the LUMO of $[(\text{TPP})\text{Ru}(\text{NO})(\text{X})]^+$, $\text{X} =$ pyridine, has 53% $\pi^*(\text{NO})$ character with significant 4d Ru (17%) and porphyrin contributions (25%), confirming that the oxidation of $[(\text{TPP})\text{Ru}(\text{NO})(\text{H}_2\text{O})]^+$ occurs on the porphyrin ring while the reduction of $[(\text{TPP})\text{Ru}(\text{NO})(\text{X})]^+$ $\text{X} =$ pyridine, is largely NO-centred with little but non-negligible contribution from X (4%).

In Chapter 4, ruthenium mononuclear complexes with the π acceptor ligands 2,2'-bipyrimidine (bpym) and 2,2':6',2''-terpyridine (terpy) are studied. The structurally characterised precursor $[\text{Ru}(\text{NO}_2)(\text{bpym})(\text{terpy})](\text{PF}_6)$ shows bpym-centred reduction and metal-centred oxidation as evident from EPR spectroscopy. The compound $[\text{Ru}(\text{NO})(\text{bpym})(\text{terpy})](\text{PF}_6)_3$, with a $\{\text{RuNO}\}^6$ configuration^[2] (angle Ru–N–O = $175.2(4)^\circ$; Figure 7.4) was obtained from $[\text{Ru}(\text{NO}_2)(\text{bpym})(\text{terpy})](\text{PF}_6)$ by acidification. The relatively labile $[\text{Ru}(\text{NO})(\text{bpym})(\text{terpy})]^{3+}$ forms a structurally characterised acetonitrile substitution product $[\text{Ru}(\text{CH}_3\text{CN})(\text{bpym})(\text{terpy})](\text{PF}_6)_2$ on treatment with $\text{CH}_3\text{OH}/\text{CH}_3\text{CN}$.

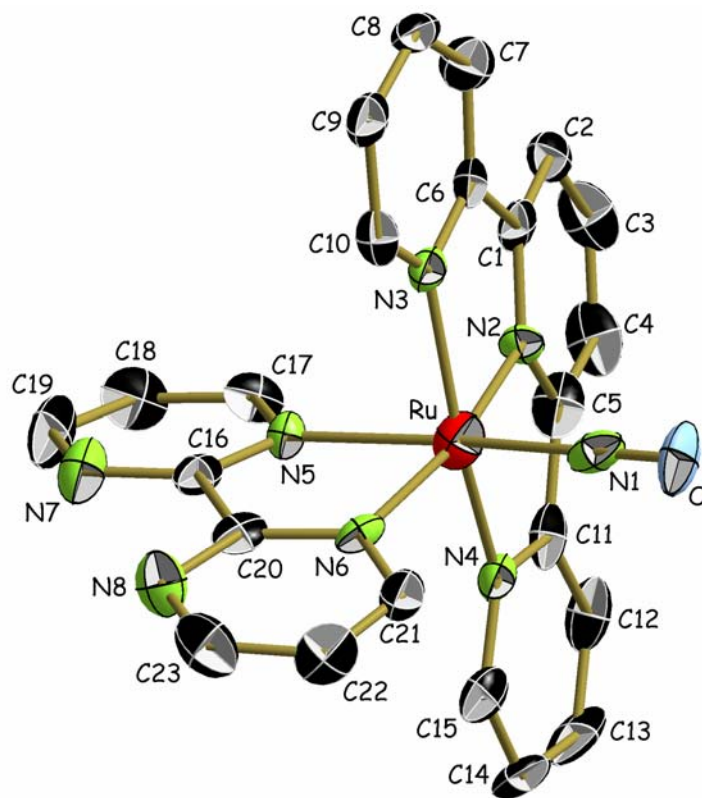


Figure 7.4. Molecular structure of the trication of $[\text{Ru}(\text{NO})(\text{bpym})(\text{terpy})](\text{PF}_6)_3$ in the crystal.

The compound $[\text{Ru}(\text{NO})(\text{bpym})(\text{terpy})](\text{PF}_6)_3$ is electrochemically reduced in three one-electron steps of which the third, leading to neutral $[\text{Ru}(\text{NO})(\text{bpym})(\text{terpy})]$, involves electrode adsorption. The first two reduction processes cause shifts of $\nu(\text{NO})$ from 1957 via 1665 to 1388 cm^{-1} (Figure 7.5), implying predominantly NO-centred electron addition.

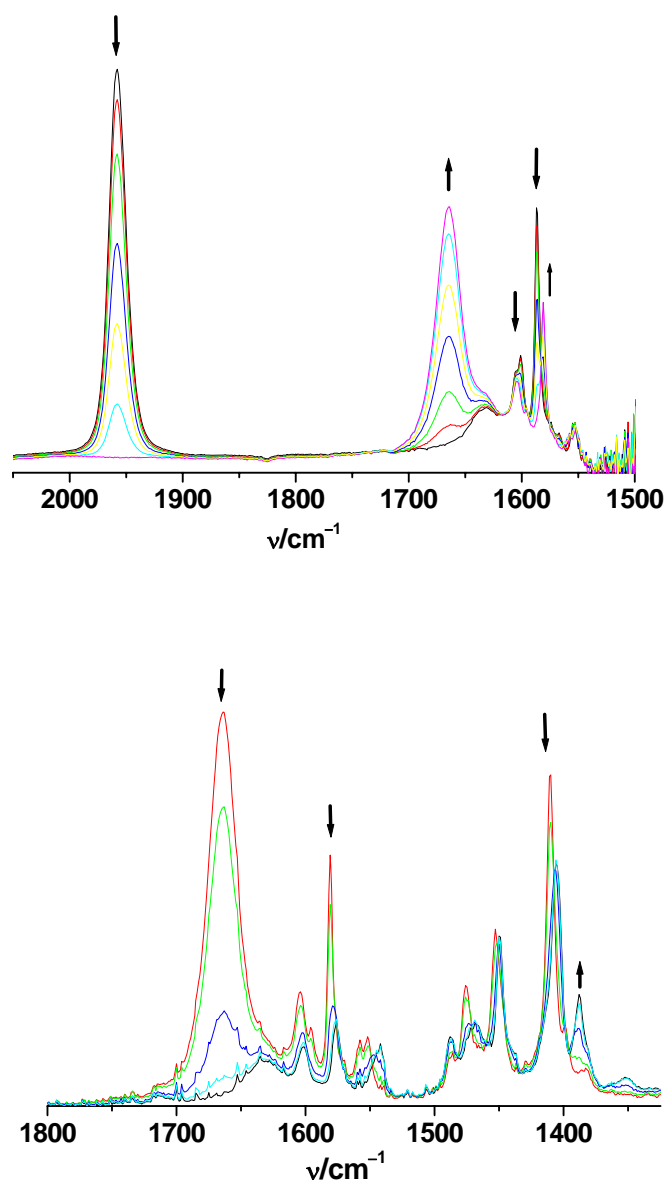


Figure 7.5. IR spectroelectrochemical response of $[\text{Ru}(\text{NO})(\text{bpym})(\text{terpy})](\text{PF}_6)_3$ in $\text{CD}_3\text{CN}/0.1 \text{ M } n\text{-Bu}_4\text{NPF}_6$ at 298 K: first (top) and second reduction step (bottom).

UV/VIS/NIR spectroscopy shows long-wavelength ligand-to-ligand charge transfer absorptions for $[\text{Ru}^{\text{II}}(\text{NO}^-)(\text{bpym})(\text{terpy})]^+$ in the visible, while the paramagnetic intermediate $[\text{Ru}(\text{NO})(\text{bpym})(\text{terpy})]^{2+}$ exhibits no distinct absorption maximum above 309 nm. EPR spectroscopy of the latter at 9.5, 95 and 190 GHz (Figure 7.6) shows the typical invariant pattern of the $\{\text{RuNO}\}^7$ configuration,^[2] however, the high-frequency measurements at 4 and 10 K reveal a splitting of the g_1 and g_2 components which is tentatively attributed to conformers resulting from the bending of RuNO. DFT

calculations support the assignments of oxidation states and the general interpretation of the electronic structure.

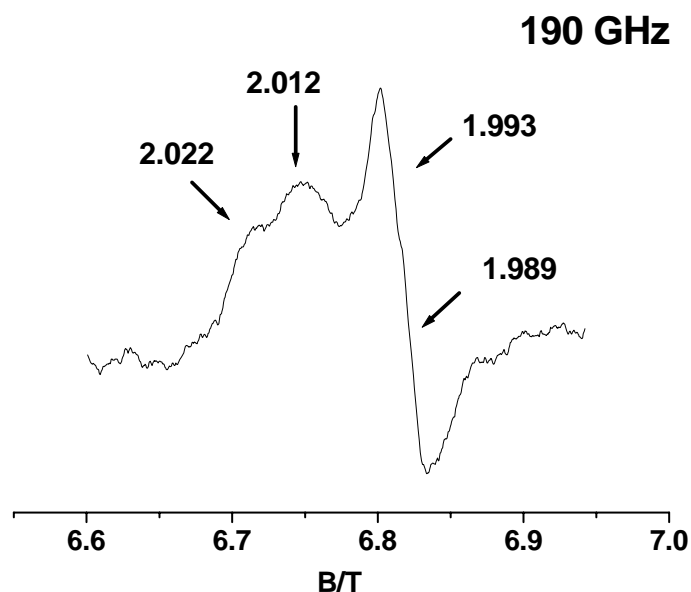
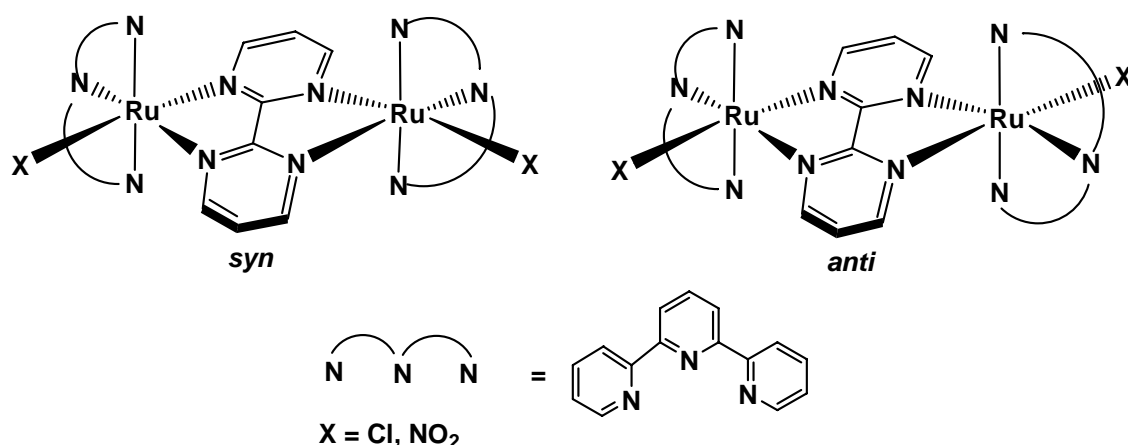


Figure 7.6. Central section (g_1 , g_2) of the G-band (190 GHz) EPR spectrum of $[\text{Ru}(\text{NO})(\text{bpym})(\text{terpy})]^{2+}$ in CH_3CN at 4.2 K.

In Chapter 5, the studies on dinuclear complexes are described. The redox series $\{(\mu\text{-bpym})[\text{RuCl}(\text{terpy})]_2\}^n$ and $\{(\mu\text{-bpym})[\text{Ru}(\text{NO}_2)(\text{terpy})]_2\}^n$, $n = (0)-(4+)$ have been studied with respect to their mixed-valent properties and attempts have been made to prepare the complex $\{(\mu\text{-bpym})[\text{Ru}(\text{NO})(\text{terpy})]_2\}^{6+}$ which contains potentially coupled electroactive metal-ligand moieties. The complexes $\{(\mu\text{-bpym})[\text{RuX}(\text{terpy})]_2\}^{2+}$, $X = \text{Cl}$ and NO_2 , are synthesised and characterised by ^1H 1D and 2D NMR, IR and mass spectroscopy. ^1H NMR spectra for $\{(\mu\text{-bpym})[\text{RuX}(\text{terpy})]_2\}^{2+}$, $X = \text{Cl}$ und NO_2 , indicate formation of both *syn* and *anti* isomers (Scheme 7.2).



Scheme 7.2. *syn* and *anti* configurations of bpy-m-bridged Ru(terpy)X complexes.

Both dinuclear complexes $\{(\mu\text{-bpy-m})[\text{RuX}(\text{terpy})]_2\}^{2+}$, $X = \text{Cl}$ and NO_2 , can undergo two reversible bpy-m-centred one-electron reduction processes and two metal-centred one-electron oxidation steps, the latter involving mixed-valent intermediates with weak intermetallic coupling as evident from low comproportionation constant K_c and weak IVCT bands in NIR. Acidification of $\{(\mu\text{-bpy-m})[\text{Ru}(\text{NO}_2)(\text{terpy})]_2\}(\text{PF}_6)_2$ does not lead to the expected $\{(\mu\text{-bpy-m})[\text{Ru}(\text{NO})(\text{terpy})]_2\}^{6+}$ but, probably because of the high charge, to the insoluble but structurally (Figure 7.7) and IR-spectroscopically characterised pseudo-base product *syn*- $\{(\mu\text{-bpy-m-}(4\text{-OH}))[\text{Ru}(\text{NO})(\text{terpy})]_2\}(\text{PF}_6)_5$. The addition of one hydroxide to one of the 4-positions of bis-chelating bpy-m interrupts the aromatic π conjugation and is accompanied by corresponding intra-pyrimidine bond length variations, however, the effect on the electronic interaction of the two different *syn* positioned $\{\text{RuNO}\}^6$ moieties remains small, possibly due to their situation *within* the central molecular π plane.

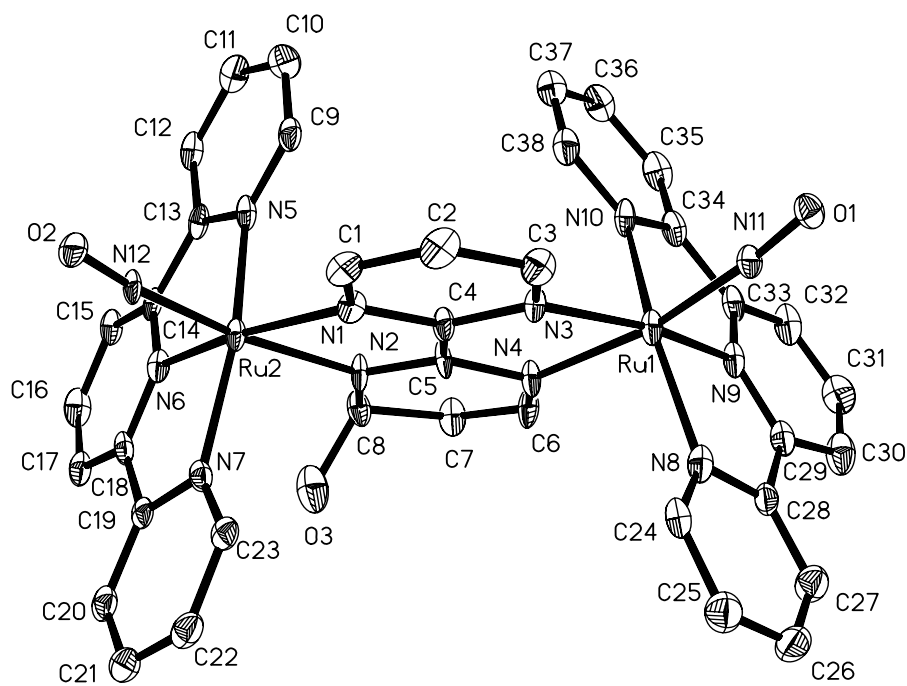


Figure 7.7. Molecular structure of the pentacation in the crystal of $\{(\mu\text{-bpym-(4-OH)})[\text{Ru}(\text{NO})(\text{terpy})]_2\}(\text{PF}_6)_5 \cdot 2.5\text{H}_2\text{O}$.

CHAPTER 8

Zusammenfassung

In dieser Arbeit wurden die Synthese und die Struktur, sowie die elektronischen Eigenschaften unterschiedlicher Übergangsmetall-Komplexe mit "non-innocent" Nitrosyl-Liganden (Schema 8.1) mit verschiedenen spektroskopischen Methoden untersucht. Sowohl die Reaktivität von gebundenem Stickstoffoxid, als auch der auftretende Elektronentransfer in Metal-Nitrosyl Komplexen wurde für unterschiedliche Metalle und verschiedene Co-Liganden untersucht.



Schema 8.1. Unterschiedliche Oxidationsstufen des Nitrosyl Liganden, welche ihn zu einem möglichen "non-innocent" Ligand machen.

In Kapitel 2 wurden experimentelle und berechnete Ergebnisse des zweistufigen Redox-Systems $[\text{Cl}_5\text{Os}(\text{NO})]^{n-}$ ($n = 1-3$) im Vergleich zu den entsprechenden ein Elektronen-Redox Systemen $[\text{Cl}_5\text{Ru}(\text{NO})]^{n-}$ und $[\text{Cl}_5\text{Ir}(\text{NO})]^{n-}$ ($n = 1,2$) diskutiert. Das Osmium System weist auffallend niedrige Oxidations und Reduktions Potentiale auf. Die Struktur der Vorstufe $(\text{PPh}_4)_2[\text{Cl}_5\text{Os}(\text{NO})]$ wurde als eine $\{\text{MNO}\}^6$ Spezies^[2] mit nahezu linearer Os–NO Anordnung von $178,5(8)^\circ$ (Abbildung 8.1) beschrieben.

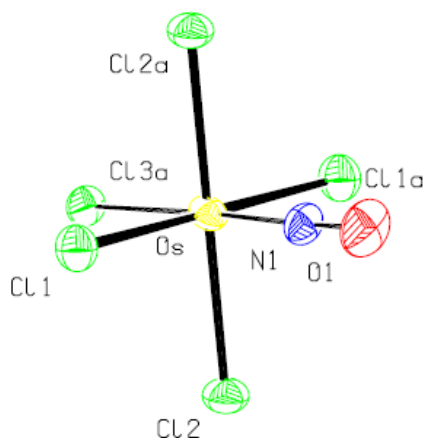


Abbildung 8.1. Molekulare Struktur des Dianion im Kristall von $(\text{Ph}_4\text{P})_2[\text{Cl}_5\text{Os}(\text{NO})] \cdot 4\text{CH}_3\text{CN}$ bei 100 K.

DFT-Berechnungen bestätigen dieses Ergebnis. Ein Vergleich der Strukturen, die für verschiedene Oxidationszustände berechnet wurden zeigt, dass in der Reihenfolge $M = \text{Ir} < \text{Os} < \text{Ru}$ eine zunehmend einfachere Reduktion der M–Cl transständigen Bindung stattfindet. Demzufolge konnte die intakte reduzierte Form $[\text{Cl}_5\text{Os}(\text{NO})]^{3-}$ weder in Lösung noch durch eine Elektrolyse in *n*-Butyronitril bei $-70\text{ }^\circ\text{C}$ beobachtet werden. Dies bestätigt auch DFT-Berechnungen und ein Vergleich mit ESR-, sowie IR-spektroelektrochemisch charakterisierten Redox-Paaren $\text{cis}-[(\text{bpy})_2\text{ClOs}(\text{NO})]^{2+/+}$ und $[(\text{CN})_5\text{Os}(\text{NO})]^{2-/3-}$. Die DFT Berechnungen weisen darauf hin, dass die Oxidation von $[\text{Cl}_5\text{Os}(\text{NO})]^{2-}$ vor allem am Metall stattfindet, das HOMO der Vorstufe setzt sich aus 58% des 5d-Orbitals von Os und aus 41% des 3d-Orbitals von Cl_{eq} zusammen. Wie beim verwandten $[(\text{CN})_5\text{Os}(\text{NO})]^{2-}$ ist die Reduktion vor allem NO-zentriert. Das LUMO von $[\text{Cl}_5\text{Os}(\text{NO})]^{2-}$ besitzt 61% π^* (NO)-Charakter mit maßgeblichem Beitrag des 5d-Orbitals von Osmium (Abbildung 8.2).

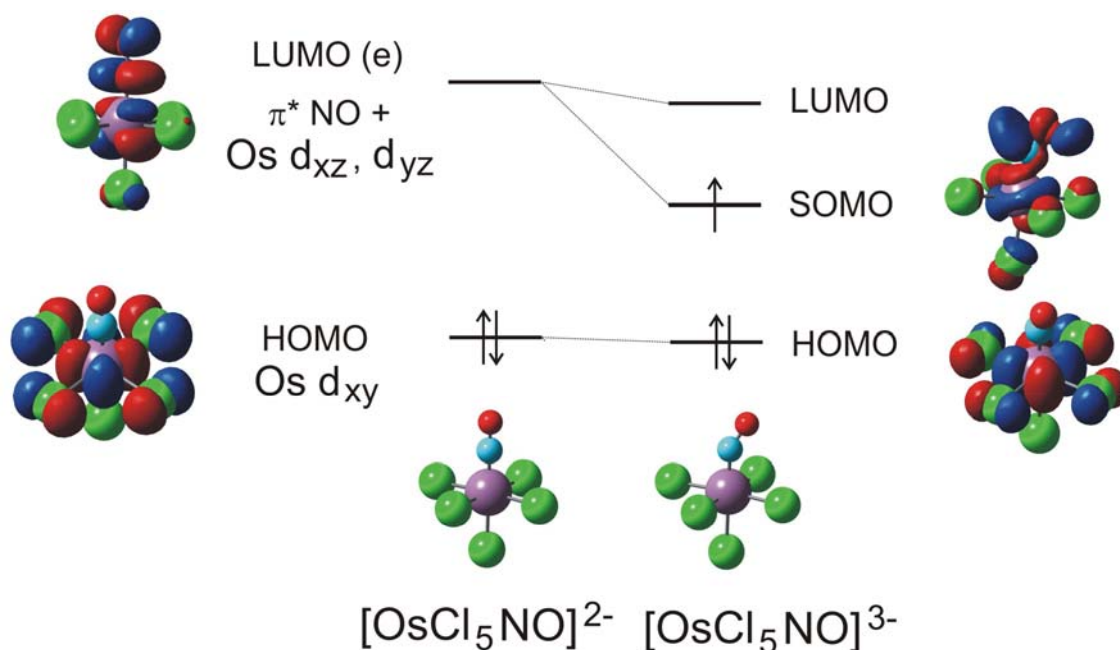


Abbildung 8.2. Darstellung der HOMO/LUMO in $[\text{Cl}_5\text{Os}(\text{NO})]^{2-}$ und $[\text{Cl}_5\text{Os}(\text{NO})]^{3-}$.

Genauere Untersuchungen der Abhängigkeit der Konfiguration von der g-Anisotropie weisen darauf hin, dass die Konfiguration des im Bezug auf die $\text{Os}^{\text{II}}\text{Cl}_4$ Ebene axial gebundenen NO-Liganden, der verschiedenen bereits in der AgCl-Datenbank veröffentlichten,^[42,43] reduzierten Formen von $[\text{Cl}_5\text{Os}(\text{NO})]^{3-}$ entweder eindeutig eklipt

oder staggert sein könnten. Es wurde berechnet, dass die staggert-Form um 105 cm^{-1} stabiler ist.

Die schwachen Absorptionsbanden $[\text{Cl}_5\text{Os}(\text{NO})]^{2-}$ bei 573, 495 und 437 nm wurden als MLCT/LLCT Übergänge in das entartete $\pi^*(\text{NO})$ LUMO bestimmt. Die Oxidierte Form $[\text{Cl}_5\text{Os}(\text{NO})]^-$ beinhaltet Os^{III} in einer $\{\text{OsNO}\}^5$ Konfiguration mit einer Spindichte von 0,711 am Osmium. In allen drei Stufen des $[\text{Cl}_5\text{Os}(\text{NO})]^{n-}$ ist die Stickstoff gebundene Form gegenüber des side-on gebundenen NO erheblich bevorzugt.

In Kapitel 3 werden ausführlich experimentelle und theoretische Studien von Ruthenium-Nitrosyl-tetraphenylporphyrin-Komplexen $[(\text{TPP})\text{Ru}(\text{NO})(\text{X})]\text{BF}_4$, TPP = tetraphenylporphyrin, X = H_2O , pyridin, 4-cyanopyridin and 4-N,N-dimethylaminopyridin beschrieben. Der Einfluss axialer Liganden auf die Redox-Eigenschaften von Ruthenium-Nitrosylporphyrin-Komplexen wurde mit Hilfe von elektrochemischen und verschiedenen spektroelektrochemischen Methoden untersucht. Die Struktur von $[(\text{TPP})\text{Ru}(\text{NO})(\text{H}_2\text{O})]\text{BF}_4$ wurde als eine $\{\text{MNO}\}^6$ Spezies^[2] mit nahezu linearer Ru-NO-Anordnung von $178,1(3)^\circ$ ermittelt (Abbildung 8.3).

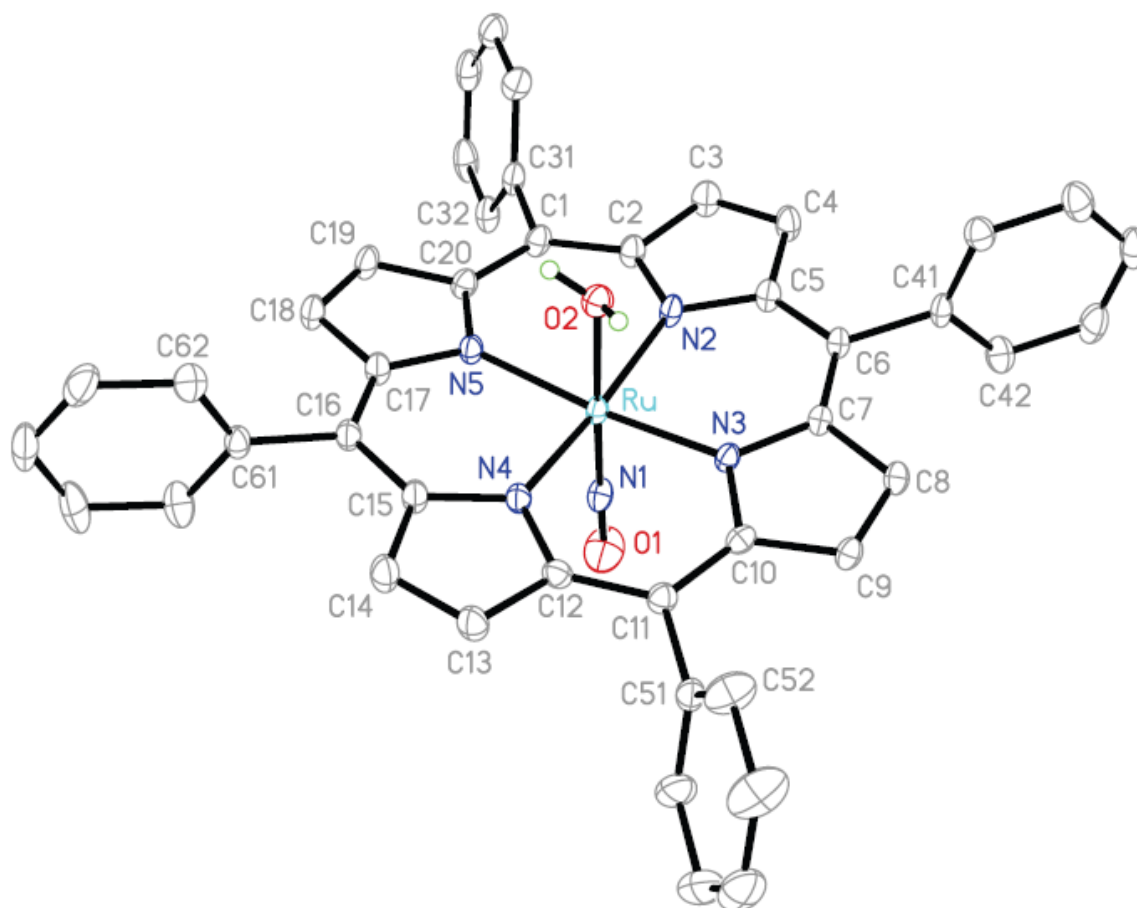


Abbildung 8.3. Molekulare Struktur des Kation im Kristall von $[(\text{TPP})\text{Ru}(\text{NO})(\text{H}_2\text{O})]\text{BF}_4 \cdot 2\text{H}_2\text{O}$ bei 173 K.

Die Verbindung $[(\text{TPP})\text{Ru}(\text{NO})(\text{H}_2\text{O})]\text{BF}_4$ durchläuft zwei ein Elektronen Prozesse im CV. Die Ergebnisse spektroelektrochemischer Messungen (IR, UV/VIS/NIR und EPR), wie einer Schwingungsbande bei 1290 cm^{-1} , eines kleinen Shifts von ν_{NO} ($\sim 20\text{ cm}^{-1}$), sowie die Beobachtung eines ESR Signals mit $g_{\text{iso}} \approx 2.00$ und einer Linienbreite von $\sim 25\text{ G}$ sprechen für ein diagnostisches Porphyrin-Radikal Anion. Dies weist darauf hin, dass die erste Oxidation im Porphyrin-Ring auftritt. Die zweite Oxidation der spektroelektrochemischen Messungen ist irreversibel.

Die Verbindungen $[(\text{TPP})\text{Ru}(\text{NO})(\text{X})]\text{BF}_4$, $\text{X} = \text{pyridin}$, 4-cyanopyridin and 4-N,N-dimethylaminopyridin, wurden NO-zentriert in einem ein-Elektronen-Schritt reduziert, wie mit Spectroelektrochemischen Studien ermittelt wurde ($\sim -300\text{ cm}^{-1}$ Verschiebung von ν_{NO}). Die ESR-Ergebnisse wurden durch den Austausch der substituierten Pyridine X nicht verändert. Die DFT-Berechnungen bestätigen die experimentellen

Ergebnisse. Die Berechnung zeigt, dass das HOMO-Orbital von $[(\text{TPP})\text{Ru}(\text{NO})(\text{H}_2\text{O})]^+$ zu 98% aus Porphyrin Orbitalen besteht, das LUMO von $[(\text{TPP})\text{Ru}(\text{NO})(\text{X})]^+$, $\text{X} = \text{pyridin}$, hat zu 53% $\pi^*(\text{NO})$ Charakter mit bedeutendem Beitrag des 4d-Orbitals von Ruthenium (17%) und Porphyrin (25%). Diese Ergebnisse bekräftigen, dass die Oxidation von $[(\text{TPP})\text{Ru}(\text{NO})(\text{H}_2\text{O})]^+$ im Porphyrin-Ring stattfindet, die Reduktion des $[(\text{TPP})\text{Ru}(\text{NO})(\text{X})]^+$ $\text{X} = \text{pyridin}$, hingegen, mit kleinem, aber nicht unbedeutenden Einfluss von X (4%) NO-zentriert ist.

In Kapitel 4 werden mononukleare Ruthenium Komplexe mit π - Akzeptor Liganden wie 2,2 bpym und 2, 2': 6', 2 terpy untersucht. Die strukturell beschriebene Vorstufe $[\text{Ru}(\text{NO}_2)(\text{bpym})(\text{terpy})](\text{PF}_6)$ zeigt die bpym- zentrierte Reduktion und eine Metall zentrierte Oxidation, wie von der ESR-Spektroskopie bestätigt werden konnte. Die Verbindung $[\text{Ru}(\text{NO})(\text{bpym})(\text{terpy})](\text{PF}_6)_3$ mit einer $\{\text{RuNO}\}^6$ Konfiguration^[2] (Winkel $\text{Ru-N-O} = 175,2(4)^\circ$; Abbildung 8.4) wurde aus $[\text{Ru}(\text{NO}_2)(\text{bpym})(\text{terpy})](\text{PF}_6)$ durch ansäuern erhalten. Die labile Verbindung $[\text{Ru}(\text{NO})(\text{bpym})(\text{terpy})]^{3+}$ bildet durch das Versetzen mit $\text{CH}_3\text{OH}/\text{CH}_3\text{CN}$ ein strukturell bestimmbares Acetonitril Substitutions-Produkt $[\text{Ru}(\text{CH}_3\text{CN})(\text{bpym})(\text{terpy})](\text{PF}_6)_2$.

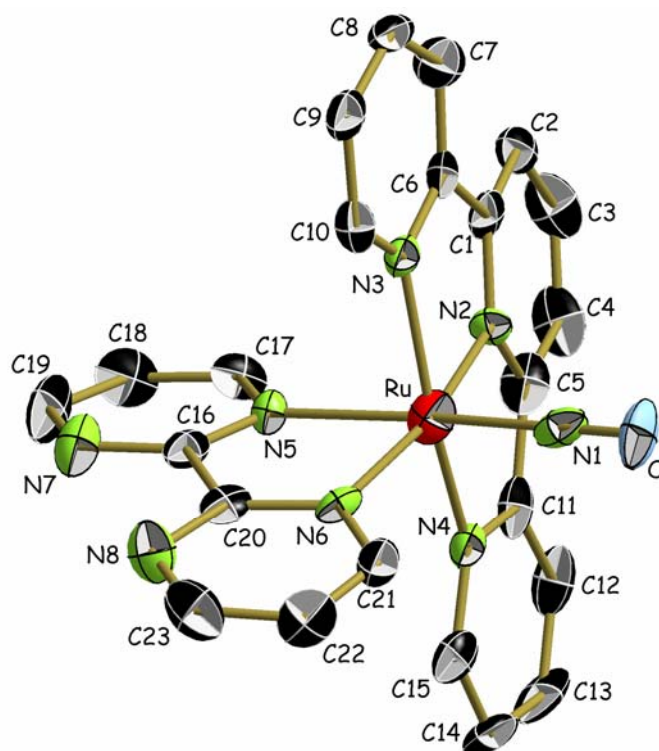


Abbildung 8.4. Molekulare Struktur des Trikatens von $[\text{Ru}(\text{NO})(\text{bpym})(\text{terpy})](\text{PF}_6)_3$ im Kristall.

Die Verbindung $[\text{Ru}(\text{NO})(\text{bpym})(\text{terpy})](\text{PF}_6)_3$ wird in drei Einelektronenschritten elektrochemisch reduziert, von denen der zum neutralen $[\text{Ru}(\text{NO})(\text{bpym})(\text{terpy})]$ führende dritte Schritt unter Adsorption an die Elektrode abläuft. Die ersten beiden Reduktionsprozesse bewirken Verschiebungen in $\nu(\text{NO})$ von 1957 über 1665 zu 1388 cm^{-1} (Abbildung 8.5), was auf eine hauptsächlich NO-zentrierte Elektronenaddition schließen lässt. Die UV/VIS/NIR-Spektroskopie zeigt langwellige Ligand-Ligand-Charge-Transfer-Absorptionen für $[\text{Ru}^{\text{II}}(\text{NO}^{-1})(\text{bpym})(\text{terpy})]^+$ im sichtbaren Bereich, während die paramagnetische Zwischenstufe $[\text{Ru}(\text{NO})(\text{bpym})(\text{terpy})]^{2+}$ kein Absorptionsmaximum oberhalb von 309 nm aufweist. EPR-Spektroskopie der letztgenannten Verbindung bei 9.5, 95 und 190 GHz (Abbildung 8.6) zeigt die typischen Merkmale der $\{\text{RuNO}\}^7$ Konfiguration^[2]. Die Hochfrequenzmessungen bei 4 und 10 K zeigen jedoch eine Aufspaltung der g_1 und g_2 Komponenten, was versuchsweise Konformeren aus dem Abknicken des RuNO zugeordnet werden kann. DFT-Berechnungen bestätigen die Zuordnung der Oxidationsstufen und die allgemeine Interpretation der elektronischen Struktur.

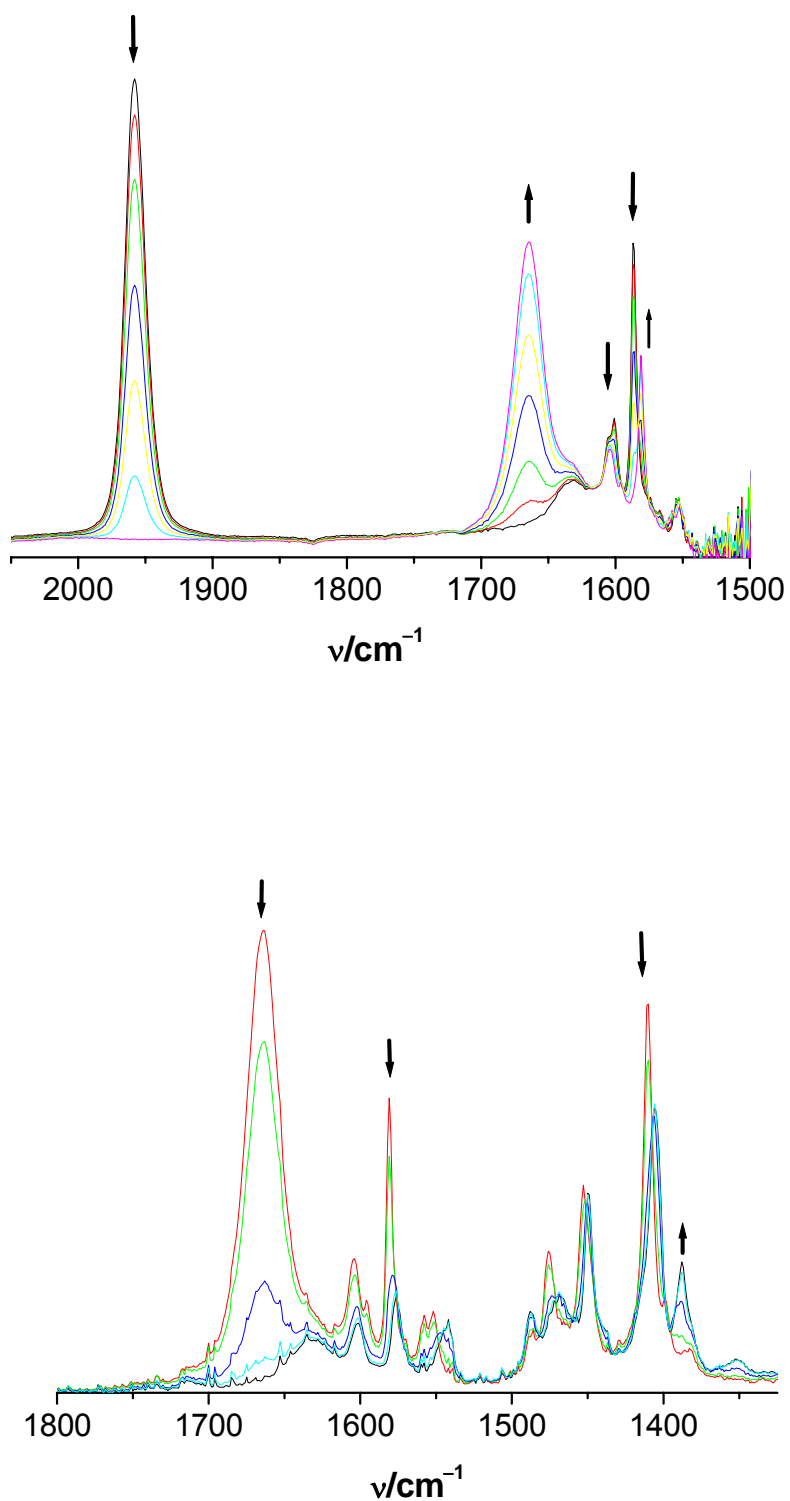


Abbildung 8.5. IR-spektroelektrochemische Spektren von $[\text{Ru}(\text{NO})(\text{bpym})(\text{terpy})](\text{PF}_6)_3$ in $\text{CD}_3\text{CN}/0.1 \text{ M } n\text{-Bu}_4\text{NPF}_6$ bei 298 K: erste (oben) und zweite Reduktion (unten).

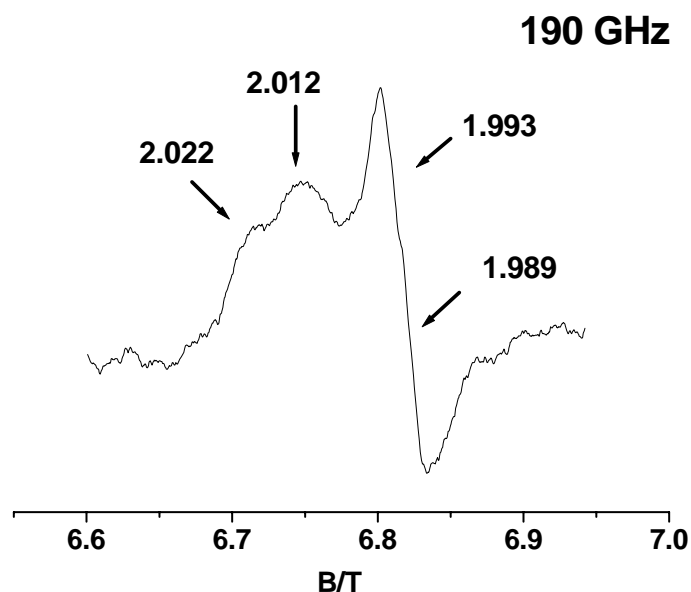
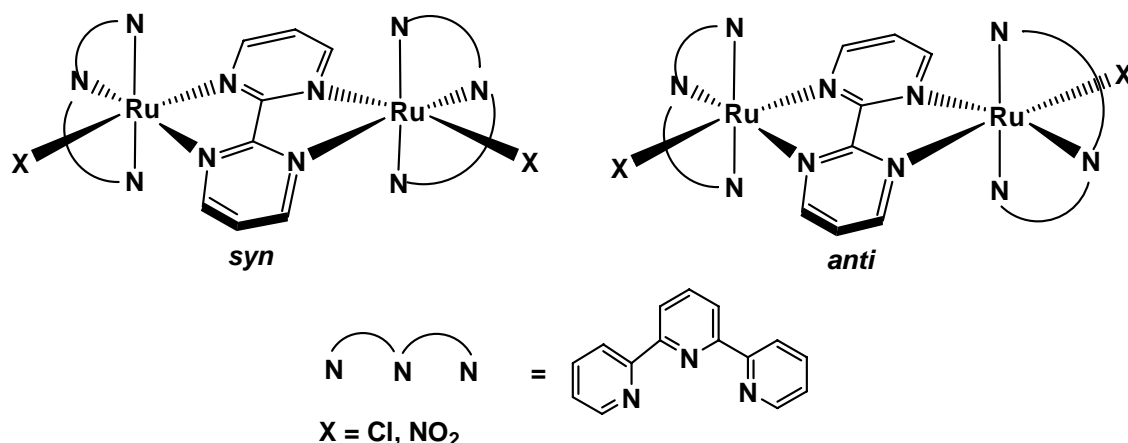


Abbildung 8.6. Mittlerer Teil (g_1 , g_2) des G-band-EPR-Spektrums (190 GHz) von $[\text{Ru}(\text{NO})(\text{bpym})(\text{terpy})]^{2+}$ in CH_3CN bei 4.2 K.

In Kapitel 5 werden die Untersuchungen an zweikernigen Komplexen beschrieben. Die Redoxreihen $\{(\mu\text{-bpym})[\text{RuCl}(\text{terpy})]_2\}^n$ und $\{(\mu\text{-bpym})[\text{Ru}(\text{NO}_2)(\text{terpy})]_2\}^n$, $n = (0)\text{-}(4+)$ wurden bezüglich ihrer gemischtvalenten Eigenschaften untersucht und es wurde versucht, den Komplex $\{(\mu\text{-bpym})[\text{Ru}(\text{NO})(\text{terpy})]_2\}^{6+}$ darzustellen, der potentiell gekoppelte elektroaktive Metall-Ligand-Einheiten enthält. Die Komplexe $\{(\mu\text{-bpym})[\text{RuX}(\text{terpy})]_2\}^{2+}$, $X = \text{Cl}$ und NO_2 wurden hergestellt und charakterisiert durch ^1H -, 1D , und 2D -NMR, IR und Massenspektroskopie. ^1H -NMR-Spektren für $\{(\mu\text{-bpym})[\text{RuX}(\text{terpy})]_2\}^{2+}$, $X = \text{Cl}$ und NO_2 weisen auf die Bildung sowohl des *syn*- als auch des *anti*- Isomeren hin (Schema 8.2).



Schema 8.2. *Syn*- und *anti*-Konfigurationen der bpy_m-verbrückten Ru(terpy)X-Komplexe.

Beide zweikernigen Komplexe $\{(\mu\text{-bpy})[\text{RuX}(\text{terpy})]_2\}^{2+}$, $\text{X} = \text{Cl}$ und NO_2 , zeigen zwei reversible bpy_m-zentrierte Einelektronen-Reduktions- und zwei metall-zentrierte Einelektronen-Oxidationsprozesse. Die letztgenannten beinhalten gemischtvalente Zwischenstufen mit schwacher intermetallischer Kopplung, wie aus der niedrigen Komproportionierungskonstanten K_c und schwachen IVCT-Banden im NIR-Bereich hervorgeht. Ansäuerung von $\{(\mu\text{-bpy})[\text{Ru}(\text{NO}_2)(\text{terpy})]_2\}(\text{PF}_6)_2$ führt nicht zu dem erwarteten $\{(\mu\text{-bpy})[\text{Ru}(\text{NO})(\text{terpy})]_2\}^{6+}$ sondern, vermutlich aufgrund der hohen Ladung, zur unlöslichen, aber strukturell (Abbildung 7.7) und IR-spektroskopisch charakterisierten Pseudo-Base *syn*- $\{(\mu\text{-bpy-m-4-OH})[\text{Ru}(\text{NO})(\text{terpy})]_2\}(\text{PF}_6)_5$. Die Addition eines Hydroxids an eine der 4-Positionen des zweifach chelatisierenden bpy_m unterbricht die aromatische π -Konjugation und wird begleitet von entsprechenden Variationen in den Bindungslängen des Pyrimidins. Der Effekt auf die elektronische Wechselwirkung der zwei *syn*-positionierten $\{\text{RuNO}\}^6$ -Einheiten bleibt jedoch gering, vermutlich wegen ihrer Stellung *innerhalb* der zentralen molekularen π -Ebene.

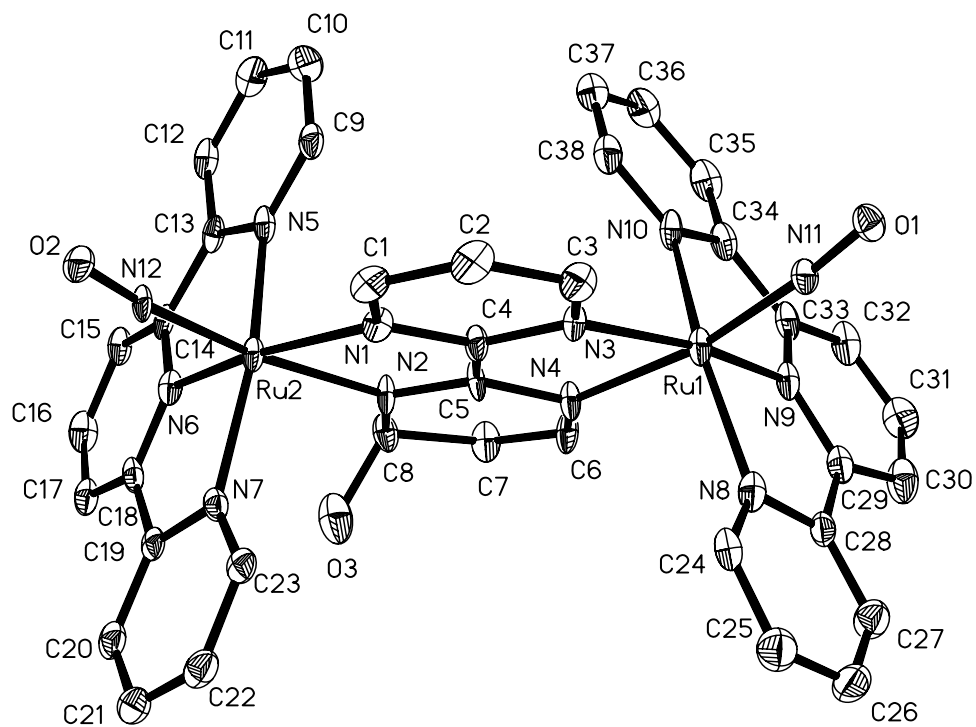


Abbildung 8.7. Molekulare Struktur des Pentakations im Kristall von $\{(\mu\text{-bpy}\text{-}(4\text{-OH}))[\text{Ru}(\text{NO})(\text{terpy})]_2\}(\text{PF}_6)_5 \cdot 2.5\text{H}_2\text{O}$.

Appendix

Bibliography

- [1] McCleverty, J. A. *Chem. Rev.* **1979**, *79*, 53.
- [2] Enemark, J. H.; Feltham, R. D. *Coord. Chem. Rev.* **1974**, *13*, 339.
- [3] Koshland, D. E. *Science* **1992**, *258*, 1861.
- [4] Palmer, R. M. J.; Ferrige, A. G.; Mocada, S. *Nature* **1987**, *327*, 524.
- [5] Murad, F. *Angew. Chem.* **1999**, *111*, 1976; *Angew. Chem. Int. Ed.* **1999**, *38*, 1856.
- [6] Wang, P. G.; Cai, T. B.; Taniguchi, N., Eds. *Nitric Oxide Donors*; Wiley-VCH: Weinheim, Germany, 2005.
- [7] Feelisch, M.; Stamler, J. S., Eds. *Methods in Nitric Oxide Research*; Wiley: Chichester, 1996.
- [8] Wang, P. G.; Xian, M.; Tang, X.; Wu, X.; Wen, Z.; Cai, T.; Janczuk, A. *Chem. Rev.* **2002**, *102*, 1091.
- [9] McCleverty, J. A. *Chem. Rev.* **2004**, *104*, 403.
- [10] Roncaroli, F.; Videla, M.; Slep, L. D.; Olabe, J. A. *Coord. Chem. Rev.* **2007**, *251*, 1903.
- [11] Westcott, B.L.; Enemark, J. L. In *Inorganic Electronic Structure and Spectroscopy*, Solomon, E. I.; Lever, A. B. P., Eds. Wiley & Sons: New York, 1999; vol. 2, p 403.
- [12] Feltham, R. D.; Enemark, J. H. *Top. Stereochem.* **1981**, *12*, 155.
- [13] Richter-Addo, G. B.; Legzdins, P. *Metal Nitrosyls*; Oxford University Press: New York, 1992.
- [14] Tolman, W. B. Ed. *Activation of Small Molecules*; Wiley-VCH: Weinheim, 2006; p 43.
- [15] Averill, B. A. *Chem. Rev.* **1996**, *96*, 2951.
- [16] Serli, B.; Zangrando, E.; Gianferrara, T.; Yellowlees, L.; Alessio, E. *Coord. Chem. Rev.* **2003**, *245*, 73.
- [17] Patra, A. K.; Mascharak, P. K. *Inorg. Chem.* **2003**, *42*, 7363.
- [18] Tfouni, E.; Krieger, M.; McGarvey, B. R.; Franco, D. W. *Coord. Chem. Rev.* **2003**, *236*, 57.
- [19] Tocheva, E. I.; Rosell, F. I.; Mauk, A. G.; Murphy, M. E. P. *Science* **2004**, *304*, 867.
- [20] Aboelella, N. W.; Reynolds, A. M.; Tolman, W. B. *Science* **2004**, *304*, 836.

-
- [21] Clarke, M. J. *Coord. Chem. Rev.* **2002**, 232, 69.
- [22] Iwamoto, M.; Hamada, H. *Catal. Today* **1991**, 10, 57.
- [23] Groothaert, M. H.; van Bokhoven, J. A.; Battiston, A. A.; Weckhuysen, B. M.; Schoonheydt, R. A. *J. Am. Chem. Soc.* **2003**, 125, 7629.
- [24] Coppens, P.; Novozhilova, I.; Kovalevsky, A. *Chem. Rev.* **2002**, 102, 861.
- [25] Jørgensen, C. K. *Oxidation Numbers and Oxidation States*, Springer Publishing: Berlin, 1969.
- [26] Ward, M. D.; McCleverty, J. A. *J. Chem. Soc., Dalton Trans.* **2002**, 275.
- [27] Veal, J. T.; Hodgson, D. J. *Inorg. Chem.* **1972**, 11, 1420.
- [28] Bottomley, F. *J. Chem. Soc., Dalton Trans.* **1975**, 2538.
- [29] Laverman, L. E.; Wanat, A.; Oszejca, J.; Stochel, G.; Ford, P. C.; van Eldik, R. *J. Am. Chem. Soc.* **2001**, 123, 285.
- [30] Marchenko, A. V.; Vedernikov, A. N.; Dye, D. F.; Pink, M.; Zaleski, J. M.; Caulton, K. G. *Inorg. Chem.* **2004**, 43, 351.
- [31] Wolak, M.; Stochel, G.; Zahl, A.; Schnepf, T.; van Eldik, R. *J. Am. Chem. Soc.* **2001**, 123, 9780.
- [32] Wanat, A.; Schnepf, T.; Stochel, G.; van Eldik, R.; Bill, E.; Wieghardt, K. *Inorg. Chem.* **2002**, 41, 4.
- [33] Sieger, M.; Sarkar, B.; Zalis, S.; Fiedler, J.; Escola, N.; Doctorovich, F.; Olabe, J. A.; Kaim, W. *Dalton Trans.* **2004**, 1797.
- [34] Ward, M. D. *Chem. Soc. Rev.* **1995**, 34, 121.
- [35] Astruc, D. *Acc. Chem. Res.* **1997**, 30, 383.
- [36] McCleverty, J. A.; Ward, M. D. *Acc. Chem. Res.* **1998**, 31, 842.
- [37] Prassides, K. Ed. *Mixed-Valency Systems: Applications in Chemistry, Physics and Biology*; Kluwer Academic Publishers: Dordrecht, 1991.
- [38] Taube, H. *Angew. Chem.* **1984**, 96, 315; *Angew. Chem. Int. Ed.* **1984**, 23, 329.
- [39] Klingstedt, F.; Arve, K.; Eränen, K.; Murzin, D. Y. *Acc. Chem. Res.* **2006**, 39, 273.
- [40] Doctorovich, F.; Salvo, F. D. *Acc. Chem. Res.* **2007**, 40, 985.
- [41] Hong, S.; Rahman, T. S.; Jacobi, K.; Ertl, G. *J. Phys. Chem. C* **2007**, 111, 12361.
- [42] Eachus, R. S.; Baetzold, R. C.; Pawlik, Th. D.; Poluektov, O. G.; Schmidt, J. *Phys. Rev. B* **1999**, 59, 8560.

-
- [43] Eachus, R. S.; Pawlik, Th. D.; Baetzold, R. C. *J. Phys.: Condens. Matter* **2000**, *12*, 8893.
- [44] Ford, P. C.; Lorkovic, I. M. *Chem. Rev.* **2002**, *102*, 993.
- [45] Patchkovskii, S.; Ziegler, T. *Inorg. Chem.* **2000**, *39*, 5354.
- [46] Karidi, K.; Garoufis, A.; Tsipis, A.; Hadjiliadis, N.; den Dulk, H.; Reedijk, J. *Dalton Trans.* **2005**, 1176.
- [47] Praneeth, V. K. K.; Neese, F.; Lehnert, N. *Inorg. Chem.* **2005**, *44*, 2570.
- [48] Ford, P. C.; Weckler, S. *Coord. Chem. Rev.* **2005**, *249*, 1382.
- [49] Paulat, F.; Lehnert, N. *Inorg. Chem.* **2007**, *46*, 1547.
- [50] Frantz, S.; Sarkar, B.; Sieger, M.; Kaim, W.; Roncaroli, F.; Olabe, J. A.; Zalis, S. *Eur. J. Inorg. Chem.* **2004**, 2902 and literature cited.
- [51] Sarkar, S.; Sarkar, B.; Chanda, N.; Kar, S.; Mobin, S. M.; Fiedler, J.; Kaim, W.; Lahiri, G. K. *Inorg. Chem.* **2005**, *44*, 6092.
- [52] Kadish, K. M.; Adamian, V. A.; Van Caemelbecke, E.; Tan, Z.; Tagliatesta, P.; Bianco, P.; Boschi, T.; Yi, G.-B.; Khan, M. A.; Richter-Addo, G. B. *Inorg. Chem.* **1996**, *35*, 1343.
- [53] Graça Zanichelli, P.; Miotto, A. M.; Estrela, H. F. G.; Rocha Soares, F.; Grassi-Kassisse, D. M.; Spadari-Bratfisch, R. C.; Castellano, E. E.; Roncaroli, F.; Parise, A. R.; Olabe, J. A.; de Brito, A. R. M. S.; Wagner Franco, D. *Inorg. Biochem.* **2004**, *98*, 1921.
- [54] Tfouni, E.; Queiroz Ferreira, K.; Gorzoni Doro, F.; Santana da Silva, R.; Novais da Rocha, Z. *Coord. Chem. Rev.* **2005**, *249*, 405.
- [55] Ford, P. C.; Laverman, L. E. *Coord. Chem. Rev.* **2005**, *249*, 391.
- [56] Ooyama, D.; Nagao, N.; Nagao, H.; Sugimoto, Y.; Howell, F. S.; Mukaida, M. *Inorg. Chim. Acta* **1997**, *261*, 45 and literature cited.
- [57] Leal, F. A.; Lorkovic, I. M.; Ford, P. C.; Lee, J.; Chen, L.; Torres, L.; Khan, M. A.; Richter-Addo, G. B. *Can. J. Chem.* **2003**, *81*, 872.
- [58] Pipes, D. W.; Meyer, T. J. *Inorg. Chem.* **1984**, *23*, 2466.
- [59] Bhattacharyya, B.; Saha, A. M.; Ghosh, P. N.; Mukherjee, M.; Mukherjee, A. K. *J. Chem. Soc., Dalton Trans.* **1991**, 501.
- [60] Wanner, M.; Scheiring, T.; Kaim, W.; Slep, L. D.; Baraldo, L. M.; Olabe, J. A.; Zalis, S.; Baerends, E. J. *Inorg. Chem.* **2001**, *40*, 5704.

-
- [61] Baumann, F.; Kaim, W.; Baraldo, L. M.; Slep, L. D.; Olabe, J. A.; Fiedler, J. *Inorg. Chim. Acta* **1999**, *285*, 129.
- [62] Ghosh, P.; Stobie, K.; Bill E.; Bothe, E.; Weyhermüller, T.; Ward, M. D.; McCleverty, J. A.; Wieghardt, K. *Inorg. Chem.* **2007**, *46*, 522.
- [63] Landry, V. K.; Pang, K.; Quan, S. M.; Parkin, G. *Dalton Trans.* **2007**, 820.
- [64] Keane, J.M.; Harman, W. D. *Organometallics* **2005**, *24*, 1786.
- [65] Gans, P.; Sabatini, A.; Sacconi, L. *Coord. Chem. Rev.* **1966**, *1*, 187.
- [66] Paulat, F.; Kuschel T.; Näther, C.; Praneeth, V. K. K.; Sander, O.; Lehnert, N. *Inorg. Chem.* **2004**, *43*, 6979.
- [67] Manoharan, P. T.; Gray, H. B. *J. Am. Chem. Soc.* **1965**, *87*, 3340.
- [68] Gray, H. B.; Manoharan, P. T.; Pearlman, J.; Riley, R. F. *Chem. Commun.* **1965**, 62.
- [69] Cheng, L.; Richter-Addo, G. B. Binding and Activation of Nitric Oxide by Metalloporphyrins and Heme in *The Porphyrin Handbook*, ed. Guillard, R; Smith, K.; Kadish, K. M. Academic Press, New York, 2000, vol. 4, ch. 33.
- [70] Alderton, W. K.; Cooper, C. E.; Knowles, R. G. *Biochem. J.* **2001**, *357*, 593.
- [71] Boon, E. M.; Huang, S. H.; Marletta, M. A. *Nat. Chem. Biol.* **2005**, *1*, 53.
- [72] Ribiero, J. M. C.; Hazzard, J. M. H.; Nussenzveig, R. H.; Champagne, D. E.; Walker, F. A. *Science* **1993**, *260*, 539.
- [73] Hrabie, J. A.; Keefer, L. K. *Chem. Rev.* **2002**, *102*, 1135.
- [74] Wyllie, G. R. A.; Schulz, C. E.; Scheidt, W. R. *Inorg. Chem.* **2003**, *42*, 5722.
- [75] Praneeth, V. K. K.; Näther, C.; Peters, G.; Lehnert, N. *Inorg. Chem.* **2006**, *45*, 2795.
- [76] Novozhilova, I. V.; Philip, C.; Lee, J.; Richter-Addo, G. B.; Bagley, K. A. *J. Am. Chem. Soc.* **2006**, *128*, 2093.
- [77] Richter-Addo, G. B.; Wheeler, R. A.; Hixson, C. A.; Chen, L.; Khan, M. A.; Ellison, M. A.; Schulz, C. E.; Scheidt, W. R. *J. Am. Chem. Soc.* **2001**, *123*, 6314.
- [78] Bohle, D. S.; Hung, C. H.; Smith, B. D. *Inorg. Chem.* **1998**, *37*, 5798.
- [79] Miranda, K. M.; Bu, X.; Lorkovic, I.; Ford, P. C. *Inorg. Chem.* **1997**, *36*, 4838.
- [80] Yi, G. -B.; Khan, M. A.; Richter-Addo, G. B. *Inorg. Chem.* **1996**, *35*, 3453.
- [81] Antipas, A.; Buchler, J. W.; Gouterman, M.; Smith, P. D. *J. Am. Chem. Soc.* **1978**, *100*, 3015.
- [82] Wyllie, G. R. A.; Scheidt, W. R. *Chem. Rev.* **2002**, *102*, 1067.

-
- [83] Bezerra, C. W. B.; da Silva, S. C.; Gambardella, M. T. P.; Santos, R. H. A.; Plicas, L. M. A.; Tfouni, E.; Franco, D. W. *Inorg. Chem.* **1999**, *38*, 5660.
- [84] Kadish, K. M. *Progr. Inorg. Chem.* **1986**, *34*, 435.
- [85] Carter, C. M.; Lee, J.; Hixson, C. A.; Powell, D. R.; Wheeler, R. A.; Shaw, M. J.; Richter-Addo, G. B. *Dalton Trans.* **2006**, 1338.
- [86] Brown, G. M.; Hopf, F. R.; Ferguson, J. A.; Meyer, T. J.; Whitten, D. G. *J. Am. Chem. Soc.* **1973**, *95*, 5939.
- [87] Kadish, K. M.; Mu, X. *Pure Appl. Chem.* **1990**, *62*, 1051.
- [88] Mu, X. H.; Kadish, K. M. *Langmuir* **1990**, *6*, 51.
- [89] Rillema, D. P.; Nagle, J. K.; Barringer, L. F.; Meyer, T. J. *J. Am. Chem. Soc.* **1981**, *103*, 56.
- [90] Scheidt, W. R.; Ellison, M. K. *Acc. Chem. Res.* **1999**, *32*, 350.
- [91] One-electron σ oxidised porphyrins are often referred to as "radical cations" because they often contain coordinated divalent metals. However, the ligands themselves are then oxidised from their normal dinegative forms, Por^{2-} , to radical anions, $\text{Por}^{\bullet-}$.
- [92] Shimomura, E. T.; Phillippi, M. A.; Goff, H. M.; Scholz, W. F.; Reed, C. A. *J. Am. Chem. Soc.* **1981**, *103*, 6778.
- [93] Fujita, E.; Chang, C. K.; Fajer, J. *J. Am. Chem. Soc.* **1985**, *107*, 7665.
- [94] Renner, M. W.; Cheng, R. J.; Chang, C. K.; Fajer, J. *J. Phys. Chem.* **1990**, *94*, 8508.
- [95] Wayland, B. B.; Newman, A. R. *Inorg. Chem.* **1981**, *20*, 3093.
- [96] Tokita, Y.; Yamaguchi, K.; Watanabe, Y.; Morishima, I. *Inorg. Chem.* **1993**, *32*, 329.
- [97] Bhaskar, G.; Krishnan, V. *Inorg. Chem.* **1985**, *24*, 3253.
- [98] Fuhrhop, J. H.; Kadish, K. M.; Davis, D. G. *J. Am. Chem. Soc.* **1973**, *95*, 5140.
- [99] Weil, J. A.; Bolton, J. R.; Wertz, J. E. *Electron Paramagnetic Resonance*, Wiley: New York, 1994.
- [100] Kaim, W.; Schwederski, B. *Bioinorganic Chemistry*, Wiley: Chichester, 1994.
- [101] Di Salvo, F.; Escola, N.; Scherlis, D. A.; Estrin, D. A.; Bondía, C.; Murgida, D.; Ramallo-López, J. M.; Requejo, F. G.; Shimon, L.; Doctorovich, F. *Chem. Eur. J.* **2007**, *13*, 8428.

-
- [102] Dillinger, S. A. T.; Schmalke, H. W.; Fox, T.; Berke, H. *Dalton. Trans.* **2007**, 3562.
- [103] Reedijk, J. *Proc. Natl. Accd. Sci. U. S. A.* **2003**, *100*, 3611.
- [104] Videla, M.; Jacinto, J. S.; Baggio, R.; Garland, M. T.; Singh, P.; Kaim, W.; Slep, L. D.; Olabe, J. A. *Inorg. Chem.* **2006**, *45*, 8608.
- [105] Sullivan, B. P.; Calvert, J. M.; Meyer, T. J. *Inorg. Chem* **1990**, *19*, 1404.
- [106] Hitchman, M. A.; Rowbottom, G. L. *Coord. Chem. Rev.* **1982**, *42*, 55.
- [107] Schubert, U.; Hofmeier, H.; Newkome, G. R. *Modern Terpyridine Chemistry*; Wiley-VCH: Weinheim, 2006.
- [108] Ernst, S. D.; Kaim, W. *Inorg. Chem.* **1989**, *28*, 1520.
- [109] Maji, S.; Chatterjee, C.; Mobin, S. M.; Lahiri, G. K. *Eur. J. Inorg. Chem.* **2007**, 3425.
- [110] Singh, P.; Sarkar, B.; Sieger, M.; Niemeyer, M.; Fiedler, J.; Zálíš, S.; Kaim, W. *Inorg. Chem.* **2006**, *45*, 4602.
- [111] Chen, Y.; Lin, F. -T.; Shepherd, R. E. *Inorg. Chem.* **1999**, *38*, 973.
- [112] Heilmann, M.; Baumann, F.; Kaim, W.; Fiedler, J. *J. Chem. Soc., Faraday Trans.* **1996**, *92*, 4227.
- [113] Stone, A. J. *Mol. Phys.* **1964**, *7*, 311.
- [114] Fischer, H. in *Free Radicals, Vol. II*; Kochi, J. K. Ed. Wiley, New York, 1973; p. 452.
- [115] Kaim, W. In *Electron Transfer in Chemistry*; Balzani, V. Ed. Wiley-VCH: Weinheim, 2001.
- [116] Fukuzumi, S.; Ohkubo, K. *Chem. Eur. J.* **2000**, *6*, 4532.
- [117] Frantz, S. *Ph. D. Thesis, University of Stuttgart*, **2003**.
- [118] Patra, S.; Sarkar, B.; Mobin, S. M.; Kaim, W.; Lahiri, G. K. *Inorg. Chem.* **2003**, *42*, 6469.
- [119] Poppe, J.; Moscherosch, M.; Kaim, W. *Inorg. Chem.* **1993**, *32*, 2640.
- [120] Kaim, W.; Ernst, S.; Kasack, V. *J. Am. Chem. Soc.* **1990**, *112*, 173.
- [121] Pöpl, A.; Hartmann, M. *Studies Surface Sci. Catal.* **2002**, *142*, 375.
- [122] Yang, T. C.; Wolfe, M. D.; Neibergall, M. B.; Mekmouche, Y.; Lipscomb, J. D.; Hoffmann, B. M. *J. Am. Chem. Soc.* **2003**, *23*, 7056.
- [123] Ernst, S.; Kaim, W. *J. Am. Chem. Soc.* **1986**, *108*, 3578.
- [124] Saji, T.; Aoyagui, S. *Electroanal. Chem. Interfac. Eletrochem.* **1975**, *58*, 401.

-
- [125] Olabe, J. A. *Adv. Inorg. Chem.* **2004**, *55*, 61.
- [126] C. Creutz, *Prog. Inorg. Chem.* **1983**, *30*, 1.
- [127] Richardson D. E.; Taube, H. *Coord. Chem. Rev.* **1984**, *60*, 107.
- [128] Demadis, K. D.; Hartshorn, D. C.; Meyer, T. J. *Chem. Rev.* **2001**, *101*, 2655.
- [129] Crutchley, R. J. *Adv. Inorg. Chem.* **1994**, *41*, 273.
- [130] Solomon, E. I.; Brunold, T. C.; Davis, M. I.; Kemsley, J. N.; Lee, S.-K.; Lehnert, N.; Neese, F.; Skulan, A. J.; Yang Y.-S.; Zhou, J. *Chem. Rev.* **2000**, *100*, 235.
- [131] Kaim, W.; Bruns, W.; Poppe, J.; Kasack, V. *J. Mol. Struct.* **1993**, *292*, 22.
- [132] Blondin, G.; Girerd, J. -J. *Chem. Rev.* **1990**, *90*, 1359.
- [133] Hush, N. S. *Coord. Chem. Rev.* **1985**, *64*, 135.
- [134] Bencini, A.; Ciofini, I.; Daul, C. A.; Ferritti, A. *J. Am. Chem. Soc.* **1999**, *121*, 11418.
- [135] Marcus, R. A. *Angew. Chem.* **1993**, *105*, 1161; *Angew. Chem. Int. Ed.* **1993**, *32*, 1111.
- [136] Dunbar, K. R.; Heintz, R. A. *Prog. Inorg. Chem.* **1997**, *45*, 283.
- [137] Creutz, C.; Taube, H. *J. Am. Chem. Soc.* **1973**, *95*, 1086.
- [138] Hush, N. S. *Prog. Inorg. Chem.* **1967**, *8*, 391.
- [139] Kaim, W.; Klein, A.; Glöckle, M. *Acc. Chem. Res.* **2000**, *33*, 755.
- [140] Robin, M. B.; Day, P. *Adv. Inorg. Chem. Radiochem.* **1967**, *10*, 247.
- [141] Braunschwig, B. S.; Creutz, C.; Sutin, N. *Chem. Soc. Rev.* **2002**, *31*, 168.
- [142] Fiedler, J.; Zalis, S.; Klein, A.; Hornung, F.; Kaim, W. *Inorg. Chem.* **1996**, *35*, 3039.
- [143] Nelsen, S. F. *Chem. Eur. J.* **2000**, *6*, 581.
- [144] Lambert, C.; Nöll, G.; Schelter, J. *Nature Mat.* **2002**, *1*, 69.
- [145] Zalis, S.; Kaim, W. *Main Group Chem.* **2007**, *6*, 267.
- [146] Kaim, W. in *New Trends in Molecular Electrochemistry*, Pombeiro, A. J. L. Ed., Fontis Media, Lausanne 2004, p 127.
- [147] Baumann, F.; Kaim, W.; Denninger, G.; Kümmerer, H.-J.; Fiedler, J. *Organometallics* **2005**, *24*, 1966.
- [148] Bunting, J. W.; Meathrel, W. G. *Can. J. Chem.* **1974**, *52*, 303.
- [149] Boubaker, T.; Goumont, R.; Jan, E.; Terrier, F. *Org. Biomol. Chem.* **2003**, *12*, 2764.
- [150] Gillard, R. D.; Hughes, C. T.; Williams, P. A. *Transition Met. Chem.* **1976**, *1*, 51

-
- [151] Zhang, X.-M.; Tong, M.-L.; Chen, X.-M. *Angew. Chem.* **2002**, *114*, 1071; *Angew. Chem. Int. Ed.* **2002**, *41*, 1029.
- [152] Kaim, W. *Inorg. Chem.* **1984**, *23*, 3365.
- [153] Schwach, M.; Hausen, H.-D.; Kaim, W. *Chem. Eur. J.* **1996**, *2*, 446.
- [154] Sieger, M.; Vogler, C.; Klein, A.; Knödler, A.; Wanner, M.; Fiedler, J.; Zalis, S.; Snoeck, T. L.; Kaim, W. *Inorg. Chem.* **2005**, *44*, 4637.
- [155] Kasack, V.; Kaim, W.; Binder, H.; Jordanov, J.; Roth, E. *Inorg. Chem.* **1995**, *34*, 1924.
- [156] Scheiring, T.; Kaim, W.; Olabe, J. A.; Parise, A. R.; Fiedler, J. *Inorg. Chim. Acta* **2000**, *300-302*, 125.
- [157] Petersen, J. D.; Murphy, W. R., Jr.; Sahai, R.; Brewer, K. J.; Ruminski, R. R. *Coord. Chem. Rev.* **1985**, *64*, 261.
- [158] Ernst, S.; Kasack, V.; Kaim, W. *Inorg. Chem.* **1988**, *27*, 1146.
- [159] Baumann, F.; Kaim, W.; Garcia Posse, M.; Katz, N. E. *Inorg. Chem.* **1998**, *37*, 658.
- [160] Kaim, W.; Lahiri, G. K. *Angew. Chem.* **2007**, *119*, 1808; *Angew. Chem. Int. Ed.* **2007**, *46*, 1778.
- [161] Braterman, P. S.; Song, J.-I.; Kohlmann, S.; Vogler, C.; Kaim, W. *J. Organomet. Chem.* **1991**, *411*, 207.
- [162] Kaim, W.; Sarkar, B. *Coord. Chem. Rev.* **2007**, *251*, 584.
- [163] Singh, P.; Fiedler, J.; Zálíš, S.; Duboc, C.; Niemeyer, M.; Lissner, F.; Schleid, Th.; Kaim, W. *Inorg. Chem.* **2007**, *46*, 9254.
- [164] Barra, A.-L.; Brunel, L.-C.; Robert, J. B. *Chem. Phys. Lett.* **1990**, *165*, 107.
- [165] Muller, F.; Hopkins, M. A.; Coron, N.; Gryndberg, M.; Brunel, L.-C.; Martinez, G. *Rev. Sci. Instrum.* **1989**, *60*, 3681.
- [166] Krejcik, M.; Danek, M.; Hartl, F. *J. Electroanal. Chem.* **1991**, *317*, 179.
- [167] Fonseca Guerra, C.; Snijders, J. G.; Te Velde, G.; Baerends, E. J. *Theor. Chim. Acc.* **1998**, *99*, 391.
- [168] van Gisbergen, S. J. A.; Snijders, J. G.; Baerends, E. J. *Comput. Phys. Commun.* **1999**, *118*, 119.
- [169] Frisch, M. J.; Trucks, G. W.; Schlegel, H. B.; Scuseria, G. E.; Robb, M. A.; Cheeseman, J. R.; Montgomery, Jr., J. A.; Vreven, T.; Kudin, K. N.; Burant, J. C.; Millam, J. M.; Iyengar, S. S.; Tomasi, J.; Barone, V.; Mennucci, B.; Cossi, M.;

Scalmani, G.; Rega, N.; Petersson, G. A.; Nakatsuji, H.; Hada, M.; Ehara, M.; Toyota, K.; Fukuda, R.; Hasegawa, J.; Ishida, M.; Nakajima, T.; Honda, Y.; Kitao, O.; Nakai, H.; Klene, M.; Li, X.; Knox, J. E.; Hratchian, H. P.; Cross, J. B.; Adamo, C.; Jaramillo, J.; Gomperts, R.; Stratmann, R. E.; Yazyev, O.; Austin, A. J.; Cammi, R.; Pomelli, C.; Ochterski, J. W.; Ayala, P. Y.; Morokuma, K.; Voth, G. A.; Salvador, P.; Dannenberg, J. J.; Zakrzewski, V. G.; Dapprich, S.; Daniels, A. D.; Strain, M. C.; Farkas, O.; Malick, D. K.; Rabuck, A. D.; Raghavachari, K.; Foresman, J. B.; Ortiz, J. V.; Cui, Q.; Baboul, A. G.; Clifford, S.; Cioslowski, J.; Stefanov, B. B.; Liu, G.; Liashenko, A.; Piskorz, P.; Komaromi, I.; Martin, R. L.; Fox, D. J.; Keith, T.; Al-Laham, M. A.; Peng, C. Y.; Nanayakkara, A.; Challacombe, M.; Gill, P. M. W.; Johnson, B.; Chen, W.; Wong, M. W.; Gonzalez, C.; Pople, J. A. Gaussian 03, Revision B.02; Gaussian, Inc.: Wallingford, CT, 2004.

[170] Becke, A. D. *Phys. Rev. A* **1988**, *38*, 3098.

[171] Perdew, J. P. *Phys. Rev. A* **1986**, *33*, 8822.

[172] van Lenthe, E.; van der Avoird, A.; Wormer, P. E. S. *J. Chem. Phys.* **1998**, *108*, 4783.

[173] van Lenthe, E.; van der Avoird, A.; Wormer, P.E. S. *J. Chem. Phys.* **1997**, *107*, 2488.

[174] Schipper, P. R. T.; Gritsenko, O. V.; van Gisbergen, S. J. A.; Baerends, E. J. *J. Chem. Phys.* **2000**, *112*, 1344.

[175] Woon, D. E.; Dunning, T. H. J. *J. Chem. Phys.* **1993**, *98*, 1358.

[176] Andrae, D.; Häussermann, U.; Dolg, M.; Stoll, H.; Preuss, H. *Theor. Chim. Acta* **1990**, *77*, 123.

[177] Perdew, J. P.; Wang, Y. *Phys. Rev. B* **1992**, *45*, 13244.

[178] Becke, A. D. *J. Chem. Phys.* **1993**, *98*, 5648.

[179] te Velde, G.; Bickelhaupt, F. M.; van Gisbergen, S. J. A.; Fonseca Guerra, C.; Baerends, E. J.; Snijders, J. G.; Ziegler, T. *J. Comput. Chem.* **2001**, *22*, 931.

[180] ADF2004.01, SCM, Theoretical Chemistry, Vrije Universiteit, Amsterdam, The Netherlands, <http://www.scm.com>.

[181] Perdew, J. P.; Burke, K.; Ernzerhof, M. *Phys. Rev. Lett.* **1996**, *77*, 3865.

[182] Hariharan, P. C.; Pople, J. A., *Theo. Chim. Acta* **1973**, *28*, 213.

[183] Woon D. E.; Dunning T. H., Jr. *J. Chem. Phys.* **1995**, *103*, 4572.

-
- [184] Kober, E. M.; Caspar, J. V.; Sullivan, B. P.; Meyer, T. J. *Inorg. Chem.* **1988**, *27*, 4587.
- [185] Hope, H. *Progr. Inorg. Chem.* **1995**, *41*, 1.
- [186] SHELXTL PC 5.03, Siemens Analytical X-Ray Instruments Inc.: Madison, WI, 1994.
- [187] Sheldrick, G. M. *Program for Crystal Structure Solution and Refinement*: Universität Göttingen, 1997.
- [188] Sheldrick, G. M. *Programme SHELXS*: Göttingen, 1997.
- [189] Sheldrick, G. M. *SHELXTL*, version 5.10; Bruker AXS Inc.: Madison, Wisconsin, 1998.
- [190] Herrendorf, W.; Bärnighausen, H. *HABITUS*: Karlsruhe, Germany, 1993.
- [191] CRYSTAL IMPACT *Programme DIAMOND, Version 2.1e*: Bonn, 2001.

Abbreviations

A	ampere/hyperfine coupling constant
AL	ancillary ligand
asym	asymmetric
av	average
ax	axial
B	magnetic field
BL	bridging ligand
bpy	2,2'-bipyridine
bpym	2,2'-bipyrimidine
br	broad
C	chemical reaction
calc.	calculated
cm	centimetre
Cp	C ₅ H ₅
d	doublet
dd	doublet of a doublet
deg	degree
dt	doublet of a triplet
δ	chemical shift
ΔG	free energy change
ΔE _{pp}	difference in electrochemical peak to peak potential
Δg	g anisotropy
Δv _{1/2}	band width at half height
e	exponential
E	potential/electron transfer reaction
E _{pa}	anodic peak potential
E _{pc}	cathodic peak potential
ε	molar extinction coefficient
EPR	electron paramagnetic resonance
EtOH	ethanol
eq	equatorial
eq.	equivalence

Eq.	equation
exp	experimental
<i>fac</i>	facial
FeCp ₂ ⁺⁰	ferrocenium/ferrocene
FT	fourier transform
g	gram
g _e	free electron g factor
G	gauss
GHz	gigahertz
H _{AB}	electronic coupling parameter
HOMO	highest occupied molecular orbital
Hz	hertz
I	nuclear spin/current
IR	infrared
irr	irreversible
iso	isotropic
IVCT	inter-valence charge transfer
k	rate constant
K	Kelvin
K _c	comproportionation constant
L	ligand
λ	wavelength
LF	ligand field
LLCT	ligand-to-ligand charge transfer
LMCT	ligand-to-metal charge transfer
LUMO	lowest unoccupied molecular orbital
m	multiplet
M	molar/metal
max	maximum
MCD	magnetic circular dichroism
MeOH	methanol
mg	milligram
MHz	megahertz
μA	microampere

mL	millilitre
MLCT	metal-to-ligand charge transfer
mm	millimetre
MMCT	metal-to-metal charge transfer
mmol	millimole
MO	molecular orbital
mol	mole
mT	millitesla
mV	millivolt
n	number of moles
ν	wavenumbers
NHE	normal hydrogen electrode
NIR	near infrared
nm	nanometre
NMR	nuclear magnetic resonance
NO	nitric oxide
n. o.	not observed
n. r.	not reported
<i>n</i> -Bu ₄ NPF ₆	<i>n</i> -tetrabutylammonium hexafluorophosphate
<i>n</i> -Bu ₄ NClO ₄	<i>n</i> -tetrabutylammonium perchlorate
<i>n</i> -PrCN	<i>n</i> -butyronitrile
°	degree
°C	degree centigrade
OTTLE cell	optically transparent thin-layer electrode cell
ox	oxidised
Ph	phenyl
Por	porphyrin
ppm	parts per million
py	pyridine
R	gas constant
red	reduced
ref.	reference
s	strong (IR band)/singlet
S	electron spin

SCE	standard calomel electrode
sh	shoulder (UV or IR band)
sim.	simulated
SOMO	singly occupied molecular orbital
sym	symmetric
t	triplet
T	temperature/Tesla
TPP	tetraphenylporphyrin
terpy	2,2':6',2''-terpyridine
UV	ultra-violet
V	volt
vs	very strong (IR band)
vs.	versus
VIS	visible
Z	atomic number

List of Publications

- [1] Pseudo-base formation in the attempted synthesis of a conjugatively coupled bis(nitrosylruthenium) complex and spectroelectrochemistry of bipyrimidine-bridged dinuclear Ru(terpy)X precursor compounds (X = Cl, NO₂). **Priti Singh**, Monika Sieger, Jan Fiedler, Cheng-Yong Su and Wolfgang Kaim, *Dalton Trans.* *in print*.
- [2] Spectroelectrochemistry and DFT analysis of a new {RuNO}ⁿ redox system with multifrequency EPR suggesting conformational isomerism in the {RuNO}⁷ state. **Priti Singh**, Jan Fiedler, Carole Duboc, Mark Niemeyer, Falk Lissner, Thomas Schleid and Wolfgang Kaim, *Inorg. Chem.*, **2007**, *46*, 9254-9261.
- [3] Singlet diradical complexes of ruthenium and osmium: Geometrical and electronic structures and their unexpected changes on oxidation. Subhas Samanta. **Priti Singh**, Jan Fiedler, Stanislav Zálíš, Wolfgang Kaim and Sreebrata Goswami, *Inorg. Chem.* *in print*.
- [4] Redox properties of ruthenium nitrosyl porphyrin complexes with different axial ligation: Structural, spectroelectrochemical (FTIR, UV-VIS-NIR, ESR) and theoretical Studies. **Priti Singh**, Atanu Kumar Das, Biprajit Sarkar, Mark Niemeyer, Federico Roncaroli, José A. Olabe, Jan Fiedler, Stanislav Zálíš and Wolfgang Kaim, *Inorg. Chem.* *in print*.
- [5] Singlet diradical complexes of chromium, molybdenum, and tungsten with azo anion radical ligands from M(CO)₆ precursors. Anasuya Sanyal, Sudipta Chatterjee, Alfonso Castineiras, Biprajit Sarkar, **Priti Singh**, Jan Fiedler, Stanislav Zalis, Wolfgang Kaim and Sreebrata Goswami, *Inorg. Chem.*, **2007**, *46*, 8584-8593.
- [6] A radical-bridged bis(ferrocenylcopper(I)) complex: Structural identity, multifrequency EPR, and spectroelectrochemistry. Sayak Roy, Monika Sieger, **Priti Singh**, Mark Niemeyer, Jan Fiedler, Carole Duboc and Wolfgang Kaim, *Inorganica Chimica acta*, *in print*.

- [7] New ruthenium nitrosyl complexes with tris (1-pyrazolyl) methane (tpm) and 2,2'-bipyridine (bpy) coligands: Structure, spectroscopy, and electrophilic and nucleophilic reactivities of bound nitrosyl. Mariela Videla, Julia'n S. Jacinto, Ricardo Baggio, Mari'a T. Garland, **Priti Singh**, Wolfgang Kaim, Leonardo D. Slep, and Jose' A. Olabe, *Inorg. Chem.*, **2006**, *45*, 8608-8617.
- [8] The metal-NO interaction in the redox systems $[\text{Cl}_5\text{Os}(\text{NO})]^{n-}$, $n = 1-3$, and *cis*- $[(\text{bpy})_2\text{ClOs}(\text{NO})]^{2+/+}$: Calculations, structural, electrochemical and spectroscopic results. **Priti Singh**, Biprajit Sarkar, Monika Sieger, Mark Niemeyer, Jan Fiedler, Stanislav Zálíš and Wolfgang Kaim, *Inorg. Chem.*, **2006**, *45*, 4602-4609.
- [9] Coupling reactions of ferrocenylacetylene with mononuclear metal carbonyls $\text{Fe}(\text{CO})_5$ and $\text{M}(\text{CO})_6$ ($\text{M} = \text{Mo}, \text{W}$): Synthesis and characterization of $[\text{Fe}(\text{CO})_2\{\eta^5\text{-}2,5\text{Fc}_2\text{C}_5\text{H}_2\text{CO}\}\text{C}(\text{Fc})=\text{CH}]$, $[\text{Fe}(\text{CO})_2\{\eta^2: \eta^2\text{-}2,5\text{-Fc}_2\text{C}_4\text{H}_2\text{Fe}(\text{CO})_3\} \mu\text{-CO}]$, $[\text{Fe}(\text{CO})_3\{\eta^2: \eta^2\text{-}2,5\text{-Fc}_2\text{C}_4\text{H}_2\text{CO}\}]$, 1,2,4-triferrocenylbenzene, 2,5-diferrocenylthiophene, and 2,5-diferrocenylselenophene. Pradeep Mathur, Amrendra K. Singh, Vinay K. Singh, **Priti Singh**, Rahul Rahul, Shaikh M. Mobin, and Carsten Thöne, *Organometallics*, **2005**, *24*, 4793-4798.

Curriculum Vitae

Name: Priti Singh
Date and place of birth: 30.07.1982 in Varanasi (India)
Sex: Female
Nationality: Indian
Marital status: Single

Schooling

January 1986 to May 1999
CHS (India)

Studies

August 1999 to June 2002
Banaras Hindu University (India); Degree: Bachelor of Science;
Subjects: Chemistry, Physics, Mathematics, English; Specialisation:
Chemistry.

August 2003 to May 2004
Indian Institute of Technology Bombay, Mumbai (India); Degree:
Master of Science; Specialisation: Inorganic Chemistry; Title of Masters
thesis: Reactivity studies of chalcogen bridged metal carbonyl clusters.

September 2004 to January 2008
Doctoral work at the *Institut für Anorganische Chemie der Universität
Stuttgart* under the guidance of Prof. Dr. W. Kaim.
Title: The electron transfer chemistry of nitrosyl complexes.

October 2004 to September 2007
College student in the Graduate College „Modern Methods of Magnetic
Resonance in Materials Science“ at the *Universität Stuttgart*.

Positions held

September 2004 to September 2007
Wissenschaftliche Hilfskraft at the *Institut für Anorganische Chemie der
Universität Stuttgart*.

October 2007 to July 2008
Wissenschaftliche Angestellte at the *Institut für Anorganische Chemie
der Universität Stuttgart*.